HZDR-049

Wissenschaftlich-Technische Berichte
HZDR-049 2014 · ISSN 2191-8708

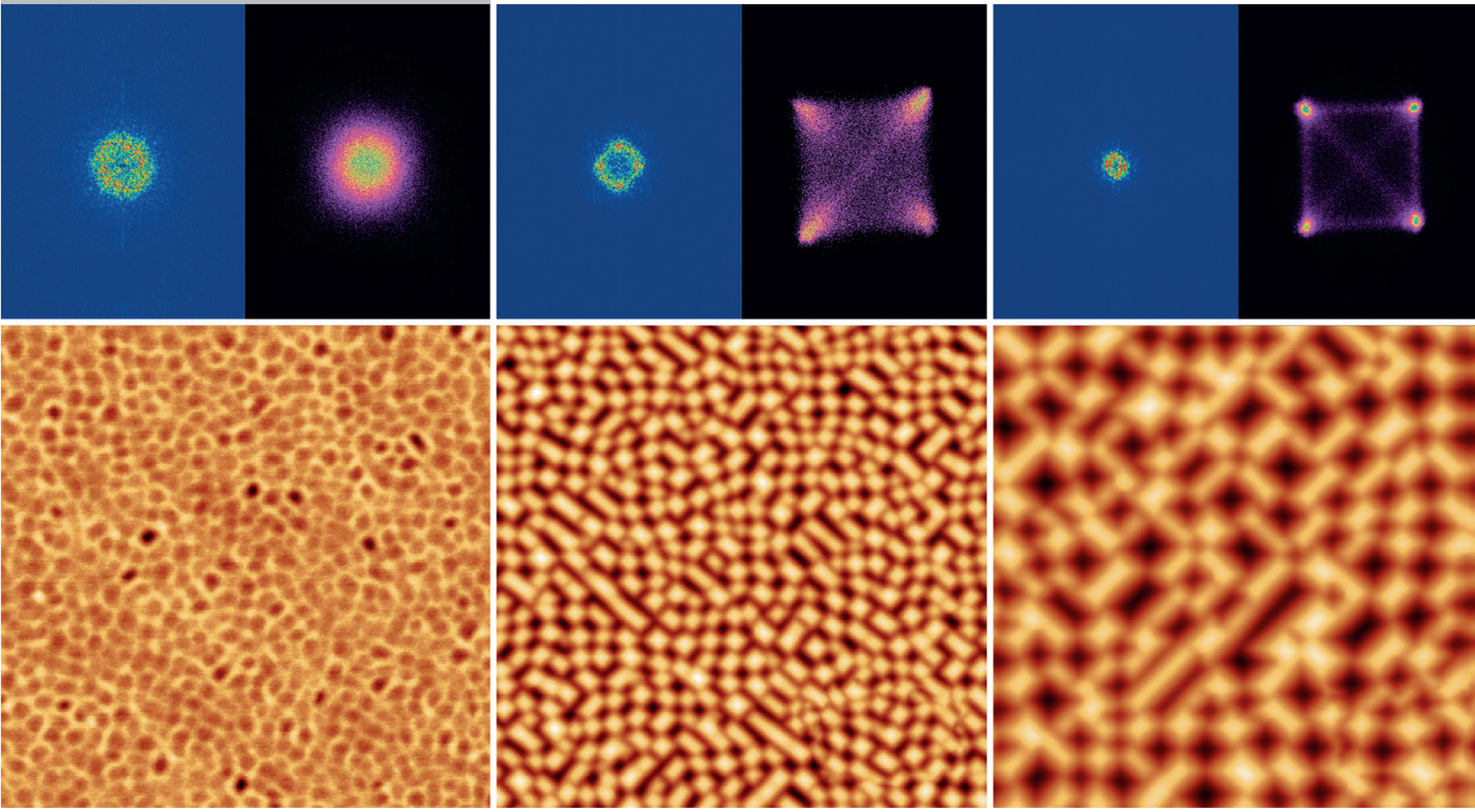

ANNUAL REPORT 2013

INSTITUTE OF ION BEAM PHYSICS
AND MATERIALS RESEARCH

HZDR

HELMHOLTZ
ZENTRUM DRESDEN
ROSSENDORF

Wissenschaftlich-Technische Berichte
HZDR–049

Annual Report 2013

Institute of Ion Beam Physics and Materials Research

Editors

A. L. Cordeiro, J. Fassbender,
V. Heera, M. Helm

HZDR
HELMHOLTZ
ZENTRUM DRESDEN
ROSSENDORF

Cover Picture

Atomic force microscope images (4 x 4 μm^2) showing checkerboard patterns on Ge (100) surfaces induced by Ar$^+$ irradiation at a temperature of 350 ^{o}C. The ion fluences are 1×10^{17} cm^{-2} (left image), 1×10^{18} cm^{-2} (middle image), and 1×10^{19} cm^{-2} (right image). At this temperature the surface remains crystalline and self-organized nanostructures grow as inverse pyramids into the surface. The pattern exhibits a fourfold symmetry with an orientation along the <100> crystal directions. The upper images show the corresponding two-dimensional Fourier transform (left) and two-dimensional angle distribution (right) of the patterns. The formation of these nanopatterns is explained by a "Reverse Epitaxy" process.

For further information see:
Xin Ou et al., Phys. Rev. Lett. **111**, 016101 (2013),
reprinted at pp. 11 - 15 of this Annual Report.

Print edition: ISSN 2191-8708
Electronic edition: ISSN 2191-8716

Published by Helmholtz-Zentrum Dresden-Rossendorf e.V.

This report is also available at http://www.hzdr.de/FWI

Helmholtz-Zentrum Dresden-Rossendorf e.V.
Institute of Ion Beam Physics and Materials Research
P.O. Box 51 01 19
01314 Dresden
Germany

Directors	Prof. Dr. M. Helm	Prof. Dr. J. Fassbender
Phone	+ 49 (351) 260 2260	+ 49 (351) 260 3096
Fax	+ 49 (351) 260 3285	+ 49 (351) 260 3285
Email	m.helm@hzdr.de	j.fassbender@hzdr.de

http://www.hzdr.de/FWI

Preface by the directors

The year 2013 was the third year of HZDR as a member of the Helmholtz Association (HGF), and we have made progress of integrating ourselves into this research environment of national research centers. In particular, we were preparing for the evaluation in the framework of the so-called program oriented funding (POF), which will hopefully provide us with a stable funding for the next five years (2015 – 2019). In particular, last fall we have submitted a large proposal in collaboration with several other research centers. The actual evaluation will take place this spring. Most of our activities are assigned to the program "**From Matter to Materials and Life**" (within the research area "Matter"). A large fraction of this program is related to the operation of large-scale research infrastructures (or user facilities), one of which is our Ion Beam Center (IBC). The second large part of our research is labelled "in-house research", reflecting the work driven through our researchers without external users, but still mostly utilizing our large-scale facilities such as the IBC, and, to a lesser extent, the free-electron laser. Our in-house research is performed in three so-called research themes, as depicted in the schematic below. What is missing there for simplicity is a small part of our activities in the program "Nuclear Waste Management and Safety" (within the research area "Energy").

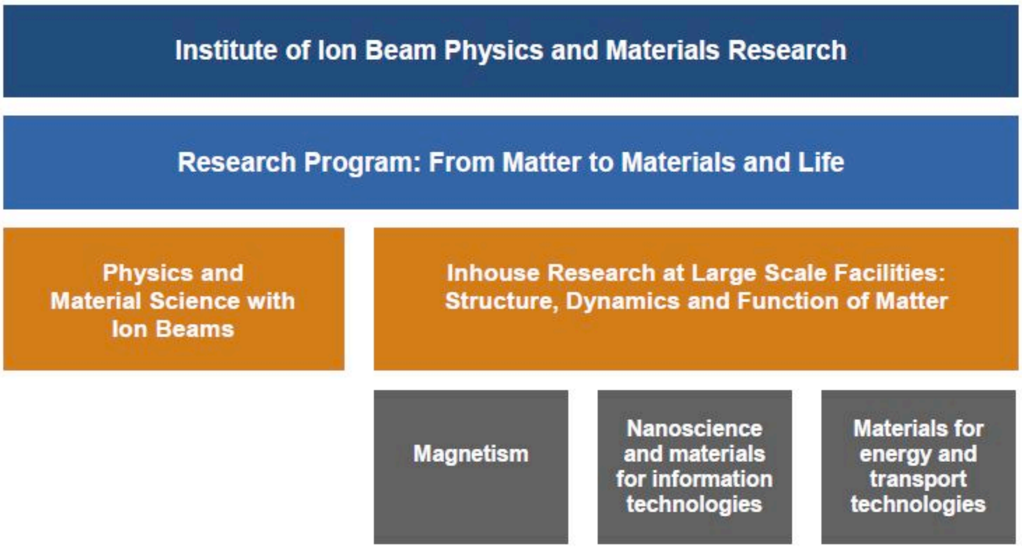

In order to make our publication list in this Annual Report a bit more reader friendly, we decided to arrange our publications according to (roughly) this division. We have kept our high level with about 150 publications in total, 11 of which are reprinted here in this Annual Report. The research spans from semiconductor physics and magnetism to materials science using ion beams. A very nice success last year was the approval of another Helmholtz Young Investigators group, namely by Dr. Alina Deac on "Spin-torque devices for information-communication technology".

A rather big change for us was the retirement of three eminent and merited scientists, who have contributed to shaping the research at our institute for many years: Dr. Bernd Schmidt, for more than two decades head of our clean room, Dr. Karl-Heinz Heinig, who has continuously fed the ion beam materials science with new and original ideas, and Dr. Andreas Kolitsch, who is now CEO of our spin off company, the HZDR Innovation that is mainly handling the implantation services for industrial customers. We are very grateful to them and wish them all the best for their next period of life.

Finally we would like to cordially thank all partners, friends, and organizations who supported our progress in 2013. Special thanks are due to the Executive Board of the Helmholtz-Zentrum Dresden-Rossendorf, the Minister of Science and Arts of the Free State of Saxony, and the Minister of Education and Research of the Federal Government of Germany. Numerous partners from universities, industry and research institutes all around the world contributed essentially, and play a crucial role for the further development of the institute. Last but not least, the directors would like to thank again all IIM staff for their efforts and excellent contributions in 2013.

Prof. Manfred Helm

Prof. Jürgen Fassbender

Contents

Selected Publications

Statistics

Selected Publications

Photo: HZDR / O. Killig

Copyright remarks

The following journal articles are reprinted with kind permission from:

Ou, X.; Keller, A.; Helm, M.; Fassbender, J.; Facsko, S.
Reverse epitaxy of Ge: Ordered and faceted surface patterns
Physical Review Letters, Vol. **111**, Issue 1, Art.-No. 016101
© 2013, The American Physical Society
DOI: 10.1103/PhysRevLett.111.016101

Wintz, S.; Bunce, C.; Neudert, A.; Körner, M.; Strache, T.; Buhl, M.; Erbe, A.; Gemming, S.; Raabe, J.; Quitmann, C.; Fassbender, J.
Topology and origin of effective spin meron pairs in ferromagnetic multilayer elements
Physical Review Letters, Vol. **110**, Issue 17, Art.-No. 177201
© 2013, The American Physical Society
DOI: 10.1103/PhysRevLett.110.177201

Rice, W. D.; Kono, J.; Zybell, S.; Winnerl, S.; Bhattacharyya, J.; Schneider, H.; Helm, M.; Ewers, B.; Chernikov, A.; Koch, M.; Chatterjee, S.; Khitrova, G.; Gibbs, H. M.; Schneebeli, L.; Breddermann, B.; Kira, M.; Koch, S.W.
Observation of forbidden exciton transitions mediated by Coulomb interactions in photoexcited semiconductor Quantum Wells
Physical Review Letters, Vol. **110**, Issue 13, Art.-No. 137404
© 2013, The American Physical Society
DOI: 10.1103/PhysRevLett.110.137404

Friedrich, D.; Schmidt, B.; Heinig, K.-H.; Liedke, B.; Mücklich, A.; Hübner, R.; Wolf, D.; Kölling, S.; Mikolajick, T.
Sponge-like Si-SiO$_2$ nanocomposite—Morphology studies of spinodally decomposed silicon-rich oxide
Applied Physical Letters, Vol. **103**, Issue 13, Art.-No. 131911
© 2013, American Institute of Physics
DOI: 10.1063/1.4820453

Liedke, B.; Heinig, K.-H.; Mücklich, A.; Schmidt, B.
Formation and coarsening of sponge-like Si-SiO$_2$ nanocomposites
Applied Physical Letters, Vol. **103**, Issue 13, Art.-No. 133106
© 2013, American Institute of Physics
DOI: 10.1063/1.4822125

Mittendorff, M.; Winnerl, S.; Kamann, J.; Eroms, J.; Weiss, D.; Schneider, H.; Helm, M.
Ultrafast graphene-based broadband THz detector
Applied Physical Letters, Vol. **103**, Issue 2, Art.-No. 021113
© 2013, American Institute of Physics
DOI: 10.1063/1.4813621

Teich, M.; Stephan, D. R.; Winnerl, S.; Schneider, H.; Wilson, L. R.; Helm, M.
Intersublevel dephasing in InAs/GaAs quantum dots below the Reststrahlen band
Applied Physical Letters, Vol. **103**, Issue 25, Art.-No. 252110
© 2013, American Institute of Physics
DOI: 10.1063/1.4857515

Xu, M.; Mittendorff, M.; Dietz, R. J. B.; Künzel, H.; Sartorius, B.; Göbel, T.; Schneider, H.; Helm, M.; Winnerl, S.
Terahertz generation and detection with InGaAs-based large-area photoconductive devices excited at 1.55 µm

Applied Physical Letters, Vol. **103**, Issue 25, Art.-No. 251114
© 2013, American Institute of Physics
DOI: 10.1063/1.4855616

Ritter, R.; Wilhelm, R. A.; Stöger-Pollach, M.; Heller, R.; Mücklich, A.;Werner, U.; Vieker, H.; Beyer, A.; Facsko, S.; Gölzhäuser, A.; Aumayr, F.
Fabrication of nanopores in 1 nm thick carbon nanomembranes with slow highly charged ions
Applied Physical Letters, Vol. **102**, Issue 6, Art.-No. 063112
© 2013, American Institute of Physics
DOI: 10.1063/1.4792511

Obry, B.; Meyer, T.; Pirro, P.; Brächer, T.; Lägel, B.; Osten, J.; Strache, T.; Fassbender, J.; Hillebrands, B.
Microscopic magnetic structuring of a spin-wave waveguide by ion implantation in a $Ni_{81}Fe_{19}$ layer
Applied Physical Letters, Vol. **102**, Issue 2, Art.-No. 022409
© 2013, American Institute of Physics
DOI: 10.1063/1.4775759

Buhl, M.; Erbe, A.; Grebing, J.; Wintz, S.; Raabe, J.; Fassbender, J.
Lateral spin transfer torque induced magnetic switching at room temperature demonstrated by x-ray microscopy
Scientific Reports, Vol. **3**, Art.-No. 2945
© 2013, Nature Publishing Group
DOI: 10.1038/srep02945

PRL **111,** 016101 (2013) PHYSICAL REVIEW LETTERS week ending 5 JULY 2013

Reverse Epitaxy of Ge: Ordered and Faceted Surface Patterns

Xin Ou,[1] Adrian Keller,[1] Manfred Helm,[1,2] Jürgen Fassbender,[1,2] and Stefan Facsko[1,*]

[1]*Institute of Ion Beam Physics and Materials Research, Helmholtz-Zentrum Dresden-Rossendorf,*
Bautzner Landstrasse 400, 01328 Dresden, Germany
[2]*Technische Universität Dresden, 01062 Dresden, Germany*

(Received 21 March 2013; published 3 July 2013)

Normal incidence ion irradiation at elevated temperatures, when amorphization is prevented, induces novel nanoscale patterns of crystalline structures on elemental semiconductors by a reverse epitaxial growth mechanism: on Ge surfaces irradiation at temperatures above the recrystallization temperature of 250 °C leads to self-organized patterns of inverse pyramids. Checkerboard patterns with fourfold symmetry evolve on the Ge (100) surface, whereas on the Ge (111) surface, isotropic patterns with a sixfold symmetry emerge. After high-fluence irradiations, these patterns exhibit well-developed facets. A deterministic nonlinear continuum equation accounting for the effective surface currents due to an Ehrlich-Schwoebel barrier for diffusing vacancies reproduces remarkably well our experimental observations.

DOI: 10.1103/PhysRevLett.111.016101 PACS numbers: 68.35.Ct, 79.20.Rf, 81.16.Rf, 81.65.Cf

Self-organized pattern formation in systems far from equilibrium is a fundamentally interesting phenomenon governed by the interplay of kinetic and diffusive mechanisms. In addition, surface patterns with nanoscale dimensions are of technological interest for applications in sublithographic surface templating and for quantum dot device fabrication [1]. They may be generated on surfaces by homoepitaxy [2,3], heteroepitaxy [4] or by energetic ion irradiation [5–7]. However, semiconductor surfaces become amorphous during ion irradiation at room temperature. At these conditions periodic ripple patterns oriented perpendicular or parallel to the ion beam direction and isotropic, hexagonally ordered, dot or hole patterns, independent of the crystal structure [8], have been observed [7]. The origin of these patterns is attributed to an interplay of surface instability due to sputtering and mass redistribution together with surface relaxation mechanisms [9,10]. At near normal incidence smoothing dominates on amorphized elemental materials [11]. On the other hand, metal surfaces remain crystalline during ion irradiation at room temperature [6]. They exhibit a much higher complexity of pattern formation due to additional instabilities resulting from anisotropies in surface diffusion and due to biased diffusion across step edges [12]. Similarities with homoepitaxy have been identified: layer by layer erosion has been observed on metals [13] as well as on semiconductor surfaces [14]. Furthermore, similar to mound formation in epitaxy, pit formation has been observed on ion irradiated metal surfaces [15,16]. Although the formation of pits has also been seen in low-fluence irradiations of semiconductors [17–19], dense and ordered patterns of faceted nanostructures, as found in homoepitaxy and heteroepitaxy, have not been observed until now on ion irradiated semiconductor surfaces.

In this letter we present the formation of regular patterns of crystalline structures induced by normal incidence ion irradiation of an elemental semiconductor, Ge, at elevated temperatures. Above the recrystallization temperature of 250 °C ion-induced bulk defects are dynamically annealed and the surface remains crystalline. By only increasing the irradiation temperature, instead of inducing surface smoothing, novel checkerboard patterns with crystalline facets appear exhibiting the symmetry of the surface. They strongly resemble mound patterns in homoepitaxial growth [2], but are reversed. The mechanism can thus be interpreted as reverse epitaxy. In analogy with the Villain instability in homoepitaxy resulting from the Ehrlich-Schwoebel (ES) barrier for an adatom descending a monoatomic step [20,21] we conclude that the formation of ion-induced crystalline patterns results from the existence of an ES barrier for the ascending of surface vacancies created by sputtering. Based on the proposed atomistic mechanisms we derived a continuum equation which describes remarkably well the experimentally observed surface evolution.

Samples cut from epi-ready Ge (100) wafers were irradiated by a broad 1 keV Ar^+ ion beam at normal incidence without any pre-treatment. The irradiations were performed in a high vacuum chamber with a Kaufman ion source. The samples were heated by a boron nitride heater from the backside. The surface topography was analyzed after irradiations *ex situ* by atomic force microscopy (AFM).

In Fig. 1 AFM images of Ge (100) surfaces irradiated with ion fluences of 3×10^{18} cm^{-2} and different surface temperatures ranging from 230 °C to 430 °C are shown. At temperatures below 250 °C the Ge surface remains smooth after irradiation [Fig. 1(a)]. At these conditions the Ge surface is amorphized by ion irradiation and smoothing by surface diffusion and mass redistribution dominates [11]. The initial roughness of the virgin Ge surface of 0.7 nm is reduced to 0.18 nm. At temperatures higher than 250 °C checkerboard patterns appear after irradiation indicating that an additional ion-induced instability appears. The structures of the pattern have a rectangular

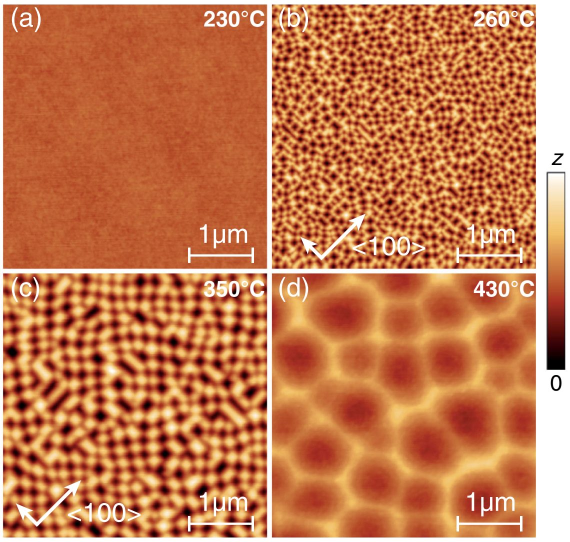

FIG. 1 (color online). AFM height images of Ge (100) surfaces after ion irradiation with an ion fluence of 3×10^{18} cm^{-2} at temperatures of 230 °C, 260 °C, 350 °C, and 430 °C. The ⟨100⟩ crystal directions are marked by arrows. (a) $z = 8$ nm; (b) $z = 38$ nm; (c) $z = 38$ nm; (d) $z = 8$ nm.

shape and an average size of ≈150 nm with an orientation in the ⟨100⟩ direction [Fig. 1(b)]. The structures size increases with irradiation temperature as a checkerboard pattern with an average size of ≈260 nm develops at 350 °C [Fig. 1(c)]. At 430 °C the structure size increases further while the symmetry is changed to an isotropic pattern of pits with diameter of 300–1000 nm. The order is much lower and the structure size distribution much broader than for the checkerboard patterns. Finally, at temperatures above 500 °C the surface is again smoothed by ion irradiation, similar to irradiations at 230 °C (not shown).

We investigated the microstructure of the patterns in cross section with transmission electron microscopy (TEM). In Fig. 2 TEM images of Ge (100) surfaces are shown, which were irradiated at temperatures of 230 °C and 260 °C, respectively. At 230 °C the surface is flat and a 2.6 nm thick amorphous Ge layer is visible. At 260 °C and higher no amorphous layer is visible. In the TEM image of the Ge surfaces irradiated at 260 °C facets are visible. In the following we use the term "facet" in a more general sense as a surface region with a predominant azimuthal and polar orientation. The facets are not atomically flat but exhibit a roughness on the nanoscale, a few Å high, induced by the stochastic nature of sputtering. The angle between the facets and the (100) plane is determined to 8°–10°.

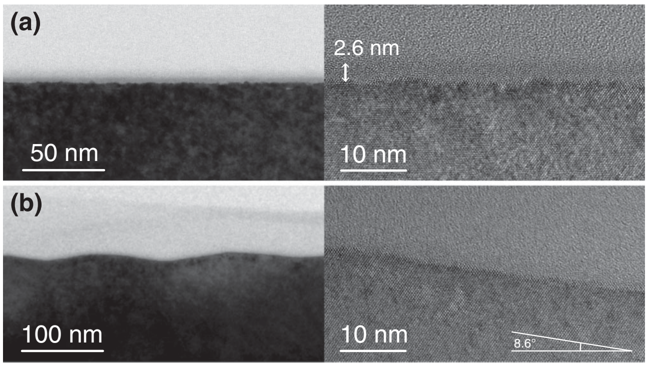

FIG. 2. TEM images of Ge surfaces in cross section irradiated at temperatures of (a) 230 °C and (b) 260 °C. In (a) a 2.6 nm thick amorphous layer can be identified, whereas in (b) no amorphous layer is visible. In Fig. 2(b) right the angle of the facet is shown with the horizontal line parallel to the (100) surface.

The transition from smoothing to roughening by ion irradiation between 230 °C and 260 °C can be attributed to the temperature at which amorphization by ion irradiation is prevented. Ion-induced vacancies and interstitials in the bulk are dynamically annealed above this temperature and only adatoms and surface vacancies remain as defects. At these temperatures we also expect that Ar is not incorporated into the crystal and diffuses out without influencing the surface kinetics. Hence, surface patterns result from the kinetics of adatoms and vacancies created by the incident ion beam; however, vacancy kinetics is expected to dominate because more vacancies are created by sputtering. In analogy to the ES barrier for adatoms, i.e., the diffusion barrier for an adatom to descent a step edge, a barrier exists for a vacancy to ascend into the next higher terrace. Thus, vacancies are trapped on lower terraces leading to reverse growth of surface structures, i.e., the formation of pyramidal pits. At higher temperature the mobility of vacancies increases and the nucleation density decreases leading to pits with larger separation and size. If the thermal energy of vacancies is high enough to overcome the ES barrier, the surface will remain smooth as experimentally observed for temperatures above 430 °C.

The evolution of crystalline surfaces is described by atomistic processes on terraces, steps, and kinks [22]. Diffusion and attachment of adatoms and vacancies at steps and kinks is expected to be anisotropic. The pyramidal pits on Ge (100) exhibit facets oriented along the ⟨100⟩ crystal direction. The emergence of these edges is attributed to an additional barrier at kink sites, similar to the barrier at step edges [23]. On the (100) surface the kink ES barrier is responsible for the repulsion of vacancies on the fast diffusing ⟨110⟩ step edges. This mechanism has also been proposed for the formation of mounds oriented in the ⟨100⟩ directions in homoepitaxy of Ge (100) [24]. The energy barrier for the diffusion around corners is expected to be smaller than for crossing step edges. Therefore, the kink ES barrier vanishes already at temperatures where the terrace ES barrier is still active and isotropic pit patterns should appear. This is indeed observed for irradiations at 430 °C [Fig. 1(d)] where the square symmetry of the pattern disappears and dense round pits are formed.

In order to further elucidate the formation mechanism we investigated the roughening and coarsening behavior of the checkerboard pattern on Ge (100) at 350 °C. Figure 3(a) shows the evolution of Ge(100) surface as well as the corresponding two-dimensional fast Fourier transform

(FFT) and two-dimensional angle distribution [25] as a function of ion fluence. The FFT reveals the symmetry and the order of the pattern, whereas from the two-dimensional angle distribution the formation of predominant facets can be deduced. After irradiations with a fluence of 1×10^{17} cm^{-2} a pit pattern with no clear orientation is visible. The angle distribution is isotropic with a maximum at 0°. At higher fluence of 1×10^{18} cm^{-2} the pattern already exhibits an orientation along the $\langle 100 \rangle$ crystal direction. The angle distribution reveals a fourfold symmetry with broad maxima around 9.5°. Finally, at 1×10^{19} cm^{-2} the angle distribution has four distinct narrow peaks around 11°. The peaks in the angle distribution are a clear signature for facet formation on the patterned Ge (100) surface. The azimuthal and polar orientation of the facets are close to the $\{106\}$ (9.5°) and $\{105\}$ (11.3°) crystal planes. The formation of these facets results from the instability due to biased diffusion of vacancies created by ion irradiation, whereas the angle of the facets is determined by kinetic or energetic stabilization of low index planes under the given kinetic restrictions. Such low index planes are observed in Ge homoepitaxy [2,3,26] and heteroepitaxy on Si [1,27,28]. The energy minimization of the $\{106\}$ or $\{105\}$ planes results from the effective reduction of dangling bonds by dimerization on the (100) terraces. On Si and Ge the (105) surface is found to be atomically rough [28] and flat (105) facets are only observed in strained Ge "hut" islands. However, we expect that under ion irradiation the stabilized low index planes are metastable, like the (100) surface, and the facet angle will increase further. In our experiments we did not observe saturation of the facet angle up to ion irradiation fluences of 1×10^{19} cm^{-2}.

For the description of the temporal evolution of the surface during ion irradiation a continuum equation is derived considering sputtering and mass distribution by the incident ion beam [9,10,29,30] and surface diffusion of ion induced vacancies on crystalline surfaces [31]. The temporal evolution of the surface height, $h(x, y, t)$, is described by a deterministic partial differential equation [32],

$$\frac{\partial h}{\partial t} = -v_0 - \nu \nabla^2 h - \nabla \boldsymbol{j}_{\mathrm{ion}} - \nabla \boldsymbol{j}_{\mathrm{diff}}, \qquad (1)$$

with v_0 the constant erosion rate of the flat Ge surface, $\nu \nabla^2 h$ the curvature dependent sputter rate [9], $\boldsymbol{j}_{\mathrm{ion}}$ the surface current resulting from the ballistic mass redistribution [10,33], and $\boldsymbol{j}_{\mathrm{diff}}$ surface currents due to diffusion [20]. Mass redistribution by ion impact is proportional to the surface curvature, $\nabla^2 h$, like the curvature dependent sputtering rate, however, with a positive coefficient for incidence angles smaller than 45° [10]. At normal and small incidence angles this stabilizing mechanism overcompensates the destabilizing sputtering term, $\nu \nabla^2 h$,

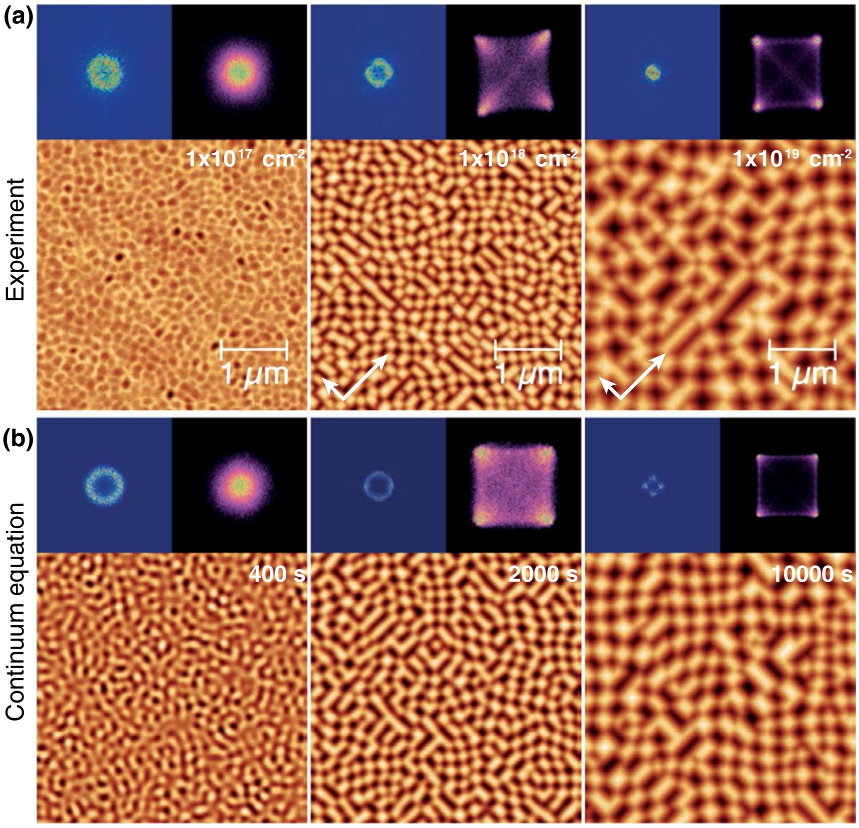

FIG. 3 (color online). (a) AFM images of Ge (100) surfaces irradiated at 350 °C and fluences of 1×10^{17} cm^{-2}, 1×10^{18} cm^{-2}, and 1×10^{19} cm^{-2}. (b) Snapshots of the numerical integration of the continuum equation with $\epsilon = 1$, $\kappa = 4$, $\sigma = -1$, and $\delta = 25$. Above the images the two-dimensional FFT (left) and the two-dimensional angle distribution (right) are shown.

and the amorphous surface is effectively smoothed at these conditions. The pattern formation on crystalline surfaces results from an additional kinetic instability due to the ES barrier. As shown later, this instability is included in the diffusive current, $\boldsymbol{j}_{\mathrm{diff}}$, and also proportional to the surface curvature with a negative coefficient. Thus, ion induced mass redistribution and sputtering can only reduce the ES instability and pattern formation is dominated by the biased diffusive surface currents. For the strong erosive regime this is a quite surprising result explaining the strong resemblance of ion induced patterns with patterns observed in homoepitaxy [2].

On amorphous surfaces, diffusion is described by the isotropic Herring-Mullins (HM) surface diffusion [34]. On crystalline surfaces, the diffusive current has to include atomistic surface currents on terraces, across terrace steps, along steps, and across kinks [35]. On the crystalline Ge (100) surface an isotropic surface diffusion has to be assumed as well described by the HM surface diffusion current, $\boldsymbol{j}_{\mathrm{HM}}$, whereas diffusion across steps is biased by the ES barrier for ascending vacancies, resulting in a net uphill mass current, $\boldsymbol{j}_{\mathrm{ES}}$. The symmetry of the crystalline Ge(100) surface is taken into account by an anisotropic current vector, $\boldsymbol{j}_{\mathrm{ES}}(\boldsymbol{m})$, which is a function of the surface slopes, $m_{(x,y)} = \partial_{(x,y)} h$ [36],

$$\boldsymbol{j}_{\mathrm{diff}} = \kappa \nabla(\nabla^2 h) + \sigma \nabla(\nabla h)^2 + \epsilon \begin{bmatrix} m_x(1 - \delta m_x^2) \\ m_y(1 - \delta m_y^2) \end{bmatrix}. \qquad (2)$$

Here, the first term is the isotropic HM surface diffusion. The second term is called the "conserved Kadar-Parisi-Zhang" term and has been introduced as a nonlinear current corresponding to the "nonconserved" nonlinearity in the Kadar-Parisi-Zhang equation $(\lambda/2(\nabla h)^2)$ [20]. This nonlinear current is known to break the up or down symmetry, which is prominently seen in the high temperature round pit patterns [Fig. 1(d)] [37]. Finally, the third term describes the anisotropic ES surface current, $\boldsymbol{j}_{\mathrm{ES}}$ [38], which is pointing uphill for positive ϵ inducing a surface instability [20]. The anisotropy of this current has its origin in the anisotropy of the ES barrier itself as well as in additional currents due to step edge diffusion [39,40]. This kind of surface current leads to the formation of facets at angles for which the current becomes zero [31,35]. Close to these points the surface current is negative (positive) for smaller (larger) angles, leading to an increase (decrease) of the slope. The parameter δ determines the angle of the facets: $\theta = \pm \arctan(\sqrt{1/\delta})$. In the continuum equation the facet angle will saturate at the given zeros of the ES surface current. So in order to describe the experimentally observed surface dynamics a higher polynomial of the surface current has to be assumed with zeros at angles for every kinetically or thermodynamically stabilized facet.

In Fig. 3(b) snapshots of the numerical integration of the continuum equation and their corresponding two-dimensional FFTs and two-dimensional angle distribution are shown [41]. After 40 000 integration steps an isotropic pattern forms exhibiting a characteristic periodicity without facets. At 200 000 integration steps facets are already fully developed. The two-dimensional angle distribution reveals distinct peaks at 11° in diagonal direction of the simulation grid. The two-dimensional FFT shows a circular region already with a slight anisotropy along the k_x and k_y axes. Finally, at 1 000 000 steps, very sharp peaks appear in the two-dimensional angle distribution at positions expected from the zeros of the ES surface current. The two-dimensional FFT now also exhibits peaks corresponding to the fourfold symmetry of the pattern. The comparison with the experiments reveals a remarkable agreement. Furthermore, the proposed continuum equation is able to describe the different temperature regimes identified in Fig. 1 by choosing proper coefficients [42].

From the experimental fluence series in Fig. 3, we determined the temporal evolution of the surface topography. In Fig. 4 the roughness and the characteristic length of the pattern, determined from the first minimum in the height-height correlation functions [43], are shown as a function of ion fluence. A power law fit to the roughness reveals a growth exponent $\beta = 0.59 \pm 0.06$, which is close to the theoretical value of 0.5 for the so- called statistical growth limit corresponding to growth by random deposition [35]. However, due to the existence of an instability, larger exponents can be expected [44]. Furthermore, the pattern coarsens; i.e., the characteristic length increases with fluence. A power law fit reveals a coarsening exponent $1/z = 0.14 \pm 0.02$. Such small exponents have also been observed for mound coarsening in homoepitaxy [16]. Theoretically, a coarsening exponent of $1/4$ is predicted for an infinite ES barrier [23]. Smaller exponents are expected for moderate barriers in step edge diffusion [23]. The numerical integration of the continuum equation gives a growth exponent of $\beta = 0.45$ and a coarsening exponent of $1/z = 0.20$, in fair agreement with the experiments.

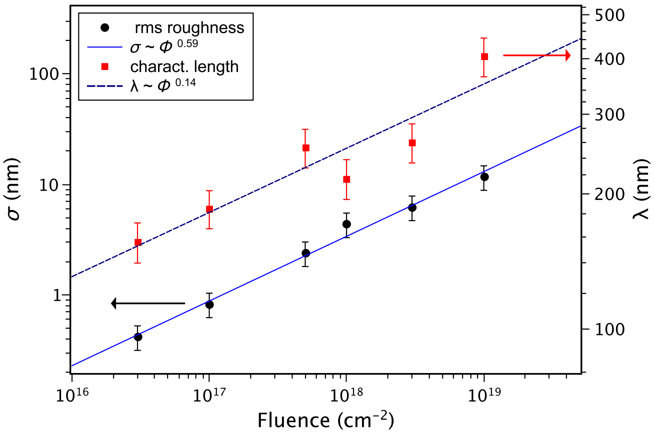

FIG. 4 (color online). Roughness and characteristic length of surface patterns on Ge(100) as a function of ion fluence. The lines represent power law fits to the data. The fluence Φ is given by ion flux times irradiation time.

Pattern formation by reverse epitaxy is a universal mechanism and can be achieved on many different crystalline materials. We identified the temperature window where patterns of crystalline structures are formed; i.e., the irradiation temperature is (i) above the dynamic recrystallization temperature of the material and (ii) low enough to establish an active ES barrier. At these conditions an excess of vacancies is created which are partially reflected at terrace steps inducing an effective uphill mass current. This instability leads to the formation of periodic patterns of inverse pyramids oriented along the crystalline directions of the surface. The faceting of the pyramids results from anisotropic surface currents due to a kink ES barrier. We could thus demonstrate that ion irradiation can induce patterns of faceted crystalline structures by a reverse epitaxy process. Therefore, this technique could establish as a complementary epitaxial method for the fabrication of high-quality crystalline semiconductor nanostructures.

The authors would like to acknowledge TEM analysis by Arndt Mücklich, fruitful discussions with Karl-Heinz Heinig, Jörg Grenzer, and Wolfhard Möller, and funding from the Deutsche Forschungsgemeinschaft (FOR845).

---

*s.facsko@hzdr.de

[1] C. Teichert, Phys. Rep. **365**, 335 (2002).

[2] J.E. Van Nostrand, S.J. Chey, M.-A. Hasan, D.G. Cahill, and J.E. Greene, Phys. Rev. Lett. **74**, 1127 (1995).

[3] J. Van Nostrand, S. Chey, and D. Cahill, Phys. Rev. B **57**, 12 536 (1998).

[4] J. Tersoff and R.M. Tromp, Phys. Rev. Lett. **70**, 2782 (1993).

[5] S. Facsko, T. Dekorsy, C. Koerdt, C. Trappe, H. Kurz, A. Vogt, and H.L. Hartnagel, Science **285**, 1551 (1999).

[6] U. Valbusa, C. Boragno, and F.B. de Mongeot, J. Phys. Condens. Matter **14**, 8153 (2002).

[7] W.L. Chan and E. Chason, J. Appl. Phys. **101**, 121301 (2007).

[8] S. Facsko, T. Bobek, H. Kurz, T. Dekorsy, S. Kyrsta, and R. Cremer, Appl. Phys. Lett. **80**, 130 (2002).

[9] R.M. Bradley and J.M.E. Harper, J. Vac. Sci. Technol. A **6**, 2390 (1988).

[10] B. Davidovitch, M.J. Aziz, and M.P. Brenner, Phys. Rev. B **76**, 205420 (2007).

[11] C.S. Madi, E. Anzenberg, K.F. Ludwig, and M.J. Aziz, Phys. Rev. Lett. **106**, 066101 (2011).

[12] S. Rusponi, G. Costantini, C. Boragno, and U. Valbusa, Phys. Rev. Lett. **81**, 2735 (1998).

[13] B. Poelsema, L.K. Verheij, and G. Comsa, Phys. Rev. Lett. **53**, 2500 (1984).

[14] P. Bedrossian, J.E. Houston, J.Y. Tsao, E. Chason, and S.T. Picraux, Phys. Rev. Lett. **67**, 124 (1991).

[15] T. Michely and G. Comsa, Surf. Sci. **256**, 217 (1991).

[16] J.A. Stroscio, D.T. Pierce, M.D. Stiles, A. Zangwill, and L.M. Sander, Phys. Rev. Lett. **75**, 4246 (1995).

[17] S.J. Chey, J.E. VanNostrand, and D.G. Cahill, Phys. Rev. B **52**, 16 696 (1995).

[18] J. Kim, D.G. Cahill, and R.S. Averback, Phys. Rev. B **67**, 045404 (2003).

[19] H.J.W. Zandvliet and E. de Groot, Surf. Sci. **371**, 79 (1997).

[20] J. Villain, J. Phys. I **1**, 19 (1991).

[21] J.G. Amar and F. Family, Phys. Rev. Lett. **77**, 4584 (1996).

[22] Z.Y. Zhang and M.G. Lagally, Science **276**, 377 (1997).

[23] J.G. Amar, Phys. Rev. B **60**, R11317 (1999).

[24] B. Shin, J.P. Leonard, J.W. McCamy, and M.J. Aziz, Appl. Phys. Lett. **87**, 181916 (2005).

[25] The two dimensional angle distribution is a histogram of pairs of angles in x and y direction with respect to the surface calculated by the surface gradients, $\partial h/\partial x$ and $\partial h/\partial y$, in x and y direction, respectively.

[26] J.E. Van Nostrand, S.J. Chey, and D.G. Cahill, J. Vac. Sci. Technol. B **13**, 1816 (1995).

[27] Y.W. Mo, D.E. Savage, B.S. Swartzentruber, and M.G. Lagally, Phys. Rev. Lett. **65**, 1020 (1990).

[28] M. Tomitori, K. Watanabe, M. Kobayashi, F. Iwawaki, and O. Nishikawa, Surf. Sci. **301**, 214 (1994).

[29] A.L. Barabási and H.E. Stanley, *Fractal Concepts in Surface Growth* (Cambridge University Press, Cambridge, England, 1995).

[30] S. Facsko, T. Bobek, A. Stahl, H. Kurz, and T. Dekorsy, Phys. Rev. B **69**, 153412 (2004).

[31] M. Siegert, Phys. Rev. Lett. **81**, 5481 (1998).

[32] Redistribution and diffusion processes are mass conserving and can therefore be described by surface currents.

[33] M. Moseler, P. Gumbsch, C. Casiraghi, A.C. Ferrari, and J. Robertson, Science **309**, 1545 (2005).

[34] W.W. Mullins, J. Appl. Phys. **30**, 77 (1959).

[35] T. Michely and J. Krug, *Islands, Mounds, and Atoms*, Springer Series in Surface Science Vol. 42, edited by G. Ertl, H. Lüth, and D.L. Mills, Patterns and Processes in Crystal Growth Far from Equilibrium (Springer Verlag, Berlin, Heidelberg, New York, 2004).

[36] M. Siegert and M. Plischke, Phys. Rev. Lett. **73**, 1517 (1994).

[37] For positive values of σ the surface evolves to patterns with mound structures, whereas for negative values of σ patterns of pit structures appear.

[38] The anisotropic ES surface current $\boldsymbol{j}_{\mathrm{ES}}$ has been introduced with an explicit term coupling the currents in x- and y-direction [31]; however, these terms are implicitly already contained in $\nabla \boldsymbol{j}_{\mathrm{ES}}$ and were therefore omitted for convenience.

[39] M.V. Ramana Murty and B. Cooper, Phys. Rev. Lett. **83**, 352 (1999).

[40] P. Politi and J. Krug, Surf. Sci. **446**, 89 (2000).

[41] See Supplemental Material at http://link.aps.org/supplemental/10.1103/PhysRevLett.111.016101 for details of the numerical integrations.

[42] See Supplemental Material at http://link.aps.org/supplemental/10.1103/PhysRevLett.111.016101 for numerical integrations at different temperatures and movies of the height evolution with different coefficients for the low- and high-temperature case.

[43] Y. Zhao, G.-C. Wang, and T.-M. Lu, *Characterization of Amorphous and Crystalline Rough Surface: Principles and Applications*, Experimental Methods in the Physical Sciences Vol. 37 (Academic Press, San Diego, 2001).

[44] R. Cuerno, H.A. Makse, S. Tomassone, S.T. Harrington, and H.E. Stanley, Phys. Rev. Lett. **75**, 4464 (1995).

PRL 110, 177201 (2013) PHYSICAL REVIEW LETTERS week ending 26 APRIL 2013

Topology and Origin of Effective Spin Meron Pairs in Ferromagnetic Multilayer Elements

Sebastian Wintz,[1,2,*] Christopher Bunce,[1,†] Andreas Neudert,[1] Michael Körner,[1] Thomas Strache,[1,‡] Matthias Buhl,[1]
Artur Erbe,[1] Sibylle Gemming,[1,3] Jörg Raabe,[4] Christoph Quitmann,[4,§] and Jürgen Fassbender[1,2]
[1]*Helmholtz-Zentrum Dresden-Rossendorf, 01328 Dresden, Germany*
[2]*Institut für Festkörperphysik, Technische Universität Dresden, 01069 Dresden, Germany*
[3]*Technische Universität Chemnitz, 09107 Chemnitz, Germany*
[4]*Swiss Light Source, Paul Scherrer Institut, 5232 Villigen, Switzerland*
(Received 8 October 2012; published 22 April 2013)

We report on pairs of converging-diverging spin vortices in Co/Rh/NiFe trilayer disks. The lateral magnetization distribution of these effective spin merons is directly imaged by means of element-selective x-ray microscopy. By this method, both the divergence and circulation states of the individual layers are identified to be antisymmetric. Reversal measurements on corresponding continuous films reveal that biquadratic interlayer exchange coupling is the cause for the effective meron pair formation. Moreover, their three-dimensional magnetization structure is determined by micromagnetic simulations. Interestingly, the magnetic induction aligns along a flux-closing torus. This toroidal topology enforces a symmetry break, which links the core polarities to the divergence configuration.

DOI: 10.1103/PhysRevLett.110.177201 PACS numbers: 75.70.Kw, 75.70.Cn, 75.75.Fk

Nontrivial topologies are highly relevant for many phenomena in physics, ranging from fundamental field theories [1] to condensed matter systems such as topological insulators [2] and high temperature superconductors [3]. In the context of magnetism, nontrivial spin textures exist, for example, as bubble [4] and vortex [5] states for which the topology is quantified by their Skyrmion number to ± 1 and $\pm 1/2$, respectively [6]. As sketched in Fig. 1(a), a spin vortex consists of a planar magnetization ($\mathbf{M}$) curl, that tilts out of the plane in the nanoscopic core region [7,8]. There are two possible configurations for the curl's rotation sense (circulation c) and also two possible orientations for the core (polarity p):

$$p = \mathrm{sgn}[\mathbf{e}_z \cdot \mathbf{M}(r = 0)], \tag{1}$$

$$c = \mathrm{sgn}\{\mathbf{e}_z \cdot [\mathbf{r} \times \mathbf{M}(r \neq 0)]\}, \tag{2}$$

resulting in two distinct vortex handednesses $h = cp$. Because of their chiral nature and their interesting dynamic properties, magnetic vortices have been intensely studied during the past decades [5,7–13]. In addition to fundamental aspects, these investigations have led to the proposal of vortex based memory cells [14] and spin-torque driven nano-oscillators [15–17]. For both concepts the integration of vortices into lateral arrays [18,19] or multilayer systems is a crucial point [20–29].

A special spin state with nontrivial topology is the meron state [30–34]. It is realized by a radially in- or outwards pointing planar spin distribution, see Fig. 1(b), for which—complementary to the $c = 0$ state—a divergence (d) can be defined to

$$d = \mathrm{sgn}[\mathbf{e}_r \cdot \mathbf{M}(r \neq 0)]. \tag{3}$$

Vortices and merons can be transformed into each other through a planar rotation of $\mathbf{M}(r)$ by 90°. In between these two extremes there is a state which is equivalent to the superposition of a meron with a purely tangential vortex. This state is referred to as an unconventional vortex [33] or *effective* meron. Experimentally, so far Phatak *et al.* have inferred the existence of such states from an approach combining Lorentz transmission electron microscopy with micromagnetic simulations [34]. Metastable pairs of effective merons with equal c's but opposing d's were identified in a trilayer disk which consisted of two ferromagnetic layers separated by a nonmagnetic spacer. The formation of these pairs was explained by assuming an antiferromagnetic (AFM) interlayer exchange coupling (IEC) [35] and a demagnetization energy barrier resulting from non-edge-parallel magnetization states.

In this Letter we now offer direct proof for the existence of effective meron pairs by means of layer-resolved magnetic imaging with scanning transmission x-ray microscopy (STXM). Furthermore, we show that they can even be the lowest energy state of the system when a biquadratic [36–38] IEC contribution is present in the corresponding trilayer films. By applying micromagnetic simulations we derive that such effective merons have a three-dimensional spin structure, where the lateral divergence $\nabla \mathbf{M}_{xy}$ is partially compensated by a vertical $\nabla \mathbf{M}_z$. Interestingly, the resulting toroidal magnetization distribution leads to a topological symmetry break that enforces a strict relation between the d and p states of the system.

In order to create effective meron pairs, trilayer thin film disks with a radius of $R = 1\ \mu$m were fabricated; see sketch in Fig. 1(c). Patterning was achieved by a sequence of electron-beam lithography, thin film deposition via electron beam evaporation, and lift-off processing. The

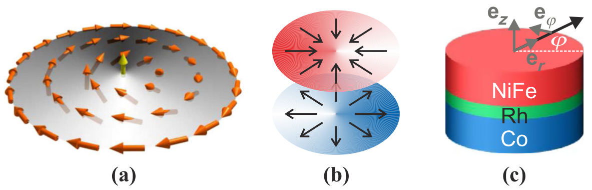

FIG. 1 (color online). Sketches of topological spin states in thin film elements. (a) Spin vortex with planar circulation and central core; magnetization orientation indicated by arrows. (b) Spin meron pair with diverging magnetization in the bottom layer and converging magnetization in the top layer. (c) Trilayer disk consisting of Co, Rh, and NiFe.

Co/Rh/NiFe trilayer stack consists of two ferromagnetic layers (Co and $\mathrm{Ni}_{81}\mathrm{Fe}_{19}$) of equal thickness ($t = 50$ nm) and a nonmagnetic Rh interlayer in between [39]. For the thickness given ($t = 0.8$ nm), Rh is expected to mediate a strong AFM IEC [40].

Figure 2 displays the remanent magnetization orientation ($\mathbf{m}_{xy} = \mathbf{M}_{xy}/M_{xy}$) state of the Co layer (lower row) and the NiFe layer (upper row) of a Co/Rh/NiFe disk as measured by STXM [41]. Figures 2(a) and 2(b) show the STXM micrographs with sensitivity m_x and m_y, respectively. The corresponding contrast scheme is indicated by the arrows in the gray scale wheels. An overlay of the micrographs 2(a) and 2(b) allows one to deduce the lateral magnetization distribution as sketched in 2(c). Obviously, each ferromagnetic layer exhibits an unconventional vortex. The average inclination of the planar $\mathbf{m}_{xy}$ with respect to the azimuthal unit vector ($\mathbf{e}_\varphi$) is $\phi_{\mathrm{Co}} = -19°$ and $\phi_{\mathrm{NiFe}} = 117°$, respectively, resulting in a planar coupling angle $\Phi = \arccos(\mathbf{m}_{xy}^{\mathrm{Co}}\mathbf{m}_{xy}^{\mathrm{NiFe}})$ of 136° (cf. Fig. 2, dashed lines) [42]. This distribution corresponds to a pair of effective spin merons with the following configuration: $c_{\mathrm{Co}} = +1$, $c_{\mathrm{NiFe}} = -1$, $d_{\mathrm{Co}} = +1$, and $d_{\mathrm{NiFe}} = -1$. Note that in contrast to Co, ϕ_{NiFe} is neither entirely constant over r nor fully rotational symmetric. In particular, the $\mathbf{m}_y$ dominated regions are slightly more extended than those of $\mathbf{m}_x$. Nonetheless, this does not affect the principle state of the system, i.e., the average angle $\phi_{\mathrm{NiFe}} = 117°$, as well as the fact that $\mathbf{m}_{xy}$ runs through all planar orientations along φ in a continuous and monotonic manner. We attribute the rotational asymmetry to sample imperfections as other effective meron structures were found to be symmetric in $\mathbf{m}_x$-sensitive measurements (not shown). In agreement with Ref. [34] the observed merons only occur in pairs, in particular, with opposing divergence ($d_1 = -d_2$). However, in contrast to Ref. [34], here also the circulations are antisymmetric ($c_1 = -c_2$). This is a crucial piece of evidence that reveals the existence of a noncollinear coupling in this system, namely, biquadratic IEC. Spin merons with symmetric circulations ($c_1 = c_2$) may exist as metastable states in purely bilinear AFM IEC systems [34]. However, they could not persist with antisymmetric circulations ($c_1 = -c_2$), as no energy barrier prevents the relaxation into the corresponding ground state of a purely tangential vortex pair [25].

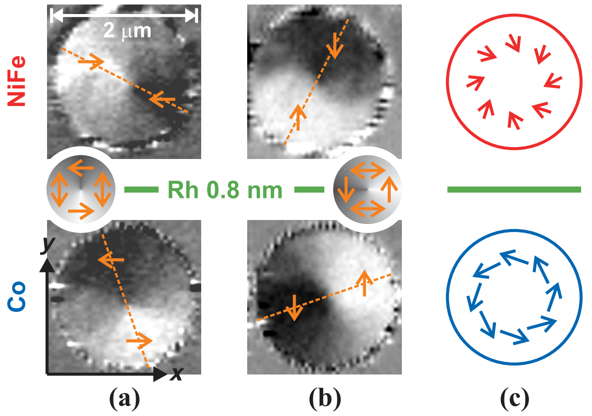

FIG. 2 (color online). Effective meron pairs in trilayer disks. (a), (b) STXM images showing the projected magnetization orientation $\mathbf{m}_x$ (a) and $\mathbf{m}_y$ (b) of the Co (bottom) and NiFe (top) layer with contrast as indicated (arrows). (c) Sketch of the resulting principle $\mathbf{M}_{xy}$ distribution.

IEC is described phenomenologically by the energy density per unit area,

$$\sigma_{\mathrm{IEC}} = -J_L \frac{\mathbf{M}_1 \cdot \mathbf{M}_2}{M_1 M_2} - J_Q \frac{(\mathbf{M}_1 \cdot \mathbf{M}_2)^2}{(M_1 M_2)^2}, \qquad (4)$$

which for the relative magnetic orientation of two ferromagnetic layers splits into a bilinear and a biquadratic contribution with the corresponding coupling constants (J_L) and (J_Q), respectively [36–38]. A negative (positive) J_L favors an antiferromagnetic (ferromagnetic) alignment of the two layers, whereas a negative J_Q energetically prefers their orthogonal ($\Phi = 90°$) orientation.

In order to validate the explanation that a biquadratic IEC is responsible for the effective meron pair stability observed, we determined the IEC constants of a Co(25)/Rh(0.8)/NiFe(25) (nm) continuous film [43]. The measured values of $J_L^f = -1.95\ \mathrm{mJ/m^2}$ and $J_Q^f = -1.05\ \mathrm{mJ/m^2}$ indeed reflect a strong biquadratic IEC contribution. However, the remanent coupling angle Φ_0^f resulting from these values is bigger than that observed in the effective meron pairs. This deviation is presumably a consequence of the altered interface roughnesses due to the different ferromagnetic layer thicknesses involved. The idea that a strong biquadratic IEC exists in this system is also supported by the response of the effective meron pair to quasistatic magnetic fields. For an external field of $\mu_0 H = -15$ mT applied along the x axis, we observed a layer-congruent displacement of the cores by about 200 nm [44]. This congruency can only be induced by IEC, since for purely dipolar coupled pairs the displacement would occur in different directions and by different magnitudes [27]. For the reasons given, we conclude that a biquadratic IEC is present in the trilayer structures and that it is necessary for the stability of the c-antisymmetric effective spin meron pairs observed.

A perfectly planar spin meron pair ($\mathbf{M}_z = 0$ everywhere) would be associated with a rather high demagnetization energy due to magnetic surface charges $\sim\mathbf{M}\cdot\mathbf{e}_r = \pm M\pi Rt$ at the cylinder jacket as well as magnetic volume charges $\sim\nabla\mathbf{M} = \pm M/r$ within the whole element, in particular, towards the center. Perpendicular magnetization components M_z and their vertical variation ($\nabla\mathbf{M}_z$) can lower this energy. The STXM experiment, however, is neither sensitive enough to detect small M_z values nor capable of resolving axial changes of $\mathbf{M}$. Therefore, we carried out micromagnetic simulations in order to determine 3D magnetization structure of effective meron pairs [45]. A trilayer disk with size and parameters in accordance with the experiment was modeled on a $256\times256\times(2+1+2)$ grid [46]. The initial magnetization states were defined to match those observed in the experiment with respect to Φ. Stationary states were accessed by integrating the Landau-Lifshitz-Gilbert equation [47] assuming a strong damping ($\alpha = 1$).

Results from these micromagnetic simulations of effective meron pairs are shown in Fig. 3. The x and z projections of the magnetic orientation $\mathbf{m}$ are displayed in 3(a). Both ferromagnetic layers (Co and NiFe) were discretized into an inner and outer sublayer with respect to the Rh interlayer. The m_x distributions [3(a), left] are in good agreement with the experimental results obtained by STXM [cf. Fig. 2(a)]. The deviations from $\mathbf{e}_\phi$ at $r = 1/2R$ are $\phi_{\mathrm{Co}}^{\mathrm{sim}} = -33°$ and $\phi_{\mathrm{NiFe}}^{\mathrm{sim}} = 106°$ leading to $\Phi^{\mathrm{sim}} = 139°$, which compares well with the experimental value of $\Phi = 136°$. The difference between the theoretical and experimental values of ϕ is most likely due to a variation of the ratio $M_{\mathrm{Co}}t_{\mathrm{Co}}/M_{\mathrm{NiFe}}t_{\mathrm{NiFe}}$ from the nominal value. Both ferromagnets (in particular NiFe) exhibit a small variation of ϕ over r.

In order to visualize the m_z distributions of the effective meron pair, the contrast scheme was enhanced by a factor of 5 in Fig. 3(a) (right). All sublayers show a dark contrast in the center and a bright contrast at the disk edge; i.e., m_z is negative in the middle and positive at the outer parts. This feature is considerably more pronounced for both inner discretization layers of the disk relative to the corresponding outer ones. For equivalent discretization layers, the m_z component of NiFe is slightly bigger than that of Co.

From the simulations we deduce that the 3D magnetization structure of an effective meron pair corresponds to a toroid that is superimposed with tangential vortex components. Figure 3(c) shows a cross-sectional sketch of such a toroidal spin distribution. While—apart from the core—the magnetization at the top and bottom face is almost oriented parallel to the film plane, it steadily tilts out of the plane towards the central interlayer. Along any vertical axis, the sign of m_z is the same for Co and NiFe. Laterally, however, m_z is changing sign from the edge to the center within each ferromagnet.

Quantitative values for the radial dependence of m_z are given in Fig. 3(d) reflecting the toroidal structure. All the separate layers simulated within the meron pair exhibit a similar variation of m_z with r. Starting from $m_z = -1$ at the center, the perpendicular component sharply decreases to values below -0.5 in the range of $r \sim 50$ nm. This feature can be seen as the actual core of the structure. At $r \approx 700$ nm the m_z distribution crosses zero and then monotonically increases to positive values below $+0.25$ at the sample edge. In contrast to the effective meron pairs, neither a single layer NiFe vortex nor the NiFe vortex of a dipolarly coupled vortex pair [48] exhibits any significant m_z components for $r > 100$ nm.

The ϕ_i^{sim} values also show a radial variation. At half the distance between center and edge, the planar coupling angle is $\Phi^{\mathrm{sim}} = 139°$. It increases, however, to almost 180° at the edge and close to the center, as $\phi_{\mathrm{Co}}^{\mathrm{sim}}$ and $\phi_{\mathrm{NiFe}}^{\mathrm{sim}}$ tend to 0° and 180°, respectively. Because of the toroidal magnetization structure, on the other hand, the effective meron pair's 3D interlayer coupling angle δ (between $\mathbf{m}^{\mathrm{Co}}$ and $\mathbf{m}^{\mathrm{NiFe}}$) may be smaller than the planar coupling angle Φ (between $\mathbf{m}_{xy}^{\mathrm{Co}}$ and $\mathbf{m}_{xy}^{\mathrm{NiFe}}$), as sketched in Fig. 3(b) [49].

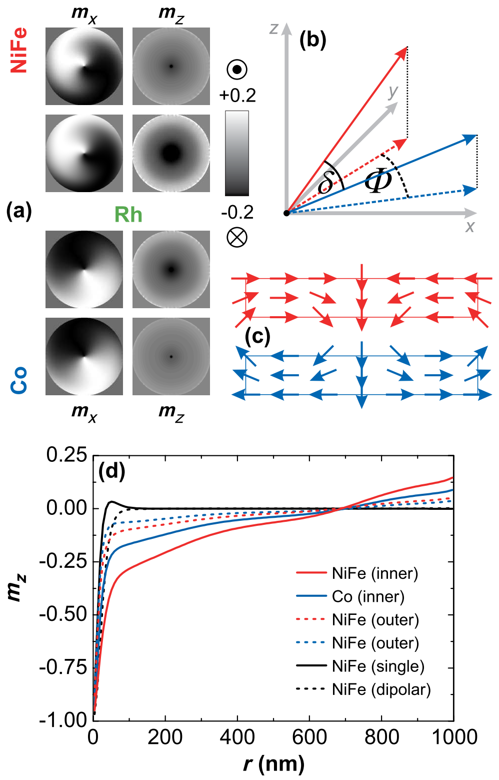

FIG. 3 (color online). Micromagnetic simulation of an effective meron pair. (a) m_x and m_z for a trilayer disk with dimensions as in the experiment, but reduced J_L. Both ferromagnets were discretized into an inner and outer sublayer. The z contrast is enhanced ($\times$ 5) to visualize the toroidal magnetization structure. (b) Sketch of the three-dimensional coupling angle δ versus the planar coupling angle Φ. (c) Cross-sectional sketch of the magnetization torus, neglecting the tangential components. (d) Radial dependence of m_z for the inner and outer discretization layers of the effective meron, compared to a single NiFe layer and a NiFe layer of a dipolarly coupled vortex pair.

The 3D magnetization structure of the effective meron pair can be explained in the following way. The dimensions of the ferromagnetic thin-film elements in the trilayer disk would lead to a formation of regular tangential vortices in an isolated case. However, the AFM IEC with significant biquadratic contribution causes a relative canting of the c-antisymmetric vortices, which results in the planar convergent or divergent magnetization pattern described. In sample regions at around half the distance between center and edge, the coupling angle matches the theoretical expectations for a continuous film. However, a purely planar convergent or divergent configuration would be associated with extensive magnetic surface and especially volume charges. For this reason, the magnetization tends to align again tangentially when getting close to the edge and the center where the charges would become most relevant. Furthermore, starting from a planar orientation at a certain distance from the center ($> 1/2R$), the magnetization tilts out of plane increasingly towards the central core and—with opposing sign—also towards the edge, which results in the flux-closing magnetization torus described. As this effect is more prominent in regions close to the Rh interface, a vertical $\nabla \mathbf{M}_z$ occurs which partially compensates the volume charge generating $\nabla \mathbf{M}_{xy}$. Furthermore, a perpendicular orientation reduces the IEC energy (apart from the core region) as the 3D coupling angle δ is always smaller than the planar coupling angle Φ. A quantitative view on the 3D toroidal flux closure of magnetic induction can be found in the Supplemental Material [50].

As a consequence of the toroidal magnetization structure, an additional topology is introduced to the vortex pair system. This topology causes the following mutual symmetry constraints with respect to the circulations, polarities, and divergences of the effective meron pair:

$$p_1 = p_2, \qquad c_1 = -c_2, \qquad d_1 = -d_2. \tag{5}$$

While the c state is still independent from p and d,

$$c_1 = -c_2 = \pm 1, \tag{6}$$

there is a topology induced symmetry break enforcing the following relation between p and d:

$$p_i = d_i \mathrm{sgn} z_i, \tag{7}$$

with the z origin being located at the interlayer position. This means that the core polarities must be aligned along the toroidal flux direction. The latter relation was verified by micromagnetic simulations which show that any $p_i = -d_i \mathrm{sgn} z_i$ configuration relaxes into the stable state proposed. Compared to the c-p correlation which was experimentally observed for single layer vortices [51], the p-d relation for an effective spin meron is strict and universal. The results presented above also imply that spin meron states can only occur in pairs unless a noncollinear exchange, such as the Dzyaloshinskii-Moriya interaction, is present in the ferromagnetic material [51,52].

In summary, this work offers direct proof for the existence of effective spin meron pairs in magnetic trilayers. In the presence of biquadratic IEC, such a pair can even be the magnetic ground state of the system. The 3D structure of an effective meron pair involves significant perpendicular components, which lead to a flux-closing toroidal magnetization distribution. The given topology causes a symmetry break, enforcing the meron cores to be aligned parallel, with the polarity pointing along the torus' orientation. The results of our study provide new insights into the topology and 3D structure of coupled multilayer spin systems. They also might be relevant for possible application concepts involving coupled vortices, such as memory cells or spin-torque oscillators. In particular, the substantially enhanced meron core size could be a key factor with respect to spin-torque excitation of vortices.

We would like to thank Aleksandar Puzić for his contribution to this work as well as Riccardo Hertel and Jeffrey McCord for fruitful discussions. We also gratefully acknowledge help from the following people at various stages: Oskar Liedke, Vicki Kühn, Bernd Scheumann, Benjamin Watts, and Julia Dschemuchadse. The STXM experiments were performed using the X07DA (PolLux) beam line at the Swiss Light Source, Paul Scherrer Institut, Villigen, Switzerland. Funding from BMBF (Contract No. 05 KS4WE1/6) is acknowledged.

---

[*] s.wintz@hzdr.de

[†] Present address: Fraunhofer-Institut für Photonische Mikrosysteme, 01109 Dresden, Germany.

[‡] Present address: Vacuumschmelze GmbH & Co. KG, 63450 Hanau, Germany.

[§] Present address: MAX IV Laboratory, 22363 Lund, Sweden.

[1] F. Bais, *Topological Excitations in Gauge Theories; An Introduction From the Physical Point of View*, Springer Lecture Notes in Mathematics Vol. 926 (Springer, New York, 1982), p. 107.
[2] L. Fu, C.L. Kane, and E.J. Mele, Phys. Rev. Lett. **98**, 106803 (2007).
[3] T. Senthil and M.P.A. Fisher, Phys. Rev. B **63**, 134521 (2001).
[4] A. P. Malozemoff and J. C. Slonczewski, *Magnetic Domain Walls in Bubble Materials* (Academic, New York, 1979).
[5] C. Kittel, Rev. Mod. Phys. **21**, 541 (1949).
[6] C. Moutafis, S. Komineas, and J. A. C. Bland, Phys. Rev. B **79**, 224429 (2009).
[7] E. Feldtkeller and H. Thomas, Phys. Kondens. Mater. **4**, 8 (1965).
[8] T. Shinjo, T. Okuno, R. Hassdorf, K. Shigeto, and T. Ono, Science **289**, 930 (2000).
[9] B.E. Argyle, E. Terrenzio, and J.C. Slonczewski, Phys. Rev. Lett. **53**, 190 (1984).
[10] S.-B. Choe, Y. Acremann, A. Scholl, A. Bauer, A. Doran, J. Stöhr, and H.A. Padmore, Science **304**, 420 (2004).
[11] R.P. Cowburn, D.K. Koltsov, A.O. Adeyeye, M.E. Welland, and D.M. Tricker, Phys. Rev. Lett. **83**, 1042 (1999).

PRL **110,** 137404 (2013) PHYSICAL REVIEW LETTERS week ending 29 MARCH 2013

Observation of Forbidden Exciton Transitions Mediated by Coulomb Interactions in Photoexcited Semiconductor Quantum Wells

W. D. Rice,[1,2] J. Kono,[1,2,*] S. Zybell,[3,4] S. Winnerl,[3] J. Bhattacharyya,[3] H. Schneider,[3] M. Helm,[3,4]
B. Ewers,[5] A. Chernikov,[5] M. Koch,[5] S. Chatterjee,[5] G. Khitrova,[6] H. M. Gibbs,[6,†] L. Schneebeli,[5]
B. Breddermann,[5] M. Kira,[5] and S. W. Koch[5]

[1]*Department of Electrical and Computer Engineering, Rice University, Houston, Texas 77005, USA*
[2]*Department of Physics and Astronomy, Rice University, Houston, Texas 77005, USA*
[3]*Helmholtz-Zentrum Dresden-Rossendorf, P. O. Box 510119, D-01314 Dresden, Germany*
[4]*Technische Universität Dresden, 01062 Dresden, Germany*
[5]*Department of Physics, Philipps-University Marburg, Renthof 5, D-35032 Marburg, Germany*
[6]*College of Optical Science, University of Arizona, Tucson, Arizona 85721-0094, USA*

(Received 18 March 2012; revised manuscript received 27 November 2012; published 26 March 2013)

We use terahertz pulses to induce resonant transitions between the eigenstates of optically generated exciton populations in a high-quality semiconductor quantum well sample. Monitoring the excitonic photoluminescence, we observe transient quenching of the $1s$ exciton emission, which we attribute to the terahertz-induced $1s$-to-$2p$ excitation. Simultaneously, a pronounced enhancement of the $2s$ exciton emission is observed, despite the $1s$-to-$2s$ transition being dipole forbidden. A microscopic many-body theory explains the experimental observations as a Coulomb-scattering mixing of the $2s$ and $2p$ states, yielding an effective terahertz transition between the $1s$ and $2s$ populations.

DOI: 10.1103/PhysRevLett.110.137404 PACS numbers: 78.55.Cr, 71.35.−y, 78.67.De

Coulombically bound electron-hole pairs, i.e., excitons, often dominate the optical properties [1] of high-quality semiconductors at low temperatures. In direct-gap semiconductors, the intraexciton energy spacing is typically in the terahertz (THz) frequency range, with the corresponding intraexcitonic transitions following the same selection rules as the dipole transitions in hydrogen atoms. Therefore, the presence of exciton populations can be unambiguously detected by monitoring the $1s$-to-$2p$ transition resonance [2–10]. One can also use strong THz pulses to induce nonlinear $1s$-to-$2p$ transitions [11–15], including Rabi flopping [16–19] and excitations in Λ systems [20].

An elegant way to study the influence of THz-induced exciton transitions is to monitor time-resolved photoluminescence (PL) spectra after combined optical and THz excitations [21]. Since only the optically active s states contribute to the PL, the THz-induced intraexcitonic $1s$-to-$2p$ population transfer can be observed as pronounced quenching of the $1s$ PL [22–24]. Similar PL quenching can be observed for quantum wells (QWs) when the THz energy is resonant with a dipole-allowed intersubband transition [25].

In this Letter, we apply this technique to monitor how a THz pulse changes the time-resolved PL long after a resonant optical pulse has generated exciton population in the system. Besides $1s$-PL quenching, we observe an unexpected transient increase of the $2s$ PL, indicating a pronounced effective $1s$-to-$2s$ transition. Using a systematic many-body theory [26], we show that the THz-induced $1s$-to-$2p$ excitation is accompanied by an efficient $2p$-to-$2s$ transition which can be attributed to cooperative Coulomb scattering. This Coulomb-assisted THz-induced $1s$-to-$2s$ coupling is unique to interacting many-body semiconductor configurations and cannot be observed in atomic systems.

In our experiments, we study the intraexcitonic transitions in a $20 \times \mathrm{In}_{0.06}\mathrm{Ga}_{0.94}\mathrm{As}$ QW structure at a lattice temperature of 10 K. The 8 nm wide QWs are separated by 130 nm GaAs barriers, rendering all nontrivial coupling effects negligible [27]. As such, the structure acts as a single QW whose PL magnitude is additively enhanced by the number of QWs [28]. The heavy-hole (hh) excitons are well separated from both the continuum and the light-hole states, allowing us to address the resonances individually and efficiently, yielding a two-band situation for the hh1 [29,30]. For this particular In-Ga ratio, the energy difference between the $1s$ and $2s$ hh1 excitons is estimated as 6.7 meV, and the $1s$-to-$2p$ transition energy is 6.9 meV.

We monitor the time-resolved PL after an excitation sequence where a THz pulse of a free-electron laser (FEL) follows an optical pulse of a Ti:Sapphire laser, as shown schematically in Fig. 1(a). The Ti:Sapphire laser emits pulses with a duration of 4 ps (FWHM) at a repetition rate of 78 MHz with a photon energy of 1.471 eV, which is in resonance with the $1s$ hh state. The repetition rate is reduced to 13 MHz by an extracavity pulse picker equipped with an acousto-optic modulator to match the repetition rate of the FEL. The FEL emits 30 ps pulses with a wavelength of 191 μm, which is in resonance with the $1s$-to-$2p$ hh exciton transition energy. The peak field

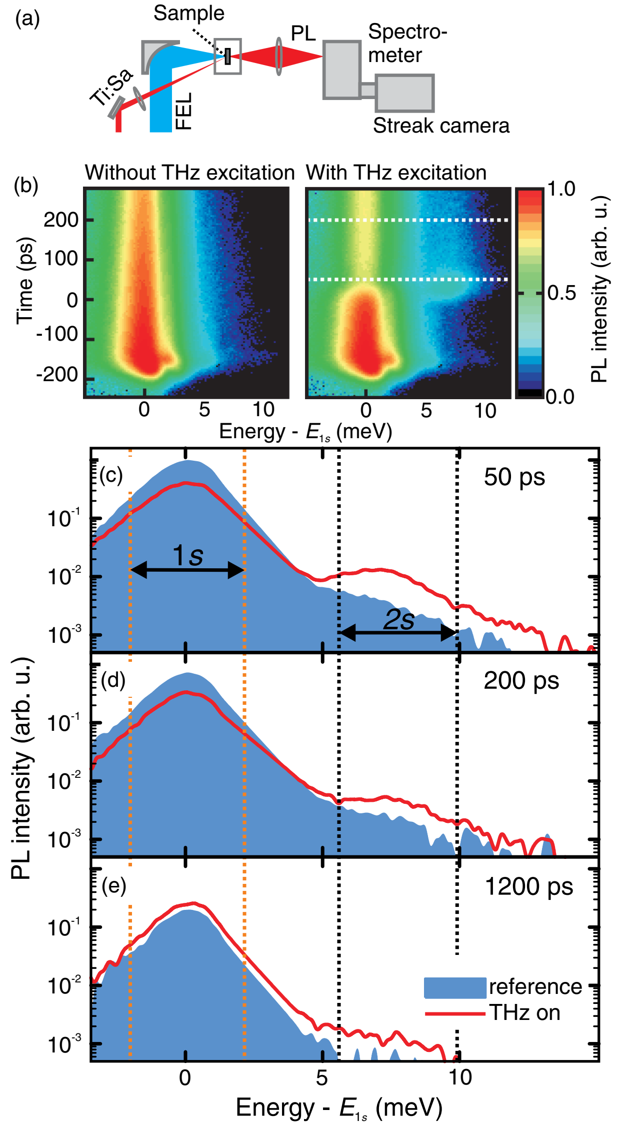

FIG. 1 (color online). (a) Schematic experimental setup. (b) False-color representation of the temporally and spectrally resolved PL without (left) and with (right) THz excitation. (c)–(e) Measured reference PL spectra (shaded area) vs THz on PL (solid red line) on a semilogarithmic scale defined at different times t after the THz excitation indicated by the horizontal dashed lines in panel (b).

strength of the FEL beam at the position of the sample is estimated to be 5 kV cm^{-1}.

The two sources are synchronized electronically, and their time delay is controlled by using a mechanical delay of the synchronizing pulses; for details, see Ref. [31]. The two beams are collinearly polarized and focused directly onto the QW. The spot sizes are chosen to be 300 and 50 μm for the FEL and the Ti:Sapphire laser, respectively. The PL is collected in a forward-scattering geometry through the transparent GaAs substrate. Only the center spot of about 20 μm in diameter is imaged within a small solid angle, carefully avoiding the transmitted laser beams as well as density-averaging effects. The PL is spectrally and temporally dispersed using a spectrometer attached to a streak camera with energy and time resolutions of 0.15 meV and 15 ps, respectively; the time is oversampled, collecting a spectrum every 4.4 ps.

The relatively weak optical excitation, estimated to be $\sim 10^{11}$ $\mathrm{photons/cm}^2$ per pulse, couples to the $1s$ polarization, which is converted into incoherent $1s$ excitons. This polarization-to-population conversion process occurs efficiently with a characteristic time scale of <10 ps, as shown in Ref. [32]. Exemplary PL data without THz excitation are given in the left panel of Fig. 1(b), where the spectrally and temporally emitted PL intensities are plotted in false colors. The time t is defined with respect to the center of the THz pulse. Following the initial excitation, the PL decays exponentially on a time scale of 600 ps. The corresponding data for dual excitation are shown in the right panel. The THz pulse arrives roughly 195 ps after the optical pulse to make sure that the THz pulse excites the incoherent $1s$ populations into the $2p$ state and partially into the ionization continuum [19]. Such a population transfer removes $1s$ populations so that the related $1s$ resonance in PL is quenched as predicted in Refs. [22,23]. Additionally, a clear spike in the $2s$ emission is visible when the FEL is incident, and the $1s$ PL recovers on a much longer time scale.

To better quantify the THz-induced changes, we plot emission spectra for three representative t with (solid line) and without (shaded area) THz excitation in Figs. 1(c)–1(e). For a short time delay of $t = 50$ ps just after the THz pulse [panel (c)], the $1s$-PL intensity decreases by 46%, verifying the usual THz-field-induced quenching scenario. In addition, the THz excitation induces a pronounced $2s$ resonance; this observation is unexpected because the direct $1s$-to-$2s$ transition is dipole forbidden, as the optical dipole, Coulomb-matrix element, and band energies are rotationally symmetric [33,34] for InGaAs QW excitations close to the Γ point. The $1s$ PL then recovers its intensity gradually while the $2s$ peak decays, as seen in (d) and (e). For $t = 1200$ ps, we observe another interesting feature: The $1s$ PL becomes larger with than without THz, indicating that more luminescing $1s$ excitons are present in the system long after the THz excitation. This is explained by THz-induced shelving of the overall exciton populations into optically dark states that cannot recombine radiatively. As the excitations relax back to the $1s$ state, we eventually observe excess $1s$ PL at later times because excitons experience a reduced overall radiative decay during the THz excitation-relaxation cycle. Note that nonradiative recombination in these samples is negligible for the chosen excitation conditions as the overall time-integrated emission intensities with and without THz excitation match within the experimental error.

We follow the time evolution of these THz-induced phenomena by determining the differential photoluminescence $\Delta\mathrm{PL}(t) = \mathrm{PL}_{\mathrm{THz}} - \mathrm{PL}_{\mathrm{ref}}$ between the cases with

($\mathrm{PL_{THz}}$) and without ($\mathrm{PL_{ref}}$) THz excitation. The measured ΔPL spectra are shown in Fig. 2(a) as a contour plot. Again, the $1s$ quench (early times), $1s$ shelving (later times), and the $2s$ excess PL are clearly visible. To monitor ΔPL dynamics in more detail, Figs. 2(b) and 2(c) present $\Delta\mathrm{PL}_{1s}$ and $\Delta\mathrm{PL}_{2s}$, corresponding to energy-integrated spectra around the indicated $1s$ and $2s$ energies, respectively, as a function of time. The strong negative dip in $\Delta\mathrm{PL}_{1s}$ results from the $1s$ quench while long-time $\Delta\mathrm{PL}_{1s}$ overshoots to a positive range, demonstrating the $1s$ shelving. The THz pulse induces a strictly positive $\Delta\mathrm{PL}_{2s}$: It increases rapidly after the THz excitation, peaking at $t = 50$ ps. Moreover, we observe no appreciable delay between the $1s$ quench and increased $2s$ PL. Hence, THz can induce a "direct" $1s$-to-$2s$ transition via the diffusive Coulomb scattering that effectively mixes the $2s$ and $2p$ states (see the Supplemental Material [35]). After that, $\Delta\mathrm{PL}_{2s}$ displays a double-decay behavior: A fast decay is followed by a slow exponential decay with roughly a 900 ps relaxation constant. This shows that the THz-induced $2s$ PL is a fast transient compared with the relaxation time scale.

To explain the unexpected $2s$-PL increase, we theoretically study how the Coulomb interaction modifies the THz-induced exciton transitions and the related PL. For this purpose, we concentrate on the excitation dynamics within one of the QWs. The microscopic properties of the excitons are defined by the two-particle correlations $c_X^{\mathbf{q},\mathbf{k}',\mathbf{k}} \equiv \Delta\langle e^\dagger_{\mathbf{k}} h^\dagger_{\mathbf{k}-\mathbf{q}} h_{\mathbf{k}'} e_{\mathbf{k}'+\mathbf{q}}\rangle$ between the electron $e^\dagger e$ and hole $h^\dagger h$ operators [26]. The corresponding electron (hole) distribution is $f^e_{\mathbf{k}} = \langle e^\dagger_{\mathbf{k}} e_{\mathbf{k}}\rangle$ ($f^h_{\mathbf{k}} = \langle h^\dagger_{\mathbf{k}} h_{\mathbf{k}}\rangle$). In the so-called main-sum approximation [1,26], the c_X dynamics is given by

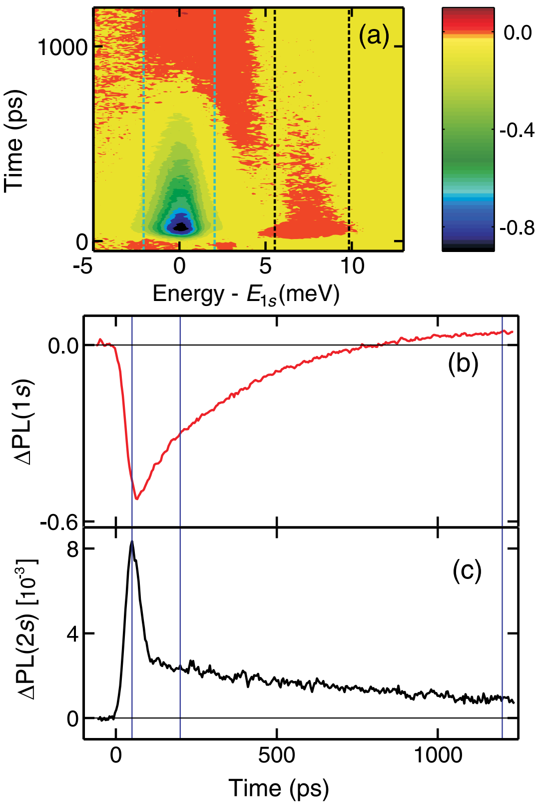

FIG. 2 (color online). THz-induced effect on PL. (a) Measured differential PL spectrum. The vertical dashed lines mark the regions of energy used for (b) $\Delta\mathrm{PL}_{1s}$ and (c) $\Delta\mathrm{PL}_{2s}$. The solid vertical lines indicate the time slices shown in Figs. 1(c)–1(e).

$$\begin{aligned} i\hbar\frac{\partial}{\partial t}c_X^{\mathbf{q},\mathbf{k}',\mathbf{k}} &= E^{eh}_{\mathbf{k},\mathbf{k}',\mathbf{q}} c_X^{\mathbf{q},\mathbf{k}',\mathbf{k}} - \boldsymbol{A}_{\mathrm{THz}}(t)\cdot \boldsymbol{j}_{\mathbf{k}'+\mathbf{q}-\mathbf{k}} c_X^{\mathbf{q},\mathbf{k}',\mathbf{k}} \\ &\quad + (1-f^e_{\mathbf{k}}-f^h_{\mathbf{k}-\mathbf{q}})\sum_{\mathbf{l}} V_{\mathbf{l}-\mathbf{k}} c_X^{\mathbf{q},\mathbf{k}',\mathbf{l}} \\ &\quad - (1-f^e_{\mathbf{k}'+\mathbf{q}}-f^h_{\mathbf{k}'})\sum_{\mathbf{l}} V_{\mathbf{l}-\mathbf{k}'} c_X^{\mathbf{q},\mathbf{l},\mathbf{k}} + T^{\mathbf{q},\mathbf{k}',\mathbf{k}}, \end{aligned} \tag{1}$$

where $E^{eh}_{\mathbf{k},\mathbf{k}',\mathbf{q}}$ contains the renormalized energy of an electron-hole pair, $V_{\mathbf{k}}$ is the Coulomb-matrix element, $\boldsymbol{A}_{\mathrm{THz}}(t)$ is the vector potential of the THz pulse, and $\boldsymbol{j}_{\mathbf{k}} = -|e|\hbar\mathbf{k}/\mu$ is the current matrix element with the reduced electron-hole mass μ. The three-particle correlations are symbolically denoted by $T^{\mathbf{q},\mathbf{k}',\mathbf{k}}$; see the Supplemental Material [35] for more details.

As shown in Ref. [26], T is dominantly built up via the Boltzmann-type Coulomb scattering where exciton correlations exchange momentum with the plasma and the other two-particle correlations. Consequently, T becomes a complicated functional of exciton populations due to the quantum kinetics involved. However, one does not need to explicitly determine the full quantum kinetics to explain the consequence of the T-related Coulomb scattering on THz transitions. Instead, we only need to consider that the incoming excitons scatter into new momentum states with a constraint that the number of incoming and outgoing c_X correlations remains constant. In other words, T generates *diffusive* Coulomb scattering among excitons, as shown in Ref. [35]. Therefore, it is clear that an exciton correlation—created in the state $c_X^{\mathbf{q},\mathbf{k}',\mathbf{k}}$ by THz transitions—can scatter to a new state such as $c_X^{\mathbf{q},\mathbf{k}'+\mathbf{K},\mathbf{k}}$ or $c_X^{\mathbf{q},\mathbf{k}',\mathbf{k}+\mathbf{K}}$, where $\mathbf{K}$ is a typical scattering wave vector.

One can explain the consequences of the diffusive Coulomb scattering on THz transitions using an ansatz

$$T_{\mathrm{diff}}^{\mathbf{q},\mathbf{k}',\mathbf{k}} = -i\hbar\gamma\left[c_X^{\mathbf{q},\mathbf{k}',\mathbf{k}} - \frac{1}{2\pi}\int_0^{2\pi} d\theta_{\mathbf{K}}\, c_X^{\mathbf{q},\mathbf{k}'+\mathbf{K},\mathbf{k}+\mathbf{K}}\right], \tag{2}$$

where $\theta_{\mathbf{K}}$ is the direction of the scattering $\mathbf{K}$ that is assumed to have a constant magnitude and γ defines the overall scattering strength. The introduced T_{diff} is a generalization of the diffusive model [32] that explains the principal effects of excitation-induced dephasing [26] beyond the constant-dephasing approximation.

To determine the effect of diffusive Coulomb scattering on the THz-generated $2p$ populations, we use the exciton transformation $\Delta N_{\mathbf{q}}^{\lambda,\nu} = \sum_{\mathbf{k},\mathbf{k}'}\phi_\lambda(\mathbf{k})\phi^\star_\nu(\mathbf{k}')c_{X,\mathrm{CM}}^{\mathbf{q},\mathbf{k}',\mathbf{k}}$, where

$\phi_\lambda(\mathbf{k})$ is the exciton wave function and $c^{\mathbf{q},\mathbf{k}',\mathbf{k}}_{X,\mathrm{CM}}$ is the center-of-mass representation of c_X [26]. The specific exciton populations are given by the diagonal elements $\Delta N^{\lambda,\lambda}_{\mathbf{q}}$ and determined by the exciton wave functions $\phi_\lambda(\mathbf{k})$ while the off-diagonal elements $\Delta N^{\lambda,\nu\neq\lambda}_{\mathbf{q}}$ define the exciton transitions. The diffusive scattering from $2p$ to $2s$ can be deduced by projecting Eqs. (1) and (2) with the exciton transformation and following the $2p$ contributions, yielding $\frac{\partial}{\partial t}\Delta N^{2s,2s}_{\mathbf{q}}|_{2p} = \Delta N^{2p,2p}_{\mathbf{q}}/\tau_{\mathrm{conv}}$, where we have defined a scattering time (see Ref. [35])

$$\frac{2\pi}{\tau_{\mathrm{conv}}} \equiv \gamma \int_0^{2\pi} d\theta_{\mathbf{K}} \left| \sum_{\mathbf{k}} \phi_{2p}(\mathbf{k})\phi^\star_{2s}(\mathbf{k}+\mathbf{K}) \right|^2. \qquad (3)$$

We see that the $2p$-to-$2s$ coupling is present as long as $\mathbf{K}$ is not zero because the $2s$ and $2p$ states are orthogonal only for $\mathbf{K} = 0$.

Besides the $2p$-to-$2s$ coupling, the Coulomb interaction also relaxes $2s$ populations toward the quasiequilibrium on a time scale τ_{rel}. The combined effect of τ_{conv} and τ_{rel} creates new Coulomb-mediated eigenstates where the $2s$ and $2p$ states become mixed; see Ref. [35]. In particular, the Coulomb-induced state mixing induces an effective THz transition between the original $1s$ and $2s$ states. Note that the dipole-allowed $1s$-to-$2p$ and $2p$-to-$2s$ transitions cannot generate efficient $1s$-to-$2s$ population conversion without Coulomb scattering because the THz pulse is off resonant with the $2p$-to-$2s$ transition.

Because of the scattering nature of $2s$-$2p$ mixing, the created $2s$ population decays with rate $\tau^{-1}_{2s} = \tau^{-1}_{\mathrm{rel}} - \tau^{-1}_{\mathrm{conv}}$, which also defines the fast decay of the excess $2s$ PL, as shown in Ref. [35]. For the late times, the $2s$ population reaches a quasiequilibrium, yielding a slower decay of the $2s$ PL on the time scale of the remaining phonon relaxation τ_{phon}.

We numerically solve THz dynamics (1) including all the relevant exciton states for the optically bright and dark excitons and the diffusive Coulomb scattering (2). The center-of-mass momentum of dark and bright excitons is fully taken into account. We also include the radiative decay of bright excitons as well as the relaxation of excitons toward the thermodynamic equilibrium on a $\tau_{\mathrm{phon}} = 900$ ps time scale, agreeing well with independent microscopic computations [6,26]. The diffusive Coulomb scattering is chosen to give $\tau_{2s} = 120$ ps ($\tau_{\mathrm{conv}} = 56.0$ ps, $\tau_{\mathrm{rel}} = 38.2$ ps) that is substantially faster than τ_{phon}. The quasistationary PL spectra are computed via the PL Elliott formula [1], as discussed in Ref. [35].

Figure 3 shows the PL changes induced by THz excitation when the diffusive Coulomb scattering is included under the same excitation conditions as in Fig. 2. The computations not only explain the qualitative behavior of $1s$ quench, exciton shelving, and excess $2s$ PL, but they quantitatively determine the $1s$ quench and $2s$ excess levels. They also explain the double decay of the $2s$ PL as switching from the fast Coulomb equilibration τ_{2s} to the slow phonon relaxation τ_{phon}. We have also performed a computation where we reduce $1/\tau_{\mathrm{conv}}$ by a factor of 20 in the c_X dynamics. The dashed line in Fig. 3(c) compares this $\Delta\mathrm{PL}_{2s}$ with the full result (solid line). We see that the full and $1/\tau_{\mathrm{conv}}$-reduced computations decay similarly at the late times; note that some excess $2s$ PL remains due to thermal relaxation from the ionized excitons toward the $1s$ and $2s$ states. However, only the full computation produces a strong $\Delta\mathrm{PL}_{2s}$ transient that decays fast. Hence, the $\Delta\mathrm{PL}_{2s}$ transient does not originate from relaxation but follows from the Coulomb-induced population transfer and the subsequent equilibration. The $\Delta\mathrm{PL}_{2s}$ peak also emerges on a time scale similar to the THz excitation, determined by the THz pulse duration (here 30 ps). Thus, the Coulomb interaction cooperates with the THz excitation to open a new $1s$-to-$2s$ transition that is much faster than the relaxation processes.

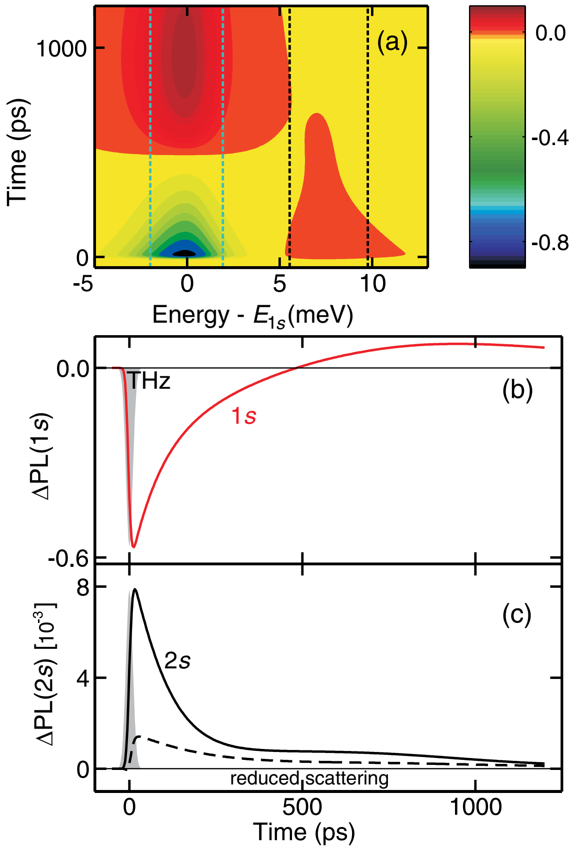

FIG. 3 (color online). THz-induced effect on PL. (a) Computed differential PL. Integrated differential $\Delta\mathrm{PL}_\lambda(t)$ for (b) $\lambda = 1s$ and (c) $\lambda = 2s$. The conditions are same as in Fig. 2.

In conclusion, our experiment-theory analysis shows the existence of Coulomb-assisted THz transitions converting $1s$ into $2s$ excitons; i.e., a process that extends the dipole selection rules as a direct consequence of many-body interactions. This effect survives even when an appreciable amount of disorder is present, as shown in Ref. [35]. The related $2p$-to-$2s$ transfer is significantly faster than other relaxation processes, making the Coulomb-induced scattering an active partner in the THz transitions. This work not only highlights a pronounced difference between excitons and atoms but also opens up a new mechanism to manipulate excitons through combining many-body and THz effects.

This work was supported, in part, by the W. M. Keck Program in Quantum Materials at Rice University (W. D. R.). The Marburg Group acknowledges financial support by the Deutsche Forschungsgemeinschaft. The Tucson Group thanks NSF and AFOSR for support.

---

[*]Corresponding author.
kono@rice.edu
[†]Deceased.

[1] M. Kira and S. W. Koch, *Semiconductor Quantum Optics* (Cambridge University Press, Cambridge, England, 2011), 1st ed.

[2] T. Timusk, H. Navarro, N. O. Lipari, and M. Altarelli, Solid State Commun. **25**, 217 (1978).

[3] D. Labrie, M. L. W. Thewalt, I. J. Booth, and G. Kirczenow, Phys. Rev. Lett. **61**, 1882 (1988).

[4] C. C. Hodge, C. C. Phillips, M. S. Skolnick, G. W. Smith, C. R. Whitehouse, P. Dawson, and C. T. Foxon, Phys. Rev. B **41**, 12 319 (1990).

[5] R. H. M. Groeneveld and D. Grischkowsky, J. Opt. Soc. Am. B **11**, 2502 (1994).

[6] M. Kira, W. Hoyer, T. Stroucken, and S. W. Koch, Phys. Rev. Lett. **87**, 176401 (2001).

[7] R. A. Kaindl, M. A. Carnahan, D. Hägele, R. Lövenich, and D. S. Chemla, Nature (London) **423**, 734 (2003).

[8] M. Kira, W. Hoyer, and S. W. Koch, Solid State Commun. **129**, 733 (2004).

[9] I. Galbraith *et al.*, Phys. Rev. B **71**, 073302 (2005).

[10] T. Suzuki and R. Shimano, Phys. Rev. Lett. **103**, 057401 (2009).

[11] K. B. Nordstrom, K. Johnsen, S. J. Allen, A.-P. Jauho, B. Birnir, J. Kono, T. Noda, H. Akiyama, and H. Sakaki, Phys. Rev. Lett. **81**, 457 (1998).

[12] M. Kubouchi, K. Yoshioka, R. Shimano, A. Mysyrowicz, and M. Kuwata-Gonokami, Phys. Rev. Lett. **94**, 016403 (2005).

[13] R. Huber, B. A. Schmid, Y. R. Shen, D. S. Chemla, and R. A. Kaindl, Phys. Rev. Lett. **96**, 017402 (2006).

[14] J. R. Danielson, Y.-S. Lee, J. P. Prineas, J. T. Steiner, M. Kira, and S. W. Koch, Phys. Rev. Lett. **99**, 237401 (2007).

[15] S. Leinß, T. Kampfrath, K. v. Volkmann, M. Wolf, J. T. Steiner, M. Kira, S. W. Koch, A. Leitenstorfer, and R. Huber, Phys. Rev. Lett. **101**, 246401 (2008).

[16] C. W. Luo, K. Reimann, M. Woerner, T. Elsaesser, R. Hey, and K. H. Ploog, Phys. Rev. Lett. **92**, 047402 (2004).

[17] S. G. Carter, V. Birkedal, C. S. Wang, L. A. Coldren, A. V. Maslov, D. S. Citrin, and M. S. Sherwin, Science **310**, 651 (2005).

[18] M. Wagner, H. Schneider, D. Stehr, S. Winnerl, A. M. Andrews, S. Schartner, G. Strasser, and Manfred Helm, Phys. Rev. Lett. **105**, 167401 (2010).

[19] B. Ewers, N. S. Köster, R. Woscholski, M. Koch, S. Chatterjee, G. Khitrova, H. M. Gibbs, A. C. Klettke, M. Kira, and S. W. Koch, Phys. Rev. B **85**, 075307 (2012).

[20] J. L. Tomaino, A. D. Jameson, Y.-S. Lee, G. Khitrova, H. M. Gibbs, A. C. Klettke, M. Kira, and S. W. Koch, Phys. Rev. Lett. **108**, 267402 (2012).

[21] R. Ulbricht, E. Hendry, J. Shan, T. F. Heinz, and M. Bonn, Rev. Mod. Phys. **83**, 543 (2011).

[22] J. Černe, J. Kono, M. S. Sherwin, M. Sundaram, A. C. Gossard, and G. E. W. Bauer, Phys. Rev. Lett. **77**, 1131 (1996).

[23] M. S. Salib, H. A. Nickel, G. S. Herold, A. Petrou, B. D. McCombe, R. Chen, K. K. Bajaj, and W. Schaff, Phys. Rev. Lett. **77**, 1135 (1996).

[24] J. Kono, M. Y. Su, T. Inoshita, T. Noda, M. S. Sherwin, S. J. Allen, Jr., and H. Sakaki, Phys. Rev. Lett. **79**, 1758 (1997).

[25] S. Zybell, H. Schneider, S. Winnerl, M. Wagner, K. Köhler, and M. Helm, Appl. Phys. Lett. **99**, 041103 (2011).

[26] M. Kira and S. W. Koch, Prog. Quantum Electron. **30**, 155 (2006).

[27] M. Hübner, J. P. Prineas, C. Ell, P. Brick, E. S. Lee, G. Khitrova, H. M. Gibbs, and S. W. Koch, Phys. Rev. Lett. **83**, 2841 (1999).

[28] M. Schäfer, M. Werchner, W. Hoyer, M. Kira, and S. W. Koch, Phys. Rev. B **74**, 155315 (2006).

[29] S. Chatterjee, C. Ell, S. Mosor, G. Khitrova, H. M. Gibbs, W. Hoyer, M. Kira, S. W. Koch, J. P. Prineas, and H. Stolz, Phys. Rev. Lett. **92**, 067402 (2004).

[30] T. Grunwald, T. Jung, D. Köhler, S. W. Koch, G. Khitrova, H. M. Gibbs, R. Hey, and S. Chatterjee, Phys. Status Solidi C **6**, 500 (2009).

[31] J. Bhattacharyya, M. Wagner, S. Zybell, S. Winnerl, D. Stehr, M. Helm, and H. Schneider, Rev. Sci. Instrum. **82**, 103107 (2011).

[32] M. Kira and S. W. Koch, Phys. Rev. Lett. **93**, 076402 (2004).

[33] M. Altarelli, U. Ekenberg, and A. Fasolino, Phys. Rev. B **32**, 5138 (1985).

[34] Z. Ikonić, V. Milanović, and D. Tjapkin, Phys. Rev. B **46**, 4285 (1992).

[35] See Supplemental Material at http://link.aps.org/supplemental/10.1103/PhysRevLett.110.137404 for a detailed discussion of the diffusive Coulomb scattering.

[12] B. Van Waeyenberge, A. Puzic, H. Stoll, K. W. Chou, T. Tyliszczak, R. Hertel, M. Fähnle, H. Brückl, K. Rott, G. Reiss, I. Neudecker, D. Weiss, C. H. Back, and G. Schütz, Nature (London) **444**, 461 (2006).

[13] S. Petit-Watelot, J.-V. Kim, A. Ruotolo, R. M. Otxoa, K. Bouzehouane, J. Grollier, A. Vansteenkiste, B. Van de Wiele, V. Cros, and T. Devolder, Nat. Phys. **8**, 682 (2012).

[14] S. Bohlens, B. Krüger, A. Drews, M. Bolte, G. Meier, and D. Pfannkuche, Appl. Phys. Lett. **93**, 142508 (2008).

[15] V. S. Pribiag, I. N. Krivorotov, G. D. Fuchs, P. M. Braganca, O. Ozatay, J. C. Sankey, D. C. Ralph, and R. A. Buhrman, Nat. Phys. **3**, 498 (2007).

[16] A. Ruotolo, V. Cros, B. Georges, A. Dussaux, J. Grollier, C. Deranlot, R. Guillemet, K. Bouzehouane, S. Fusil, and A. Fert, Nat. Nanotechnol. **4**, 528 (2009).

[17] V. Sluka, A. Kákay, A. M. Deac, D. E. Bürgler, R. Hertel, and C. M. Schneider, J. Phys. D **44**, 384002 (2011).

[18] J. Shibata, K. Shigeto, and Y. Otani, Phys. Rev. B **67**, 224404 (2003).

[19] H. Jung, K.-S. Lee, D.-E. Jeong, Y.-S. Choi, Y.-S. Yu, D.-S. Han, A. Vogel, L. Bocklage, G. Meier, M.-Y. Im, P. Fischer, and S.-K. Kim, Sci. Rep. **1**, 10 (2011).

[20] K. S. Buchanan, K. Y. Guslienko, A. Doran, A. Scholl, S. D. Bader, and V. Novosad, Phys. Rev. B **72**, 134415 (2005).

[21] K. W. Chou, A. Puzic, H. Stoll, G. Schütz, B. Van Waeyenberge, T. Tyliszczak, K. Rott, G. Reiss, H. Brückl, I. Neudecker, D. Weiss, and C. H. Back, J. Appl. Phys. **99**, 08F305 (2006).

[22] P. Vavassori, V. Bonanni, A. Busato, D. Bisero, G. Gubbiotti, A. O. Adeyeye, S. Goolaup, N. Singh, C. Spezzani, and M. Sacchi, J. Phys. D **41**, 134014 (2008).

[23] J. Wu, D. Carlton, E. Oelker, J. S. Park, E. Jin, E. Arenholz, A. Scholl, C. Hwang, J. Bokor, and Z. Q. Qiu, J. Phys. Condens. Matter **22**, 342001 (2010).

[24] J. Kurde, J. Miguel, D. Bayer, J. Sánchez-Barriga, F. Kronast, M. Aeschlimann, H. A. Dürr, and W. Kuch, New J. Phys. **13**, 033015 (2011).

[25] S. Wintz, T. Strache, M. Körner, M. Fritzsche, D. Markó, I. Mönch, R. Mattheis, J. Raabe, C. Quitmann, J. McCord, A. Erbe, and J. Fassbender, Appl. Phys. Lett. **98**, 232511 (2011).

[26] S. Wintz, T. Strache, M. Körner, C. Bunce, A. Banholzer, I. Mönch, R. Mattheis, J. Raabe, C. Quitmann, J. McCord, A. Erbe, K. Lenz, and J. Fassbender, Phys. Rev. B **85**, 134417 (2012).

[27] S. Wintz, C. Bunce, A. Banholzer, M. Körner, T. Strache, R. Mattheis, J. McCord, J. Raabe, C. Quitmann, A. Erbe, and J. Fassbender, Phys. Rev. B **85**, 224420 (2012).

[28] O. V. Sukhostavets, G. R. Aranda, and K. Y. Guslienko, J. Appl. Phys. **111**, 093901 (2012).

[29] A. A. Awad, A. Lara, V. Metlushko, K. Y. Guslienko, and F. G. Aliev, Appl. Phys. Lett. **100**, 262406 (2012).

[30] C. J. Stevenson and J. Kyriakidis, Phys. Rev. B **84**, 075303 (2011).

[31] M. Ezawa, Phys. Rev. B **83**, 100408(R) (2011).

[32] J. Wu, D. Carlton, J. S. Park, Y. Meng, E. Arenholz, A. Doran, A. T. Young, A. Scholl, C. Hwang, H. W. Zhao, J. Bokor, and Z. Q. Qiu, Nat. Phys. **7**, 303 (2011).

[33] M. Yan, H. Wang, and C. Campbell, J. Magn. Magn. Mater. **320**, 1937 (2008).

[34] C. Phatak, A. K. Petford-Long, and O. Heinonen, Phys. Rev. Lett. **108**, 067205 (2012).

[35] P. Grünberg, R. Schreiber, Y. Pang, M. B. Brodsky, and H. Sowers, Phys. Rev. Lett. **57**, 2442 (1986).

[36] J. Unguris, R. J. Celotta, and D. T. Pierce, Phys. Rev. Lett. **67**, 140 (1991).

[37] M. Rührig, R. Schäfer, A. Hubert, R. Mosler, J. A. Wolf, S. Demokritov, and P. Grünberg, Phys. Status Solidi A **125**, 635 (1991).

[38] J. C. Slonczewski, Phys. Rev. Lett. **67**, 3172 (1991).

[39] The disks were patterned along a straight line with structure spacing $>2R$. X-ray transparent silicon nitride ($t = 100$ nm) was used as substrate. A thin Cr cap layer preserves the stack from oxidation. Upon the disks, a Cu microstrip of $t = 150$ nm was placed in a second fabrication step for use as an excitation source for future experiments.

[40] S. S. P. Parkin, Phys. Rev. Lett. **67**, 3598 (1991).

[41] J. Raabe, G. Tzvetkov, U. Flechsig, M. Böge, A. Jaggi, B. Sarafimov, M. G. C. Vernooij, T. Huthwelker, H. Ade, D. Kilcoyne, T. Tyliszczak, R. H. Fink, and C. Quitmann, Rev. Sci. Instrum. **79**, 113704 (2008).

[42] Note that the state of this individual disk is representative for the whole set of virgin structures investigated. However, the relative coupling angle Φ can slightly vary between different structures.

[43] See Supplemental Material at http://link.aps.org/supplemental/10.1103/PhysRevLett.110.177201 for details on the measurement of J_L^f and J_Q^f.

[44] See Supplemental Material at http://link.aps.org/supplemental/10.1103/PhysRevLett.110.177201 for details on the response of meron pairs to static magnetic fields.

[45] M. R. Scheinfein, http://llgmicro.home.mindspring.com.

[46] Simulation size $[\pi \times 1000^2 \times (50 + 0.8 + 50)]$ nm^3, saturation magnetizations $M_s^{\mathrm{NiFe}} = 0.74 \times 10^6$ A/m and $M_s^{\mathrm{Co}} = 1.27 \times 10^6$ A/m, standard exchange constants $A^{\mathrm{NiFe}} = 1.05 \times 10^{-11}$ J/m and $A^{\mathrm{Co}} = 3.05 \times 10^{-11}$ J/m, $J_Q = 1.05$ mJ/m^2, neglected intrinsic anisotropies $K_u^i = 0$. Vacuum permeability was assumed for the interlayer. In order to match the experimental coupling angle of $\Phi \sim 135°$, the ratio J_L/J_Q was set to 1.41 by reducing J_L to -1.51 mJ/m^2 compared to the experimental trilayer value of -1.95 mJ/m^2. This adaption of J_L/J_Q reduces the overall saturation field as is expected for roughness induced effects.

[47] T. Gilbert, IEEE Trans. Magn. **40**, 3443 (2004).

[48] NiFe single layer simulation $(\pi \times 1000^2 \times 50)$ nm^3 on a $256 \times 256 \times 5$ grid. Trilayer simulation of a Co50/vacuum0.8/NiFe50 (nm) vortex pair with antiferromagnetic circulations and parallel cores $[\pi \times 1000^2 \times (50 + 0.8 + 50)]$nm^3 on a $256 \times 256 \times (2 + 1 + 2)$ grid. All other parameters were set in accordance with the values given earlier.

[49] See Supplemental Material at http://link.aps.org/supplemental/10.1103/PhysRevLett.110.177201 for details on the simulated angle distributions.

[50] See Supplemental Material at http://link.aps.org/supplemental/10.1103/PhysRevLett.110.177201 for quantitative details on the toroidal flux closure.

[51] M.-Y. Im, P. Fischer, K. Yamada, T. Sato, S. Kasai, Y. Nakatani, and T. Ono, Nat. Commun. **3**, 983 (2012).

[52] A. N. Bogdanov and U. K. Rössler, Phys. Rev. Lett. **87**, 037203 (2001).

APPLIED PHYSICS LETTERS **103**, 131911 (2013)

Sponge-like Si-SiO$_2$ nanocomposite—Morphology studies of spinodally decomposed silicon-rich oxide

D. Friedrich,[1] B. Schmidt,[1] K. H. Heinig,[1] B. Liedke,[1] A. Mücklich,[1] R. Hübner,[1] D. Wolf,[2] S. Kölling,[3] and T. Mikolajick[4,5]
[1]*Helmholtz-Zentrum Dresden – Rossendorf, Bautzner Landstr. 400, 01328 Dresden, Germany*
[2]*Triebenberg Laboratory, Institute of Structure Physics, Technische Universität Dresden, 01062 Dresden, Germany*
[3]*Fraunhofer Center Nanoelectronic Technologies, Königsbrücker Str. 180, 01099 Dresden, Germany*
[4]*NaMLab GmbH, Nöthnitzer Str. 64, 01187 Dresden, Germany*
[5]*Technische Universität Dresden, Nöthnitzer Str. 64, 01187 Dresden, Germany*

(Received 28 June 2013; accepted 23 August 2013; published online 25 September 2013; corrected 26 September 2013)

Sponge-like Si nanostructures embedded in SiO$_2$ were fabricated by spinodal decomposition of sputter-deposited silicon-rich oxide with a stoichiometry close to that of silicon monoxide. After thermal treatment a mean feature size of about 3 nm was found in the phase-separated structure. The structure of the Si-SiO$_2$ nanocomposite was investigated by energy-filtered transmission electron microscopy (EFTEM), EFTEM tomography, and atom probe tomography, which revealed a percolated Si morphology. It was shown that the percolation of the Si network in 3D can also be proven on the basis of 2D EFTEM images by comparison with 3D kinetic Monte Carlo simulations. © *2013 AIP Publishing LLC*. [http://dx.doi.org/10.1063/1.4820453]

In sub-stoichiometric silica SiO$_x$ ($x \lesssim 2$), also known as silicon-rich oxide (SRO), thermal treatment leads to phase separation of excess Si in a matrix of stoichiometric oxide (SiO$_2$) according to $\mathrm{SiO}_x \rightarrow \frac{x}{2}\mathrm{SiO}_2 + \left(1-\frac{x}{2}\right)\mathrm{Si}$. For stoichiometries of $x \gtrsim 1.4$ of the thermodynamically not stable SiO$_x$[1] isolated Si nanoclusters (Si NCs) are formed.[2,3] In this case, the excess Si defined by $\left(1-\frac{x}{2}\right)$ is below 30 at. %, i.e., below 16 vol. % of Si. For an excess Si of about 30 vol. % or higher, spinodal decomposition into a sponge-like morphology of the Si-SiO$_2$ nanocomposite is expected.[2–4] The formation of a sponge-like Si morphology, i.e., a nanowire network, is a promising process of the synthesis of nanostructured Si absorbers for 3rd generation solar cells. This is because a significant band gap widening due to quantum confinement in thin nanowires can be combined with a good electrical conductivity of the percolated nanowire network. We suggest that the approach of "quantum sponge structure for silicon based optoelectronics," coming from electrochemically etched porous Si,[5] can be transferred to large-scale thin film technology. However, problems of this technology like surface defect states, long term instability due to ambient impact on the open porous Si, and an inhomogeneous Si morphology can be reduced by our approach of embedding the sponge-like Si into a SiO$_2$ matrix.[5] In this case, the Si-SiO$_2$ nanocomposite is a dense structure with coherent low-defective Si-SiO$_2$ interfaces.

SiO$_x$ films of variable thickness can be prepared by physical vapor deposition (PVD) or chemical vapor deposition (CVD). The sizes of Si NCs and the characteristic lengths of sponge-like Si nanostructures depend on the annealing temperature, the annealing time, the stoichiometry of the SiO$_x$[2–4,6,7] as well as on impurities such as N and H for CVD,[8,9] and for very thin layers on the SiO$_x$ layer thickness.[4,6,7,10] In order to obtain a Si NC superlattice in a SiO$_2$ matrix, which is another concept of utilizing quantum confinement effects for photovoltaics, SiO$_x$/SiO$_2$ thin multilayers with some tens of periods and single layer thicknesses of about 2 nm are deposited successively and annealed subsequently.[6,7] The thickness and stoichiometry of each single SiO$_x$ layer and moreover the SiO$_2$ interlayer thicknesses have to be controlled very accurately since both an unimodal Si NC size distribution and narrow Si NC spacings are critical for obtaining quantum size effect while keeping the electrical resistivity low.[7] High rate deposition of a single thick SiO$_x$ film with homogeneous Si excess, followed by thermally activated Si nano-structuring, is a simpler process and therefore a cost effective alternative. At about 30 vol.% or higher excess Si, percolated Si nanostructures grow homogeneously in the SiO$_2$ matrix during appropriate thermal treatment.

In this Letter, 3D sponge-like morphologies, which were formed by spinodal decomposition of sputter-deposited SiO$_x$ films during rapid thermal annealing (RTA), are investigated. The SiO$_x$ stoichiometry was around $x \approx 1$, i.e., the excess Si was 50 at. % corresponding to 30 vol. % of phase-separated Si. Structural characterization was carried out by energy-filtered transmission electron microscopy (EFTEM) imaging, EFTEM tomography, and, for comparison, by atom probe tomography (APT).

200 nm thick SiO$_x$ films were deposited at room temperature on p-type (100) Si wafers by magnetron sputtering in Ar plasma at a pressure of 0.67 Pa with a deposition rate of 0.3 nm·s^{-1}. The substrate holder rotated 5.5 cm beneath the two simultaneously operating 8 in. Si (340 W) and SiO$_2$ (1000 W) sputter targets. Approximately 1–2 atomic layers were deposited per rotation of the substrate holder under each target, assuring an almost random distribution of Si and O atoms in the deposited films. During subsequent RTA in Ar (5N) ambient, the samples were heated from room temperature up to 1000, 1100, and 1150 °C at a heating rate of about 130 K·s^{-1}, and then annealed for 30 s. The silicon concentrations in the as-deposited and in the annealed films were measured by Rutherford backscattering spectroscopy

and yielded $x \approx 1$ in both cases. Oxidation of the excess Si during RTA by humidity and oxygen impact from the ambient was not observed.[11,12]

Si sponge-like nanostructures were investigated by transmission electron microscopy (TEM) using an image-corrected Titan 80–300 FEI microscope equipped with a Gatan Imaging Filter 863. The thickness of the cross sectional specimen, prepared by dimpling and Ar^+ ion milling, was estimated to be around 50 nm by electron energy loss spectroscopy (log-ratio method) with about 20% error.[13] Fig. 1 compares TEM images of a $SiO_{x\approx 1}$ film, decomposed into Si and SiO_2 during annealing at 1100 °C for 30 s, with an image simulated by 3D kinetic Monte-Carlo (kMC) method. In the high-resolution TEM image [Fig. 1(a)] Bragg-oriented Si NCs are visible and indicate crystallization of phase-separated Si during RTA. Larger volumes of precipitated Si crystallize preferably, while smaller precipitates remain amorphous.[6] Accordingly, by TEM imaging of only the crystallized Si fraction, the mean Si structure size is rather overestimated. The thickness of a-Si shells around c-Si and the structure size of the a-Si precipitates remain uncertain.[14,15] For small Si structures, phase separation even without crystallization of the Si precipitates can occur, which underlines the importance of EFTEM studies for Si nanostructures [Fig. 1(b)].[2,14–16] Imaging exclusively with electrons, which suffered an energy loss of 17(±2) eV due to excitation of valence band plasmons in Si, allows to identify phase-separated c-Si and a-Si.[2,14–16] The expected sponge-like Si morphology as well as partial crystallization of Si in phase-separated SiO_x were found by EFTEM studies [Fig. 1(b)], which show that the Si structures have characteristic sizes of a few nanometers.

The sponge-like Si morphologies imaged by EFTEM were compared with nanostructures predicted by atomistic kMC simulations.[17] For the large-scale 3D kMC simulations [see Figs. 1(c), 2(d)–2(f)], a $55 \times 55 \times 55\,\text{nm}^3$ cell with randomly distributed Si excess atoms in a SiO_2 matrix and with periodic boundary conditions for all space coordinates was used in order to mimic the $SiO_{x\approx 1}$ phase. The number of kMC steps (170 000) is a measure of the annealing time. Since the published values of temperature-dependent (self-)diffusion coefficients in SiO_x vary strongly, one cannot directly relate experimental annealing time to a number of kMC steps.[2,14,18] The kMC method based on the Ising model was used, where the migration barrier of the diffusion is assumed to be the same for all nearest neighbor configurations.[17] The reaction pathway of the SiO_x decomposition is then mainly governed by the normalized bond energy $\varepsilon = E_B \times (k_B \times T)^{-1}$, where E_B is the bond energy and $k_B \times T$ the thermal energy. In order to perform the numerical simulation of phase separation in large volumes, the kinetics was accelerated by an enhanced temperature. In Fig. 1(c), the volume concentration of the excess Si within a 50 nm thick slice of the kMC simulation cell was integrated along the thickness and projected onto a plane. In this plot, which models an EFTEM image, a high local content of excess Si appears bright. The similarity of Figs. 1(b) and 1(c) verifies the conformity of the experimentally observed and simulated sponge-like Si morphologies. However, this is no ultimate proof that the EFTEM images are not generated by a projection of randomly distributed Si NCs.

EFTEM images of SiO_x annealed at 1000, 1100, and 1150 °C for 30 s are depicted in Figs. 2(a)–2(c), respectively. The characteristic structure sizes (ξ) of the Si-SiO_2 nanocomposites, which were estimated by using the first zero points of the pair-correlation functions,[19] increase systematically with annealing temperature: $\xi_{1000\,°C} = 2.2$ nm [Fig. 2(a)], $\xi_{1100\,°C} = 2.8$ nm [Fig. 2(b)], and $\xi_{1150\,°C} = 3.8$ nm [Fig. 2(c)]. Simultaneously, the crystalline fraction of the phase-separated Si rises, as analyzed by Raman spectroscopy (not shown here). The growth of the characteristic size of the sponge-like morphology with increasing temperature for isochronic annealing is in agreement with our kMC predictions of nanosponge coarsening with increasing time during isothermal annealing (not shown here).

The excess Si in 12 nm thin slices of the kMC simulation cells is depicted in Figs. 2(d)–2(f) as 3D plots. The morphologies of $SiO_{x\approx 1}$ after annealing at 1000, 1100, and 1150 °C imaged by EFTEM Figs. 2(a)–2(c) were found to agree very well with the corresponding simulated morphologies. Since the EFTEM-like image of a kMC simulation cell [Fig. 1(c)] and the excess Si of the experimental EFTEM image [Fig. 1(b)] are quite similar, one can assume that both images originate from the same Si morphology. Hence, the percolation of the simulated sponge-like Si morphologies [Figs. 2(d)–2(f)] suggests that the excess Si within phase-separated SiO_x, imaged by EFTEM [Figs. 2(a)–2(c)], is percolated as well. Therefore, the comparison of EFTEM

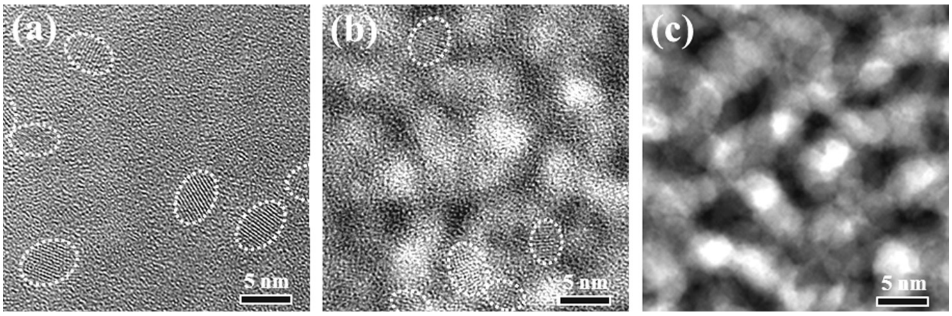

FIG. 1. Comparison of cross-sectional TEM images of a $SiO_{x\approx 1}$ sample decomposed into Si and SiO_2 during annealing at 1100 °C for 30 s with an image produced by kMC simulation of phase separation. (a) High-resolution TEM image showing only the c-Si fraction with Bragg-oriented lattice planes; (b) EFTEM image ($E_{loss} = 17$ eV) showing all phase-separated c-Si and a-Si. Here, the Bragg-oriented crystalline Si grains (marked) can be identified too. (c) EFTEM-like 2D image produced with 3D kMC simulation data of $SiO_{x\approx 1}$ phase separation, showing a similar morphology like in (b). The Si appears bright, whereas the SiO_2 is dark.

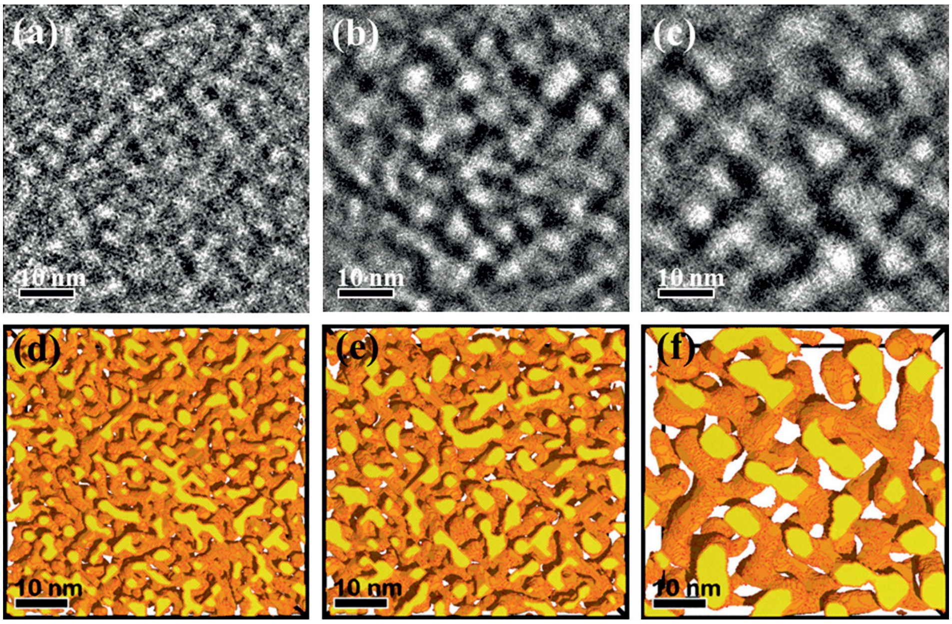

FIG. 2. Cross-sectional EFTEM images ($E_{\text{loss}} \approx 17\,\text{eV}$) of $\text{SiO}_{x\approx1}$ after annealing for 30 s at (a) 1000 °C, (b) 1100 °C, and (c) 1150 °C in comparison with 3D morphologies predicted by kMC simulations for corresponding annealing conditions (d) $\varepsilon = 4$, (e) $\varepsilon = 3$, and (f) $\varepsilon = 2$. In the 2D images (a)–(c), the Si appears bright. In the 3D images (d)–(f), the yellow areas resemble a cut through Si due to slicing a thin layer out of the simulation box, whereas the orange color visualizes the interface between the 3D Si nanosponge and SiO_2. In this plot, SiO_2 is assumed to be transparent.

images with 3D kMC simulations helps to get access to the correct 3D view of the sponge-like Si nanostructure.

EFTEM images can show the distribution of Si and SiO_2 phases in a planar projection, but they still are not providing full 3D information. In order to assure the sponge-like Si morphology, EFTEM imaging combined with electron tomography[20] was employed for reconstructing the 3D distribution of the sponge-like Si nanostructures. For this purpose, EFTEM images were recorded at a Philips microscope CM200 FEG with a Gatan Imaging Filter 678, while tilting the specimen between −70° and +70° with an increment of 2°. The alignment, i.e., the correction of displacements between the observed images due to imperfections of the goniometer, was carried out using the IMOD software.[21] The 3D reconstruction of the Si morphology was performed with the weighted simultaneous iterative reconstruction technique.[22]

Although EFTEM can give two- and three-dimensional morphology information, it cannot provide a fully quantitative concentration analysis. Atom probe tomography can potentially fulfill both, the need for a sufficient spatial resolution and simultaneously a quantitative compositional analysis.[23] Therefore, additionally, APT characterization of the Si-SiO_2 nanocomposite was performed using the laser-assisted local electrode atom probe (LEAP 3000XSi$^{\text{TM}}$) from Cameca with a pico-second laser operating at 0.2 nJ energy, having a wavelength of 532 nm, a pulse repetition rate of 400 kHz, and a spot size of approximately 10 μm. The base temperature of the sample during the experiment was kept at 30 K. Fig. 3 shows the results of 3D imaging of the Si nanosponge after spinodal decomposition of $\text{SiO}_{x\approx1}$ obtained by EFTEM tomography [Fig. 3(a)] and by APT [Fig. 3(b)].

Like in 2D EFTEM, the accuracy of the Si-SiO_2 interface of EFTEM tomography in Fig. 3(a) is about 1 nm.[15] In order to obtain a clearly defined 3D Si structure with a sharp interface, the intensity threshold in the tomogram was adjusted to ≈ 30 vol. % of excess Si. This corresponds to the decomposition of $\text{SiO}_{x=1}$, whereas for lowered excess Si, the connected structures gradually decay into isolated Si NCs, as supported by kMC simulations and experiments.[2,3] A possible overlapping of stacked spherical Si NCs in the projection, which might look like a sponge-like morphology in 2D EFTEM imaging, can be excluded by the two tomography methods APT and EFTEM tomography. The Si percolation in Fig. 3(a) is less pronounced compared to results of kMC simulations. An underestimation of the thinnest, presumably amorphous, Si filaments might be caused by limited resolution for reconstruction of small Si structures (<2 nm) in tomograms. Additionally, a somewhat broader energy distribution of the a-Si plasmon resonance compared to c-Si may reduce the number of detectable electrons within the fixed energy loss window by a few percent.[13]

Published EFTEM tomograms of CVD $\text{SiO}_{x\approx1}$ films, annealed at 1100 °C for 3 h, show isolated non-spherical Si NCs.[15] Compared to sputter-deposited SiO_x with equal Si concentration, it was observed that less excess Si can precipitate in CVD films.[8,9] In particular, in CVD films, the N (typically above 10 at. % N) from N_2O can react with Si to form

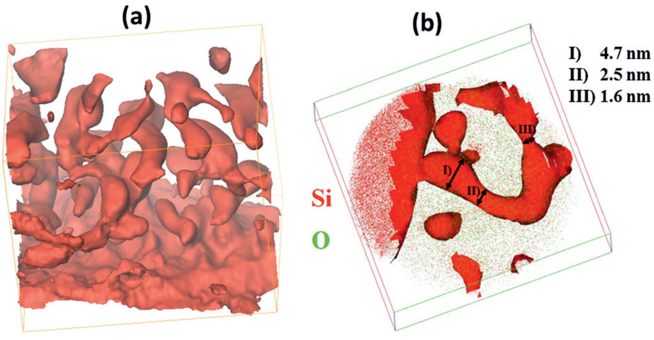

FIG. 3. 3D imaging of sputter-deposited $\text{SiO}_{x\approx1}$, phase-separated by heat treatment for 30 s at 1100 °C by (a) EFTEM tomography and (b) APT. EFTEM tomogram (a) of decomposed $\text{SiO}_{x\approx1}$ above the Si-SiO_x interface confirms a 3D sponge-like morphology as expected after spinodal decomposition of $2\,\text{SiO}_1 \rightarrow \text{Si} + \text{SiO}_2$. Si (red) and SiO_2 (transparent) are imaged applying an intensity threshold on electron energy loss mapping ($E_{\text{loss}} = 17\,\text{eV}$) resulting in ≈ 30 vol. % Si within a $28 \times 31 \times 24\,\text{nm}^3$ large volume. The Si capping and Si precipitation (red) in the APT image (b) can be distinguished from the embedding SiO_2 matrix. A 70 at. % Si isoconcentration surface was set as the Si-SiO_2 interface. Si structure sizes between 1.6 nm and 4.7 nm were found within the investigated $3600\,\text{nm}^3$ large volume.

oxynitride compounds, thus reducing the volume of excess Si to precipitate.[9]

The nanosponge structure sizes apparent in EFTEM tomography were confirmed within an error of about 1 nm by APT [Fig. 3(b)]. Published APT investigations on $SiO_{x\approx1}/SiO_2$ multilayers,[4] which were annealed for 1 h, show a morphology similar to ours for an annealing temperature of 900 °C, and isolated Si NCs after annealing at 1100 °C. A comparison of these results with our Si-SiO_2 morphologies is difficult, due to their very thin SiO_x layers. There, the Si NC formation at higher temperature is interpreted as an advanced state of ripening in a confined geometry of 4 nm thick SiO_x surrounded by SiO_2 films.[4] Thus, the ripening of interconnected excess Si leads to crossing of the initial SiO_x/SiO_2 interface by the Si precipitates.[4] Therefore, the stoichiometry in this film increases to $SiO_{x>1}$, which leads to the formation of isolated Si NCs.[3]

In summary, we have shown that sponge-like Si-SiO_2 nanocomposites can be fabricated by rapid thermal processing of sputter-deposited $SiO_{x\approx1}$ films. This morphology results from spinodal decomposition of $SiO_{x\approx1}$ into 30 vol. % excess Si and SiO_2. The Si-SiO_2 morphology was studied by means of cross-sectional EFTEM imaging, EFTEM tomography and APT. Morphologies predicted by kMC simulations agree very well with those of EFTEM and APT analyses. The characteristic sizes of percolated Si structures were determined to be 2–4 nm, which is in the size range where quantum confinement effects are expected, therefore giving rise to application as photovoltaic absorber material.

The authors would like to thank M. Missbach and A. Kunz for TEM lamellae preparation, B. Scheumann for layer deposition, as well as K.-H. Stegemann for helpful discussion. This work was financially supported by “Bundesministerium für Bildung und Forschung” (BMBF) under the 2 + 2 project contract No. TUR 09/211

[1] S. M. Schnurre, J. Gröbner, and R. Schmid-Fetzer, J. Non-Cryst. Solids **336**, 1 (2004).

[2] T. Müller, K.-H. Heinig, W. Möller, C. Bonafos, H. Coffin, N. Cherkashin, G. Ben Assayag, S. Schamm, G. Zanchi, and A. Claverie, Appl. Phys. Lett. **85**, 2373 (2004).

[3] T. Müller, K.-H. Heinig, and W. Möller, Appl. Phys. Lett. **81**, 3049 (2002).

[4] M. Roussel, E. Talbot, R. Pratibha Nalini, F. Gourbilleau, and P. Pareige, Ultramicroscopy **132**, 290 (2013).

[5] O. Bisi, S. Ossicini, and L. Pavesi, Surf. Sci. Rep. **38**, 1 (2000).

[6] C. Ternon, C. Dufour, F. Gourbilleau, and R. Rizk, Eur. Phys. J. B **41**, 325 (2004).

[7] F. Gourbilleau, C. Ternon, D. Maestre, O. Palais, and C. Dufour, J. Appl. Phys. **106**, 013501 (2009).

[8] G. Franzò, M. Miritello, S. Boninelli, R. Lo Savio, M. G. Grimaldi, F. Priolo, F. Iacona, G. Nicotra, C. Spinella, and S. Coffa, J. Appl. Phys. **104**, 094306 (2008).

[9] S. Mirabella, G. Di Martino, I. Crupi, S. Gibilisco, M. Miritello, R. Lo Savio, M. A. Di Stefano, S. Di Marco, F. Simone, and F. Priolo, J. Appl. Phys. **108**, 093507 (2010).

[10] K. Binder, J. Non-Equilib. Thermodyn. **23**, 1 (1998).

[11] S. Guha, S. B. Qadri, R. G. Musket, M. A. Wall, and T. Shimizu-Iwayama, J. Appl. Phys. **88**, 3954 (2000).

[12] B. Schmidt, D. Grambole, and F. Herrmann, Nucl. Instrum. Methods B **191**, 482 (2002).

[13] R. Egerton, Rep. Prog. Phys. **72**, 016502 (2009).

[14] F. Iacona, C. Bongiorno, C. Spinella, S. Boninelli, and F. Priolo, J. Appl. Phys. **95**, 3723 (2004).

[15] A. Yurtsever, M. Weyland, and D. A. Muller, Appl. Phys. Let. **89**, 151920 (2006).

[16] S. Schamm, C. Bonafos, H. Coffin, N. Cherkashin, M. Carradaa, G. Ben Assayag, A. Claverie, M. Tencé, and C. Colliex, Ultramicroscopy **108**, 346 (2008).

[17] M. Strobel, K.-H. Heinig, and W. Möller, Phys. Rev. B **64**, 245422 (2001).

[18] T. Takahashi, S. Fukatsu, K. M. Itoh, M. Uematsu, A. Fujiwara, H. Kageshima, Y. Takahashi, and K. Shiraishi, J. Appl. Phys. **93**, 3674 (2003).

[19] D. A. Huse, Phys. Rev. B **34**, 7845 (1986).

[20] P. A. Midgley and M. Weyland, Ultramicroscopy **96**, 413 (2003).

[21] J. Kremer, D. N. Mastronarde, and J. R. McIntosh, J. Struct. Biol. **116**, 71 (1996).

[22] D. Wolf, A. Lubk, and H. Lichte, Ultramicroscopy **136**, 15 (2013).

[23] M. K. Miller, A. Cerezo, M. G. Hetherington, and G. D. W. Smith, *Atom Probe Field Ion Microscopy* (Oxford University Press, New York, 1996).

APPLIED PHYSICS LETTERS **103**, 133106 (2013)

Formation and coarsening of sponge-like Si-SiO_2 nanocomposites

B. Liedke, K.-H. Heinig, A. Mücklich, and B. Schmidt
Helmholtz-Zentrum Dresden – Rossendorf, Bautzner Landstr. 400, 01328 Dresden, Germany

(Received 27 June 2013; accepted 9 September 2013; published online 24 September 2013)

It has been recently found by energy filtered transmission electron microscopy (EFTEM) that metastable $SiO_{x\approx 1}$ films decay into a Si nanowire network embedded in SiO_2 by spinodal decomposition during thermal treatment. To have a guideline for nanocomposites fabrication, details of the morphology evolution have been studied by comparison of EFTEM images with kinetic Monte-Carlo (kMC) simulations. Pair correlation functions calculated by kMC have been adjusted to that extracted from EFTEM. This comparison leads to the conclusion about characteristic lengths of 3D morphologies. Combining kMC with EFTEM delivers the understanding for tailoring the properties like quantum confinement of the spongy Si. *© 2013 AIP Publishing LLC*.

[http://dx.doi.org/10.1063/1.4822125]

Si-SiO_2 based nanocomposites have recently attracted a lot of interest due to their application potential in Li batteries,[1] memories and light-emitting Si devices,[2,3] and solar cells.[4] The main advantages of these nanocomposites are directly related to the small size of the Si structures, which provides in batteries an increased surface area of the anode and higher tolerance to swelling,[1] allows in transistors for direct tunneling between nanocrystals,[2,3] acts in solar cells as intermediate reflectors,[4] and increases there the band gap by the quantum size effect.[5]

There are many reports about quantum confinement in Si nanocrystals,[6,7] nanowires,[8,9] and porous structures.[10] As reported by Cuony *et al.*,[4] electrons will be confined not only in nanocrystals but also in more complicated morphologies like Si filaments. The full control of the quantum confinement effect is only possible by a tailored synthesis of the Si-SiO_2 nanocomposite and with reaction pathways for selection of desired sizes in the nanostructures. Diameters of nanocrystals and nanowires are usually determined using electron microscopy techniques. The pore size distribution of porous structures is measured conventionally by the gas desorption method or by nuclear magnetic resonance.[11] The determination of characteristic length in more complex 3D morphologies such as percolated Si nanostructure embedded in SiO_2 formed by spinodal decomposition[12] or nanoporous Au made by dealloying[13] requires more sophisticated approaches.

Because of missing mass contrast between Si and SiO_2 in conventional TEM, in the past, high-resolution TEM was employed to image at least the silicon fraction having the lattice aligned with the electron beam.[14,15] However, imaging specifically electrons which lost a well-defined energy by excitation of valence band plasmons (which is different for Si and SiO_2), the Energy Filtered Transmission Electron Microscopy (EFTEM) shows all of the phase separated Si in Si-SiO_2 nanocomposites.[9]

Analyzing an EFTEM image of a nanostructured Si-SiO_2 nanocomposite numerically, a characteristic length (ξ) of the system can be defined by the first zero point of its pair correlation function.[16] For very thin 2D films as in Ref. 7, ξ_{2D} is obviously a good quantity to characterize the morphology. However, the ξ_{3D} of thick 3D nanocomposites cannot be related straightforward to ξ_{2D} of the EFTEM images, which are 2D projections of the 3D morphologies of about 50 nm thick TEM specimen. By adjusting simulated ξ_{2D}^{kMC} of EFTEM-like images calculated by large scale 3D kinetic lattice Monte-Carlo simulations[17] to the ξ_{2D}^{EFTEM} of experimental EFTEM images, we can predict the ξ_{3D} of the 3D morphology by analyzing the kinetic Monte-Carlo (KMc) data in 3D. Additionally, the kMC simulations provide the reaction pathways of the spinodal decomposition, which was proven by simulations of the formation of a thin layer of percolated Si nanoclusters in gate oxides.[7]

The details of the kMC simulation of the SiO_x phase separation can be found in Refs. 7, 9, and 17. Here, a simulation cell of $2^8 \times 2^8 \times 2^8 \approx 16$ million lattice sites (i.e., about $56 \times 56 \times 56$ nm^3) have been employed to elaborate the features of the experimental decomposition of SiO_x deposited on a Si substrate, i.e., periodic boundary condition in x-y plane were used in this case. To minimize the influence of the boundary condition on the ξ^{kMC}, large simulation cells of $2^9 \times 2^9 \times 2^9$ lattice sites (i.e., about $111 \times 111 \times 111$ nm^3) with periodic boundary condition in x, y, and z directions have been chosen. The Si excess is set to 30 vol. %, which corresponds to the stoichiometry of $SiO_{x=1}$. The initial condition for SiO_x is taken into account by uniformly distributed Si excess atoms inside the SiO_2 matrix. The excess Si atoms diffuse and precipitate, thus leading to spinodal decomposition under thermal treatment. Both the annealing time, defined as a number of Monte-Carlo (MC) steps, as well as the annealing temperature have been chosen to match the morphology measured by EFTEM.[17]

The EFTEM images compared here with kMC simulations were taken by the image-corrected Titan 80-300 (FEI) microscope equipped with Gatan Tridiem 863 imaging spectrometer. The microscopy specimens were prepared from a $SiO_{x=1}$ layer deposited by magnetron sputtering onto (001) Si substrate and annealed subsequentially at 1100 °C for 30s. Electrons, decelerated by 17 ± 1.5 eV due to the excitation of a valence-band plasmon resonance in Si, are imaged in Fig. 1(a). Si is at least partially in the crystalline state as it is marked by white circles where lattice planes, aligned

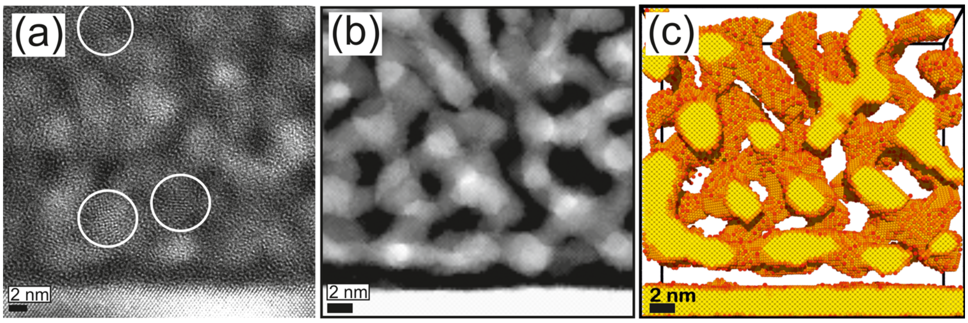

FIG. 1. Comparison of cross-section EFTEM image of a spinodally decomposed SiO_1 layer on (001) Si annealed at 1100 °C for 30s (a) with an EFTEM-like image predicted by a kMC simulation (b), (c). In (a), the bright areas denote Si excess in SiO_2. The regions with Bragg-aligned crystalline Si are marked by circles. In (b), the number of Si excess atoms in each column of 9 nm thick slice defines the gray scale. Figure (c) shows the slice of Figure (b) in a 3D presentation, where SiO_2 is assumed to be transparent and the orange and the yellow atoms are at the Si-SiO_2 interface and the cut plane of the slice, respectively.

according to the Bragg condition, are visible. At the bottom of Fig. 1(a) the lattice planes of the (001) Si substrate can be seen.

As the 2D EFTEM image cannot unambiguously proof the formation of a sponge-like morphology in 3D, we simulate a corresponding 2D EFTEM image from 3D kMC calculation data (an example is shown in Fig. 1(b)). To treat the Si substrate, the Si excess concentration of the bottom layer is set to 100 vol. % (white area at the bottom of Fig. 1(b)). In order to mimic the EFTEM image of Fig. 1(a), for the EFTEM-like image of Fig. 1(b), a 9 nm thick slice is taken from the full kMC simulation cell. Then, the Si atoms are counted in each 9 nm high column of atoms normal to the image plane. The resulting numbers are assigned to a gray scale and plotted in Fig. 1(b). In Fig. 1(c), the same slice of this kMC simulation is shown as a 3D morphology.

Even details of the phase separation process, like at the boundary to the Si substrate a zone denuded completely of Si, are reproduced by the kMC simulation. This is because at the Si interface the Si substrate acts as an efficient sink for Si excess dissolved in SiO_x.

The 3D characteristic length ξ_{3D}^{kMC} of a sponge calculated by kMC is determined by two independent methods both giving a power law scaling behavior as plotted in Fig. 2(a). In the first one, (Fig. 2(b)) the 3D pair correlation function $\boldsymbol{G}$ is calculated in space $\boldsymbol{R}$ and time t as $\boldsymbol{G}(\boldsymbol{R},t) = \sum_{\boldsymbol{k}} e^{i\boldsymbol{kR}}\boldsymbol{S}(\boldsymbol{k},t)$, where $\boldsymbol{S}(\boldsymbol{k},t)$ is the structure factor of the sponge expressed in reciprocal space $\boldsymbol{k}$.[18] A radial average of $\boldsymbol{G}(\boldsymbol{R},t)$ delivers a spatial 1D function $G(R,t)$ The characteristic length of the first method ξ_1^{kMC} is conventionally defined as the first zero point of $G(R,t)$, i.e., $G(R_0,t) = 0$ and $\xi_1^{kMC} = R_0$ (see Fig. 2(b)).[18–20] In the second method, we use the thinning algorithm of Lee *et al.*[21] to create the skeleton (Fig. 2(d)) of the sponge-like morphology (Fig. 2(c)). For each point of the skeleton the nearest distance to the Si-SiO_2 interface is calculated. The distance stands for a local radius of a wire being a fragment of sponge. The characteristic length ξ_2^{kMC} is then twice the average of all local radii of the skeleton, i.e., the local diameters of wires. The skeleton method provides direct information about the frequency of skeleton diameters as plotted in inset of Fig. 2(a). A broadening of the diameter distributions with increase of annealing time is seen in the inset. As shown in Fig. 2(a), the length ξ_1^{kMC} calculated from the pair correlation, is about 9% higher compared to the skeleton

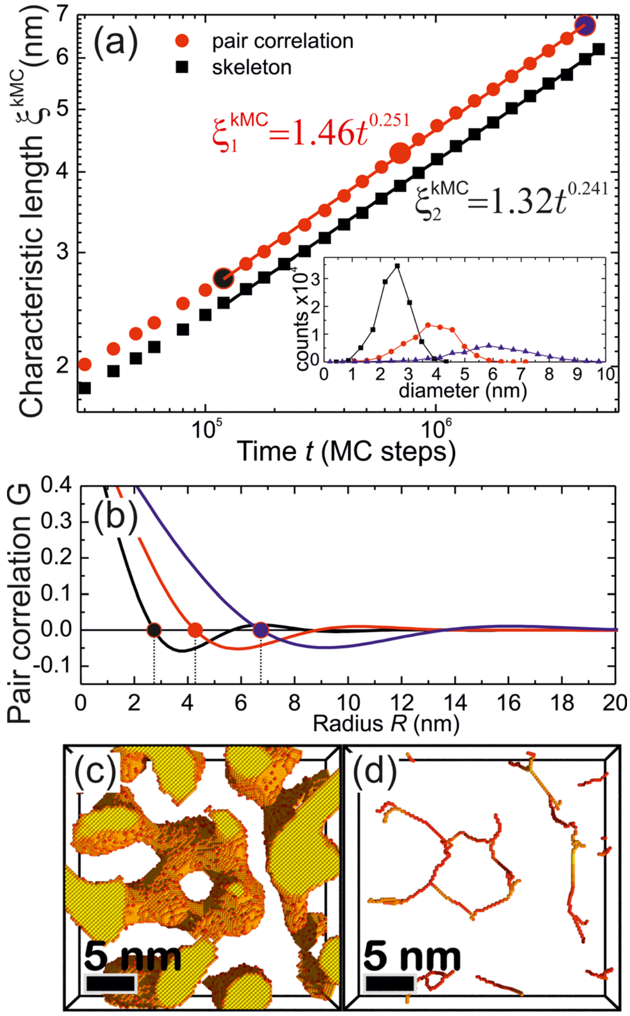

FIG. 2. Structure size calculation of sponge-like 3D morphology simulated with KMC. (a) power-law scaling of the characteristic lengths ξ_1^{kMC}, ξ_2^{kMC} during annealing with power-law exponents 0.251(1) and 0.241(1), respectively. (b) Method to obtain ξ_1^{kMC} using the pair correlation function. Three functions are given for three annealing times after 120 k, 700 k, and 4.44M MC steps, where the characteristic lengths are marked by dots at first-zero points of the functions. The three sizes are plotted in (a) as large circles. (c)-(d) method to obtain ξ_2^{kMC} by a distance map of the 3D skeleton. Figure (d) depicts a skeleton of the structure (c). The color at different skeleton points corresponds to the distance between the skeleton point and the nearest Si-SiO_2 interface point. ξ_2^{kMC} is the mean value of all these distances. The distribution of these distances is plotted as an inset of (a) for the three annealing times.

values of ξ_2^{kMC}. However, both methods exhibit the same scaling behavior. In the following, the pair correlation method will be used as a reference of the mean wire diameter calculated for 2D projection of simulation cell and for full 3D simulation cell using ξ_{2D}^{kMC} and ξ_{3D}^{kMC}, respectively.

The two characteristic lengths $\xi_1^{\mathrm{kMC}}(t)$ and $\xi_2^{\mathrm{kMC}}(t)$ exhibit very similar coarsening with scaling exponents of 0.251 and 0.241, respectively. These values are consistent with an exponent of 1/4 obtained by Szabo.[19] However, more recent studies[20] report a Lifshitz-Slyozov scaling with an exponent of 1/3. It should be noted that the value 1/3 was obtained with a much smaller system dimension of L=128, where L is the linear dimension of the cubic simulation cell (in the present study L=512 is used). As suggested already by Szabo,[19] there should be a crossover from 1/4 to 1/3 scaling exponent for much longer simulation times presumably not achieved here yet. It should be also noted that coarsening of morphologies, as in Fig. 1(a), have been studied experimentally so far by variation of the annealing temperature, not annealing time.[22] The results are in reasonable agreement with kMC simulations (not shown here). In this Letter, a more detailed discussion of scaling cannot be pursued.

To relate the characteristic length $\xi_{2D}^{\mathrm{EFTEM}}$ of the 2D projection as obtained from EFTEM to the real length ξ_{3D} of 3D sponge-like morphology, simulated EFTEM-like images of slices with different thicknesses of a kMC simulation cell are depicted in Figs. 3(a)–3(c) together with an experimental cross-sectional EFTEM image in Fig. 3(d). From this visual comparison, we can roughly estimate that the experimental specimen thickness is ~54 nm as in the simulated image of Fig. 3(c).

Nevertheless, one can plot the dependence of the characteristic length of 2D projection ξ_{2D} on the thickness of the slice out of the simulation cell (Fig. 3(e)). The inset in Fig. 3(c) shows the absolute values of ξ_{2D}^{kMC} at different slice thicknesses and simulation times. The normalized ξ_{2D}^{kMC} is obtained by normalization of each plot of the inset with the characteristic length of 3D morphology ξ_{3D}^{kMC}, which is identical to the ξ_{2D}^{kMC} of infinite thin slices. If the slice thickness amounts to 1 monolayer only, the pair correlation delivers the most accurate estimation of characteristic length ξ_{3D}^{kMC} (Fig. 3(a)). By increasing the slice thickness, the ξ_{2D}^{kMC} drops asymptotically to about 80% of the ξ_{3D}^{kMC}. Depending on the annealing time (i.e., the coarsening), the asymptotic value of ξ_{2D}^{kMC} is reached for slice thicknesses between 15 and 25 nm (see Fig. 3(e)). Thus, only unrealistically thin specimen thicknesses (below 1 nm) would deliver realistic values of characteristic lengths ξ_{3D}. Assuming 50 nm specimen thickness of EFTEM image in Fig. 3(d), the characteristic size of sponge will be underestimated by 20%, i.e., the $\xi_{2D}^{\mathrm{EFTEM}}$ value of 2.61 has to be corrected by the factor 1.2 in order to get the ξ_{3D}, which is then 3.13 nm. Having high-quality 3D experimental data, e.g., provided by EFTEM tomography,[23] one can estimate the size even more accurately using the skeleton method described above.

In summary, the synthesis of Si-SiO$_2$ nanocomposites consisting of sponge-like Si embedded in the SiO$_2$ matrix has been studied by kinetic Monte-Carlo simulations. Comparison of simulated EFTEM-like images with experimental EFTEM investigations has been proven to open access to 3D features of the Si-SiO$_2$ nanocomposites without expensive methods such as EFTEM tomography or atomic probe tomography. The predictions of the kMC simulations on the spinodal decomposition of the deposited SiO$_1$ into silicon nanosponge morphology during annealing are in reasonable agreement with experiments. The combination of EFTEM studies with atomistic simulation deepens the understanding for the nanosilicon synthesis and delivers a guideline for band gap engineering by silicon nanosponge coarsening.

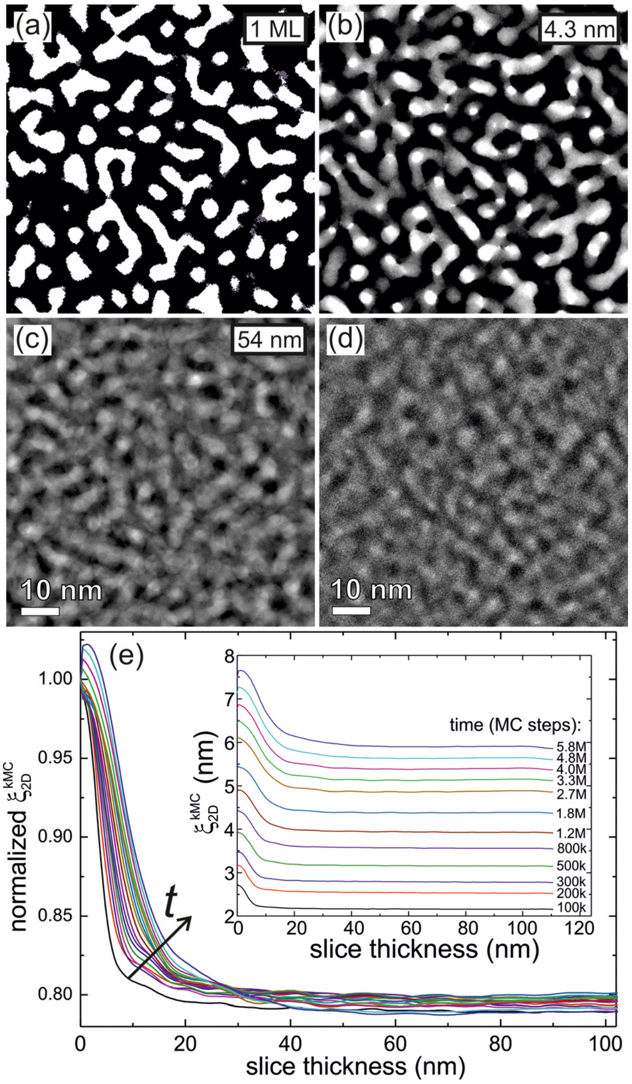

FIG. 3. (a)-(c) Simulated EFTEM-like images of slices with different thicknesses of the kMC simulation cell at t=200 k MC steps: (a) 1 monolayer, (b) 4.3 nm, and (c) 54 nm. White pixels correspond to 100% of Si excess through the slice, whereas black correspond to pure SiO$_2$. (d) An experimental EFTEM image after annealing. $\xi_{2D}^{\mathrm{EFTEM}}$ of Figure (d) is 2.61 nm. (e) The normalized ξ_{2D}^{kMC} as a function of the slice thickness for different annealing times, where the arrow indicates the dependence on time. The inset shows the same but not normalized ξ_{2D}^{kMC} at simulation times between 100 k (bottom) and 5.8M (top) MC steps. The ξ_{2D}^{kMC} are calculated by the 2D pair correlation method (see Fig. 2(b)). As the ξ_{3D}^{kMC} is identical to ξ_{2D}^{kMC} of infinite thin slices, the values along the vertical axis for different times t are plotted in Fig. 2(b).

The authors would like to thank J. Kelling for his support with a kMC simulation, D. Friedrich, Ü. Keleş, C. Bulutay, and R. Hübner for useful discussions. This work was financially supported by "Bundesministerium für Bildung und

Forschung" (BMBF) under the 2+2 project contract No. TUR 09/211.

[1] F. Dai, R. Yi, M. L. Gordin, S. R. Chen, and D. H. Wang, RSC Adv. **2**(33), 12710–12713 (2012).

[2] B. Schmidt, K. H. Heinig, L. Röntzsch, T. Muller, K. H. Stegemann, and E. Votintseva, Nucl. Instrum. Methods Phys. Res. B **242**(1-2), 146–148 (2006).

[3] V. Beyer, B. Schmidt, K. H. Heinig, and K. H. Stegemann, Appl. Phys. Lett. **95**(19), 193501 (2009).

[4] P. Cuony, D. T. L. Alexander, I. Perez-Wurfl, M. Despeisse, G. Bugnon, M. Boccard, T. Söderström, A. Hessler-Wyser, C. Hébert, and C. Ballif, Adv. Mater. **24**(9), 1182–1186 (2012).

[5] A. G. Cullis and L. T. Canham, Nature **353**(6342), 335–338 (1991).

[6] L. Pavesi, L. D. Negro, C. Mazzoleni, G. Franzò, and F. Priolo, Nature **408**(6811), 440–444 (2000).

[7] T. Müller, K. H. Heinig, and W. Möller, Appl. Phys. Lett. **81**(16), 3049–3051 (2002).

[8] D. D. D. Ma, C. S. Lee, F. C. K. Au, S. Y. Tong, and S. T. Lee, Science **299**(5614), 1874–1877 (2003).

[9] T. Müller, K. H. Heinig, W. Möller, C. Bonafos, H. Coffin, N. Cherkashin, G. B. Assayag, S. Schamm, G. Zanchi, A. Claverie, M. Tence, and C. Colliex, Appl. Phys. Lett. **85**(12), 2373–2375 (2004).

[10] O. Bisi, S. Ossicini, and L. Pavesi, Surf. Sci. Rep. **38**(1-3), 1–126 (2000).

[11] J. H. Strange, M. Rahman, and E. G. Smith, Phys. Rev. Lett. **71**(21), 3589–3591 (1993).

[12] J. van Hapert, A. Vredenberg, E. van Faassen, N. Tomozeiu, W. Arnoldbik, and F. Habraken, Phys. Rev. B **69**(24), 245202 (2004).

[13] J. Erlebacher, M. J. Aziz, A. Karma, N. Dimitrov, and K. Sieradzki, Nature **410**(6827), 450–453 (2001).

[14] B. J. Hinds, F. Wang, D. M. Wolfe, C. L. Hinkle, and G. Lucovsky, J. Vac. Sci. Technol. B **16**(4), 2171–2176 (1998).

[15] I. Balberg, E. Savir, J. Jedrzejewski, A. G. Nassiopoulou, and S. Gardelis, Phys. Rev. B **75**(23), 235329 (2007).

[16] S. Majumder and S. K. Das, Phys. Rev. E **81**(5), 050102 (2010).

[17] M. Strobel, K. H. Heinig, and W. Möller, Phys. Rev. B **64**(24), 245422 (2001).

[18] A. Chakrabarti, R. Toral, and J. D. Gunton, Phys. Rev. B **39**(7), 4386–4394 (1989).

[19] G. Szabó, Phys. Rev. E **57**(5), 6172–6175 (1998).

[20] S. Ahmad, S. K. Das, and S. Puri, Phys. Rev. E **85**(3), 031140 (2012).

[21] T. C. Lee, R. L. Kashyap, and C. N. Chu, CVGIP: Graph. Models Image Process. **56**(6), 462–478 (1994).

[22] D. Friedrich, B. Schmidt, K.-H. Heinig, B. Liedke, A. Mücklich, R. Hübner, D. Wolf, S. Kölling, and T. Mikolajik, "Sponge-like Si-SiO$_2$ nanocomposite - Morphology studies of spinodally decomposed silicon-rich oxide," Appl. Phys. Lett. (in press).

[23] M. Roussel, E. Talbot, R. P. Nalini, F. Gourbilleau and P. Pareige, Ultramicroscopy **132**, 290 (2013).

APPLIED PHYSICS LETTERS **103**, 021113 (2013)

Ultrafast graphene-based broadband THz detector

Martin Mittendorff,[1,2,a)] Stephan Winnerl,[1] Josef Kamann,[3] Jonathan Eroms,[3]
Dieter Weiss,[3] Harald Schneider,[1] and Manfred Helm[1,2]
[1]*Helmholtz-Zentrum Dresden-Rossendorf, P.O. Box 510119, 01314 Dresden, Germany*
[2]*Technische Universität Dresden, 01062 Dresden, Germany*
[3]*Universität Regensburg, 93040 Regensburg, Germany*

(Received 23 May 2013; accepted 26 June 2013; published online 11 July 2013)

We present an ultrafast graphene-based detector, working in the THz range at room temperature. A logarithmic-periodic antenna is coupled to a graphene flake that is produced by exfoliation on SiO_2. The detector was characterized with the free-electron laser FELBE for wavelengths from 8 μm to 220 μm. The detector rise time is 50 ps in the wavelength range from 30 μm to 220 μm. Autocorrelation measurements exploiting the nonlinear photocurrent response at high intensities reveal an intrinsic response time below 10 ps. This detector has a high potential for characterizing temporal overlaps, e.g., in two-color pump-probe experiments. © *2013 AIP Publishing LLC*. [http://dx.doi.org/10.1063/1.4813621]

Since the first graphene flakes have been produced and investigated by Novoselov *et al.*,[1] the development of optoelectronic graphene-based devices has been extremely fast. The special band structure of graphene,[2] where conduction and valence band touch each other in the Dirac point, provides nearly constant photon absorption for the range from the visible light down to far infrared (FIR) radiation.[3] Combined with extremely high carrier mobility[4] and fast carrier relaxation[5] this enables one to realize ultrafast optoelectronic devices for an extremely wide spectral range. Detectors for near-infrared radiation (NIR), which can be used for telecommunication purposes with frequencies of up to 16 GHz, have been demonstrated.[6] In these devices, a photocurrent is induced by an asymmetry in the detector, which is provided by two different metals serving as contacts to the flake. Recently, detectors based on graphene field-effect transistors have been developed for THz frequencies. On the one hand, a high-speed bolometer working at helium temperature has been demonstrated,[7] on the other hand, a rectifying transistor operating at room temperature has been reported.[8] For the latter only cw detection has been shown. The detector presented in this work combines room temperature operation with ultrafast response, including the potential to serve as an ultra-broadband detector up to the visible range.

The active material of our device is a graphene flake with a size of ~10 μm × 10 μm, produced by mechanical exfoliation of natural graphite onto a 300 nm thick layer of SiO_2 on silicon. The single-layer behavior of the flake is verified by Raman spectroscopy. Broadband THz response is achieved by processing a logarithmic-periodic antenna[9] onto the graphene flake by means of electron-beam lithography. The center of the antenna is structured into an interdigitated comb (see Fig. 1), which provides the contact to the graphene flake. The outer diameter of the antenna is 1 mm, which limits the maximum wavelength of the detected radiation. Wavelengths that are smaller than the shortest elements of the antenna (~10 μm) cannot efficiently couple to the antenna. Those wavelengths, however, can be focused to a spot of a size comparable to the graphene flake and thereby couple to the flake directly. For contacting the antenna to a coaxial cable (50 Ω with SMA connector) two contact pads with the size of 500 μm × 500 μm are connected via 20 μm wide and 500 μm long strip lines to the outermost part of the antenna.

Two different types of detectors were tested. A first set of detectors was produced on substrates of undoped Si with a resistivity of 10 kΩ cm underneath the SiO_2. For this set, the antenna metallization consists of 60 nm Au on top of 5 nm Ti. The Si for the second set is heavily p-doped with a resistivity of about 5 mΩ cm. In this case, two different metals were used for the two arms of the antenna. One arm consists of a 60 nm thick layer of Pd, the second one of a 20 nm thick layer of Ti with 40 nm Au on top. The intention to use two different metals is to break the symmetry of the device and thereby increase the photocurrent.[6] The combination of graphene flakes with a logarithmic-periodic antenna results in a device resistance in the range of several hundred Ω, the device on high-resistive substrate used for the measurements had a resistance of 280 Ω.

The devices were characterized using the free-electron laser (FEL) at Dresden-Rossendorf (FELBE). It provides infrared and THz pulses in the wavelength range from 5 μm to 250 μm with a repetition rate of 13 MHz. The average power for our experiments was between 1 mW and 1 W which corresponds to pulse energies between 80 pJ and 80 nJ. The FEL beam was focused on the devices by off-axis parabolic mirrors with focal lengths of 50 mm to 100 mm. The rise time of the devices was measured with a sampling oscilloscope with a bandwidth of 30 GHz. A high frequency amplifier was used to increase the amplitude of the signals and the signal-to-noise ratio. Additionally, we performed measurements of the time-integrated photocurrent with a lock-in amplifier. In this case, the FEL beam was modulated by a mechanical chopper. This technique allowed us to measure very small photocurrents to investigate the linear regime of the detector. A bias voltage could be applied to the detectors for all measurements using a bias tee. The lock-in technique was furthermore used in autocorrelation measurements. Each FEL pulse was split up into

---

[a)]M.Mittendorff@hzdr.de

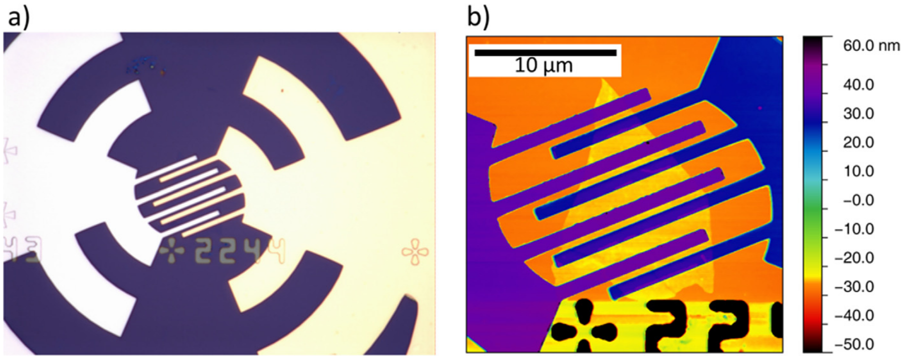

FIG. 1. a) Inner part of the antenna with interdigitated structure; (b) AFM image of the interdigitated structure with the graphene flake: The blue and violet parts are the contacts, the graphene flake is diamond-shaped in yellow.

two pulses and subsequently recombined collinearly by a pair of Si wafers. The time delay between the pulses was varied by a mechanical delay stage.

In Fig. 2(a), the fast electric response to an FEL pulse of a detector fabricated on the high-resistive substrate is shown. The rise-time of the signal is (50 ± 10) ps. We assume the second pulse to be caused by signal reflections at the contact to the coaxial signal cable. By applying a bias voltage of 100 mV, the amplitude of the measured signal could be increased above 1 mV. Changing the substrate material from high-resistive Si to low-resistive Si strongly decreases the high speed performance of the device. For the low-resistive Si, the rise time is in the range of 100 ps, while the signal pulse length is increased to above 1 ns (see Fig. 2(b)). The amplitude of the signal is strongly decreased compared to the signal of the device on high-resistive substrate, while the area under the pulse stays roughly constant. This is consistent with the observed time-integrated photocurrent, which is similar in both cases. For both types of detectors, we could not observe any fast signals at wavelengths below 20 μm, while the time-integrated photocurrent remained constant (see Fig. 3(b)).

The saturation behavior of all devices (with different substrates and metallizations) was determined by measuring the photocurrent in dependence of the FEL pulse energy. The measured data were fitted by the expression

$$I_{phot} \propto \frac{E/E_{sat}}{1+E/E_{sat}}. \tag{1}$$

From the fit the saturation pulse energy E_{sat} was extracted[10] (see Figs. 3(a) and 3(c)). At this pulse energy, the photocurrent I_{phot} is suppressed by 50% compared to the fictitious photocurrent without saturation.

The saturation energy increases with decreasing wavelength (cf. Fig. 3(c)), which is consistent with the increasing density of states for higher energies. For the measurement at a wavelength of 31 μm ($E_{photon} = 40$ meV), the error bar is very large due to the nearly linear power dependence of the photocurrent and the associated high tolerance of the fit parameters. For even higher photon energies (75 meV and 149 meV) we could not observe any saturation and the photocurrent was increasing linearly with the FEL pulse energy. The responsivity was in the range of 5 nA/W for all wavelengths (cf. Fig. 3(b)). With the strong saturation at long wavelengths, the devices can serve as nonlinear detectors in autocorrelation setups.[11] In this configuration, the temporal resolution is not limited by the electronic circuit but by the intrinsic mechanism resulting in the saturated photocurrent response. In Fig. 3(d), the measured autocorrelation signal obtained at a wavelength of 42 μm ($E_{photon} = 30$ meV) as well as calculated data are displayed. In the experiment, the time delay was varied continuously resulting in an intensity-autocorrelation trace without interference fringes. The autocorrelation trace exhibits a dip at zero time delay due to the saturated photocurrent response of the detector. The calculation was performed for a Gaussian FEL pulse (full width at half maximum: 7 ps[12]) with replicas, caused by the Si beam splitter and combiner. The replicas were delayed by multiples of 7 ps with respect to the initial pulse, i.e., the pulses merge to one prolonged pulse. The autocorrelation signal was calculated based on the nonlinear current described by Eq. (1). The fit to the experimental data was performed with

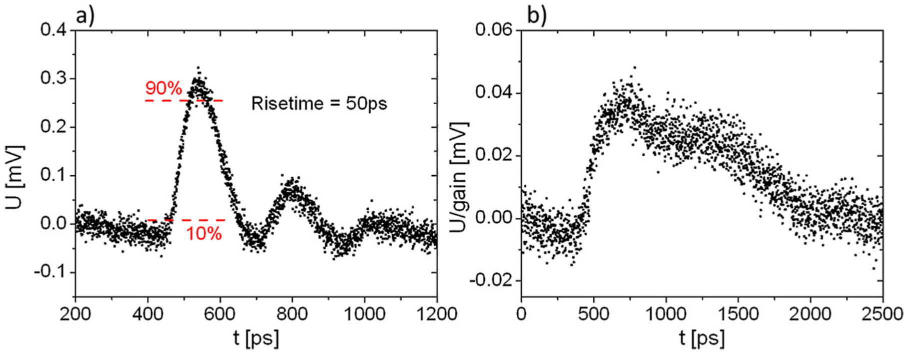

FIG. 2. a) Signal shapes measured with a device on high-resistive substrate at a wavelength of 68 μm and an average FEL power of 72 mW. For this measurement neither a bias voltage was applied, nor was the high speed amplifier used. (b) Signal shape measured with a device on low-resistive substrate. A bias voltage of 0.1 V was applied, additionally the high frequency amplifier was employed, for a better comparison the voltage was divided by the gain (50) of the amplifier.

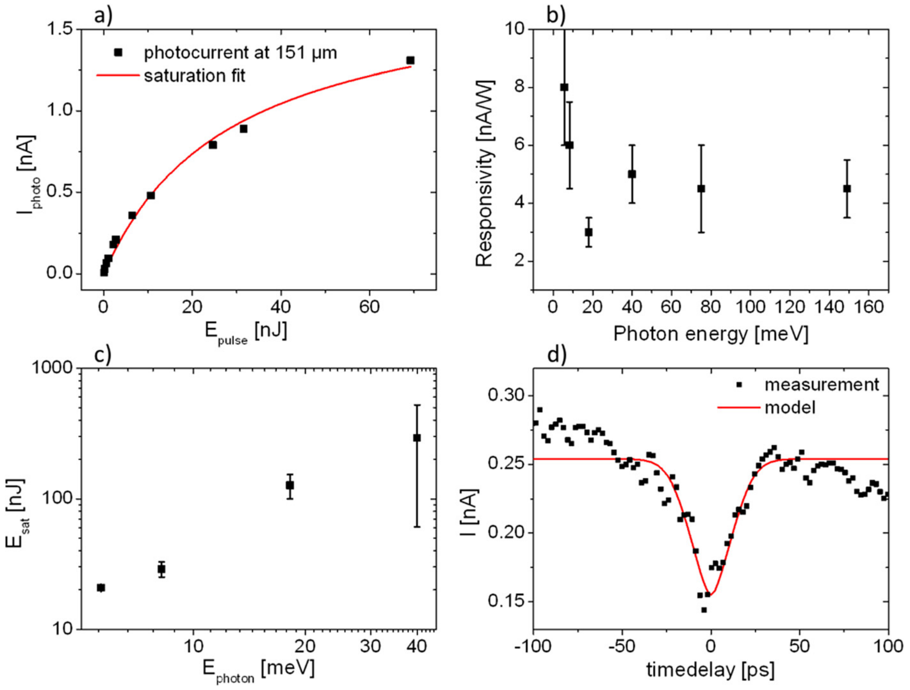

FIG. 3. a) Time-integrated photocurrent as a function of the FEL pulse energy at 151 μm. (b) Responsivity measured with the lock-in amplifier at different photon energies. (c) Saturation pulse energy E_{sat} as a function of the photon energy. (d) Autocorrelation signal at a wavelength of 42 μm and a FEL-pulse duration of 7 ps.

only one adjustable parameter for scaling of the absolute pulse energy. The shapes of the dips of the experimental and calculated curve agree well (cf. Fig. 3(d)), indicating that the intrinsic response time of the detector is similar or shorter than the duration of the FEL pulse. The intrinsic response time of a few ps is consistent with results of pump-probe experiments at room temperature.[5]

The coupling of the antenna to the graphene flake was verified in measurements with different rotation angles between the orientation of the antenna and the polarization of the radiation. In Fig. 4, the results of these measurements are plotted for two different wavelengths. At 151 μm, the angle of the maximum photocurrent is rotated by $\sim$70° compared to the maximum for 68 μm. As radiation of different wavelength couples to different parts of the antenna exhibiting resonant dimensions, this proves the operation of the antenna.

Finally, it was tested whether a pure antenna on the Si/SiO_2 substrate without a graphene flake also produces current signals under THz irradiation. No signals were found with the sampling oscilloscope, hence all observed fast signals of the previous measurements can clearly be attributed to the graphene flake. In contrast, small photocurrents were observed with a lock-in amplifier for the sample without graphene flake, which we assume to be caused by parasitic effects. These signals were about 10 times smaller than the signals of the devices with graphene flake.

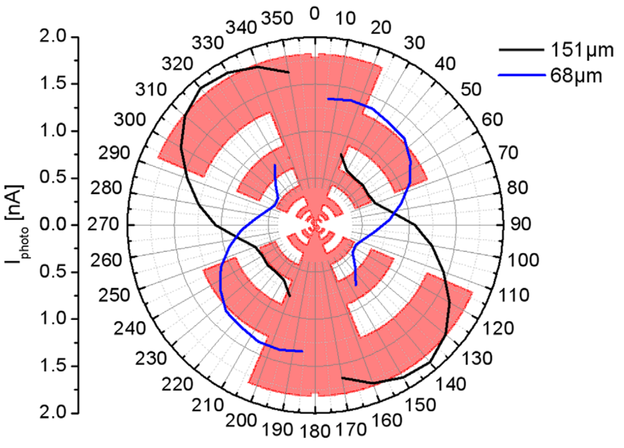

FIG. 4. Polarization dependent photocurrent for two different wavelengths, in the background the orientation of the antenna is depicted.

The detection mechanisms leading to a photocurrent in graphene induced by a NIR laser have been discussed in detail by Freitag *et al.*[13] They distinguish three main effects contributing to the current, namely a photovoltaic effect, a thermoelectric effect and a photo-induced bolometric effect. The Fermi energy in the graphene layer determines the dominating mechanism of photocurrent generation. Assuming the Fermi energy in the range of 100 meV in our graphene flake, the effect dominating in our devices might be the photo-induced bolometric effect. As the band structure in graphene is symmetric for electrons and holes, it does not matter whether the Fermi energy is positive or negative. The thermodynamic properties of the two dimensional electron gas in graphene have recently been investigated by Fong *et al.*[14] A heat capacity of the electron gas of was 2×10^{-21} J/(K μm^2) at 5 K was determined by bolometric mixing. Because of this small value graphene is a very promising material for ultrasensitive bolometers in the far infrared range at low temperatures. Also McKitterick *et al.*[15] predict the possibility of single-photon detection at THz frequencies with graphene bolometers.

Most important for the detection of THz radiation is the capability to absorb photons with low energy. This is still possible via interband absorption, because at room temperature the Fermi edge is smeared out and the low frequency absorption is not blocked. More importantly, phonon assisted intraband absorption dominates at low energies.[5] For photocurrent generation an asymmetry of the detector is required. The presence of a photocurrent at zero bias points towards an intrinsic asymmetry in the graphene flake. This might be caused by local doping due to the substrate or the contacts. We note that contacting the flake with different metals for the two antenna arms did not result in an increase of the photocurrent. Apparently this provides only a negligible additional asymmetry as compared to the asymmetry provided by the flake itself.

The experimental results suggest that the detector response time is strongly affected by the substrate (cf. Figs. 2(a) and 2(b)). On the low-resistive substrate, the antenna forms two capacitors connected in series with SiO_2 as dielectric material. After charging during the FEL pulse, the capacitors are discharged via the read-out electronics and the graphene flake. The calculated capacitance of the antenna, assuming perfectly conducting plates and 300 nm of SiO_2 as dielectric material, is 11 pF. This results in an RC time constant of 0.6 ns, considering a load of 50 Ω. This RC time constant is in good agreement with the experimentally observed decay of the signal for the low-resistive substrate (cf. Fig. 2(b)). We suggest that the same mechanism may strongly suppress the fast signal components of the detectors on the high-resistive substrate for wavelengths below 20 μm. In this case, the substrate resistivity may be decreased due to thermally activated carriers caused by phonon absorption in Si. At the high average power, needed to measure the pulses with the oscilloscope, the devices strongly heat up. At a temperature of 500 K the electron density is increased to $10^{14}\,\mathrm{cm}^{-3}$ which corresponds to a resistivity of 40 Ω cm. This resistance may contribute to a considerable RC time constant. High-resistive substrates without absorption in the desired wavelength range, like diamond or SiC, should circumvent this problem and enable one to develop ultrabroadband detectors.

Finally, the performance of the graphene-based detector is compared with other fast THz detectors working at room temperature. The use of the bolometric response for fast detectors at room temperature was reported by Dobrovolsky *et al.*[16] They presented a mercury-cadmium-telluride hot-electron bolometer which is much more sensitive (6 mA/W[17]) but also much slower (response time 50 ns) as compared to our detector. Photon drag detectors[18] also are more sensitive (80 nA/W) and slower (1 ns) than the graphene detector. Rectifying detectors such as intraminiband superlattice detectors[19] or nanosize field-effect transistors[20] exhibit a strongly decreased responsivity for frequencies exceeding a few THz. Nevertheless, superlattice detectors offer an attractive combination of responsivity and speed (e.g., at 6 THz: responsivity: 50 μA/W, rise time: 20 ps). Recently, field-effect transistors have been optimized for fast response times. They achieve response times of 30 ps and responsivity values of 30 nA/W.[21,22] In summary, the graphene detector is among the fastest detectors for the mid infrared and THz range. While its sensitivity is low, it is still suitable when applied to intense sources. In contrast to many other detectors, the graphene-based detector is easy to produce. Although we used electron-beam lithography for our device, simpler methods such as contact lithography should also be sufficient. Furthermore the spectral range of the detector is expected to span from THz to the ultraviolet when non-absorbing substrates are used.

In conclusion, we demonstrated a fast graphene-based detector working in the THz range at room temperature. The rise time of 50 ps enables the application for timing, e.g., in two-color pump-probe experiments. The presented detectors are very simple to produce, easy to handle, and very robust. The saturation behavior enables one to perform autocorrelation measurements for pulse-shape analysis on a ps timescale. In addition, we demonstrated the important role of the substrate and the possibility to increase the wavelength range of the detector by using different substrate materials like SiC or diamond.

We thank Peter Michel and the ELBE team for their dedicated support. Furthermore, we acknowledge financial support via the Priority Programme 1459 Graphene from the German Science Foundation DFG (Grant Nos. Wi3114/3-1 and Ga501/11-1).

[1] K. S. Novoselov, A. K. Geim, S. V. Morozov, D. Jiang, Y. Zhang, S. V. Dubonos, I. V. Grigorieva, and A. A. Firsov, Science **306**, 666 (2004).
[2] P. R. Wallace, Phys. Rev. **71**, 622 (1947).
[3] A. B. Kuzmenko, E. van Heumen, F. Carbone, and D. van der Marel, Phys. Rev. Lett. **100**, 117401 (2008).
[4] K. S. Novoselov, A. K. Geim, S. V. Morozov, D. Jiang, M. I. Katsnelson, I. V. Grigorieva, S. V. Dubonos, and A. A. Firsov, Nature **438**, 197 (2005).
[5] S. Winnerl, M. Orlita, P. Plochocka, P. Kossacki, M. Potemski, T. Winzer, E. Malic, A. Knorr, M. Sprinkle, C. Berger, W. A. de Heer, H. Schneider, and M. Helm, Phys. Rev. Lett. **107**, 237401 (2011).
[6] T. Mueller, F. Xia, and P. Avouris, Nat. Photonics **4**, 297 (2010).
[7] J. Yan, M.-H. Kim, J. A. Elle, A. B. Sushkov, G. S. Jenkins, H. M. Milchberg, M. S. Fuhrer, and H. D. Drew, Nat. Nanotechnol. **7**, 472 (2012).
[8] L. Vicarelli, M. S. Vitiello, D. Coquillat, A. Lombardo, A. C. Ferrari, W. Knap, M. Polini, V. Pellegrini, and A. Tredicucci, Nature Mater. **11**, 865 (2012).
[9] R. Mendis, C. Sydlo, J. Sigmund, M. Feiginov, P. Meissner, and H. L. Hartnagel, IEEE Antennas Propag. Lett. **4**, 85 (2005).
[10] W. Shi, J. Xu, and X.-C. Zhang, Chin. Opt. Lett. **1**, 308 (2003).
[11] S. Winnerl, W. Seiwerth, E. Schomburg, J. Grenzer, K. F. Renk, C. J. G. M. Langerak, A. F. G. van der Meer, D. G. Pavel'ev, Yu. Koschurinov, A. A. Ignatov, B. Melzer, V. Ustinov, S. Ivanov, and P. S. Kop'ev, Appl. Phys. Lett. **73**, 2983 (1998).
[12] The pulse duration is deduced from the spectral width of the Fourier limited FEL pulse, see also J. Bhattacharyya, M. Wagner, S. Zybell, S. Winnerl, D. Stehr, M. Helm, and H. Schneider, Rev. Sci. Instrum. **82**, 103107 (2011).
[13] M. Freitag, T. Low, F. Xia, and P. Avouris, Nat. Photonics **7**, 53 (2013).
[14] K. C. Fong and K. C. Schwab, Phys. Rev X **2**, 031006 (2012).
[15] C. B. McKiterick, D. E. Prober, and B. S. Karasik, J. Appl. Phys. **113**, 044512 (2013).
[16] V. Dobrovolsky and F. Sizov, Semicond. Sci. Technol. **22**, 103 (2007).
[17] The current responsivity was calculated from the published voltage responsivity considering an impedance of 50 Ohm of the readout electronics.
[18] S. D. Ganichev, Y. V. Terent'ev, and I. D. Yaroshetskii, Sov. Tech. Phys. Lett. **11**, 20 (1985).
[19] F. Klappenberger, A. A. Ignatov, S. Winnerl, E. Schomburg, W. Wegscheider, K. F. Renk, and M. Bichler, Appl. Phys. Lett. **78**, 1673 (2001).
[20] W. Knap, S. Rumyantsev, M. S. Vitiello, D. Coquillat, S. Blin, N. Dyakonova, M. Shur, F. Teppe, A. Tredicucci and T. Nagatsuma, Nanotechnology **24**, 214002 (2013).
[21] S. Preu, H. Lu, M. S. Sherwin, and A. C. Gossard, Rev. Sci. Instrum. **83**, 053101 (2012).
[22] S. Preu, M. Mittendorff, S. Winnerl, H. Lu, A. C. Gossard, and H. B. Weber, "accepted for publication by Opt. Express," e-print arXiv: 1303.4755.

APPLIED PHYSICS LETTERS **103**, 252110 (2013)

Intersublevel dephasing in InAs/GaAs quantum dots below the Reststrahlen band

M. Teich,[1,2,a)] D. R. Stephan,[1,2] S. Winnerl,[1] H. Schneider,[1] L. R. Wilson,[3] and M. Helm[1,2]
[1]*Institute of Ion Beam Physics and Materials Research, Helmholtz-Zentrum Dresden-Rossendorf, P.O. Box 510119, 01314 Dresden, Germany*
[2]*Technische Universität Dresden, 01062 Dresden, Germany*
[3]*Department of Physics and Astronomy, University of Sheffield, Sheffield S3 7RH, United Kingdom*

(Received 30 October 2013; accepted 8 December 2013; published online 20 December 2013)

Using transient four-wave mixing in the terahertz range, we have measured the s-p inter-sublevel dephasing time in self-assembled InAs/GaAs quantum dots for transition energies below the Reststrahlen band. Dephasing times of up to 600 ps at a photon energy of 18 meV have been determined. By comparing pump-probe and four-wave mixing measurements, we show that there is no significant influence of any pure dephasing process at low temperature. The linear temperature dependence is consistent with acoustic phonon scattering. © *2013 AIP Publishing LLC*.
[http://dx.doi.org/10.1063/1.4857515]

Self-assembled quantum dots (QD) are among the main contenders as suitable solid-state implementation for quantum information processing. In particular, interband excitonic transitions in single quantum dots have been investigated extensively,[1] due to their extremely narrow linewidth (μeV) and corresponding long dephasing times (ns).[2,3] These are necessary in order to perform several qubit operations before decoherence sets in. Yet another option could be the application of intersublevel transitions within, e.g., the conduction band of quantum dots. Such transitions, though sometimes used for infrared detectors,[4] have been much less investigated in relation to quantum information processing.[5] This may be partly due to their somewhat less accessible energy range of 10–100 meV, corresponding to terahertz (THz) or infrared frequencies. However, it has been demonstrated by the observation of Rabi oscillations between shallow impurity states in semiconductors that fundamental qubit operation can also be implemented in the THz range.[6,7]

Before such applications, in quantum dots, can more realistically be pursued, a thorough knowledge of relaxation and dephasing processes is indispensable. Over the past years, such an understanding has partly been achieved for intersublevel transitions in quantum dots. It is now well accepted that relaxation processes can be properly described in the so-called strong-coupling polaron picture.[8] In n-type InAs/GaAs quantum dots of typical dimensions, the level spacing between the fundamental s and p states is around 50–60 meV, well above the optical phonon energy. In such samples, the relaxation times have been measured by pump-probe (PP) spectroscopy to be in the order of 50–100 ps (Refs. 9 and 10) and the dephasing times were determined by four-wave-mixing experiments to be slightly shorter at low temperatures.[11] In p-type quantum dots, dephasing times of 10 ps were measured in the mid-infrared at room temperature.[12]

Although it is not straightforward to grow slightly larger quantum dots with s-p level spacing in the 10–20 meV range, i.e., smaller than the optical phonon energy, such samples have been produced by post-growth thermal annealing, which leads to a shallower electron confinement.[13,14] Using pump-probe experiments, some of the present authors have measured that the population relaxation time T_1 becomes exceedingly long, up to 1500 ps for quantum dots with 15 meV level separation.[15] The important question remains whether the dephasing or coherence times, which are the relevant parameters for qubit operation, become equally long, or whether there is some undesired, faster, pure dephasing process. In order to clarify and answer this important question, we have performed pump-probe as well as transient four-wave mixing (FWM) experiments on such quantum dot ensembles, using a THz free-electron laser (FEL). We demonstrate that the dephasing times T_2 can also reach very large values of hundreds of picoseconds and are related to the population lifetime by $T_2 = (2 \pm 0.3)\ T_1$ at low temperature, which is close to the theoretical limit of $T_2 = 2T_1$.[16] This indicates a rather small influence of pure dephasing processes at low temperatures.

The investigated QD samples that are n-type self-assembled InAs/GaAs QDs grown on (100) GaAs by molecular-beam epitaxy (MBE), in the Stranski-Krastanov mode. The samples consist of 80 layers of QDs (with an areal density of $4 \times 10^{10}\mathrm{cm}^{-2}$) separated by 50 nm wide GaAs barriers. A silicon doped layer grown 2 nm below the QDs provides a population of the conduction band sublevel ground state with one electron per dot. By applying post-growth thermal annealing, the s-p transition energy is shifted to lower energies due to the reduced confinement caused by intermixing of InAs and GaAs.[13] Figs. 1(b) and 1(c) show the linear absorption spectra of two quantum dot samples, annealed at 875 °C and 850 °C, respectively, recorded in a Fourier transform infrared (FTIR) spectrometer at T = 10 K.[15] The spectra are different for two orthogonal polarizations, the so-called anisotropy splitting of the p-states. Due to the anisotropic shape of the QDs, the p_y state (in [1-10] direction) is situated about 3.5 meV higher in energy than the p_x state (in [110] direction).

While pump-probe measurements yield the population lifetime T_1 of the upper state,[15] transient, but time-integrated four-wave mixing is a technique to determine the dephasing

---

[a)] Electronic mail: m.teich@hzdr.de

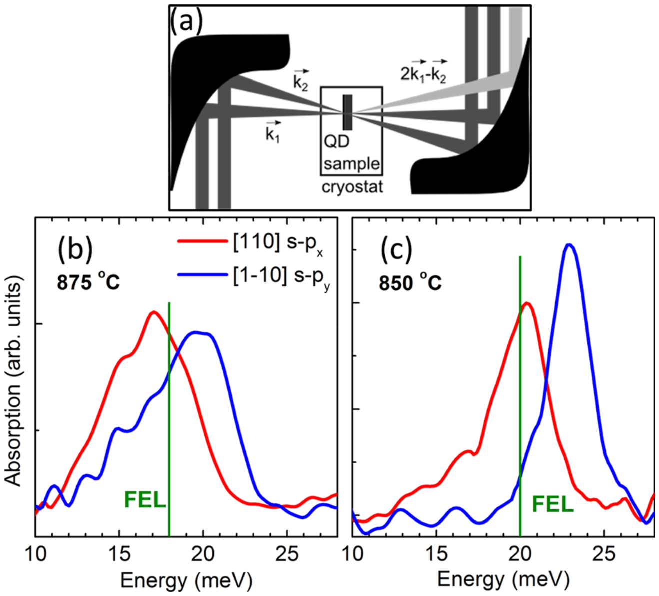

FIG. 1. (a) Pump-probe and four-wave mixing beam geometry. (b) and (c) FTIR absorption measurements of two different thermally annealed QD samples used in this work. The (green) vertical line depicts the applied excitation energy. The width of that line corresponds to the FWHM of the FEL spectrum. Reproduced by permission from Zibik *et al.*, Nature Materials **8**, 803 (2009). Copyright 2013 by Nature Publishing Group.[15]

time T_2. In order to calculate T_2, it is necessary to know whether the absorption line is homogeneously or inhomogeneously broadened. For an ensemble of quantum dots, the absorption is predominantly inhomogeneously broadened due to variations in quantum dot size. In the present case (see Figs. 1(b) and 1(c)), the inhomogeneous linewidth (FWHM) is approximately 3–6 meV, depending on the sample annealing temperature. In this case, the relation between FWM decay time, $\tau_{\rm FWM}$ and T_2, is given by $T_2 = 4\tau_{\rm FWM}$ (for a homogeneously broadened system it would be $T_2 = 2\tau_{\rm FWM}$).[16] This technique has been applied since the early days of ultrafast spectroscopy to bulk semiconductors[17] and quantum wells,[18] and also to intersubband transitions in quantum wells in the mid-infrared range.[19]

The degenerate pump-probe and time-integrated four-wave mixing, measurements were performed at the infrared/THz free-electron laser, FELBE, delivering tunable picosecond THz pulses at a repetition rate of 13 MHz. We employed photon energies of 18 meV (69 μm wavelength) and 20 meV (62 μm), respectively, with a relative spectral width of approximately 1%. Using this approach, we can selectively excite QD sub-ensembles of a certain size within this inhomogeneous ensemble. The samples were mounted in a liquid helium cryostat, and both FEL beams (wavevectors $\vec{k}_1$ and $\vec{k}_2$ enclosing an angle of 10°) were focused by an off-axis parabolic mirror, to a spot size diameter of approximately 500 μm (see also Fig. 1(a)). The diffracted beam signal (photon echo) in the direction of $2\vec{k}_2 - \vec{k}_1$ was detected with a bolometer. We used a lock-in amplifier, locked to the modulation frequency (≈330 Hz) of an optical chopper that was placed in the pump arm for pump-probe measurements and in the $\vec{k}_2$ arm for FWM measurements, in order to minimize stray light, as depicted in Fig. 1(a). With this method, we were able to resolve absorption changes down to 0.05% in the pump-probe measurements and to detect a background-free FWM signal. The homogeneous linewidth (FWHM) Γ_2 is inversely proportional to the dephasing time T_2 that is calculated by the sum of the population relaxation broadening $\hbar/T_1$ and the contribution of pure dephasing processes $2\hbar/T_2^*$, i.e.,

$$\Gamma_2 = \frac{2\hbar}{T_2} = \frac{\hbar}{T_1} + \frac{2\hbar}{T_2^*}. \tag{1}$$

When dephasing is solely due to population relaxation, i.e., so-called pure dephasing does not play any role, Eq. (1) yields $T_2 = 2T_1$. For an increasing contribution of pure dephasing processes, the inequality $T_2 < 2T_1$ becomes stronger.

In Figure 2, pump-probe (top) and FWM (bottom) measurements at a photon energy of 18 meV and temperature of T = 10 K are shown for the QD sample annealed at 875 °C. The s-p_x transition was excited using linear polarization in the [110] direction. The FWM signal was measured under the same conditions as the pump-probe measurement, but with an estimated peak intensity of 10–40 W/mm^2, in both arms. As discussed in previous work,[15] there is a bi-exponential decay of the pump-probe signal for photon energies of 18 meV and below. For higher energies, such as 20 meV, a mono-exponential decay is observed. The first decay constant is attributed to the population exchange (thermalization) among the p_x and p_y states. The second decay is determined by the s-p relaxation time. From Fig. 2 (upper panel), we observe that the s-p_x relaxation time is 293 ± 10 ps. We have to consider that, in case of inhomogeneous broadening, the FWM signal appears as a photon echo at twice the delay time. To take account of this property, the time intervals to determine p_x–p_y and FWM time constants

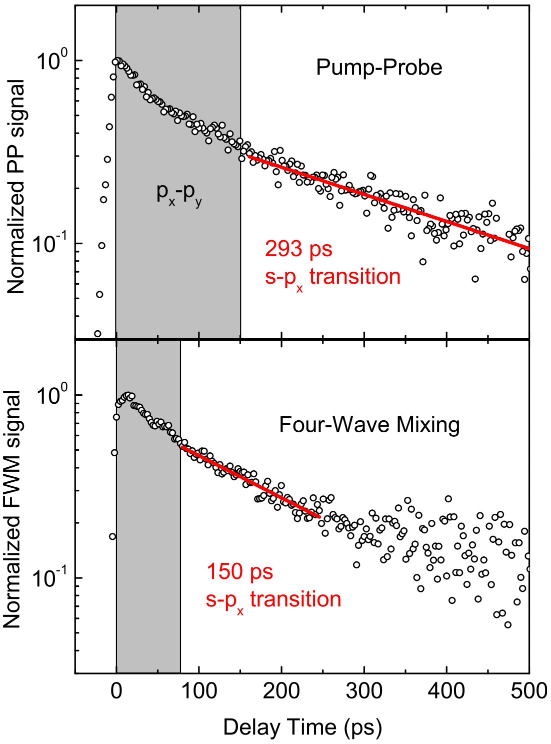

FIG. 2. Pump-probe and four-wave mixing measurements at 10 K (sample annealed at 875 °C). The s-p_x transition is pumped with an energy of 18 meV, and the polarization is directed along [110] direction. The grey shaded area was excluded from the fitting. Top: PP signal, bottom: FWM signal.

were chosen to differ by a factor of two. The FWM (lower panel) signal has a time constant of $\tau_{\mathrm{FWM}} = 150 \pm 20$ ps, i.e., the dephasing time is four times as long, $T_2 = 600$ ps. For the s-p_x transition, the measurements result in a relation between dephasing and population lifetime $T_2 = (2 \pm 0.3)\, T_1$. This means that pure dephasing processes do not play a major role at 10 K. Note that a similar ratio of 1.7 was observed above the Reststrahlen band[11] at low temperature. We also measured pump-probe and FWM with FEL polarization in s-p_y direction (not shown here). The s-p_y relaxation time ($T_1 = 230$ ps) was shorter than the s-p_x one, as observed and discussed in a previous publication.[15] Together with the dephasing time ($T_2 = 390$ ps), we get $T_2 = (1.7 \pm 0.3)\, T_1$.

Now, we turn to the other sample, annealed at 850 °C and exited at a photon energy of 20 meV, showing a mono-exponential population decay. In Fig. 3, we present the pump-probe measurement at 10 K (top) and the FWM measurements (bottom) recorded at different temperatures. This QD sample shows a s-p relaxation time of $\tau_{\mathrm{PP}} = 82 \pm 10$ ps. The dephasing time T_2 at 10 K was measured to be $T_2 = 4\tau_{\mathrm{FWM}} = 168$ ps, which corresponds to a factor of (2 ± 0.3) between T_1 and T_2. This indicates again that there are no major pure dephasing processes at 10 K. Yet upon increasing the temperature to 100 K, the FWM time constant decreases from 42 to 27 ps. In previous FWM measurements of n-type QDs above the Reststrahlen band,[11] the homogeneous linewidth was extracted to be 15 μeV at 10 K and 100 μeV at 100 K, showing a strong temperature dependence, due to polaron coupling.[20] In contrast, the homogeneous linewidth extracted from our measurements for n-type QDs *below* the Reststrahlen band, increases only very weakly with temperature from 8 μeV to 12 μeV, as is depicted in Fig. 4. The temperature dependence is linear with a small slope of 0.052 μeV/K. Thus, the homogeneous linewidth seems to be quite robust against increase in temperature. The result can be interpreted to originate from acoustic phonon scattering, as it was already measured in similar form for electrons in a quantum well.[18] Theoretical calculations were carried out for measurements of the dephasing times above the Reststrahlen band[11,20] and were in good agreement with the experimental results. It would be interesting to extend the theory to excitation energies below the Reststrahlen band, giving insight to the mechanisms of pure dephasing and its temperature dependence, but this is beyond the scope of the present paper.

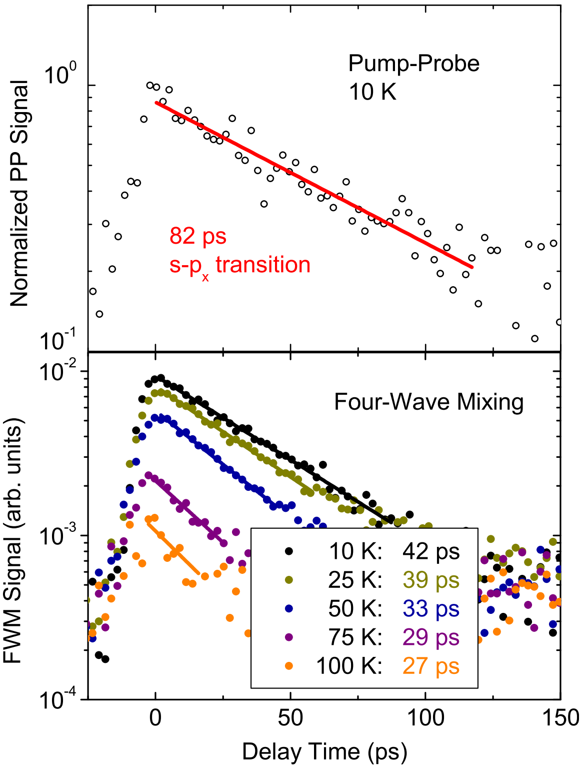

FIG. 3. Top: Pump-probe measurement of the s-p_x transition (pumped with 20 meV) of the 850 °C annealed QD sample at 10 K. Bottom: Temperature dependence of the FWM signal from 10 to 100 K. The fitted time constants are indicated for each temperature.

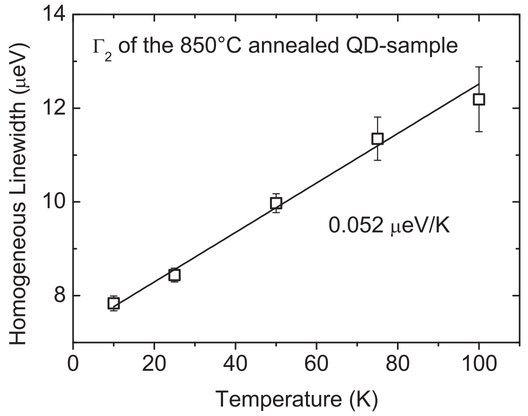

FIG. 4. Temperature dependence of the homogeneous linewidth Γ_2 for the 850 °C annealed QD sample extracted from the measurements in Fig. 3. The linewidth increases linearly with increasing temperature.

In conclusion, using transient four-wave mixing at THz frequencies, we have measured the dephasing times of different thermally annealed InAs/GaAs quantum dot samples, where the fundamental s-p inter-sublevel transition is well below the optical phonon energy. Dephasing times of up to 600 ps have been found. A comparison with pump-probe measurements performed under the same conditions yields a relation between population relaxation and dephasing time, close to the theoretical limit of $T_2 = 2T_1$ at 10 K, i.e., no pure dephasing mechanism is present. The extracted homogeneous linewidths are, as small as, 8 μeV and 2.4 μeV for the two investigated samples, at low temperature. From the present and the previous results,[15] one can presume that in even shallower QDs (with s-p energy spacing of 15 meV), T_2 would be even larger than a nanosecond. These results indicate that quantum dots exhibit comparable or even less dephasing than Rydberg impurities,[7] which makes these semiconductor nanostructures interesting for quantum information processing in the THz spectral range.

We thank P. Michel, W. Seidel, and FELBE Team for their dedicated support. We also thank H. Y. Liu for growing the samples. This work was partially supported by the German Ministry of Education and Research (BMBF; grant no. 05K10BRA).

[1] X. Xu, B. Sun, P. Berman, D. Steel, A. Bracker, D. Gammon, and L. Sham, Science **317**, 929 (2007).

[2] P. Borri, W. Langbein, S. Schneider, U. Woggon, R. L. Sellin, D. Ouyang, and D. Bimberg, Phys. Rev. Lett. **87**, 157401 (2001).

[3] D. Birkedal, K. Leosson, and J. M. Hvam, Phys. Rev. Lett. **87**, 227401 (2001).
[4] H. C. Liu, M. Gao, J. McCaffrey, Z. R. Wasilewski, and S. Fafard, Appl. Phys. Lett. **78**, 79 (2001).
[5] M. S. Sherwin, A. Imamoglu, and T. Montroy, Phys. Rev. A **60**, 3508 (1999).
[6] B. E. Cole, J. B. Williams, B. T. King, M. S. Sherwin, and C. R. Stanley, Nature **410**, 60 (2001).
[7] P. T. Greenland, S. A. Lynch, A. F. G. van der Meer, B. N. Murdin, C. R. Pidgeon, B. Redlich, N. Q. Vinh, and G. Aeppli, Nature **465**, 1057 (2010).
[8] S. Hameau, Y. Guldner, O. Verzelen, R. Ferreira, G. Bastard, J. Zeman, A. Lemaître, and J. M. Gérard, Phys. Rev. Lett. **83**, 4152 (1999).
[9] S. Sauvage, P. Boucaud, R. P. S. M. Lobo, F. Bras, G. Fishman, R. Prazeres, F. Glotin, J. M. Ortega, and J.-M. Gérard, Phys. Rev. Lett. **88**, 177402 (2002).
[10] E. A. Zibik, L. R. Wilson, R. P. Green, G. Bastard, R. Ferreira, P. J. Phillips, D. A. Carder, J. -P. R. Wells, J. W. Cockburn, M. S. Skolnick, M. J. Steer, and M. Hopkinson, Phys. Rev. B **70**, 161305 (2004).
[11] E. A. Zibik, T. Grange, B. A. Carpenter, R. Ferreira, G. Bastard, N. Q. Vinh, P. J. Phillips, M. J. Steer, M. Hopkinson, J. W. Cockburn, M. S. Skolnick, and L. R. Wilson, Phys. Rev. B **77**, 041307 (2008).
[12] S. Sauvage, P. Boucaud, T. Brunhes, M. Broquier, C. Crépin, J.-M. Ortega, and J.-M. Gérard, Phys. Rev. B **66**, 153312 (2002).
[13] D. Pan, E. Towe, S. Kennerly, and M.-Y. Kong, Appl. Phys. Lett. **76**, 3537 (2000).
[14] E. Zibik, W. Ng, L. Wilson, M. Skolnick, J. Cockburn, M. Gutierrez, M. Steer, and M. Hopkinson, Appl. Phys. Lett. **90**, 163107 (2007).
[15] E. A. Zibik, T. Grange, B. A. Carpenter, N. E. Porter, R. Ferreira, G. Bastard, D. Stehr, S. Winnerl, M. Helm, H. Y. Liu, M. S. Skolnick, and L. R. Wilson, Nature Mater. **8**, 803 (2009).
[16] *Optical Techniques for Solid-State Materials Characterization*, edited by R. P. Prasankumar and A. J. Taylor (CRC Press, Inc., Boca Raton, 2012).
[17] P. C. Becker, H. L. Fragnito, C. H. B. Cruz, R. L. Fork, J. E. Cunningham, J. E. Henry, and C. V. Shank, Phys. Rev. Lett. **61**, 1647 (1988).
[18] L. Schultheis, A. Honold, J. Kuhl, K. Köhler, and C. W. Tu, Phys. Rev. B **34**, 9027 (1986).
[19] R. A. Kaindl, S. Lutgen, M. Woerner, T. Elsaesser, B. Nottelmann, V. M. Axt, T. Kuhn, A. Hase, and H. Künzel, Phys. Rev. Lett. **80**, 3575 (1998).
[20] R. Ferreira, A. Berthelot, T. Grange, E. Zibik, G. Cassabois, and L. Wilson, J. Appl. Phys. **105**, 122412 (2009).

APPLIED PHYSICS LETTERS **103**, 251114 (2013)

Terahertz generation and detection with InGaAs-based large-area photoconductive devices excited at 1.55 μm

Ming Xu,[1,2] Martin Mittendorff,[2,3] Roman J. B. Dietz,[4] Harald Künzel,[4] Bernd Sartorius,[4]
Thorsten Göbel,[4] Harald Schneider,[2] Manfred Helm,[2,3] and Stephan Winnerl[2]
[1]*Applied Physics Department, Xi'an University of Technology, No. 58 Yanxiang Road, Xi'an 710054, China*
[2]*Helmholtz-Zentrum Dresden-Rossendorf, Bautzner Landstraße 400, 01328 Dresden, Germany*
[3]*Technische Universität Dresden, 01062 Dresden, Germany*
[4]*Fraunhofer Institute for Telecommunication, Heinrich-Hertz-Institute, Einsteinufer 37,*
10587 Berlin, Germany

(Received 10 July 2013; accepted 8 December 2013; published online 20 December 2013)

We report on scalable large-area terahertz emitters and detectors based on $In_{0.53}Ga_{0.47}As$/$In_{0.52}Al_{0.48}As$ heterostructures for excitation with 1.55 μm radiation. Different geometries involving three different electrode gap sizes are compared with respect to terahertz (THz) emission, bias field distribution, and Joule heating. The field distribution becomes more favorable for THz emission as gap size increases, while Joule heating exhibits the opposite dependence. Devices with three different gap sizes, namely 3 μm, 5 μm, and 7.5 μm, have been investigated experimentally, the emitter with a gap size of 7.5 μm showed the best performance. The scalable devices are furthermore employed as detectors. The scalable electrode geometry enables spatially integrated detection, which is attractive for specific applications, e.g., where an unfocused THz beam has to be used. © *2013 AIP Publishing LLC*. [http://dx.doi.org/10.1063/1.4855616]

Photoconductive antennas for generation and detection of terahertz (THz) radiation are employed in both pulsed and continuous-wave (cw) spectroscopy systems. For low THz frequencies (<3 THz) and moderate excitation pulse energies, photoconductive emitters are significantly more efficient as compared to nonlinear crystals.[1] Scalable large-area photoconductive emitters with interdigitated electrodes offer high efficiencies for excitation energies above 0.1 nJ, where photoconductive antennas with electrode gaps in the micrometer range typically exhibit strong saturation of the emission.[2–6] For devices based on GaAs, the scalable concept has been employed for emitters of single cycle,[2–4] few cycle,[7] and cw[8] radiation, as well as for detectors of pulsed[9] and cw[10] THz radiation. Hence, for systems operated with Ti:sapphire lasers (excitation wavelength ~ 800 nm), a complete technology platform for generation and detection of THz radiation is available based on efficient scalable photoconductive devices. It is highly attractive to extend this platform to devices that can be excited with fiber lasers operating at 1.55 μm, because these lasers are compact, offer turn-key operation, and are more cost efficient. This task is challenging, because small-gap semiconductors, such as InGaAs, are highly conductive. Materials suitable for photoconductive emitter and detector antennas with small electrode gaps have been realized by low-temperature growth,[11] ion implantation,[12] and fabrication of heterostructures.[13,14] Due to their geometry, scalable large-area photoconductive devices require materials with lower conductance, as compared to conventional antennas, i.e., the engineering of suitable materials is even more challenging. Recently, scalable photoconductive emitters based on InGaAs/InAlAs heterostructures excited with 1.55 μm radiation have been demonstrated for generation of THz pulses.[15,16] The substrate described in Ref. 15 contains ErAs nanoparticles that provide extra trapping centers to reduce the conductivity, the material used in Ref. 16 was grown at low temperature.

In this Letter, we vary the gap size between the electrodes of a scalable large-area emitter based on a low-temperature gown InGaAs/InAlAs multilayer in order to optimize the strength of the emitted THz pulses. Moreover, detection of THz radiation by the same device is demonstrated, constituting a further advance of THz technology using fiber lasers.

The photoconductive material for the scalable emitter and detector devices consists of 100 periods of 12 nm thick beryllium doped $In_{0.53}Ga_{0.47}As$ layers separated by 8 nm thick $In_{0.52}Al_{0.48}As$ barrier layers. All layers are lattice matched to the semi-insulating InP substrate. They were grown by molecular beam epitaxy at low temperature. The thickness of the complete multilayer, which serves as the active layer in the THz experiments, is 2 μm. Further details about the multilayer structure have been published in Ref. 13. Scalable photoconductive devices were processed by patterning interdigitated electrodes on the material. Emitters were prepared with device areas of 0.3 mm × 0.3 mm and 0.25 mm × 0.25 mm. In order to avoid destructive interference of THz waves generated in neighbouring gaps, and, equivalently, in order to assure a non-zero photocurrent in case of THz detection, every second gap was covered by a second metallization layer. The second metallization was insulated from the electrodes by a 1 μm thick Si_3N_4 layer. In Fig. 1(a), the layout of the three emitters with different gap sizes is depicted. The gap size d_{gap} was varied (3.5 μm, 5 μm, and 7.5 μm), while the width w of the electrodes was kept constant at 5 μm. This results in different ratios, $d_{gap}/(2d_{gap} + 2w)$, of the illuminated active area to the total device area. For the structures with 3 μm, 5 μm, and 7.5 μm gap size, this ratio is 19%, 25%, and 30%, respectively. The width of the second metallization stripes is 10 μm for all emitters.

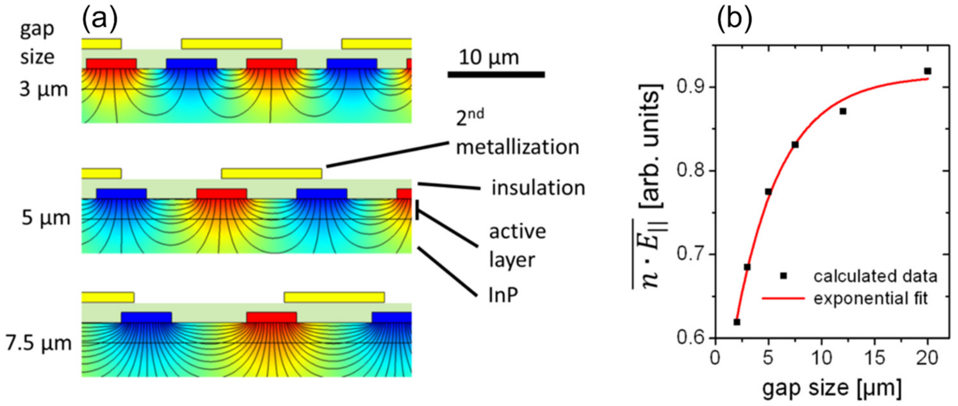

FIG. 1. Cross section of the scalable emitter devices (a). The electrodes (blue and red rectangles) are covered by a continuous insulation layer and a microstructured second metallization layer. In the semiconductor material, the calculated bias field distribution is shown by field lines. The color code indicates areas of similar electric potential. The product of the photo excited carrier density and the component of the electric field parallel to the surface is displayed in part (b). This quantity is proportional to the emitted THz field.

The scalable emitters were investigated in a standard THz time-domain spectroscopy system as described in Ref. 16. An amplified fiber laser system, emitting 100 fs pulses at a wavelength of 1.55 μm with a repetition rate of 78 MHz, was employed for exciting the emitter. A part of the pump beam was split off and frequency doubled for electro-optic sampling (EOS), with a 200 μm thick ZnTe crystal. The EOS signal was recorded with a lock-in amplifier. The THz signal was modulated by applying a rectangular bias voltage. The nominal bias field between the electrodes is determined by $E_{bias} = U_{bias}/d_{gap}$. In a second set of experiments, the EOS crystal was replaced by the scalable photoconductive device. The THz-field induced photocurrent was measured using a lock-in amplifier (SR830) with integrated transimpedance amplifier. In these experiments, a modulation of the signal was obtained by mechanically chopping the THz beam, while a constant bias voltage of 13 V was applied to the emitter. This type of modulation was chosen because modulating the bias voltage of the emitter resulted in a strong electronic cross talk into the detection channel.

In order to study the THz fields from emitters with different electrode gap size, all devices were similarly excited with an average power of 75 mW focused to a spot size (full width at half maximum) of 100 μm. With increasing gap size, the peak THz field measured by EOS increased significantly. One trivial reason for this behavior is the increase of illuminated photoconductive area with increasing gap size. To account for this effect, we scaled the peak THz fields of the emitters with gap sizes of 5 μm and 7.5 μm to the data of the emitter with $d_{gap} = 3\,\mu$m, assuming that the peak THz field scales linearly with the illuminated area. This assumption was verified previously.[16] Interestingly, after this scaling process, the peak fields from the devices with larger gap size are still systematically larger as compared to the fields from the devices with smaller gap size (cf. Fig. 2(a)). For example, the THz field increased by 70% (14%) for the emitter with 7.5 μm (5 μm) gap size as compared to the emitter with 3 μm gap size at $E_{bias} = 18$ kV/cm. To understand this effect, the spatial distribution of the bias field was calculated using the finite-element code COMSOL Multiphysics®. An effective-medium dielectric constant was used for the heterostructure in the active layer. The bias voltage was varied for the different gap sizes in order to keep U_{bias}/d_{gap} constant. As depicted in Fig. 1(a), the field distribution in case of the larger gap size is characterized by more field lines parallel to the semiconductor surface. Only field components parallel to the surface contribute to the THz radiation emitted into the far field propagating perpendicularly to the emitter surface. For a more quantitative description of the emitted THz field, we calculated the field parallel to the surface and consider the density n of photogenerated carriers. The latter depends on the depth z according to $n(z) \sim \exp(-\alpha \cdot z)$, where $\alpha = 6000/\mathrm{cm}$ is the effective-medium absorption coefficient of the heterostructure. The product of the carrier density and the static field parallel to the surface, averaged laterally over one gap of the structure and over the thickness of the photoconductive layer, is plotted in Fig. 1(b). It increases significantly with increasing gap size for gaps below 10 μm. For gap sizes significantly larger than the thickness of the active layer, the field naturally becomes almost independent of the gap size and converges to the maximum value. Within the investigated range of gap sizes, the trend can be

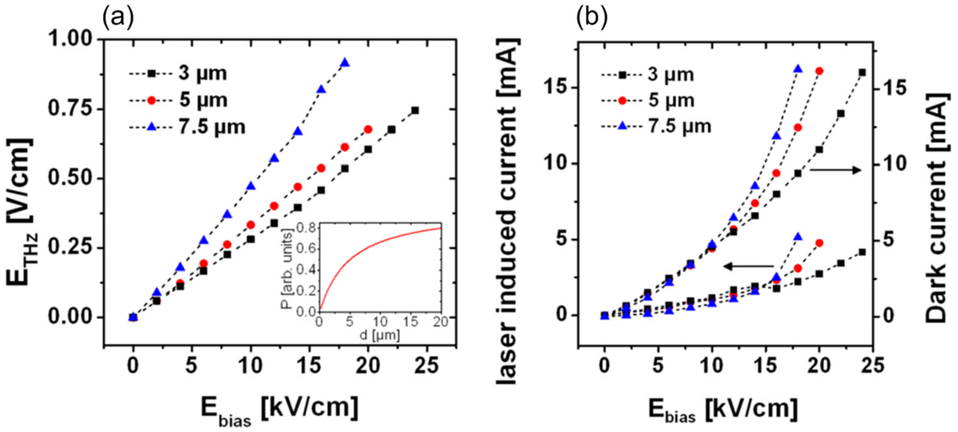

FIG. 2. (a) Peak THz field as a function of the nominal bias field for different gap sizes. The presented data for emitters with a gap size of 5 μm (7.5 μm) are the peak THz fields multiplied by 0.76 (0.63) to take the different illuminated areas into account. In the inset, the dissipated power at a fixed bias field can be seen as a function of the gap size. (b) Laser induced current and dark current as a function of the bias field in different gap size emitters.

described well by the function $\overline{nE_{\parallel}} = \overline{nE_{bias}} - \overline{nE_{\parallel 0}} \times \exp(d_{gap}/d_0)$ with the fit parameter $d_0 = 4.4\,\mu$m (cf. Fig. 1(b)). Since only the static field is considered, dynamic effects, such as enhanced emission close to the anode,[17] are not taken into account. Nevertheless, the calculated weighted average fields can explain the increased THz emission from emitters with larger gap size. This explanation is corroborated by previous experiments, where the gap size was kept constant, but the electrode metallization was applied either to the top or the sides of the etched photoconductive layer. In that study, an increased THz emission was found for the side contacts.[15] Larger gap sizes, which are favourable for the field distribution, however, involve two disadvantages. The first disadvantage is the simple fact that larger gap sizes require higher bias voltages for similarly strong bias fields, e.g., for a gap size of $20\,\mu$m a voltage of 50 V is needed to achieve a field of 25 kV/cm. Therefore a main advantage of scalable emitters is lost. The more serious disadvantage of large gap sizes, especially of InGaAs-based emitters, is a heating issue that is discussed below.

In Fig. 2(b), the values of dark current and laser induced current are shown for the emitters of different gap size with respect to the bias field. The laser induced current is the sum of the photocurrent and a current increase caused by the laser induced heating of the device. A superlinear increase of the dark current is observed. For fields below 10 kV/cm, the value of the dark current is almost independent of the gap size. For higher fields the dark current increases with increasing gap size. This behavior can be attributed to Joule heating, resulting in interband generation of extra carriers. The ratio of area in which power is dissipated compared to the total device area increases with gap size. The maximum bias fields applied to the emitters had to be lowered for the devices with larger gap size (cf. Fig. 2) in order to avoid destruction of the emitters by runaway Joule heating. Joule heating is a known limit of the performance of InGaAs-based scalable THz emitters.[15,16] To estimate the influence of the gap size to the Joule heating, we calculated the power dissipated by the bias voltage. Considering a constant depth and length of each gap, the resistance of a single gap is proportional to the gap size. The number of gaps, which are connected in parallel, is given by $n_{gaps} = l/(d_{gap} + w)$, where l is the length of the active area. Therefore, the resistance of a whole device is proportional to ${d_{gap}}^2 + d_{gap} \times w$. To keep the applied bias field constant, the bias voltage has to be proportional to the gap size. Therewith, the dissipated power is proportional to ${d_{gap}}^2/({d_{gap}}^2 + d_{gap} \times w)$. This dependence, which shows an increased dissipated power for larger gap sizes, can be seen in the inset of Fig. 2(a). Considering this limitation in favour of smaller gap sizes in combination with the effect of the bias field distribution discussed above, which favours larger gap sizes, we conclude that gaps in the range from about $7\,\mu$m to $10\,\mu$m represent a good compromise. Note that for $d_{gap} = 10\,\mu$m the average bias field in the horizontal direction reaches 90% of the nominal field E_{bias}, therefore, only a marginal increase of the THz emission are possible for larger gap sizes. In our calculations, a change of the gap size from $10\,\mu$m to $20\,\mu$m increases the field component parallel to the surface only by 5%, while the Joule heating is increased by 20%.

In the experiments on THz detection, a scalable microstructured device (electrode gap: $3\,\mu$m, area $150\,\mu$m $\times\, 150\,\mu$m, device resistance $7\,$kΩ) replaced the EOS detection unit. For comparison with EOS signals, a first set of detection experiments was performed at a gating beam wavelength of $0.78\,\mu$m. The average power of the gating beam was 10 mW. Increasing the gating power did not result in a higher signal-to-noise ratio (SNR) of the THz-induced photocurrent signal. The spot size of the gating beam was adjusted in order to maximize the THz-induced photocurrent signal. In Fig. 3, the photocurrent signal and its first temporal derivative are compared with the EOS detection signal. For frequencies below ~4 THz, the EOS signal is proportional to the electric THz field. The response of the photoconductive detector, on the other hand, depends on the carrier lifetime in the material, as well as, the transit time of the carriers. Ignoring the transit time, the THz-induced photocurrent is proportional to a convolution of the transient conduction of the material with the THz field.[18] For the material employed in our experiment, a carrier lifetime comparable to the THz pulse duration can be estimated.[13] Hence, a deconvolution of the photocurrent with the transient conductance results in an extracted THz field with a shape in between the photocurrent signal and its first derivative (not shown), such that this effect is overestimated by calculating the first temporal derivative of the photocurrent. In Fig. 3(b), one can see that the roll-off for the higher frequencies is still a lot stronger as compared to the EOS signal. Taking into account the transit

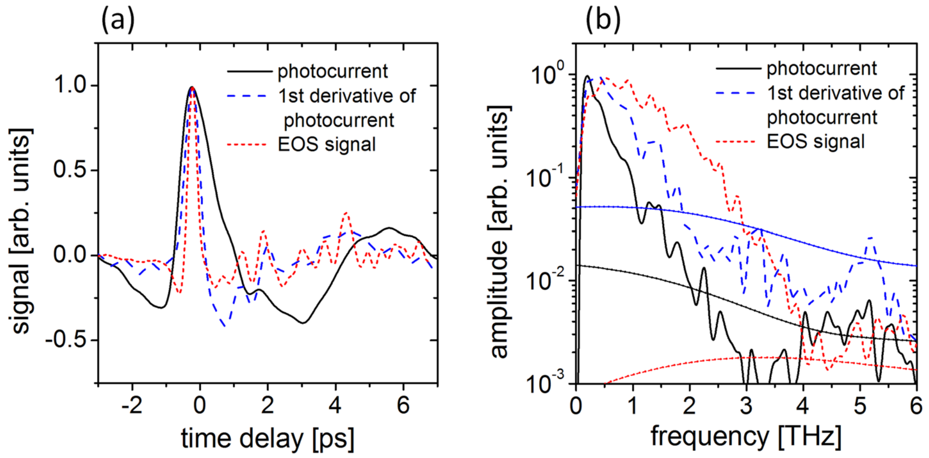

FIG. 3. (a) Comparison of photocurrent, first derivative of the photocurrent, and EOS signal (all normalized). For clarity, the traces are shifted along the time axis. (b) Spectra of the photocurrent, first derivative of the photocurrent and of the EOS signal (all normalized). The smooth lines with circles indicate the noise level for each spectrum.

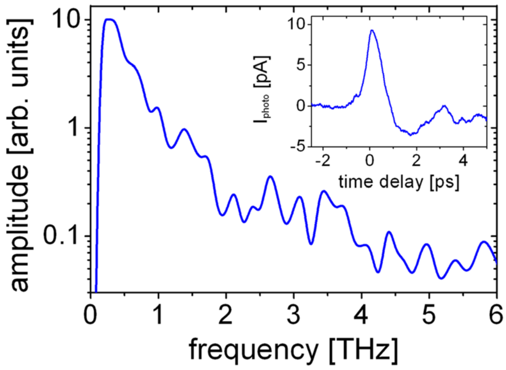

FIG. 4. Photocurrent spectrum measured at a probe wavelength of 1.55 μm. In the inset, the photocurrent pulse is shown.

time, an additional 3 dB frequency arising from the life-time roll-off can be calculated by $\nu_{3dB} = \frac{1}{2\pi\tau}$, where τ represents the carrier life time.[5] Assuming this life time to be ~1 ps, ν_{3dB} is around 160 GHz, which fits quite well to the measured data.

Finally, detection was performed using 1.55 μm radiation for gating of the scalable photoconductive device. In this case, the photocurrent spectrum shows a maximum around 0.2 THz and falls off by two orders of magnitude till 2 THz (cf. Fig. 4). The spectrum is similar to the one obtained with 0.78 μm radiation (cf. Fig. 3(b)). The similarity indicates that both gating wavelengths induce similar carrier dynamics on the timescale provided by the THz pulse.

For the higher frequency components, the SNR obtained with the EOS technique was higher as compared to the technique using scalable photoconductive detectors (cf. Fig. 3(b)). In experiments with microstructured InGaAs-based antennas, a clear improvement was found when the dark current was reduced by mesa structuring.[19] However, scalable emitters rely on the large area and, therefore, do not offer this possibility of optimization. Nevertheless, scalable detectors offer advantages for specific applications, where spatially integrated detection is required, or where tight focusing of the beam is not possible or not desired. Furthermore, scalable detectors of special geometries allow for polarization-mode sensitive measurements, e.g., by distinguishing radially and azimuthally polarized Bessel-Gauss modes.[20] Finally measuring the THz beam profile by scanning a focused gating beam across the detector is feasible in an easy way with scalable photoconductive detectors.

In conclusion, we demonstrated scalable large-area devices based on low-temperature grown InGaAs/InAlAs, suitable for generation and detection of THz pulses when excited by a fiber laser with 1.55 μm wavelength. Considering the bias field distribution and Joule heating, electrode gap sizes in the range from 7 to 10 μm were found to be optimum. While scalable emitters are highly attractive for standard applications, scalable detectors are limited by a fairly low signal-to noise ratio caused by the large dark current. However, scalable detectors are well suited for specific applications, such as selective detection, e.g., of radially, azimuthally or linearly polarized beams, or spatially integrated detection of poorly focused beams.

M.X. would like to thank for support from the Major State Basic Research Development Program of China under Grant 2014CB339802, the National Natural Science Foundation of China under Grant 51107099 and 51377133, the Postdoctoral Science Foundation of China under Grant 2013M542369, the Doctoral Fund of Ministry of Education of China under Grant 20116118110014, the Scientific Research Plan Project of Shaanxi Province under Grant 2012KW-04 and 2013KJXX-35, and the Scientific Research Program funded by Shaanxi Provincial Education Department under Grant 2013JK0610.

[1] T. Löffler, T. Hahn, M. Thomson, F. Jacob, and H. Roskos, Opt. Express **13**, 5353 (2005).
[2] A. Dreyhaupt, S. Winnerl, T. Dekorsy, and M. Helm, Appl. Phys. Lett. **86**, 121114 (2005).
[3] M. Awad, M. Nagel, and H. Kurz, Appl. Phys. Lett. **91**, 181124 (2007).
[4] M. Beck, H. Schäfer, G. Klatt, J. Demsar, S. Winnerl, M. Helm, and T. Dekorsy, Opt. Express **18**, 9251 (2010).
[5] S. Preu, G. H. Döhler, S. Malzer, L. Wang, and A. C. Gossard, J. Appl. Phys. **109**, 061301 (2011).
[6] S. Winnerl, J. Infrared Millim. Terahz Waves **33**, 431 (2012).
[7] J. Krause, M. Wagner, S. Winnerl, M. Helm, and D. Stehr, Opt. Express **19**, 19114 (2011).
[8] A. Eshaghi, M. Shahabadi, and L. Chrostowski, J. Opt. Soc. Am. B **29**, 813 (2012).
[9] F. Peter, S. Winnerl, S. Nitsche, A. Dreyhaupt, H. Schneider, and M. Helm, Appl. Phys. Lett. **91**, 081109 (2007).
[10] A. Eshaghi, M. Shahabadi, L. Chrostowski, and S. Kamal, J. Opt. Soc. Am. B **29**, 3254 (2012).
[11] A. Takazato, M. Kamakura, T. Matsui, J. Kitagawa, and Y. Kadoya, Appl. Phys. Lett. **91**, 011102 (2007).
[12] M. Suzuki and M. Tonouchi, Appl. Phys. Lett. **86**, 051104 (2005).
[13] B. Sartorius, H. Roehle, H. Künzel, J. Böttcher, M. Schlak, D. Stanze, H. Venghaus, and M. Schell, Opt. Express **16**, 9565 (2008).
[14] R. J. B. Dietz, M. Gerhard, D. Stanze, M. Koch, B. Sartorius, and M. Schell, Opt. Express **19**, 25911 (2011).
[15] S. Preu, M. Mittendorff, H. Lu, H. B. Weber, S. Winnerl, and A. C. Gossard, Appl. Phys. Lett. **101**, 101105 (2012).
[16] M. Mittendorff, M. Xu, R. J. B. Dietz, H. Künzel, B. Sartorius, H. Schneider, M. Helm, and S. Winnerl, Nanotechnology **24**, 214007 (2013).
[17] E. Castro-Camus, J. Lloyd-Hughes, and M. B. Johnston, Phys. Rev. B **71**, 195301 (2005).
[18] S. Winnerl, F. Peter, A. Dreyhaupt, B. Zimmermann, M. Wagner, H. Schneider, M. Helm, and K. Köhler, IEEE J. Sel. Top. Quantum Electron. **14**, 449 (2008).
[19] H. Roehle, R. J. B. Dietz, H. J. Hensel, J. Böttcher, H. Künzel, D. Stanze, M. Schell, and B. Sartorius, Opt. Express **18**, 2296 (2010).
[20] S. Winnerl, B. Zimmermann, F. Peter, H. Schneider, and M. Helm, Opt. Express **17**, 1571 (2009).

APPLIED PHYSICS LETTERS **102**, 063112 (2013)

Fabrication of nanopores in 1 nm thick carbon nanomembranes with slow highly charged ions

Robert Ritter,[1] Richard A. Wilhelm,[2,3] Michael Stöger-Pollach,[4] René Heller,[2] Arndt Mücklich,[2] Udo Werner,[5] Henning Vieker,[5] André Beyer,[5] Stefan Facsko,[2] Armin Gölzhäuser,[5] and Friedrich Aumayr[1,a)]

[1]*Institute of Applied Physics, TU Wien-Vienna University of Technology, 1040 Vienna, Austria*
[2]*Institute of Ion Beam Physics & Materials Research, Helmholtz-Zentrum Dresden-Rossendorf, 01328 Dresden, Germany*
[3]*Technische Universität Dresden, 01062 Dresden, Germany*
[4]*USTEM, TU Wien-Vienna University of Technology, 1040 Vienna, Austria*
[5]*Fakultät für Physik, Universität Bielefeld, 33615 Bielefeld, Germany*

(Received 6 November 2012; accepted 4 February 2013; published online 14 February 2013)

We describe the use of slow highly charged ions as a simple tool for the fabrication of nanopores with well-defined diameters typically between 10 and 20 nm in freestanding, 1 nm thick carbon nanomembranes (CNMs). When CNMs are exposed to a flux of highly charged ions, for example Xe^{40+}, each individual ion creates a circular nanopore, the size of which depends on the kinetic and potential energy of the impinging ion. The controlled fabrication of nanopores with a uniform size opens a path for the application of CNM based filters in nanobiotechnology. © *2013 American Institute of Physics*. [http://dx.doi.org/10.1063/1.4792511]

Research on nanolayers, i.e., extremely thin films with a thickness below 10 nm, is a fast growing area within nanoscience and technology. Ignited by the discovery of graphene, which is—most likely—the thinnest mechanically stable two-dimensional material, engineered nanolayers currently receive an enormous attention, and a variety of two-dimensional nanostructures are currently developed and tested. Among them, carbon nanomembranes (CNMs) made from self-assembled monolayers (SAMs)[1] play a prominent role as they provide a modular construction system for diverse types of membranes.[2] CNMs are functional two-dimensional carbon materials; their thickness and other properties can be exactly tailored by an appropriate choice of the molecular precursors and the fabrication conditions. CNMs are made by radiation-induced cross-linking of surface bound self-assembled monolayers of aromatic molecules. The resulting two-dimensional polymeric film is then released from the substrate, cf. Fig. 1(a), and transferred onto arbitrary locations. CNMs show a high mechanical stability and can withstand pressures of up to ~1 bar[3,4] and can be freely suspended over openings and gaps that are more than 100 μm wide.[5,6] Fig. 1(b) shows a Helium ion microscopy (HIM) image of a 1 nm thick CNM that has been transferred onto a copper grid with hexagonal openings of ~60 μm width. Note that the free-standing CNM uniformly covers the entire grid, and that only one "membrane defect" is found in the lower part of the image (see arrow); here, a rupture in the CNM leaves an opening partly covered, which can act as a guide to the eye that nicely demonstrates the uniformity of this CNM. Fig 1(c) shows a higher magnification HIM image of a copper mesh covered by a CNM. Here, the CNM almost looks like "plastic foil" wrapped over a hexagonal copper rim. It can be stated that this intuitive picture of a CNM as a "nanoscale saran wrap" is quite reasonable; mechanical tests yielded a Young modulus of about 10 GPa, i.e., a typical value for polymer films.

CNMs share some similarity with graphene, as they are extremely thin carbon (~1 nm). However, in contrast to graphene, their surfaces can be easily chemically modified by chemical lithography[7] to produce functional 2D materials. The surfaces of CNMs can be engineered with complex architectures, such as patterns of proteins,[8] dyes,[9,10] or polymer brushes.[11,12] These customized CNMs have been used as microscopy supports,[5] nanosieves,[13] "Janus" membranes,[10] and layered structures.[14] Combining tailored CNMs with other different types of nanomembranes (graphene, sieves, and SiN) opens a path to engineer functional nanolayers for electronic, optical, lab-on-a-chip, and micro-/nanomechanical (MEMS/NEMS) devices.

In this work, we explore the perforation of CNMs with pores of uniform sizes, so they can be applied as sieves or filters. We use highly charged ions (HCI), i.e., atoms where the electrons are almost completely stripped resulting in positive ions with an electric charge q between 20+ and 40+ as a tool for pore fabrication. Studies on the interaction of slow ($v < v_{Bohr}$, E_{kin} in the keV range) HCI have been performed with a broad range of materials in recent years.[15,16] A particularly strong interest in the utilization of slow HCI as projectiles impacting solid surfaces has arisen from the distinct advantage that energy deposition and associated defect formation is limited to the topmost atomic layers. This is in stark contrast to the damage cascade initiated by swift (MeV–GeV) heavy ions. Here, a possible nanostructure formation at the surface is always accompanied by the formation of tracks, which can reach several hundreds of nm deep into the solid.[16,17]

For individual slow HCI, it has been found that their high potential energy alone, i.e., the sum of the binding energies of all missing electrons, can be sufficient to cause permanent damage on some materials, for example, nanosized

---

[a)] e-mail: aumayr@iap.tuwien.ac.at.

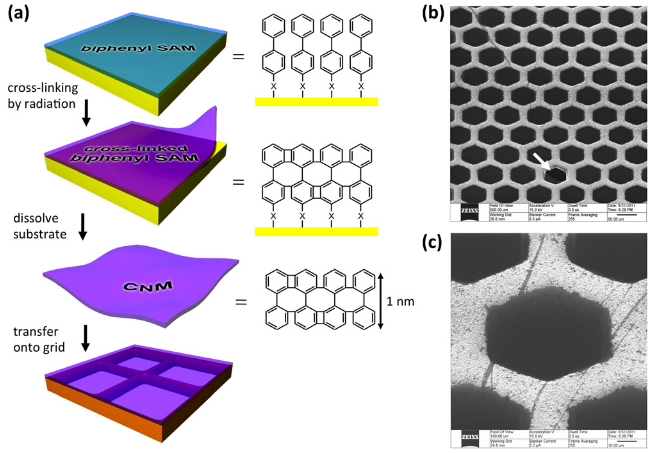

FIG. 1. (a) Schematic of CNM fabrication: a SAM of aromatic molecules, here biphenyls, is formed on a surface and cross-linked by radiation. After the supporting substrate is dissolved, a CNM with the thickness of the monolayer, here 1 nm, is generated and transferred onto a metal grid. (b) HIM image of a CNM that is placed free-standing on a Cu grid with hexagonal 60 μm wide meshes. (c) High magnification HIM image showing a CNM suspending over an opening in the Cu grid.

hillocks on a CaF_2 surface.[18] In this case, even approaching zero kinetic energy, every single ion produces a hillock, if the ion's potential energy exceeds a certain threshold value. In the case of CaF_2, this threshold could be linked to a solid-liquid phase transition. The existence of potential energy thresholds, above which observable topographic modifications can be achieved, seems to be a more general feature in slow HCI—solid interaction. Even so, latent material damage can set in at much lower potential energies. Recent studies on CaF_2[19] and BaF_2[20] show that areas structurally weakened by sub-threshold ion bombardment can be revealed in the form of triangular[19] or pyramidal[20] pits by exposure to a chemical etchant.

The appearance of nanostructures induced by slow HCI depends on the target material properties and, as a consequence thereof, on how energy is dissipated in the surface-near region. So far, the found spectrum ranges from hillocks (CaF_2[18] and $SrTiO_3$[21]), pits, or craters (KBr,[22] PMMA,[23] and Si[24]), to caldera-type structures (TiO_2[25]) and regions of enhanced friction (HOPG[26] and mica[27]).

In the following, we present investigations on the effect of slow HCI irradiation on CNMs. Although, coming from a very different starting point as compared to a solid bulk material, we find that single slow HCI, because of their very localized energy deposition, are able to produce nanosized pores in the membranes, without creating further visible damage. Our results indicate that the pore size can be tuned (increased) with the potential energy, but also depends on the kinetic energy of the impacting ions.

For the irradiation of the CNMs, a source of the Dresden EBIT[28] (electron beam ion trap) type, located at Helmholtz-Zentrum Dresden-Rossendorf (HZDR), was employed, able to deliver Xe^{q+} ions in charge states of up to $q = 40$. The projectile ions could be extracted at voltages varying from 4500 V (no deceleration) down to below 100 V after passing a two-stage deceleration system.

Up to 4 CNMs (produced from biphenylthiol (BPT) and suspended on copper grids with a mesh width of 60 μm, purchased from CNM Technologies (Bielefeld, Germany)) at once were transferred to the target chamber in a standard scanning electron microscopy (SEM) holder and irradiated under normal incidence with charge states $20 \leq q \leq 40$ at varying kinetic energies (20–1400 eV/amu) and fluences (10^9–10^{10} ions/cm^2). After the irradiation procedure and with no further treatment, all CNMs were either immediately transferred to a transmission electron microscope (TEM) at HZDR (FEI TITAN 80-300 with image correction, 300 keV electron energy) or investigated at USTEM TU Wien (FEI TECNAI F20, 200 keV electron energy). TEM images of irradiated CNMs (see, Figs. 2(c) and 2(d) and insets in Fig. 3) clearly show that pores have been formed as a result of individual ion impact events. The respective number densities of found pores are in excellent agreement with the applied fluences, i.e., practically every individual slow HCI has left behind a pore on its passage through the membrane. Our TEM investigations show that for all employed combinations of potential energy (ion charge state) and kinetic energy, pores are formed in the membranes if the charge state exceeds 25+. Two irradiations with Xe^{21+} ions performed with both highest and lowest possible kinetic energies as well as irradiations with Xe projectiles in lower charge states did not yield any evidence for pore formation, indicating that a minimum potential energy (threshold) is necessary to achieve such. After the first observation of pores with TEM, a number of other microscopy techniques were employed (see, Fig. 2) to image ion-induced pores: HIM images of selected samples (Xe^{40+}, $E_{kin} = 180$ keV, Fig. 2(a) and Xe^{40+}, $E_{kin} = 4$ keV, Fig. 2(b)) were taken at the Universität Bielefeld using a Zeiss Orion Plus Helium Ion Microscope (35.7 kV He ion current of 0.5 pA). SEM images of a single sample (Xe^{40+}, $E_{kin} = 12$ keV, Figs. 2(e) and 2(f)) were taken at USTEM TU Wien with a FEI QANTA 200 FEG. Atomic force microscopy (AFM) images of selected samples (Xe^{35+}, $E_{kin} = 12$ keV, Figs. 2(g) and 2(h) and Xe^{40+}, $E_{kin} = 40$ keV) were recorded at IAP TU Wien with a CYPHER AFM (Asylum Research) operated under ambient conditions in intermittent contact mode with commercially available silicon cantilevers with a supersharp diamond-like carbon tip (nominal tip radius of 1 nm). Image display was performed with the WSXM software.[29]

For the determination of the potential energy dependence of the pore size, a series of irradiations (Xe^{q+}, $q = 20$, 25, 30, 35, and 40) was performed at a fixed kinetic energy (40 keV) for the impacting ions. For the acquisition of the size distribution of pores formed in CNMs, TEM images (since they were available for all charge states and offer high resolution) were displayed in IMAGEJ[30] and analyzed according to the following procedure: Pores in the images were magnified, marked, and subsequently analyzed regarding their area distribution with an automatic particle analysis. The mean diameter was then deducted assuming a circular shape for each imaged pore.

Our results give a strong indication for an increase of pore size with increasing potential energy (see, Fig. 3), apart from an apparent dip in the Xe^{35+} case. This dip has been reproduced in a second experiment and, for the moment, can be attributed to an inverse kinetic energy dependence in comparison to other charge states investigated in this study. While

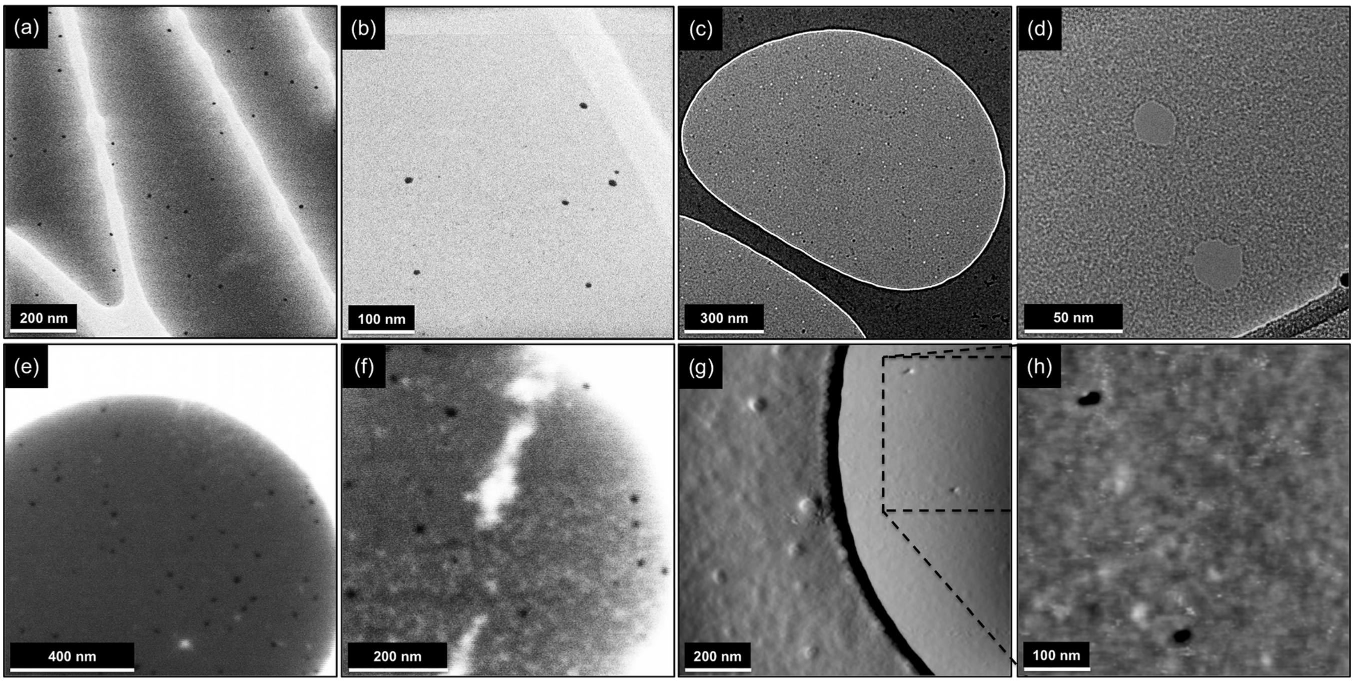

FIG. 2. Pores in CNMs imaged with different microscopy techniques after irradiation with slow highly charged ions; (a) HIM image of pores induced by Xe^{40+} ($E_{kin} = 180$ keV) ions. (b) HIM image, Xe^{40+} ($E_{kin} = 4$ keV). (c) TEM overview image, Xe^{40+} ($E_{kin} = 180$ keV). (d) TEM image, Xe^{40+} ($E_{kin} = 40$ keV). (e) and (f) SEM images, Xe^{40+} ($E_{kin} = 12$ keV). (g) AFM amplitude image, Xe^{35+} ($E_{kin} = 12$ keV). (h) AFM height image (zoomed in from (g)). While the TEM images pores as bright spots, with all other techniques (HIM, SEM, and AFM), they appear as dark spots.

the average pore size produced by an ion of a given charge state (e.g., Xe^{30+} and Xe^{40+}) tends to increase when the kinetic energy is raised, the opposite trend is observed for Xe^{35+} ions, i.e., slower ions induce larger pores. Thorough studies on the effect of kinetic energy variations are currently underway.

Comparing the above-described method to produce perforated CNMs with other schemes of nanopore fabrication, it becomes clear that highly charged ions are a very versatile drilling tool for ultra thin membranes. Basically, the membrane needs only be placed in the path of the ion and the ion produces a circular pore upon impact whose diameter is defined within a few nanometers. Neither resist material nor development steps are needed. Other CNM perforation procedures like EUV-interference lithography[13] have the drawback that they only work when the monolayer is still on a supporting substrate and need to be transferred to the desired location, while the HCI patterning can basically be performed *in situ*. Compared to conventional ion-induced drilling methods, like focused ion beam lithography (FIB) with Ga, Ne, or He ions, HCI patterning has the further advantage that each single impact produces one nanopore. In Helium ion beam lithography, for example, it was shown that the impact of about 100 He ions per square Å is not sufficient to mill away a freely suspended graphene membrane.[31] Furthermore, for reasonable exposure times, a much higher pore density (typically 10^9–10^{10}/cm^2) can be achieved with slow HCI as compared to a FIB.

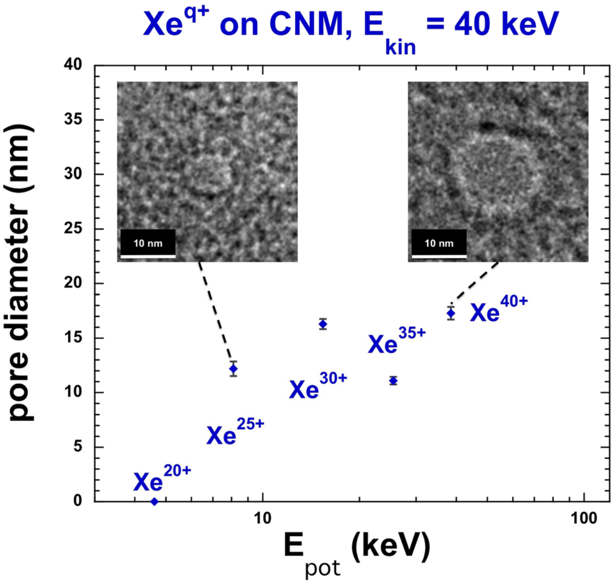

FIG. 3. Evolution of pore diameters in CNMs induced by slow HCIs as a function of ion potential energy: The pore diameter increases from threshold charge state (Xe^{25+}), to highest available charge state (Xe^{40+}) when the kinetic energy of the ions is left constant (40 keV). TEM images of single pores for these cases are displayed to illustrate the observed size increase.

The formation of nanopores in CNMs by slow HCI can qualitatively be understood as a consequence of the multiple neutralization and de-excitation processes taking place when a slow HCI approaches a surface (see, e.g., Refs. 32–35 and references therein). Many electrons from the target are transferred into highly excited states of the projectile ("hollow-atom" formation), and subsequently emitted via auto-ionization and other Auger processes.[32] Remaining unbalanced holes cause structural weakening of the target. The Auger decay of the hollow atom leads to the emission of electrons with low to intermediate energies up to a few hundred eV.[32,33] Part of the ion's potential energy stored in the incoming HCI will thus be deposited in the form of many holes and electron-hole pairs in the CNM.

For charge states below but close to the determined threshold of 25+ ($E_{pot} = 8.1$ keV), e.g., Xe^{21+}, even at kinetic energies ($E_{kin} = 94$ keV, dE/dx = 2.45 keV/nm) close to the nuclear stopping power maximum ($E_{kin} = 160$ keV and dE/dx = 2.95 keV/nm) derived from stopping and range of ions in matter (SRIM)[36] calculations, no pores have been observed after irradiation. Besides this fact, the time for the ion to pass the membrane in our experiments is between 2 fs (highest kinetic energy of 180 keV) and 14 fs (lowest kinetic energy of 3.3 keV), which is lower than the neutralization time for HCIs in carbon materials of ca. 10 fs.[33] For the presented potential energy series at a fixed kinetic energy of 40 keV (see, Fig. 3), ions require only 4 fs for passage through the membrane. Additional interaction processes will take place well before contact and after exiting the membrane, as predicted by the "classical over-the-barrier model,"[37] but the ion will remain far from neutral. This leads to the conclusion that the potential energy is (especially for short times) only partially deposited in the material and also the electronic stopping power might be significantly higher than the average value taken from SRIM, since SRIM uses the equilibrium charge state (neutral in the employed E_{kin} regime), but the actual charge state remains far from equilibrium within the CNM. The influence of varying kinetic energies, which is still subject to discussion, might be strongly connected to this effect of partial potential energy deposition and enhanced electronic stopping in the far-from-equilibrium-regime. The kinetic energy of the projectile further determines the depth within which the de-excitation of the projectile is completed. Simulations on CaF_2 calculate this depth to $\sim$1 nm for 150 q eV (= 4.5 keV for q = 30) and to $\sim$4 nm for 10 q keV (= 300 keV for q = 30) Xe^{q+} projectiles (see, Fig. 4 of Ref. 18). In regions where the ionization density exceeds a certain critical value (threshold), fragments of the membrane are no longer bound and can be ejected or desorbed from the target surface.[17,23]

We consider two theoretical models for pore formation in the CNMs: Coulomb explosion,[38] i.e., kinetic energy transfer to target atoms after the explosion of an area strongly depleted of charge as a result of electron emission processes, could play a role in our experiments, although it has been ruled out as a mechanism for electronic sputtering for Xe charge states below 25.[35] As of now, however, it was not possible to analyze ejected fragments of the membrane. A considerable yield of charged fragments would be a strong indication for Coulomb explosion. Second, sputtering by intense, ultrafast electronic excitations is considered. This model was originally developed to describe structural instabilities in covalent solids due to the creation of a dense electron-hole plasma induced by femtosecond laser irradiation,[39,40] but has also shown validity in slow HCI ion surface interaction.[41] Structural instabilities arise directly from the promotion of electrons from the bonding valence band state to an anti-bonding state in the conduction band. Each electron-hole excitation causes a repulsive force between atoms[33] and can eventually result in material rupture.

In summary, we have shown that 1 nm thick CNMs are susceptible to damage creation by individual slow HCI. Impacts of Xe^{q+} ions in charge states $q \geq 25$ induce nanoscopic pores in the membranes, which have been imaged by a multitude of high resolution imaging techniques. Pores with diameters ranging from 30 nm down to only 3 nm have been observed and analyzed. For a fixed impact energy, the pore diameter increases with the potential energy of the HCI. The dependence of the pore size on the kinetic energy of the incident ions is still subject to studies and discussions.

While, in this work, we have focused mainly on the general aspects of pore production with slow HCI and possible imaging techniques, we are convinced that the continued work on this subject in the near future will lead to (a) a better understanding of the underlying mechanisms and (b) adaptable pore sizes, which can be fine-tuned by ion beam parameters. Once this knowledge has been established, CNMs treated with slow HCI might become of interest for use as nanosieves in a broad range of scientific applications. Nanopores formed in conducting CNMs[3] might also hold promise for studies on DNA translocation[42] and sequencing.

R.R. is a recipient of a DOC-fellowship of the Austrian Academy of Sciences. The Deutsche Forschungsgemeinschaft (DFG) is gratefully acknowledged for financial support under Project No. HE 6174/1-1. This work has been supported by the European Community as an Integrating Activity "Support of Public and Industrial Research Using Ion Beam Technology (SPIRIT)" under EC Contract No. 227012. Support from EURATOM-ÖAW and the Austrian FWF is acknowledged. A.B. and A.G. acknowledge financial support from the Volkswagenstiftung and the Deutsche Forschungsgemeinschaft (SFB 613).

[1] W. Eck, A. Küller, M. Grunze, B. Völkel, and A. Gölzhäuser, Adv. Mater. **17**, 2583 (2005).

[2] A. Turchanin and A. Gölzhäuser, Prog. Surf. Sci. **87**, 108 (2012).

[3] A. Turchanin, A. Beyer, C. T. Nottbohm, X. Zhang, R. Stosch, A. S. Sologubenko, J. Mayer, P. Hinze, T. Weimann, and A. Gölzhäuser, Adv. Mater. **21**, 1233 (2009).

[4] X. Zhang, A. Beyer, and A. Gölzhäuser, Beilstein J. Nanotechnol. **2**, 826 (2011).

[5] C. T. Nottbohm, A. Beyer, A. S. Sologubenko, I. Ennen, A. Hutten, H. Rosner, W. Eck, J. Mayer, and A. Gölzhäuser, Ultramicroscopy **108**, 885 (2008).

[6] A. Gölzhäuser and C. Wöll, ChemPhysChem **11**, 3201 (2010).

[7] A. Beyer, A. Godt, I. Amin, C. T. Nottbohm, C. Schmidt, J. Zhao, and A. Gölzhäuser, Phys. Chem. Chem. Phys. **10**, 7233 (2008).

[8] A. Turchanin, A. Tinazli, M. El-Desawy, H. Großmann, M. Schnietz, H. H. Solak, R. Tampé, and A. Gölzhäuser, Adv. Mater. **20**, 471 (2008).

[9] A. Biebricher, A. Paul, P. Tinnefeld, A. Gölzhäuser, and M. Sauer, J. Biotechnol. **112**, 97 (2004).

[10] Z. Zheng, C. T. Nottbohm, A. Turchanin, H. Muzik, A. Beyer, M. Heilemann, M. Sauer, and A. Gölzhäuser, Angew. Chem., Int. Ed. **49**, 8493 (2010).

[11] I. Amin, M. Steenackers, N. Zhang, A. Beyer, X. Zhang, T. Pirzer, T. Hugel, R. Jordan, and A. Gölzhäuser, Small **6**, 1623 (2010).

[12] I. Amin, M. Steenackers, N. Zhang, R. Schubel, A. Beyer, A. Gölzhäuser, and R. Jordan, Small **7**, 683 (2011).

[13] M. Schnietz, A. Turchanin, C. T. Nottbohm, A. Beyer, H. H. Solak, P. Hinze, T. Weimann, and A. Gölzhäuser, Small **5**, 2651 (2009).

[14] C. T. Nottbohm, A. Turchanin, A. Beyer, R. Stosch, and A. Gölzhäuser, Small **7**, 874 (2011).

[15] F. Aumayr, A. S. El-Said, and W. Meissl, Nucl. Instrum. Methods Phys. Res. B **266**, 2729 (2008).

[16] F. Aumayr, S. Facsko, A. S. El-Said, C. Trautmann, and M. Schleberger, J. Phys.: Condens. Matter **23**, 393001 (2011).

[17] L. Chadderton, Radiat. Meas. **36**, 13 (2003).

[18] A. S. El-Said, R. Heller, W. Meissl, R. Ritter, S. Facsko, C. Lemell, B. Solleder, I. C. Gebeshuber, G. Betz, M. Toulemonde, W. Moller, J. Burgdörfer, and F. Aumayr, Phys. Rev. Lett. **100**, 237601 (2008).

[19] A. S. El-Said, R. A. Wilhelm, R. Heller, S. Facsko, C. Lemell, G. Wachter, J. Burgdörfer, R. Ritter, and F. Aumayr, Phys. Rev. Lett. **109**, 117602 (2012).

[20] A. S. El-Said, R. Heller, F. Aumayr, and S. Facsko, Phys. Rev. B **82**, 033403 (2010).
[21] T. Peters, C. Haake, J. Hopster, V. Sokolovsky, A. Wucher, and M. Schleberger, Nucl. Instrum. Methods Phys. Res. B **267**, 687 (2009).
[22] R. Heller, S. Facsko, R. A. Wilhelm, and W. Möller, Phys. Rev. Lett. **101**, 096102 (2008).
[23] R. Ritter, R. A. Wilhelm, R. Ginzel, G. Kowarik, R. Heller, A. S. El-Said, R. M. Papaléo, W. Rupp, J. R. Crespo López-Urrutia, J. Ullrich, S. Facsko, and F. Aumayr, EPL **97**, 13001 (2012).
[24] M. Tona, H. Watanabe, S. Takahashi, N. Nakamura, N. Yoshiyasu, M. Sakurai, T. Terui, S. Mashiko, C. Yamada, and S. Ohtani, Surf. Sci. **601**, 723 (2007).
[25] M. Tona, Y. Fujita, C. Yamada, and S. Ohtani, Phys. Rev. B **77**, 155427 (2008).
[26] R. Ritter, G. Kowarik, W. Meissl, L. Süss, L. Maunoury, H. Lebius, C. Dufour, M. Toulemonde, and F. Aumayr, Nucl. Instrum. Methods Phys. Res. B **268**, 2897 (2010).
[27] R. Ritter, G. Kowarik, W. Meissl, A. S. El-Said, L. Maunoury, H. Lebius, C. Dufour, M. Toulemonde, and F. Aumayr, Vacuum **84**, 1062 (2010).
[28] F. Grossmann, R. Heller, M. Kreller, U. Kentsch, S. Landgraf, V. P. Ovsyannikov, M. Schmidt, F. Ullmann, and G. Zschornack, Nucl. Instrum. Methods Phys. Res. B **256**, 565 (2007).
[29] I. Horcas, R. Fernandez, J. M. Gomez-Rodriguez, J. Colchero, J. Gomez-Herrero, and A. M. Baro, Rev. Sci. Instrum. **78**, 013705 (2007).
[30] M. D. Abramoff, P. J. Magalhaes, and S. J. Ram, Biophoton. Int. **11**, 36 (2004), available at: http://igitur-archive.library.uu.nl/med/2011-0512-200507/ImageJ.pdf.
[31] M. C. Lemme, D. C. Bell, J. R. Williams, L. A. Stern, B. W. H. Baugher, P. Jarillo-Herrero, and C. M. Marcus, ACS Nano **3**, 2674 (2009).
[32] A. Arnau, F. Aumayr, P. M. Echenique, M. Grether, W. Heiland, J. Limburg, R. Morgenstern, P. Roncin, S. Schippers, R. Schuch, N. Stolterfoht, P. Varga, T. J. M. Zouros, and H. P. Winter, Surf. Sci. Rep. **27**, 117 (1997).
[33] T. Schenkel, A. V. Hamza, A. V. Barnes, and D. H. Schneider, Prog. Surf. Sci. **61**, 23 (1999).
[34] H. P. Winter and F. Aumayr, J. Phys. B **32**, R39 (1999).
[35] F. Aumayr and H. P. Winter, Philos. Trans. R. Soc. London **362**, 77 (2004).
[36] J. F. Ziegler, J. P. Biersack, and U. Littmark, *The Stopping and Range of Ions in Matter* (Pergamon, New York, 1985).
[37] J. Burgdörfer, P. Lerner, and F. W. Meyer, Phys. Rev. A **44**, 5674 (1991).
[38] I. S. Bitensky and E. S. Parilis, Nucl. Instrum. Methods Phys. Res. B **21**, 26 (1987).
[39] P. Stampfli, Nucl. Instrum. Methods Phys. Res. B **107**, 138 (1996).
[40] P. Stampfli and K. H. Bennemann, Appl. Phys. A **60**, 191 (1995).
[41] T. Schenkel, A. V. Hamza, A. V. Barnes, D. H. Schneider, J. C. Banks, and B. L. Doyle, Phys. Rev. Lett. **81**, 2590 (1998).
[42] C. A. Merchant, K. Healy, M. Wanunu, V. Ray, N. Peterman, J. Bartel, M. D. Fischbein, K. Venta, Z. Luo, A. T. C. Johnson, and M. Drndic, Nano Lett. **10**, 2915 (2010).

APPLIED PHYSICS LETTERS **102**, 022409 (2013)

Microscopic magnetic structuring of a spin-wave waveguide by ion implantation in a $Ni_{81}Fe_{19}$ layer

Björn Obry,[1] Thomas Meyer,[1] Philipp Pirro,[1] Thomas Brächer,[1,2] Bert Lägel,[3] Julia Osten,[4] Thomas Strache,[4] Jürgen Fassbender,[4] and Burkard Hillebrands[1]
[1]*Fachbereich Physik and Forschungszentrum OPTIMAS, Technische Universität Kaiserslautern, D-67663 Kaiserslautern, Germany*
[2]*Graduate School Materials Science in Mainz, D-67663 Kaiserslautern, Germany*
[3]*Nano Structuring Center, Technische Universität Kaiserslautern, D-67663 Kaiserslautern, Germany*
[4]*Institut für Ionenstrahlphysik und Materialforschung, Helmholtz-Zentrum Dresden-Rossendorf, D-01328 Dresden, Germany, and Technische Universität Dresden, D-01062 Dresden, Germany*

(Received 19 November 2012; accepted 26 December 2012; published online 15 January 2013)

We investigate the spin-wave excitation in microscopic waveguides fabricated by localized Cr^+ ion implantation in a ferromagnetic $Ni_{81}Fe_{19}$ film. We demonstrate that spin-wave waveguides can be conveniently made by this technique. The magnetic patterning technique yields an increased damping and a reduction in saturation magnetization in the implanted regions that can be extracted from Brillouin light scattering measurements of the spin-wave excitation spectra. Furthermore, the waveguide performance as well as the internal field of the waveguide depend on the doping fluence. The results prove that localized ion implantation is a powerful tool for the patterning of magnon spintronic devices. © *2013 American Institute of Physics*. [http://dx.doi.org/10.1063/1.4775759]

The field of spin dynamics and spintronics has greatly benefited from micro- and nanopatterning techniques. The advancement of research on small magnetic structures[1–4] strongly depends on the possibility to fabricate structures of accurate sizes and shapes. Based on these developments, the focus of many investigation has turned to the realization of spin logic devices, which use the electron spin[5] or spin waves as information carrier.[6–8]

In order to establish a pure spin-wave logic architecture, there is a need for spin-wave conduits for the transport of spin information between the individual logic devices. Thus, the fabrication and investigation of spin-wave waveguides[9–12] has become a major research topic in the field of magnon spintronics. Currently, spin-wave waveguides with nanometer thicknesses and widths of several micrometers are fabricated by topographically patterning thin magnetic stripes onto a substrate that is usually nonmagnetic. However, the potential of other waveguide fabrication techniques has not been explored up to now, although they might contribute to an improvement of waveguide properties that were not accessible so far, such as, e.g., the inhomogeneity of the internal magnetic field.[13] In that respect, ion implantation of ferromagnetic films is a promising technique for the fabrication of thin films with microscopic magnetic substructures.[14–16] The different components contributing to the change in the magnetic properties due to Cr^+ ion implantation in $Ni_{81}Fe_{19}$ films have been thoroughly investigated.[17]

In this letter, a purely magnetic microscopic structuring of spin-wave waveguides by localized ion implantation in a $Ni_{81}Fe_{19}$ film is presented. We have designed a stripe shaped area with unchanged magnetic properties, embedded in a film with a reduced saturation magnetization M_S and an increased damping α. It is shown that the spin-wave distribution within the stripe has similar properties as in a topographically patterned $Ni_{81}Fe_{19}$ reference waveguide, if M_S in the surrounding implanted region is decreased below at least 66% of its original value. The spin-wave excitation spectra also indicate an influence of the reduced magnetization of the implanted region on the internal magnetic field of the $Ni_{81}Fe_{19}$ stripe. Hence, by localized ion implantation, it is possible to create and adjust the properties of spin-wave waveguides by pure magnetic patterning.

A schematic of the sample setup is shown in Fig. 1. A 20 nm thick $Ni_{81}Fe_{19}$ film is grown onto a Si/SiO_2 (200 nm) substrate by molecular beam epitaxy (MBE). Subsequently, a lithographically structured polymethyl methacrylate (PMMA) resist mask is fabricated on top of the film via electron beam lithography. The magnetic patterning is achieved by exposing

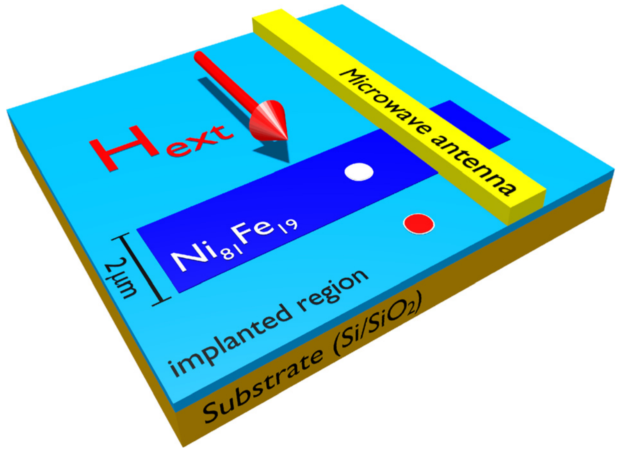

FIG. 1. Schematic sample setup. A $Ni_{81}Fe_{19}$ film with a thickness of 20 nm is grown on top of a Si/SiO_2 substrate. By localized implantation of Cr^+ ions, the magnetic properties of the implanted parts of the film are changed while a shielded region yields a 2 μm wide $Ni_{81}Fe_{19}$ stripe with unchanged properties embedded in the film. A subsequently produced Cu microwave antenna serves as excitation source for spin waves. The two measurement positions for the investigations from Fig. 2 are marked by a red and white circle, respectively. The external magnetic field is applied along the short axis of the $Ni_{81}Fe_{19}$ stripe.

the sample to a broad beam irradiation of 30 keV Cr$^+$ ions. This localized ion implantation in the areas which are not covered by the PMMA leads to the creation of 2 μm wide stripes with unchanged magnetic properties embedded in the implanted film. Due to the doping, this surrounding film has been modified in its saturation magnetization and damping. Using lift-off, a Cu antenna with a width of 1 μm and a thickness of 500 nm is fabricated across the stripes for the excitation of spin waves in the ferromagnetic film by the Oersted field of an applied microwave current. Depending on the ion fluence the modification of the $Ni_{81}Fe_{19}$ properties changes accordingly, and thus, the influence on the spin-wave properties varies. For this reason, a series of samples has been fabricated with varying Cr$^+$ fluences of 2.2×10^{15} ions/cm^2 (sample A), 6.6×10^{15} ions/cm^2 (sample B), and 1.1×10^{16} ions/cm^2 (sample C).

For an initial characterization of the magnetization dynamics inside the modified film, the spin-wave excitation spectrum is recorded using Brillouin light scattering (BLS) microscopy. This technique is based on the inelastic scattering of laser light with spin waves and stands out due to its high sensitivity combined with a high spectral and spatial resolution.[18] The spin-wave excitation spectra are taken at the position of the stripe and in the implanted region, respectively, as indicated by the two circles in Fig. 1. For this, an in-plane static magnetic field of $\mu_0 H_{\mathrm{ext}} = 30\,\mathrm{mT}$ is applied perpendicularly to the stripe's long axis, and a microwave current with varying frequency is applied to the antenna. The left column of Fig. 2 shows the resulting spin-wave excitation spectra. The doping causes a shift of the excitation spectra to lower frequencies in the irradiated areas. This allows for a quantitative analysis of the reduction of the saturation magnetization by calculating the spin-wave dispersion relation[19,20] and treating M_S as a fit parameter to match the experimental data (see solid lines in the right column of Fig. 2). With increasing ion fluence, a reduction of M_S to values of $0.80 M_S^0$ (sample A), $0.66 M_S^0$ (sample B), and $0.52 M_S^0$ (sample C) is determined, where $M_S^0 = 860\,\mathrm{kA/m}$ is the saturation magnetization of the non-irradiated $Ni_{81}Fe_{19}$ film. Using the approach shown in Ref. 21, the same magnetization values are found by polar magneto-optical Kerr effect measurements on equally implanted $Ni_{81}Fe_{19}$ films. Furthermore, the decrease in the BLS signal in the implanted region (solid lines) with respect to the unchanged stripe regions (dotted lines) indicates an increase in the damping constant α in accordance to Ref. 17. However, a quantitative analysis of the change in α is not possible, since the absolute spin-wave intensities of different samples vary drastically and cannot be compared.

The results are in good agreement with the previous investigations of Cr$^+$ implanted $Ni_{81}Fe_{19}$ films[17] which, in addition, revealed a radiation-induced damage of the film surface and interface to a buffer layer. In the present case, atomic force microscopy (AFM) measurements of the surface profile show a thickness reduction of the $Ni_{81}Fe_{19}$ layer in the implanted area of up to 5 nm. The reduced film thickness of the implanted region has been considered in the above calculations of the spin-wave dispersion relation. However, its influence is negligible compared to the change in M_S for the dipolar dominated spin waves analyzed in this study. Moreover, a possible difference in the stripe width between different samples (caused by the varying irradiation fluence of the Cr$^+$ ions) can be excluded by the AFM measurements.

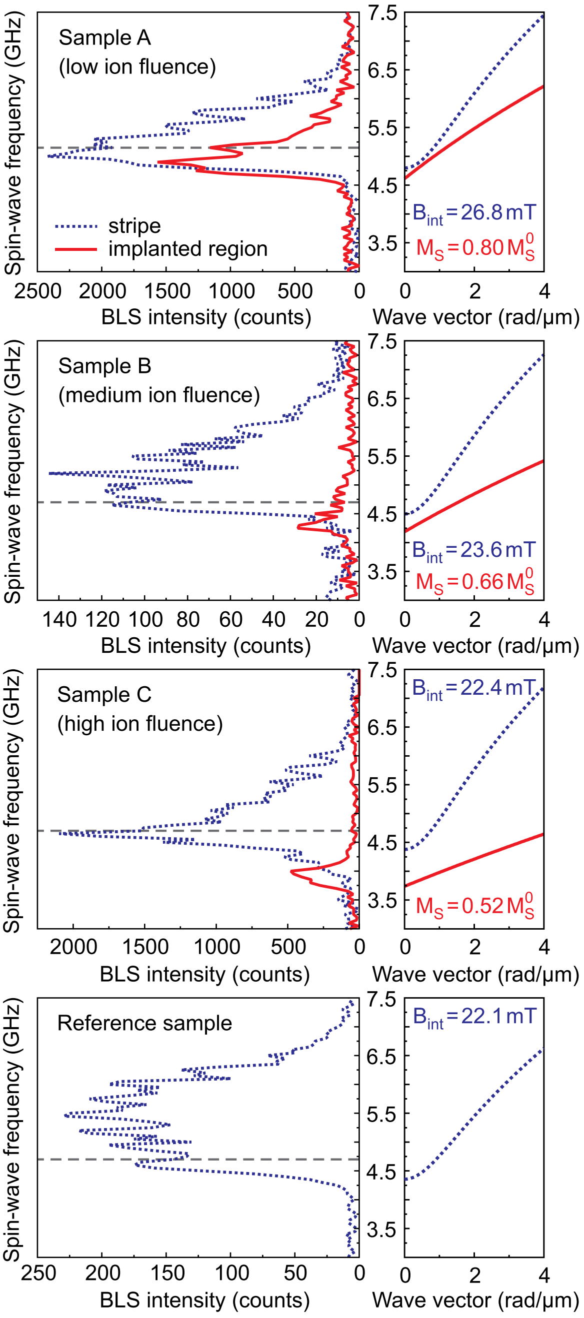

FIG. 2. Experimentally observed spin-wave resonance spectra (left column) and calculated dispersion relations (right column) of magnetically patterned samples with different ion fluences compared to a topographically patterned reference sample. The resonance spectra have been recorded on the non-irradiated stripe (dotted lines) as well as on the implanted region of the film (solid lines) using Brillouin light scattering microscopy. The dashed lines in the left column indicate the frequency of the measurements in Fig. 3(a). The right column contains fitting values for the internal magnetic field and the normalized saturation magnetization.

Figure 2 also displays experimental spin-wave excitation spectra, which have been recorded on the non-irradiated stripe region (dotted lines) as well as on a topographically patterned $Ni_{81}Fe_{19}$ stripe serving as a reference. A comparison of the respective lower onset frequency (ferromagnetic resonance) of the spectrum shows that with increasing ion fluence the excitation spectrum is shifted to lower frequencies and approaches the spectrum of the reference sample. Since the stripe area has not been changed in its material properties, i.e., M_S is unchanged, the influence on the spin-wave spectrum must be a result of the modification in the magnetic properties of the surrounding film. This long range interaction of the implanted film on the stripe region is reflected in the demagnetizing fields B_{demag}, which are created at the edges of the stripe. In the case of a small reduction of M_S in the implanted region, the stray field in the stripe will be negligible, resulting in an internal field $B_{\mathrm{int}} = \mu_0 H_{\mathrm{ext}} + B_{\mathrm{demag}} \approx \mu_0 H_{\mathrm{ext}}$. However, for a strong reduction in the saturation magnetization in the irradiated region, a higher stray field originates from the boundaries of the stripe, which is directed opposite to the external field. Using B_{int} as a fitting parameter in the calculation of the dispersion relation[22] allows for an evaluation of the internal field from the experimental data. The resulting B_{int} values given in Fig. 2 confirm the above assumptions: With increasing ion fluence, the internal magnetic field of the samples converges to the field value of the reference sample, which represents the minimum (i.e., zero) magnetic moment outside the stripe area and thus the highest possible stray-field induced reduction of B_{int}. Thus, the fabrication of spin-wave waveguides by ion implantation allows for a manipulation of the internal magnetic field inside the waveguide. It should be noted that the presence of a nonzero magnetization in the implanted areas might further affect the dynamic pinning at the stripe edges, leading to a modification of the effective width w_{eff} of the stripe.[13] However, even an impact of a change in w_{eff} by 25% on the excitation spectrum will be one order of magnitude smaller than the effect by the change in B_{int}. As a consequence, any change in the dynamic pinning can be neglected.

As a next step, the spin-wave intensity distribution in the implanted films is investigated with respect to the suitability of the $Ni_{81}Fe_{19}$ stripe to act as a spin-wave waveguide. Spin waves are excited by the antenna with a frequency close to the ferromagnetic resonance, as indicated by the dashed lines in the left column of Fig. 2. An in-plane static external magnetic field of $\mu_0 H_{\mathrm{ext}} = 30\,\mathrm{mT}$ is applied perpendicularly to the stripe's long axis (Damon-Eshbach geometry). The spin-wave propagation along the stripe is studied using BLS microscopy by recording two-dimensional maps of the spatial spin-wave intensity distribution with a resolution of about 300 nm. Beside the implanted films, the topographically patterned reference waveguide has also been studied. The results are shown in Fig. 3(a). The spin-wave intensity is color coded and plotted as a function of the position on the film with the antenna being at $x = 0\,\mathrm{mm}$, the dashed lines indicate the stripe position. Compared to the reference waveguide, the spin-wave intensity pattern in the case of sample A differs significantly. Although a higher decay length can be assumed in the stripe region, there is significant excitation of spin waves in the implanted regions. In contrast, the spin-wave intensity distribution is concentrated to the stripe region in the case of samples B and C and resembles the reference waveguide pattern, indicating a waveguide-like behavior. This change in the waveguide performance can be understood using the results of Fig. 2. For each sample, the respective excitation frequency is indicated by a dashed line. While for sample A, the excitation efficiency in both the implanted and the stripe region is similar, a pronounced difference is obtained in the case of samples B and C. This is attributed to both a change in M_S and in α, since the former prevents the spreading of spin waves in the regions outside the stripe by shifting and narrowing the excitation spectrum in frequency while the latter decreases their lifetime. Consequently, the excitation and subsequent propagation of spin waves is confined to the stripe regions, leading to a waveguide-like behavior.

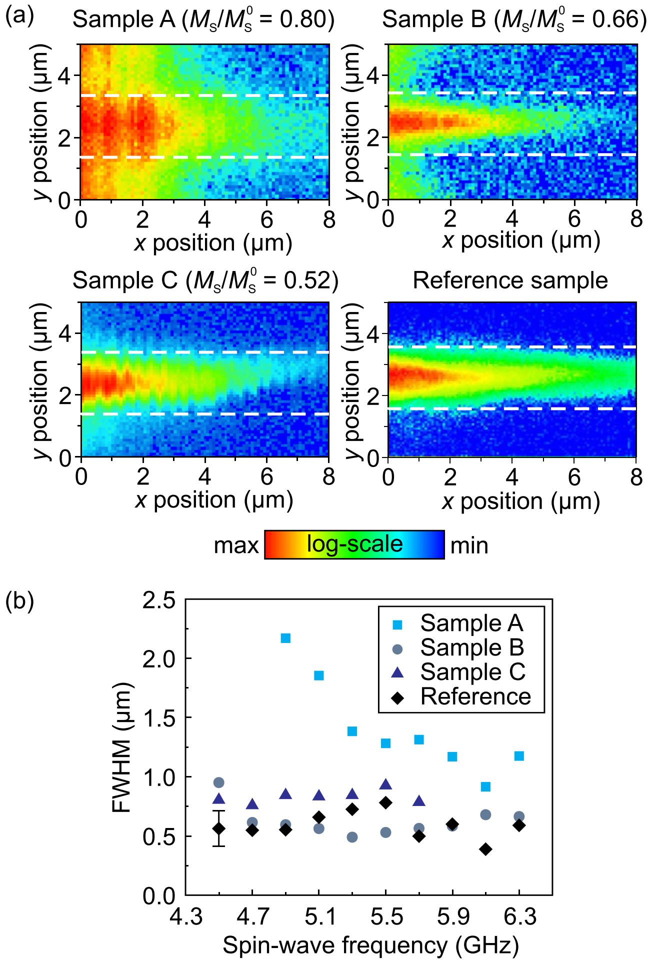

FIG. 3. (a) Color-coded spin-wave intensity distribution in the magnetically patterned $Ni_{81}Fe_{19}$ films and the reference waveguide. The position of the stripe with unchanged magnetic properties is indicated by the white dashed lines. Spin waves are excited by the antenna at $x = 0\,\mu\mathrm{m}$. (b) Dependence of the width of the transverse spin-wave mode profiles on the spin-wave frequency. The width of the mode profiles has been measured by evaluating the FWHM. The experimental precision is indicated by the error bar.

For a more quantitative view on the waveguide performance, the transverse spin-wave intensity profiles are measured by scanning the BLS laser focus along the short axis of the stripe. The width of the intensity distribution is analyzed by determining the full width at half maximum (FWHM). Figure 3(b) depicts the resulting FWHM values as a function of the applied spin-wave excitation frequency. In the case of sample A the FWHM strongly decreases with increasing excitation frequency. This deviates from the observation on samples B and C, where the width of the profiles is unaffected by the change in the microwave frequency. The latter also exhibit the same FWHM values as the reference waveguide within the experimental precision as indicated by the error bar, again justifying the above assumption of neglecting any changes in the dynamic pinning at the stripe edges due to their small size. In the reference waveguide, the lateral confinement of the spin waves along the waveguide width leads to the formation of quantized transverse waveguide modes.[1] The width of these modes depends on the transverse wave vector component, which is quantized along the short stripe axis and hence constant for a given mode number. Obviously, this quantization along the short stripe axis is given in samples B and C due to the mismatch of the dispersion relations of the implanted region and that of the stripe, respectively (see Fig. 2), which prevents the propagation of spin waves excited in the stripe into the implanted region. However, in the case of sample A, the two dispersion relations converge with decreasing frequency, resulting in an increased spreading of spin waves over the whole film in accordance to the experimental results shown in Fig. 3(b). Thus, the results prove that the stripes of samples B and C can be considered as genuine spin-wave waveguides and that a reduction of the saturation magnetization in the implanted area to 66% of its original value is sufficient to channel the spin waves inside the magnetically patterned $Ni_{81}Fe_{19}$ stripe.

In conclusion, a purely magnetic patterning of a spin-wave waveguide has been achieved by localized Cr^+ ion implantation in a $Ni_{81}Fe_{19}$ film. The waveguide performance depends on the induced changes in the magnetic properties and hence can be controlled by the doping intensity. Moreover, having a waveguide inside a region with a nonzero saturation magnetization allows for an adjustment of the internal field of the waveguide. These results show that the fabrication of spin-wave waveguides by means of localized ion implantation provides potential for the manipulation of various waveguide properties and thus pioneers applications for spin-wave conduits in the field of magnon spintronics.

The authors wish to thank the Nano Structuring Center (NSC) of the TU Kaiserslautern for support with the sample preparation and R. Neb for the evaporation of the $Ni_{81}Fe_{19}$ films. Financial support by the DFG within the Graduiertenkolleg (GRK 792) is gratefully acknowledged.

[1] C. Mathieu, J. Jorzick, A. Frank, S. O. Demokritov, A. N. Slavin, B. Hillebrands, B. Bartenlian, C. Chappert, D. Decanini, F. Rousseaux, and E. Cambril, Phys. Rev. Lett. **81**, 3968 (1998).
[2] S. O. Demokritov and B. Hillebrands, in *Spin Dynamics in Confined Magnetic Structures I*, Topics in Applied Physics Vol. 83, edited by B. Hillebrands and K. Ounadjela (Springer, Berlin, 2002), p. 65.
[3] V. E. Demidov, S. Urazhdin, and S. O. Demokritov, Nature Mater. **9**, 984 (2010).
[4] M. Madami, S. Bonetti, G. Consolo, S. Tacchi, G. Carlotti, G. Gubbiotti, F. B. Mancoff, M. A. Yar, and J. Åkerman, Nat. Nanotechnol. **6**, 635 (2011).
[5] I. Žutić, J. Fabian, and S. D. Sarma, Rev. Mod. Phys. **76**, 323 (2004).
[6] A. Khitun, M. Bao, and K. L. Wang, J. Phys. D **43**, 264005 (2010).
[7] A. A. Serga, A. V. Chumak, and B. Hillebrands, J. Phys. D **43**, 264002 (2010).
[8] B. Lenk, H. Ulrichs, F. Garbs, and M. Münzenberg, Phys. Rep. **507**, 107 (2011).
[9] K. Vogt, H. Schultheiss, S. J. Hermsdoerfer, P. Pirro, A. A. Serga, and B. Hillebrands, Appl. Phys. Lett. **95**, 182508 (2009).
[10] P. Pirro, T. Brächer, K. Vogt, B. Obry, H. Schultheiss, B. Leven, and B. Hillebrands, Phys. Status Solidi B **248**, 2404 (2011).
[11] T. Sebastian, Y. Ohdaira, T. Kubota, P. Pirro, T. Brächer, K. Vogt, A. A. Serga, H. Naganuma, M. Oogane, Y. Ando, and B. Hillebrands, Appl. Phys. Lett. **100**, 112402 (2012).
[12] P. Clausen, K. Vogt, H. Schultheiss, S. Schäfer, B. Obry, G. Wolf, P. Pirro, B. Leven, and B. Hillebrands, Appl. Phys. Lett. **99**, 162505 (2011).
[13] K. Y. Guslienko, R. W. Chantrell, and A. N. Slavin, Phys. Rev. B **68**, 024422 (2003).
[14] J. Fassbender and J. McCord, J. Magn. Magn. Mater. **320**, 579–596 (2008).
[15] R. Neb, T. Sebastian, P. Pirro, B. Hillebrands, S. Pofahl, R. Schäfer, and B. Reuscher, Appl. Phys. Lett. **101**, 112406 (2012).
[16] L. Folks, R. E. Fontana, B. A. Gurney, J. R. Childress, S. Maat, J. A. Katine, J. E. E. Baglin, and A. J. Kellock, J. Phys. D **36**, 2601 (2003).
[17] J. Fassbender, J. von Borany, A. Mücklich, K. Potzger, W. Möller, J. McCord, L. Schultz, and R. Mattheis, Phys. Rev. B **73**, 184410 (2006).
[18] V. E. Demidov, S. O. Demokritov, B. Hillebrands, M. Laufenberg, and P. P. Freitas, Appl. Phys. Lett. **85**, 2866 (2004).
[19] Following the calculations from Ref. 20 assuming a $Ni_{81}Fe_{19}$ film with a thickness $t = 20$ nm, a gyromagnetic ratio $\gamma = 28\,\mathrm{GHz/T}$, an exchange stiffness constant $A = 1.6 \times 10^{-11}$ J/m, and a magnetic field $\mu_0 H_{\mathrm{ext}} = 30\,\mathrm{mT}$.
[20] B. A. Kalinikos and A. N. Slavin, J. Phys. C: Solid State Phys. **19**, 7013 (1986).
[21] D. Markó, T. Strache, K. Lenz, J. Fassbender, and R. Kaltofen, Appl. Phys. Lett. **96**, 022503 (2010).
[22] According to Ref. 20 assuming a $Ni_{81}Fe_{19}$ stripe with thickness $t = 20$ nm and width $w = 2\,\mu$m, a gyromagnetic ratio $\gamma = 28\,\mathrm{GHz/T}$, exchange stiffness constant $A = 1.6 \times 10^{-11}$ J/m, and a saturation magnetization $M_S = 860\,\mathrm{kA/m}$.

SCIENTIFIC REPORTS

OPEN

SUBJECT AREAS:
MAGNETIC DEVICES
MAGNETIC PROPERTIES AND MATERIALS
APPLIED PHYSICS
SPINTRONICS

Lateral spin transfer torque induced magnetic switching at room temperature demonstrated by x-ray microscopy

M. Buhl[1,2], A. Erbe[1], J. Grebing[1], S. Wintz[1,2], J. Raabe[3] & J. Fassbender[1,2]

[1]Helmholtz-Zentrum Dresden-Rossendorf, [2] Technische Universität Dresden, [3]Paul Scherrer Institut.

Received
10 April 2013

Accepted
5 September 2013

Published
15 October 2013

Correspondence and requests for materials should be addressed to A.E. (a.erbe@hzdr.de)

Changing and detecting the orientation of nanomagnetic structures, which can be used for durable information storage, needs to be developed towards true nanoscale dimensions for keeping up the miniaturization speed of modern nanoelectronic components. Therefore, new concepts for controlling the state of nanomagnets are currently in the focus of research in the field of nanoelectronics. Here, we demonstrate reproducible switching of a purely metallic nanopillar placed on a lead that conducts a spin-polarized current at room temperature. Spin diffusion across the metal-metal (Cu to CoFe) interface between the pillar and the lead causes spin accumulation in the pillar, which may then be used to set the magnetic orientation of the pillar. In our experiments, the detection of the magnetic state of the nanopillar is performed by direct imaging via scanning transmission x-ray microscopy (STXM).

The state of small magnetic entities has been used for data storage for some decades. Developments, *e.g.* based on giant magnetoresistance (GMR)[1,2] or tunnelmagnetoresistance (TMR)[3,4] effects, have enabled the nanoscale integration of these entities into large area devices such as hard disk drives. The state of these structures is usually set by the application of external magnetic fields. The generation of these fields at the location of the nanoscale magnetic memory requires the very precise positioning of a magnetic write head with respect to the element. This process, however, has not only the drawback of being time-consuming and technologically involved, but is also accompanied by parasitic stray fields that may limit the achievable storage density. Therefore, techniques allowing for magnetic switching without the necessity of applying an external field have been investigated extensively during the past years in the field of spintronics[5], a terminus which stands for the concept of using the electron spin for information storage and manipulation. The torque which is exerted by a spin polarized current on the electrons in a conductor depends on the relative orientation of the corresponding spin moments. A spin polarized current entering a ferromagnetic element thus may change the magnetization orientation of this element and by this information can be stored inside it. The underlying effect, called spin transfer torque (STT)[6,7], has been studied intensively in several magnetization switching experiments using time-resolved STXM[8–10]. However, most of the structures investigated so far have in common that they require vertical integration of the memory cell in the so-called current perpendicular to the plane (CPP) configuration, making the circuit design and fabrication rather complicated. In contrast, demonstration of STT induced switching of magnetic nanostructures with a purely horizontal contact layout would open various efficient possibilities for large scale integration of STT magnetic memories. In our layout, the number of necessary lithography steps is reduced to 2 as opposed to at least 3 steps in the case of vertical magnetic nanostructures. In addition, the technologically challenging side-wall isolation of the magnetic pillars is not necessary in our design.

We have developed a layout consisting of a nanoscale, elliptic magnetic structure ("nanopillar") and two micronscaled, rectangular magnetic elements ("polarizers") as shown in figure 1. Both, the central pillar and the surrounding polarizers are fabricated from CoFe at a thickness of 8 nm. The magnetic anisotropy at this thickness enforces the magnetization to be oriented in the plane of the film. In addition, the elliptical shape of the central pillar leads to anisotropy energy in the plane of the pillar, which is minimized for a magnetization along the long axis of the ellipse. Thus, two energetically equivalent magnetic configurations arise as ground states for the pillar.

The electrical connection between the polarizers and the pillar is provided by a Cu line of 5 nm thickness and 100 nm width that also extends to underneath the polarizers. The total length of the Cu line between the polarizers is 280 nm, which is of the order of the typical spin coherence length in pure Cu at room temperature[11]. Our circuit thus allows us to generate a spin-polarized current below one of the polarizers, which flows

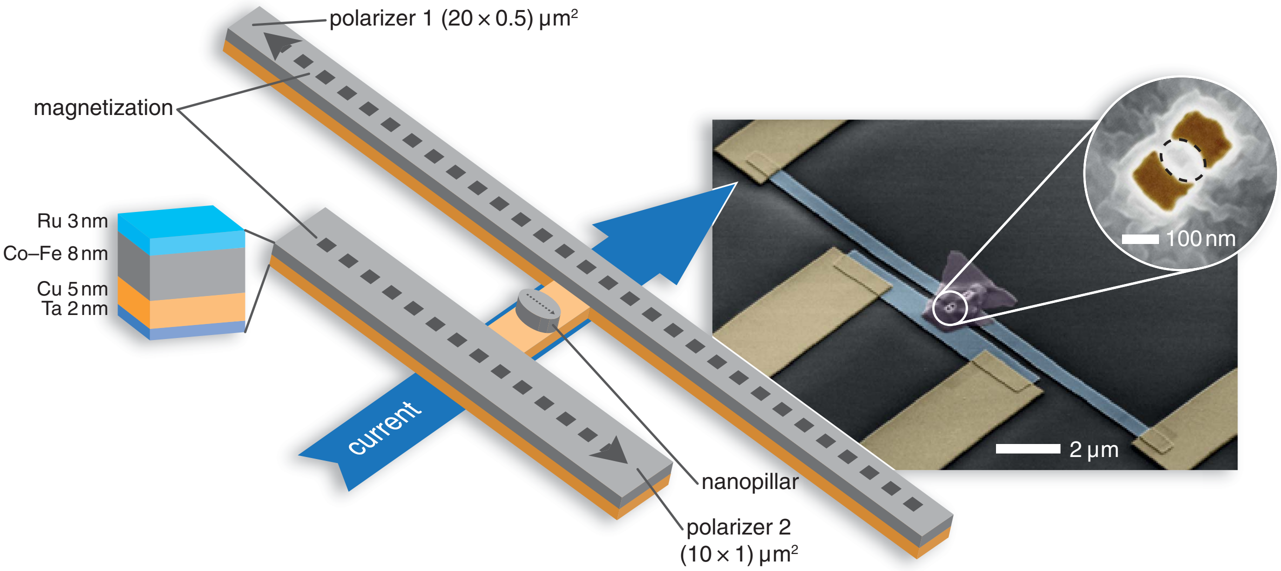

Figure 1 | Schematic layout of the current in plane spin transfer torque (STT CIP) structure (left) and scanning electron microscopy (SEM) images (right). The magnetic pillar (marked by dashed lines in the zoom shown upper right) is placed in between two polarizers with aspect ratios 10 µm × 1 µm and 20 µm × 0.5 µm, respectively. Due to the different aspect ratios the magnetizations of the polarizers can be set antiparallel, as sketched by the dotted arrows. A Cu line is used to carry a spin polarized under the polarizers and the pillar. Depending on its polarization, this current switches the pillar between the two magnetization directions, which are energetically favored due to the elliptic shape of the pillar (left and right in the zoom shown in the center).

underneath the pillar into the direction of the second polarizer. This kind of design is called a current in plane (CIP) configuration. Theoretical calculations have shown that in such CIP configuration the efficiency for STT induced magnetization switching due to spin diffusion is of similar order as in CPP configurations, i.e. configurations in which the charge current passes directly through the pillar[12]. Recent experiments have indeed demonstrated electrical measurements for the switching of magnetic nanostructures in CIP configurations[13] at low temperatures (between 10 K and 77 K). Here, we show the first experimental realization of directly imaging the magnetic state of a nanostructure in CIP configuration before and after switching events by using STXM[14] and exploiting x-ray magnetic circular dichroism (XMCD) effects. Corresponding micrographs and the construction of the magnetic contrast images are demonstrated in figure 2. Furthermore, the size scale and the layout of our sample even allow for the operation and detection of CIP STT switching at room temperature. This opens the way for a fundamental characterization of the switching mechanisms in static and dynamic experiments as well as for the development of possible applications incorporating CIP configurations in this area.

Results

The magnetization of the pillar can be reversed by current pulses passing underneath the polarizers leading to configurations with the magnetization pointing in either of the two directions of the long axis ("left" or "right" in the following discussion). The initial magnetization orientation of the pillar depends on the externally applied magnetic field and the stray fields originating from the polarizers. Using an external magnet, fields in the range of $-30\ \mathrm{mT} < \mu_0 H_{\mathrm{ext}} < 30\ \mathrm{mT}$ are generated at the location of the sample. By applying such fields, configurations with a bistable pillar magnetization and two oppositely magnetized polarizers can be obtained, as shown in figure 2. This is the main prerequisite for an experimental condition where switching between the two magnetization orientations of the pillar is possible by spin transfer torque *only*.

In this configuration a current pulse, which has become spin-polarized beneath the initial polarizer, passes underneath the pillar. The magnetization of the pillar is imaged before and after the pulse. Figure 3 illustrates the reproducible switching of the pillar's magnetization state from left (dark contrast) to right (bright contrast) and back without external field.

This switching process was repeated several times in a single structure and was also measured in various samples produced on different chips, in order to show the reproducibility of our results. The details of the switching process (e.g. necessary current density) vary for the individual nanostructures, but the general switching behavior proved to be reliable and reproducible. In total, we have successfully demonstrated switching with and without supporting field in five different samples produced in two different production runs. The details of the switching events are summarized in the supplementary information (SI).

Discussion

In order to prove the significance of the STT effect for the switching processes observed we will discuss and subsequently exclude other possible switching mechanisms, such as induced by stray fields, Oerstedt fields, or device heating, in the following.

In order to confirm that the magnetic field in the center of our structure is indeed zero, micromagnetic simulations of the stray field originating from the polarizers in the configuration shown in figure 3 were carried out (details of the simulation can be found in the SI). As expected, the polarizer induced stray fields at the location of the pillar are negligible ($\mu_0 H < 0.1$ mT). We have further tested the influence of magnetic fields on the magnetization of the pillar by performing measurements at externally applied, supporting fields H_{ext} (shown in the SI). The values of the current density needed to perform switching, j_{sw} in the nanopillars are similar for all elements, regardless of the value of H_{ext}. We can thus conclude that application of H_{ext} does not alter the switching for the majority of the structures. It is, however, remarkable that a small number of samples can be switched with applied H_{ext}, only. This supporting field then needs to be close to the switching field without additional spin transfer torque. In most cases, however, the values of j_{sw} are symmetric around 0 T. This indicates that the influence of stray fields originating from the polarizers is

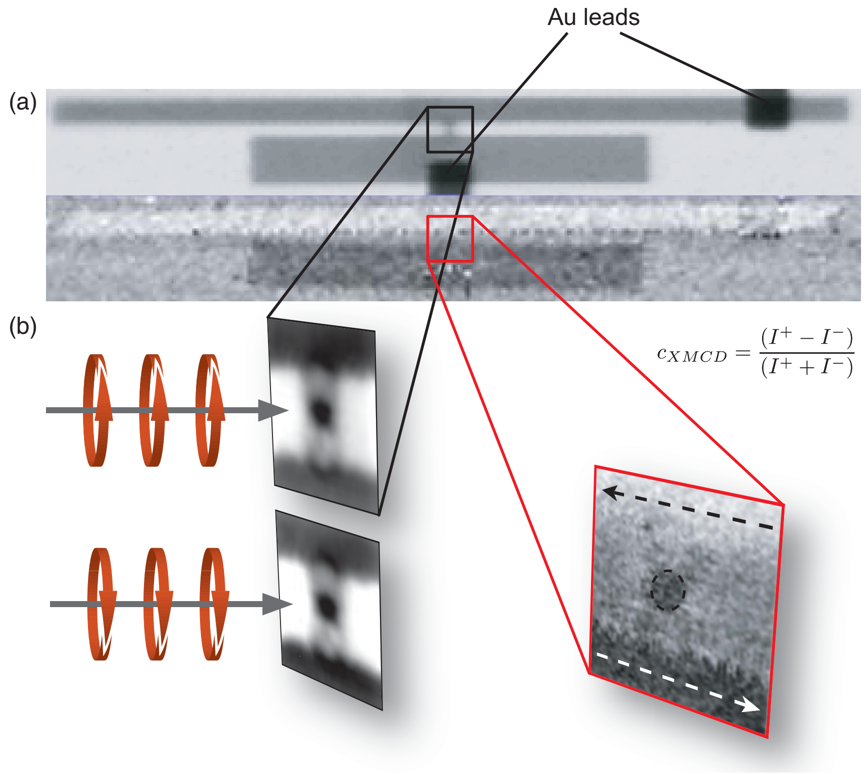

Figure 2 | (a) STXM image of the central area of the spin torque device including the two polarizers and the magnetic pillar in the center. The upper image shows the direct absorption contrast caused by the metallic layers. The images are recorded at the absorption maximum of Co, *i.e.* $E = 780$ eV. The lower image shows the contrast given by different absorption of the transmitted x-rays due to XMCD indicating the magnetization directions of the two polarizers. In our images black structures correspond to the magnetization pointing to the right side (positive values of H), and white structures to the magnetization pointing to the left side (negative H). This contrast is achieved by depicting the normalized intensity difference $c_{\mathrm{XMCD}} = \frac{I^+ - I^-}{I^+ + I^-}$ of the two images taken at different polarizations. (b) Zoom on the central pillar and construction of the magnetic contrast images. The central region containing the nanopillar (highlighted by the dashed circle) is scanned with circularly polarized x-rays. The contrast of spin-polarized regions depends on the polarization, thus subtraction of the images shows the magnetic contrast in the structure. It can be seen in (a) that the Au leads connecting the polarizers to the current pulser disappear in the magnetic contrast image.

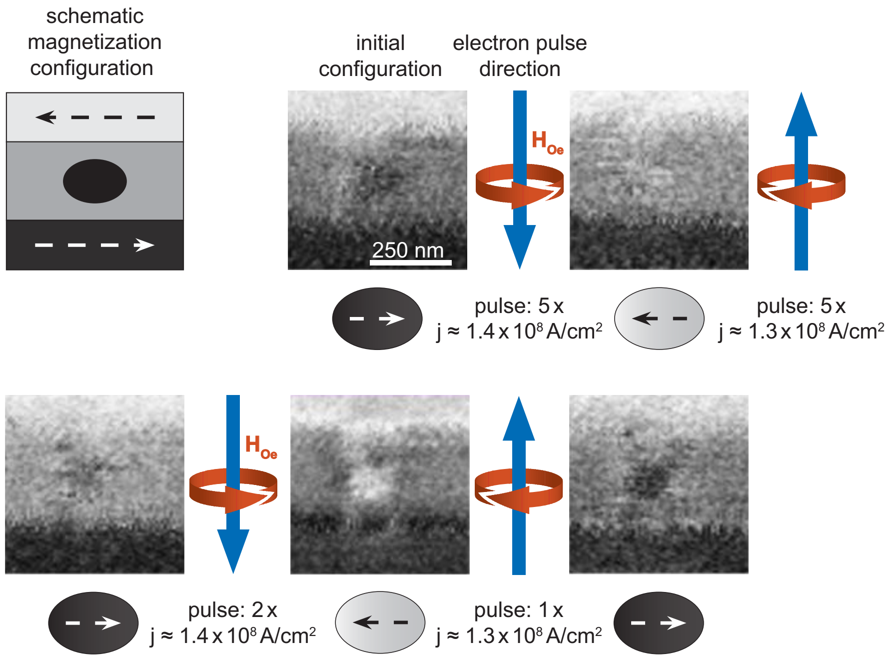

Figure 3 | **Switching of the pillar without supporting magnetic field.** It is shown that switching in both directions can be performed at identical absolute values of the current density using 5 and 2 consecutive pulses, as well as single pulses.

negligible in our geometry. As already mentioned, this statement is supported by micromagnetic simulations shown in the SI. A parallel arrangement of the magnetization of the polarizers leads to increased stray fields in the gap between the polarizers. We can induce switching in this configuration, as well, opposite to the direction favored by the stray fields, giving an additional hint for the fact that stray fields play a negligible role in our experiments.

An electrical current flowing through a nanowire is accompanied by a magnetic field, the so-called Oersted field indicated by the red arrows in figure 3. The direction and amplitude of this field for a wire of approximately 100 nm in diameter carrying a current of 4 mA can be estimated to be of the order $\mu_0 H \approx 8$ mT pointing in the plane of the pillar[15]. This field is of the order, but still below, the critical field needed for reversing the magnetization of the pillar. The direction of the Oersted field is pointing in the opposite direction of the spin torque in all switching events summarized in figure 3 and in the SI. We also performed experiments in which current pulses polarized in the initial magnetization direction of the pillar but with an Oersted field in the opposite direction were applied. In none of these experiments switching could be observed for the material composition discussed in this paper.

In order to estimate the thermal contribution to the magnetic switching of the pillar we need to estimate its magnetic energy. For an elliptical pillar with axes a and b we can calculate the demagnetization energies along the axes E_a and E_b, assuming a uniform magnetization along these axes[16]. For our geometry and a saturation magnetization $M_s = 1.9$ T/μ_0 we obtain a planar shape anisotropy energy $E_a - E_b = 2.5 \times 10^{-18}$ J. This energy is much larger than the thermal energy at temperatures, which are observed during the switching event (600 K, $k_B T = 8.2 \times 10^{-21}$ J). Therefore we can conclude that the nanopillars in the experiments are thermally stable even if the currents driven through the Cu wire lead to heating of the entire structure. In order to estimate the amount of heating, we have measured the resistance variation for an applied dc-current. As discussed in detail in the SI we can provide an upper boundary for the temperature of the wire $T_{\mathrm{wire}} < 600$ K. This value is far below the Curie temperature of the bulk Co ($T_{\mathrm{Curie}}(\mathrm{Co}) = 1400$ K), as well. The superparamagnetic limit for Co nanostructures, which exceed volumes of 1×10^{-15} m^3, lies above 1000 K, therefore bulk values for Curie temperature are relevant here. As even for elevated temperatures the ratio of thermal and anisotropy energy is $\ll 1$, thermal effects can be neglected as mechanism significantly supporting the magnetization switching in our case.

We now turn to the discussion, whether our results can be explained by pure spin transfer torque switching. The geometry shown in figure 1 is optimized for the experiments performed using STXM. Therefore, no electrical transport measurements through the nanopillar can be performed in order to obtain values for the spin diffusion length in the Cu stripe or the degree of spin polarization of the conduction electrons of the CoFe elements. Without experimental values for these quantities, an estimate of the spin current passing underneath the pillar during each current pulse cannot be achieved. We therefore have to limit our discussion to a qualitative comparison between our structure and the structure reported by Yang *et al.*[13]. In both structures, a Cu line connects two magnetic structures, one of which is used as a polarizer, the other one as a detector for the spin polarized current. Our data are recorded on pillars consisting of CoFe, while the nanostructures in[13] are made from permalloy. The distance between the pillar and the polarizer is 90 nm in our structures as opposed to 270 nm reported in[13] or 400 nm in[17]. This explains, why we are able to observe spin transfer torque in our structures at room temperature in a CIP configuration.

We have shown that elliptical nanopillars can be switched between their two preferred magnetic states by passing a spin-polarized current underneath the pillars, and we can image the different states before and after the switching using STXM. For our structures (elliptical pillars with dimensions of 100 nm × 120 nm) we can exclude all other switching sources as, for example stray fields, Oersted fields or heating. This study, therefore, provides an unambiguous demonstration of the switching by spin transfer torque (STT) in a current in plane (CIP) geometry and paves the way for future developments of such structures aiming at integration of these structures into fully planar device architectures. Furthermore, time-resolved studies of the dynamics of this switching mechanism will be possible in the future.

Methods

The devices were fabricated on Si_3N_4membranes with a thickness of 100 nm. The metallic multilayers were deposited by magnetron sputtering before patterning the nanostructures in order to ensure optimal layer quality and interface integrity. The layers consist of 2 nm Ta for adhesion, 5 nm Cu for the conduction of the spin-polarized electrons, 8 nm of $Co_{80}Fe_{20}$, and a Ru capping layer of 3 nm. By varying the Fe content of the CoFe layer we can adjust the magnetic softness of the pillar[18] and, thus, the coercive field needed to switch the magnetization. Addition of Fe to the stack reduces, however, the imaging contrast of our structure in the STXM experiments (see below).

The metallized membranes were subsequently structured using electron beam lithography and dry etching using both positive and negative lithography steps. The metallic layers are removed using argon ion beam etching. In a first step, the polarizers and their connection including the pillar are defined by removing the stack at all other areas of the sample. The following lithography step removes the CoFe layer on top of the Cu leaving Cu leads between the polarizers and the pillar in the center of the structure. The areas with uncovered Cu would oxidize when exposed to air and are, therefore, covered with SiO_2 *in situ*. A scanning electron micrograph of the sample after these fabrication steps is shown in figure 1. The final processing step provides electrical contacts to the polarizers. These contacts are made of Au and are fabricated in a lift-off process. The samples are contacted on a circuit board with high-frequency source-drain connections.

The switching of the magnetic state of the nanopillar is performed by driving a pulse of spin-polarized current underneath and through the pillar. In order to generate this current pulse we apply a voltage pulse across the structure, leading to a current passing the polarizers and the Cu connection under the pillar. Depending on the resistance ratio between the Cu connection and the CoFe pillar, a fraction of the current flows through the pillar directly, as well. For the geometry and material composition in our experiment, we estimate that a fraction of 1/5 flows through the pillar leading to additional spin accumulation in the pillar. The different aspect ratios of the polarizers (shown in figure 1) lead to different coercive fields[19]; the magnetization points along the long axis of the polarizers and parallel to the surface of the sample. As a consequence the polarizers can be set in either one of the two available states with magnetization pointing to the left or to the right (see figure 1 for details) and in an antiparallel configuration, as well. The magnetization of the polarizers defines the majority charge carriers injected into the Cu lead connecting the two polarizers. Therefore we have the possibility to pass a spin-polarized current through the Cu connector, which is polarized in either one of the two directions, left or right. When the magnetization of the pillar at the center of the structure is antiparallel to the polarization of the current, spin transfer torque (STT)[20] acts on the spins in the pillar because of spin diffusion through the Cu/CoFe interface. The goal of our experiments is twofold: to demonstrate that STT is strong enough to switch the direction of magnetization of the pillar at nondestructive current levels, and to image the magnetic state of the pillar before and after switching.

In order to characterize the magnetic state of our structures, we perform magnetic imaging in a scanning transmission x-ray microscope (STXM) at the swiss light source (SLS) beamline X07DA (Pollux). Using circularly polarized x-rays we image the spin density of the unoccupied d-band exploiting the effect of x-ray magnetic circular dichroism (XMCD)[21] effect. The x-rays are focused by passing through a zone-plate with minimal structure sizes of 15 nm. This setup allows a resolution of structure sizes down to about 30 nm in the images for normal experimental conditions. Typical dimensions of the magnetic pillars in our experiments are 100 nm × 120 nm. We can, therefore, image the magnetization of individual pillars with high quality. The samples are mounted on the scanning stage of the beamline together with a metal-cored coil providing a static magnetic field parallel to the magnetization direction of the polarizers. This external field is used to define the magnetization of the polarizers and, in some of the experiments, as a supporting field aiding the switching of the pillar.

We perform measurements of the magnetic behavior of the pillar and the polarizers by changing the static magnetic field H_{ext} step by step and recording STXM images at each value of H_{ext}. A STXM overview of the whole configuration in antiparallel alignment can be seen in figure 2. Here, the magnetization of the pillar in the center always points parallel to one and anti-parallel to the other of the two polarizers. Thus, passing a current underneath the device in one direction can switch the magnetization of the pillar. Driving the current in the opposite direction provides spin polarization in the direction of the magnetization of the pillar at the interface and, therefore, does not lead to changes in the magnetization. Switching without a supporting magnetic field can be performed in both directions by varying the direction of the current as long as the magnetization directions of the polarizers do not change.

We would like to thank Alina Deac, Jürgen Lindner, Sibylle Gemming, and Kay Potzger for fruitful discussions, Kerstin Bernert, Gabi Steinbach, Julia Osten, and Tom Henschel for help during the experiments, and Patrick Matthes and Manfred Albrecht for sample preparation. This work was in part supported by BMBF.

1. Binasch, G., Grunberg, P., Saurenbach, F. & Zinn, W. Enhanced Magnetoresistance in Layered Magnetic-Structures with Antiferromagnetic Interlayer Exchange. *Phys. Rev. B* **39**, 4828 (1989).
2. Baibich, M. N. *et al.* Giant Magnetoresistance of (001)Fe/(001) Cr Magnetic Superlattices. *Phys. Rev. Lett.* **61**, 2472 (1988).
3. Moodera, J. S., Kinder, L. R., Wong, T. M. & Meservey, R. Large Magnetoresistance at Room-Temperature in Ferromagnetic Thin-Film Tunnel-Junctions. *Phys. Rev. Lett.* **74**, 3273 (1995).
4. Julliere, M. Tunneling Between Ferromagnetic-Films. *Phys. Lett. A* **54**, 225 (1975).
5. Sinova, J. & Zutic, I. New moves of the spintronics tango. *Nature Mat.* **11**, 368 (2012).
6. Slonczewski, J. C. Current-driven excitation of magnetic multilayers. *J. Magn. Magn. Mater.* **159**, L1 (1996).
7. Berger, L. Emission of spin waves by a magnetic multilayer traversed by a current. *Phys. Rev. B* **54**, 9353 (1996).
8. Acremann, Y. *et al.* Time-Resolved Imaging of Spin Transfer Switching: Beyond the Macrospin Concept. *Phys. Rev. Lett.* **96**, 217202 (2006).
9. Strachan, J. *et al.* Direct Observation of Spin-Torque Driven Magnetization Reversal through Nonuniform Modes. *Phys. Rev. Lett.* **100**, 247201 (2008).
10. Bernstein, D. *et al.* Nonuniform switching of the perpendicular magnetization in a spin-torque-driven magnetic nanopillar. *Phys. Rev. B* **83**, 180410 (2011).
11. Ji, Y., Hoffmann, A., Pearson, J. E. & Bader, S. B. Enhanced spin injection polarization in Co/Cu/Co nonlocal lateral spin valves. *Appl. Phys. Lett.* **88**, 1 (2006).
12. Wessely, O., Umerski, A. & Mathon, J. Theory of spin-transfer torque in the current-in-plane geometries. *Phys. Rev. B* **80**, 014419 (2009).
13. Yang, T., Kimura, T. & Otani, Y. Giant spin-accumulation signal and pure spin-current-induced reversible magnetization switching. *Nature Phys.* **4**, 851 (2008).
14. Raabe, J. *et al.* PolLux: A new facility for soft x-ray spectromicroscopy at the Swiss Light Source. *Rev. sci. instr.* **79**, 113704 (2008).
15. Moon, K. W., Lee, J. C., Rhie, K., Shin, K. H. & Choe, S. B. Detection of Local Oersted Field Generated at the Junction Between Ferromagnetic Nanowire and Electrode. *IEEE Trans. Magn.* **47**, 2508 (2011).
16. Beleggia, M., De Graef, M., Millev, Y. T., Goode, D. A. & Rowlands, G. Demagnetization factors for elliptic cylinders. *J. Phys. D-Appl. Phys.* **38**, 3333 (2005).
17. Kimura, T., Otani, Y. & Hamrle, J. Switching magnetization of a nanoscale ferromagnetic particle using nonlocal spin injection. *Phys. Rev. Lett.* **96**, 037201 (2005).
18. Wang, S. X., Sun, N. X., Yamaguchi, M. & Yabukami, S. Sandwich films - Properties of a new soft magnetic material. *Nature* **407**, 150 (2000).
19. Meiklejohn, W. H. & Bean, C. P. New magnetic anisotropy. *Phys. Rev.* **105**, 904 (1957).
20. Zutic, I., Fabian, J. & Sarma, S. Spintronics: Fundamentals and applications. *Rev. Mod. Phys.* **76**, 323 (2004).
21. Schutz, G. *et al.* Absorption of circularly polarized x-rays in iron. *Phys. Rev. Lett.* **58**, 737 (1987).

Author contributions

M.B. and J.G. carried out the device fabrication. M.B., A.E., J.G., S.W. and J.R. performed the STXM experiments. A.E., M.B., S.W. and J.G. interpreted the data. J.F. and A.E. designed the experiment, M.B. and J.G. prepared the figures. All authors discussed the results and contributed to the manuscript preparation.

Additional information

Supplementary information accompanies this paper at http://www.nature.com/scientificreports

Competing financial interests: The authors declare no competing financial interests.

How to cite this article: Buhl, M. *et al.* Lateral spin transfer torque induced magnetic switching at room temperature demonstrated by x-ray microscopy. *Sci. Rep.* **3**, 2945; DOI:10.1038/srep02945 (2013).

Statistics

Image: S. Münster / 3DKosmos.de

Publications and patents

Books and chapters

1. Schmidt, B.; Wetzig, K.
   Ion beams in materials processing and analysis
   Springer, 2013
2. Bischoff, L.; Böttger, R.; Philipp, P.; Schmidt, B.
   Nanostructures by mass-separated FIB
   In: Wang, Z. (Ed.): FIB Nanostructures, Series: Lecture Notes in Nanoscale Science and Technology, Volume 20, Springer, 2013, 465-525

Publications in journals

Magnetism

1. Buhl, M.; Erbe, A.; Grebing, J.; Wintz, S.; Raabe, J.; Fassbender, J.
   Lateral spin transfer torque induced magnetic switching at room temperature demonstrated by x-ray microscopy.
   *Scientific Reports **3**, 2945 (2013)*
2. Fowley, C.; Diao, Z.; Faulkner, C. C.; Kally, J.; Ackland, K.; Behan, G.; Zhang, H. Z.; Coey, J. M. D.
   Local modification of magnetic anisotropy and ion milling of Co/Pt multilayers using a He^+ ion beam microscope
   *Journal of Physics D: Applied Physics **46**, 195501 (2013)*
3. Körner, M.; Lenz, K.; Gallardo, R. A.; Fritzsche, M.; Mücklich, A.; Facsko, S.; Lindner, J.; Landeros, P.; Fassbender, J.
   Two-magnon scattering in permalloy thin films due to rippled substrates
   *Physical Review B **88**, 054405 (2013)*
4. Liedke, M. O.; Körner, M.; Lenz, K.; Fritzsche, M.; Ranjan, M.; Keller, A.; Cizmár, E.; Zvyagin, S.; Facsko, S.; Potzger, K.; Lindner, J.; Fassbender, J.
   Crossover in the surface anisotropy contributions of ferromagnetic films on rippled Si surfaces
   *Physical Review B **87**, 024424 (2013)*
5. McCord, J.; Erkartal, B.; von Hofe, T.; Kienle, L.; Quandt, E.; Grenzer, J.; Roshchupkina, O.
   Revisiting magnetic stripe domains - anisotropy gradient and stripe asymmetry
   *Journal of Applied Physics **113**, 073903 (2013)*
6. Obry, B.; Meyer, T.; Pirro, P.; Brächer, T.; Lägel, B.; Neb, R.; Osten, J.; Strache, T.; Fassbender, J.; Hillebrands, B.
   Microscopic magnetic structuring of a spin-wave waveguides by ion implantation in a $Ni_{81}Fe_{19}$ layer
   *Applied Physics Letters **102**, 022409 (2013)*
7. Obry, B.; Pirro, P.; Braecher, T.; Chumak, Andrii V.; Osten, J.; Ciubotaru, F.; Serga, Alexander A.; Fassbender, J.; Hillebrands, B.
   A micro-structured ion-implanted magnonic crystal
   *Applied Physics Letters **102**, 202403 (2013)*
8. Wintz, S.; Bunce, C.; Neudert, A.; Körner, M.; Strache, T.; Buhl, M.; Erbe, A.; Gemming, S.; Raabe, J.; Quitmann, C.; Fassbender, J.
   Topology and origin of effective spin meron pairs in ferromagnetic multilayer elements
   *Physical Review Letters **110**, 177201 (2013)*

Nanoscience and materials for information technologies

9. Abendroth, B.; Moebus, T.; Rentrop, S.; Strohmeyer, R.; Vinnichenko, M.; Weling, T.; Stocker, H.; Meyer, D. C.
Atomic layer deposition of TiO_2 from tetrakis(dimethylamino) titanium and H_2O
*Thin Solid Films **545**, 176 (2013)*

10. Anders, C.; Heinig, K.-H.; Urbassek, H.
Polyatomic bismuth impacts into germanium: Molecular dynamics study
*Physical Review B **87**, 245434 (2013)*

11. Böttger, R.; Heinig, K.-H.; Bischoff, L.; Liedke, B.; Facsko, S.
From holes to sponge at irradiated Ge surfaces with increasing ion energy - An effect of defect kinetics?
*Applied Physics A **113**, 53 (2013)*

12. Böttger, R.; Heinig, K.-H.; Bischoff, L.; Liedke, B.; Hübner, R.; Pilz, W.
Silicon nanodot formation and self-ordering under bombardment with heavy Bi_3 ions
*Physica Status Solidi (RRL) **7**, 501 (2013)*

13. Böttger, R.; Keller, A.; Bischoff, L.; Facsko, S.
Mapping the local elastic properties of nanostructured germanium surfaces: From nanoporous sponges to self-organized nanodots
*Nanotechnology **24**, 115702 (2013)*

14. Drachenko, O.; Kozlov, D.; Ikonnikov, A. V.; Spirin, K. E.; Gavrilenko, V.; Schneider, H.; Helm, M.; Wosnitza, J.
Long spin relaxation time of holes in InGaAs/GaAs quantum wells probed by cyclotron resonance spectroscopy
*Physical Review B **87**, 075315 (2013)*

15. Erbe, A.; Wiesenhütter, U.; Grebing, J.; Fassbender, J.
Contacting metallic nanoparticles on transparent substrates
*Physica Status Solidi (A) **210**, 1311 (2013)*

16. Fiedler, J.; Heera, V.; Voelskow, M.; Mücklich, A.; Reuther, H.; Skorupa, W.; Gobsch, G.; Helm, M.
Superconducting layers by gallium implantation and short-term annealing in semiconductors
*Acta Physica Polonica A **123**, 916 (2013)*

17. Fischer, T.; Pronin, A. V.; Skrotzki, R.; Herrmannsdörfer, T.; Wosnitza, J.; Fiedler, J.; Heera, V.; Helm, M.; Schachinger, E.
Optical study of superconducting Ga-rich layers in silicon
*Physical Review B **87**, 014502 (2013)*

18. Gao, K.; Prucnal, S.; Mücklich, A.; Skorupa, W.; Zhou, S.
Fabrication of $Si_{1-x}Ge_x$ alloy on silicon by Ge-ion-implantation and short-time-annealing
*Acta Physica Polonica A **123**, 858 (2013)*

19. Gao, K.; Prucnal, S.; Skorupa, W.; Helm, M.; Zhou, S.
Origin and enhancement of the 1.3 µm luminescence from GaAs treated by ion-implantation and flash lamp annealing
*Journal of Applied Physics **114**, 093511 (2013)*

20. Hanzig, J.; Zschornak, M.; Hanzig, F.; Mehner, E.; Stöcker, H.; Abendroth, B.; Röder, C.; Talkenberger, A.; Schreiber, G.; Rafaja, D.; Gemming, S.; Meyer, D. C.
Migration-induced field-stabilized polar phase in strontium titanate single crystals at room temperature
*Physical Review B **88**, 024104 (2013)*

21. Heera, V.; Fiedler, J.; Hübner, R.; Schmidt, B.; Voelskow, M.; Skorupa, W.; Skrotzki, R.; Herrmannsdörfer, T.; Wosnitza, J.; Helm, M.
Silicon films with gallium rich nanograins - from superconductor to insulator
*New Journal of Physics **15**, 083022 (2013)*

22. Kaspar, T.; Fiedler, J.; Skorupa, I.; Bürger, D.; Mücklich, A.; Fritzsche, M.; Schmidt, O. G.; Schmidt, H.
Persistent current reduction in metal-semiconductor FETs with a ZnCoO channel in an external magnetic field
*IEEE Electron Device Letters **34**, 1271 (2013)*

23. Keller, A.; Kopyra, J.; Gothelf, K.; Bald, I.
Electron-induced damage of biotin studied in the gas phase and in the condensed phase at a single-molecule level
*New Journal of Physics **15**, 083045 (2013)*

24. Lehmann, J.; Hübner, R.; Skorupa, W.; von Borany, J.; Mikolajick, T.; Schäfer, A.; Schubert, J.; Mantl, S.
Millisecond flash lamp annealing for $LaLuO_3$ and $LaScO_3$ high-k dielectrics
*Microelectronic Engineering **109**, 381 (2013)*

25. Liu, S. P.; Artois, J.; Schmid, D.; Wieser, M.; Bornemann, B.; Weisbrod, S.; Marx, A.; Scheer, E.; Erbe, A.
Electronic transport through short dsDNA measured with mechanically controlled break junctions: New thiol–gold binding protocol improves conductance
*Physica Status Solidi (B) **250**, 2342 (2013)*

26. Luo, W. B.; Jing, J.; Shuai, Y.; Zhu, J.; Zhang, W. L.; Zhou, S.; Gemming, S.; Du, N.; Schmidt, H.
Epitaxial growth of $SrTiO_3$ (0 0 1) films on multilayer buffered GaN (0 0 0 2) by pulsed laser deposition
*Journal of Physics D: Applied Physics **46**, 065307 (2013)*

27. Luo, W.; Zhu, J.; Shuai, Y.; Zhang, W.; Zhang, Y.; Zhou, S.; Gemming, S.; Schmidt, H.
Effects of the TiO_2 buffer thickness on $SrTiO_3$ (111) epitaxial films grown on GaN (0002)
*Journal of Applied Physics **113**, 154103 (2013)*

28. Mittendorff, M.; Winnerl, S.; Kamann, J.; Eroms, J.; Weiss, D.; Schneider, H.; Helm, M.
Ultrafast graphene-based broadband THz detector
*Applied Physics Letters **103**, 021113 (2013)*

29. Mittendorff, M.; Xu, M.; Dietz, R. J. B.; Künzel, H.; Sartorius, B.; Schneider, H.; Helm, M.; Winnerl, S.
Large area photoconductive THz emitter for 1.55 µm excitation based on an InGaAs heterostructure
*Nanotechnology **24**, 214007 (2013)*

30. Ou, X.; Keller, A.; Helm, M.; Fassbender, J.; Facsko, S.
Reverse epitaxy of Ge: Ordered and faceted surface patterns
*Physical Review Letters **111**, 016101 (2013)*

31. Ou, X.; Shuai, Y.; Luo, W.; Siles, P. F.; Kögler, R.; Fiedler, J.; Reuther, H.; Zhou, S.; Hübner, R.; Facsko, S.; Helm, M.; Mikolajick, T.; Schmidt, O. G.; Schmidt, H.
Forming-free resistive switching in multiferroic $BiFeO_3$ thin films with enhanced nanoscale shunts
*ACS Applied Materials and Interfaces **5**, 12764 (2013)*

32. Posselt, M.
Importance of configurational contributions to the free energy of nanoclusters
*AIP Advances **3**, 072137 (2013)*

33. Prucnal, S.; Liedke, M. O.; Zhou, Shengqiang.; Voelskow, M.; Mücklich, A.; Turek, M.; Zuk, J.; Skorupa, W.
Conductivity type and crystal orientation of GaAs nanocrystals fabricated in silicon by ion implantation and flash lamp annealing
*Nuclear Instruments and Methods in Physics Research B **312**, 104 (2013)*

34. Prucnal, S.; Rebohle, L.; Sun, J. M.; Skorupa, W.; Drozdziel, A.; Pyszniak, K.; Turek, M.; Zuk, J.
Sensitization of the blue-green electroluminescence by gadolinium coupled to Si nanocluster embedded in a SiO_2 matrix
*Materials Science - Medziagotyra **19**, 125 (2013)*

35. Prucnal, S.; Turek, M.; Gao, K.; Zhou, S.; Pyszniak, K.; Drozdziel, A.; Zuk, J.; Skorupa, W.
    III-V quantum dots in dielectrics made by ion implantation and flash lamp annealing
    *Acta Physica Polonica A **123**, 935 (2013)*

36. Ranjan, M.; Facsko, S.; Fritzsche, M.; Mukherjee, S.
    Plasmon resonance tuning in Ag nanoparticles arrays grown on ripple patterned templates
    *Microelectronic Engineering **102**, 44 (2013)*

37. Rice, W. D.; Kono, J.; Zybell, S.; Winnerl, S.; Bhattacharyya, J.; Schneider, H.; Helm, M.; Ewers, B.; Chernikov, A.; Chatterjee, S.; Khitrova, G.; Gibbs, Hyatt M.; Schneebeli, L.; Breddermann, B.; Kira, M.; Koch, S.
    Observation of forbidden exciton transitions mediated by Coulomb interactions in photoexcited semiconductor quantum wells
    *Physical Review Letters **110**, 137404 (2013)*

38. Ritter, R.; Wilhelm, R. A.; Stöger-Pollach, M.; Heller, R.; Mücklich, A.; Werner, U.; Vieker, H.; Beyer, A.; Facsko, S.; Gölzhäuser, A.; Aumayr, F.
    Fabrication of nanopores in 1 nm thick carbon nanomembranes with slow highly charged ions
    *Applied Physics Letters **102**, 063112 (2013)*

39. Shuai, Y.; Ou, X.; Luo, W.; Du, N.; Wu, C.; Zhang, W.; Bürger, D.; Mayr, C.; Schüffny, R.; Zhou, S.; Helm, M.; Schmidt, H.
    Nonvolatile multilevel resistive switching in Ar^+ irradiated $BiFeO_3$ thin films
    *IEEE Electron Device Letters **34**, 54 (2013)*

40. Shuai, Y.; Ou, X.; Luo, W.; Mücklich, A.; Bürger, D.; Zhou, S.; Wu, C.; Chen, Y.; Zhang, W.; Helm, M.; Mikolajick, T.; Schmidt, O.; Schmidt, H.
    Key concepts behind forming-free resistive switching incorporated with rectifying transport properties
    *Scientific Reports **3**, 2208 (2013)*

41. Steinbach, G.; Schreiber, M.; Gemming, S.
    DFT investigation of the heterostructure GaP (001) on Si (001)
    *Nanoscience and Nanotechnology Letters **5**, 73 (2013)*

42. Teich, M.; Stephan, D. R.; Winnerl, S.; Schneider, H.; Wilson, L. R.; Helm, M.
    Intersublevel dephasing in InAs/GaAs quantum dots below the Reststrahlen band
    *Applied Physics Letters **103**, 252110 (2013)*

43. Teich, M.; Wagner, M.; Schneider, H.; Helm, M.
    Semiconductor quantum well excitons in strong, narrowband terahertz fields
    *New Journal of Physics **15**, 065007 (2013)*

44. Winnerl, S.; Göttfert, F.; Mittendorff, M.; Schneider, H.; Helm, M.; Winzer, T.; Malic, E.; Knorr, A.; Orlita, M.; Potemski, M.; Sprinkle, M.; Berger, C.; de Heer, W. A.
    Time-resolved spectroscopy on epitaxial graphene in the infrared spectral range: Relaxation dynamics and saturation behavior
    *Journal of Physics: Condensed Matter **25**, 054202 (2013)*

45. Xu, M.; Mittendorff, M.; Dietz, R.; Künzel, H.; Sartorius, B.; Göbel, T.; Schneider, H.; Helm, M.; Winnerl, S.
    Terahertz generation and detection with InGaAs-based large-area photoconductive devices excited at 1.55 µm
    *Applied Physics Letters **103**, 251114 (2013)*

Materials for energy and transport technologies

46. Ballesteros, A.; Altstadt, E.
    RPV long term operation: Open issues
    *Strength of Materials **45**, 392 (2013)*

47. Bergner, F.; Pareige, C.; Kuksenko, V.; Malerba, L.; Pareige, P.; Ulbricht, A.; Wagner, A.
    Critical assessment of Cr-rich precipitates in neutron-irradiated Fe–12 at%Cr: Comparison

of SANS and APT
Journal of Nuclear Materials ***442****, 463 (2013)*

48. Donchev, A.; Schütze, M.; Kolitsch, A.; Yankov, R.
Economic surface treatment of Ti-alloys to improve their resistance against environmental high temperature attack
Key Engineering Materials ***551****, 109 (2013)*

49. Friedrich, D.; Schmidt, B.; Heinig, K. H.; Liedke, B.; Mücklich, A.; Hübner, R.; Wolf, D.; Kölling, S.; Mikolajick, T.
Sponge-like Si-SiO$_2$ nanocomposite – morphology studies of spinodally decomposed silicon-rich oxide
Applied Physics Letters ***103****, 131911 (2013)*

50. Gago, R.; Soldera, F.; Hübner, R.; Lehmann, J.; Munnik, F.; Vázquez, L.; Redondo-Cubero, A.; Endrino, J. L.
X-ray absorption near-edge structure of hexagonal ternary phases in sputter-deposited TiAlN films
Journal of Alloys and Compounds ***561****, 87 (2013)*

51. Gundogdu, S.; Sungur Ozen, E.; Hübner, R.; Heinig, K.-H.; Aydinli, A.
Laser induced sponge-like Si in Si-rich oxides for photovoltaics
Optics Express ***21****, 24368 (2013)*

52. Hinsche, N. F.; Mertig, I.; Zahn, P.
Lorenz function of Bi$_2$Te$_3$/Sb$_2$Te$_3$ superlattices
Journal of Electronic Materials ***42****, 1406 (2013)*

53. Keles, U.; Liedke, B.; Heinig, K.-H.; Bulutay, C.
Networks of silicon nanowires: A large-scale atomistic electronic structure analysis
Applied Physics Letters ***103****, 203103 (2013)*

54. Krause, M.; Mücklich, A.; Wilde, C.; Vinnichenko, M.; Gemming, S.; Abrasonis, G.
Structure, optical and mechanical properties of direct current magnetron sputtered carbon: Vanadium nanocomposite thin films
Nanoscience and Nanotechnology Letters ***5****, 94 (2013)*

55. Kunze, T.; Posselt, M.; Gemming, S.; Konicek, A. R.; Carpick, R. W.; Pastewka, L.; Moseler, M.
Wear, plasticity, and rehybridization in tetrahedral amorphous carbon
Tribology Letters ***53****, 119 (2014)*

56. Liedke, B.; Heinig, K.-H.; Mücklich, A.; Schmidt, B.
Formation and coarsening of sponge-like Si-SiO$_2$ nanocomposites
Applied Physics Letters ***103****, 133106 (2013)*

57. Neubert, M.; Cornelius, S.; Fiedler, J.; Gebel, T.; Liepack, H.; Kolitsch, A.; Vinnichenko, M.
Overcoming challenges to the formation of high-quality polycrystalline TiO$_2$:Ta transparent conducting films by magnetron sputtering
Journal of Applied Physics ***114****, 083707 (2013)*

58. Terentyev, D.; Bergner, F.; Osetsky, Y.
Cr segregation on dislocation loops enhances hardening in ferritic Fe−Cr alloys
Acta Materialia ***61****, 1444 (2013)*

59. Wagner, A.; Bergner, F.; Ulbricht, A.; Dewhurst, C. D.
Small-angle neutron scattering of low-Cu RPV steels neutron-irradiated at 255°C and post-irradiation annealed at 290°C
Journal of Nuclear Materials ***441****, 487 (2013)*

Other topics and external users of ion beam center and free-electron laser

60. Akhmadaliev, S.; Heller, R.; Hanf, D.; Rugel, G.; Merchel, S.
The new 6 MV AMS-facility DREAMS at Dresden
Nuclear Instruments and Methods in Physics Research B ***294****, 5 (2013)*

61. Anwand, W.; Butterling, M.; Johnson, J. M.; Reuther, H.; Wagner, A.; Skorupa, W.; Brauer, G.
Flash lamp annealing of tungsten surfaces marks a new way to optimized slow positron yields
*Journal of Physics: Conference Series **443**, 012072 (2013)*

62. Arnold, M.; Aumaître, G.; Bourlès, D. L.; Keddadouche, K.; Braucher, R.; Finkel, R. C.; Nottoli, E.; Benedetti, L.; Merchel, S.
The French accelerator mass spectrometry facility ASTER after 4 years: Status and recent developments on ^{36}Cl and ^{129}I
*Nuclear Instruments and Methods in Physics Research B **294**, 24 (2013)*

63. Baraban, L.; Makarov, D.; Schmidt, O.; Cuniberti, G.; Leiderer, P.; Erbe, A.
Control over Janus micromotors by the strength of a magnetic field
*Nanoscale **5**, 1332 (2013)*

64. Beck, M.; Rousseau, I.; Klammer, M.; Leiderer, P.; Mittendorff, M.; Winnerl, S.; Helm, M.; Gol’tsman, G. N.; Demsar, J.
Transient increase of the energy gap in superconducting NbN thin films excited by resonant narrow-band terahertz pulses
*Physical Review Letters **110**, 267003 (2013)*

65. Berencen, Y.; Wutzler, R.; Rebohle, L.; Hiller, D.; Ramirez, J. M.; Rodriguez, J. A.; Skorupa, W.; Garrido, B.
Intense green-yellow electroluminescence from Tb^{+}-implanted silicon-rich silicon nitride/oxide light emitting devices
*Applied Physics Letters **103**, 111102 (2013)*

66. Beyer, R.; Burghardt, H.; von Borany, J.
Germanium nanocrystals in SiO_2: Relevance of the defect state distribution at the Si-SiO_2 interface
*Physica Status Solidi (C) **10**, 607 (2013)*

67. Böttge, C. N.; Breddermann, B.; Schneebeli, L.; Kira, M.; Koch, S. W.; Bhattacharyya, J.; Schneider, H.; Helm, M.
Terahertz-induced effects on excitons in magnetic field
*Physica Status Solidi (C) **10**, 1218 (2013)*

68. Braucher, R.; Bourlès, D.; Merchel, S.; Vidal Romani, J.; Fernadez-Mosquera, D.; Marti, K.; Leanni, L.; Chauvet, F.; Arnold, M.; Aumaître, G.; Keddadouche, K.
Determination of muon attenuation lengths in depth profiles from *in situ* produced cosmogenic nuclides
*Nuclear Instruments and Methods in Physics Research B **294**, 484 (2013)*

69. Braz Fernandes, F. M.; Mahesh, K. K.; Martins, R. M. S.; Silva, R. J. C.; Baehtz, C.; von Borany, J.
Simultaneous probing of phase transformations in Ni-Ti thin film shape memory alloy by synchrotron radiation-based X-ray diffraction and electrical resistivity
*Materials Characterization **76**, 35 (2013)*

70. Bugoi, R.; Constantinescu, B.; Popescu, A. D.; Munnik, F.
Archaeometallurgical studies of bronze age objects from the Romanian cultural heritage
*Romanian Reports in Physics **65**, 1234 (2013)*

71. Bugoi, R.; Poll, I.; Manucu-Adamesteanu, G.; Neelmeijer, C.; Eder, F.
Investigations of Byzantine glass bracelets from Nufaru, Romania using external PIXE-PIGE methods
*Journal of Archaeological Science **40**, 2881 (2013)*

72. Buljan, M.; Radić, N.; Ivanda, M.; Bogdanović-Radović, I.; Karlušić, M.; Grenzer, J.; Prucnal, S.; Dražić, G.; Pletikapić, G.; Svetličić, V.; Jerčinović, M.; Bernstorff, S.; Holy, V.
Ge quantum dot lattices in Al_2O_3: A material with excellent mechanical and size-tuneable optical properties
*Journal of Nanoparticle Research **15**, 1485 (2013)*

73. Buljan, M.; Roshchupkina, O.; Santic, A.; Holy, V.; Baehtz, C.; Mücklich, A.; Horak, L.; Vales, V.; Radic, N.; Bernstorff, S.; Grenzer, J.
Growth of a three-dimensional anisotropic lattice of Ge quantum dots in an amorphous

alumina matrix
Journal of Applied Crystallography ***46****, 709 (2013)*

74. Butterling, M.; Anwand, W.; Cornelius, S.; Potzger, K.; Smekhova, A.; Vinnichenko, M.; Wagner, A.
Optimization of growth parameters of TiO_2 thin films using a slow positron beam
Journal of Physics: Conference Series ***443****, 012073 (2013)*

75. Christiansen, T. L.; Drouet, M.; Martinaviciusc, A.; Somers, M. A. J.
Isotope exchange investigation of nitrogen redistribution in expanded austenite
Scripta Materialia ***69****, 582 (2013)*

76. Cizek, J.; Melikhova, O.; Vlcek, M.; Lukac, F.; Vlach, M.; Prochazka, I.; Anwand, W.; Brauer, G.; Mücklich, A.; Wagner, S.; Uchida, H.; Pundt, A.
Hydrogen-induced microstructural changes of Pd films
International Journal of Hydrogen Energy ***38****, 12115 (2013)*

77. Dekov, V. M.; Rouxel, O.; Asael, D.; Hålenius, U.; Munnik, F.
Native Cu from the oceanic crust: Isotopic insights into native metal origin
Chemical Geology ***359****, 136 (2013)*

78. Dienst, A.; Casandruc, E.; Zhang, L.; Eckstein, M.; Fausti, D.; Hoffmann, M.; Khanna, V.; Dean, N.; Gensch, M.; Winnerl, S.; Seidel, W.; Pyon, S.; Takayama, T.; Takagi, H.; Cavalleri, A.
Optical excitation of Josephson plasma solitons in a cuprate supercondutor
Nature Materials ***12****, 535 (2013)*

79. Du, N.; Shuai, Y.; Luo, W.; Mayr, C.; Schueffny, R.; Schmidt, O. G.; Schmidt, H.
Practical guide for validated memristance measurements
Review of Scientific Instruments ***84****, 023903 (2013)*

80. Dubiel, S. M.; Cieslak, J.; Reuther, H.
Mössbauer-spectroscopic study of the effect of He^+ irradiation on model Fe−Cr alloys
Nuclear Instruments and Methods in Physics Research B ***302****, 48 (2013)*

81. Dubiel, S. M.; Cieslak, J.; Reuther, H.
Effect of He^+ irradiation on Fe−Cr alloys: Mössbauer-effect study
Journal of Nuclear Materials ***434****, 235 (2013)*

82. Dupuy, J. C.; Prudon, G.; Dubois, C.; Kögler, R.; Akhmadaliev, S.; Perrat-Mabilon, A.
Self-consistent isotopic comparative method used to determine dependence of secondary-yields on oxygen concentration in Si-O system up to 33%
Surface and Interface Analysis ***45****, 369 (2013)*

83. Eder, F. M.; Neelmeijer, C.; Pearce, N. J. G.; Bichler, M.; Sterba, J. H.; Ntaflos, T.; Merchel, S.
Volcanic glass under fire − A comparison of three complementary analytical methods
X-Ray Spectrometry ***42****, 412 (2013)*

84. El-Said, A. S.; Wilhelm, R. A.; Facsko, S.; Trautmann, C.
Surface nanostructuring of $LiNbO_3$ by high-density electronic excitations
Nuclear Instruments and Methods in Physics Research B ***315****, 265 (2013)*

85. El-Said, A. S.; Wilhelm, R. A.; Heller, R.; Akhmadaliev, Sh.; Facsko, S.
Creation of surface nanostructures on Al_2O_3 by slow highly charged ions
Nuclear Instruments and Methods in Physics Research B ***317****, 170 (2013)*

86. Feige, J.; Wallner, A.; Fifield, L. K.; Korschinek, G.; Merchel, S.; Rugel, G.; Steier, P.; Winkler, S. R.
AMS measurements of cosmogenic and supernova-ejected radionuclides in deep-sea sediment cores
European Physical Journal Web of Conferences ***63****, 03003 (2013)*

87. Finkel, R. C.; Arnold, M.; Aumaître, G.; Benedetti, L.; Bourlès, D. L.; Keddadouche, K.; Merchel, S.
Improved ^{36}Cl performance at the ASTER HVE 5 MV accelerator mass spectrometer national facility
Nuclear Instruments and Methods in Physics Research B ***294****, 121 (2013)*

88. Gago, R.; Vazquez, L.; Agullo-Rueda, F.; Vinnichenko, M.; Carcelen, V.; Olvera, J.; Plaza, J. L.; Dieguez, E.
Self-organized surface nanopatterns on Cd(Zn)Te crystals induced by medium-energy ion beam sputtering
*Journal of Physics D: Applied Physics **46**, 455302 (2013)*

89. Hampe, D.; Gleisberg, B.; Akhmadaliev, S.; Rugel, G.; Merchel, S.
Determination of ^{41}Ca with LSC and AMS: Method development, modifications and applications
*Journal of Radioanalytical and Nuclear Chemistry **296**, 617 (2013)*

90. Hassdenteufel, A.; Hebler, B.; Schubert, C.; Liebig, A.; Teich, M.; Helm, M.; Aeschlimann, M.; Albrecht, M.; Bratschitsch, R.
Thermally assisted all-optical helicity dependent magnetic switching in amorphous $Fe_{100-x}Tb_x$ alloy films.
*Advanced Materials **25**, 3122 (2013)*

91. He, R.; Sun, S.; Xu, M.; Chen, F.; Akhmadaliev, Sh.; Zhou, S.
Planar optical waveguide in $SrTiO_3$ crystal fabricated by carbon ion irradiation
*Nuclear Instruments and Methods in Physics Research B **308**, 6 (2013)*

92. Čížek, J.; Lukáč, F.; Vlček, M.; Vlach, M.; Procházka, I.; Traeger, F.; Rogalla, D.; Becker, H.-W.; Anwand, W.; Brauer, G.; Wagner, S.; Uchida, H.; Pundt, A.; Bähtz, C.
Anisotropy of hydrogen diffusivity in ZnO
*Defect and Diffusion Forum **333**, 39 (2013)*

93. Jia, J.; Rüter, C. E.; Akhmadaliev, Sh.; Zhou, S.; Chen, F.; Kip, D.
Ridge waveguide lasers in Nd:YAG crystals produced by combining swift heavy ion irradiation and precise diamond blade dicing
*Optical Materials Express **3**, 433 (2013)*

94. Jia, Y.; de Aldana, J.; Akhmadaliev, Sh.; Zhou, S.; Chen, F.
Femtosecond laser micromachined ridge waveguide lasers in Nd:YAG ceramics
*Optical Materials **36**, 228 (2013)*

95. Jordan, N.; Ritter, A.; Foerstendorf, H.; Scheinost, A. C.; Weiß, S.; Heim, K.; Grenzer, J.; Mücklich, A.; Reuther, H.
Adsorption mechanism of selenium(VI) onto maghemite
*Geochimica et Cosmochimica Acta **103**, 63 (2013)*

96. Khanbabaee, B.; Biermanns, A.; Pietsch, U.; Grenzer, J.; Facsko, S.
Depth profiling of Fe-implanted Si(100) by means of X-ray reflectivity and extremely asymmetric X-ray diffraction
*Journal of Applied Crystallography **46**, 505 (2013)*

97. Kidambi, P. R.; Bayer, B. C.; Blume, R.; Wang, Z.-J.; Baehtz, C.; Weatherup, R. S.; Willinger, M.-G.; Schloegl, R.; Hofmann, S.
Observing graphene grow: Catalyst-graphene interactions during scalable graphene growth on polycrystalline copper
*Nano Letters **13**, 4769 (2013)*

98. Kimling, J.; Gerhardt, T.; Kobs, A.; Vogel, A.; Wintz, S.; Im, M.-Y.; Fischer, P.; Oepen, H. P.; Merkt, U.; Meier, G.
Tuning of the nucleation field in nanowires with perpendicular magnetic anisotropy
*Journal of Applied Physics **113**, 163902 (2013)*

99. Kozik, T.; Minarik, S.
New possibilities for investigation of the technological texture based on electric parameters: Theoretical analysis and experimental verification
*Journal of Electrical Engineering **64**, 376 (2013)*

100. Kreller, M.; Zschornack, G.; Kentsch, U.
Deceleration of Ar^{9+} ions within a tapered glass capillary
*Nuclear Instruments and Methods in Physics Research B **305**, 37 (2013)*

101. Kreuter, C.; Siems, U.; Nielaba, P.; Leiderer, P.; Erbe, A.
Transport phenomena and dynamics of externally and self-propelled colloids in confined

geometry
*European Physical Journal - Special Topics **222**, 2923 (2013)*

102. Liedke, B.; Heinig, K.-H.; Möller, W.
Surface morphology and interface chemistry under ion irradiation − Simultaneous atomistic simulation of collisional and thermal kinetics
*Nuclear Instruments and Methods in Physics Research B **316**, 56 (2013)*

103. Llorca, J.; Roszjar, J.; Cartwright, J. A.; Bischoff, A.; Pack, A.; Ott, U.; Merchel, S.; Rugel, G.; Fimiani, L.; Ludwig, P.; Allepuz, D.; Casado, J. V.
The Ksar Ghilane 002 shergottite – The 100th registered martian meteorite fragment
*Meteoritics & Planetary Science **48**, 493 (2013)*

104. Ludwig, P.; Egli, R.; Bishop, S.; Chernenko, V.; Frederichs, T.; Rugel, G.; Merchel, S.; Orgeira, M. J.
Characterization of primary and secondary magnetite in marine sediment by combining chemical and magnetic unmixing techniques
*Global and Planetary Change **110**, 321 (2013)*

105. Maaßdorf, A.; Zeimer, U.; Grenzer, J.; Weyers, M.
Linear thermal expansion coefficient determination using in situ curvature and temperature dependent X-ray diffraction measurements applied to metalorganic vapor phase epitaxy-grown AlGaAs
*Journal of Applied Physics **114**, 033501 (2013)*

106. Mackova, A.; Malinský, P.; Sofer, Z.; Šimek, P.; Sedmidubský, D.; Mikulics, M.; Wilhelm, R. A.
A study of the structural properties of GaN implanted by various rare-earth ions
Nuclear *Instruments and Methods in Physics Research B **307**, 446 (2013)*

107. Mäntymäki, M.; Hämäläinen, J.; Puukilainen, E.; Munnik, F.; Ritala, M.; Leskelä, M.
Atomic layer deposition of LiF thin films from Lithd and TiF_4 precursors
*Chemical Vapor Deposition **119**, 111 (2013)*

108. Marcham, M. K.; Shelford, L. R.; Cavill, S. A.; Keatley, P. S.; Yu, W.; Shafer, P.; Neudert, A.; Childress, J. R.; Katine, J. A.; Arenholz, E.; Telling, N. D.; van der Laan, G.; Hicken, R. J.
Phase-resolved X-ray ferromagnetic resonance measurements of spin pumping in spin valve structures
*Physical Review B **87**, 180403(R) (2013)*

109. Marcham, M. K.; Yu, W.; Keatley, P. S.; Shelford, L. R.; Shafer, P.; Cavill, S. A.; Qing, H.; Neudert, A.; Childress, J. R.; Katine, J. A.; Arenholz, E.; Telling, N. D.; van der Laan, G.; Hicken, R. J.
Influence of a Dy overlayer on the precessional dynamics of a ferromagnetic thin film
*Applied Physics Letters **102**, 062418 (2013)*

110. Mazalski, P.; Kurant, Z.; Maziewski, A.; Liedke, M. O.; Fassbender, J.; Baczewski, L. T.; Wawro, A.
Ion irradiation induced enhancement of out-of-plane magnetic anisotropy in ultrathin Co films
*Journal of Applied Physics **113**, 17C109 (2013)*

111. Merchel, S.; Braucher, R.; Alfimov, V.; Bichler, M.; Bourlès, D. L.; Reitner, J. M.
The potential of historic rock avalanches and man-made structures as chlorine-36 production rate calibration sites
*Quaternary Geochronology **18**, 54 (2013)*

112. Merchel, S.; Bremser, W.; Bourlès, D. L.; Czeslik, U.; Erzinger, J.; Kummer, N.-A.; Leanni, L.; Merkel, B.; Recknagel, S.; Schaefer, U.
Accuracy of ^{9}Be-data and its influence on ^{10}Be cosmogenic nuclide data
*Journal of Radioanalytical and Nuclear Chemistry **298**, 1871 (2013)*

113. Mohseni, S. M.; Sani, S. R.; Persson, J.; Anh Nguyen, T. N.; Chung, S.; Pogoryelov, Y.; Muduli, P. K.; Iacocca, E.; Eklund, A.; Dumas, R. K.; Bonetti, S.; Deac, A.; Hoefer, M. A.; Åkerman, J.
Spin torque generated magnetic droplet solitons
*Science **339**, 1295 (2013)*

114. Nasdala, L.; Grambole, D.; Ruschel, K.
Review of effects of radiation damage on the luminescence emission of minerals, and the example of He-irradiated $CePO_4$
*Mineralogy and Petrology **107**, 441 (2013)*

115. Nasdala, L.; Grambole, D.; Wildner, M.; Gigler, A. M.; Heinschwang, T.; Zaitsev, A. M.; Harris, J. W.; Milledge, J.; Schulze, D. J.; Hofmeister, W.; Balmer, W. A.
Radio-colouration of diamond: A spectroscopic study
*Contributions to Mineralogy and Petrology **165**, 843 (2013)*

116. Nichau, A.; Schnee, M.; Schubert, J.; Besmehn, A.; Rubio-Zuazo, J.; Breuer, U.; Bernardy, P.; Holländer, B.; Mücklich, A.; Castro, G. R.; von Borany, J.; Buca, D.; Mantl, S.
Photoemission spectroscopy study of the lanthanum lutetium oxide/silicon interface
*Journal of Chemical Physics **138**, 154709 (2013)*

117. Normann, H. B.; Vines, L.; Privitera, V.; Skorupa, W.; Schumann, T.; Svensson, B. G.; Monakhov, E. V.
Phosphorus in-diffusion from a surface source by millisecond flash lamp annealing for shallow emitter solar cells
*Applied Physics Letters **102**, 132108 (2013)*

118. Pardo, A.; Buijnsters, J. G.; Endrino, J. L.; Gómez-Aleixandre, C.; Abrasonis, G.; Bonet, R.; Caro, J.
Effect of the metal concentration on the structural, mechanical and tribological properties of self-organized a-C:Cu hard nanocomposite coatings
*Applied Surface Science **280**, 791 (2013)*

119. Peplinski, B.; Adam, C.; Adamczyk, B.; Muller, R.; Schadrack, R.; Michaelis, M.; Emmerling, F.; Reuther, H.; Menzel, M.
Evidence of formation of the tridymite form of $AlPO_4$ in some municipal sewage sludge ashes
*Powder Diffraction **28**, S425 (2013)*

120. Perez-Flores, J. C.; Baehtz, C.; Kuhna, A.; Garcia-Alvaradoa, F.
Hollandite-type TiO_2: A new negative electrode material for sodium-ion batteries
*Journal of Materials Chemistry A **2**, 1825 (2014)*

121. Preu, S.; Mittendorff, M.; Winnerl, S.; Lu, H.; Gossard, A. C.; Weber, H. B.
Ultra-fast transistor-based detectors for precise timing of near infrared and THz signals
*Optics Express **21**, 17941 (2013)*

122. Prinz, J.; Schreiber, B.; Olejko, L.; Oertel, J.; Rackwitz, J.; Keller, A.; Bald, I.
DNA origami substrates for highly sensitive surface-enhanced raman scattering
*Journal of Physical Chemistry Letters **4**, 4140 (2013)*

123. Putero, M.; Coulet, M.-V.; Ouled-Khachroum, T.; Muller, C.; Baehtz, C.; Raoux, S.
Unusual crystallization behavior in Ga-Sb phase change alloys
*APL Materials **1**, 0621011 (2013)*

124. Putero, M.; Coulet, M.-V.; Ouled-Khachroum, T.; Muller, C.; Baehtz, C.; Raoux, S.
Phase transition in stoichiometric GaSb thin films: Anomalous density change and phase segregation
*Applied Physics Letters **103**, 2319121 (2013)*

125. Richter, R.; Neelmeijer, C.
The Waldenburg beakers and Johann Kunckel: Analytical and technological study of four corner-cut colored glasses
*Studies in Conservation **57**, 234 (2013)*

126. Riedel, R.; Shemmary, A. A.; Gensch, M.; Golz, T.; Harmand, M.; Medvedev, N.; Prandolini, M. J.; Sokolowski-Tinten, K.; Toleikis, S.; Wegner, U.; Ziaja, B.; Stojanovic, N.; Tavella, F.
Single-shot pulse duration monitor for extreme ultraviolet and X-ray free-electron lasers
*Nature Communications **4**, 1731 (2013)*

127. Ristow, O.; Merklein, M.; Grossmann, M.; Hettich, M.; Schubert, M.; Bruchhausen, A.; Grebing, J.; Erbe, A.; Mounier, D.; Gusev, V.; Scheer, E.; Dekorsy, T.; Barretto, E. C. S.
Ultrafast spectroscopy of super high frequency mechanical modes of doubly clamped

beams
Applied Physics Letters ***103****, 233114 (2013)*

128. Ritter, R.; Shen, Q.; Wilhelm, R. A.; Heller, R.; Ginzel, R.; Crespo López-Urrutia, J. R.; Facsko, S.; Teichert, C.; Aumayr, F.
Novel aspects on the irradiation of HOPG surfaces with slow highly charged ions
Nuclear Instruments and Methods in Physics Research B ***315****, 252 (2013)*

129. Ritter, R.; Wilhelm, R. A.; Ginzel, R.; Schadauer, P.; Heller, R.; Rupp, W.; López-Urrutia, J. R. C.; Facsko, S.; Aumayr, F.
Effect of chemical etching on poly (methyl methacrylate) irradiated with slow highly charged ions
Physica Scripta ***T156****, 014065 (2013)*

130. Scheer, E.; Böhler, T.; Edtbauer, A.; Egle, S.; Erbe, A.; Pietsch, T.
Switchable zero-bias anomaly in individual C60 molecules contacted with tunable aluminum electrodes
Low Temperature Physics ***39****, 259 (2013)*

131. Schmidt, K.; Akhmadaliev, S.; Anders, M.; Bemmerer, D.; Boretzky, K.; Caciolli, A.; Degering, D.; Dietz, M.; Dressler, R.; Elekes, Z.; Fülöp, Z.; Gyürky, G.; Hannaske, R.; Junghans, A. R.; Marta, M.; Menzel, M.-L.; Munnik, F.; Schumann, D.; Schwengner, R.; Szücs, T.; Wagner, A.; Yakorev, D.; Zuber, K.
Resonance triplet at E_α = 4.5 MeV in the ^{40}Ca(α,γ)^{44}Ti reaction
Physical Review C ***88****, 025803 (2013)*

132. Stößer, R.; Feist, M.; Willgeroth, C.; Emmerling, F.; Menzel, M.; Reuther, H.
The “quiete Goldschmidt” - A mechanochemical, thermoanalytical, and spectroscopic study of selected steps of the aluminothermic reaction
Journal of Solid State Chemistry ***202****, 173 (2013)*

133. Tan, Y.; Luan, Q.; Liu, F.; Akhmadaliev, S.; Zhou, S.; Chen, F.
Swift carbon ion irradiated Nd:YAG ceramic optical waveguide amplifier
Optics Express ***21****, 13992 (2013)*

134. Thoss, F.; Thomas, J.; Oswald, S.; Potzger, K.; Reuther, H.; Ehrenberg, H.; Eckert, J.; Giebeler, L.
Amorphous Li-Al-based compounds: Novel approach for designing high performance electrode materials for Li-ion batteries
Inorganics ***1****, 14 (2013)*

135. Tsvetkova, T.; Wright, C. D.; Hosseini, P.; Bischoff, L.; Zuk, J.
Implantation temperature effects on the nanoscale optical pattern fabrication in a-SiC:H films by Ga$^+$ focused ion beams
Acta Physica Polonica A ***123****, 952 (2013)*

136. Tsvetkova, T.; Wright, C. D.; Kitova, S.; Bischoff, L.; Zuk, J.
Effects of implantation temperature and thermal annealing on the Ga$^+$ ion beam induced optical contrast formation in a-SiC:H
Nuclear Instruments and Methods in Physics Research B ***307****, 71 (2013)*

137. Tsyganov, I.; Lode, A.; Hanke, T.; Kolitsch, A.; Gelinsky, M.
Osteoblast responses to novel titanium-based surfaces produced by plasma- and ion beam technologies
RSC Advances ***28****, 11205 (2013)*

138. Tyschenko, I. E.; Volodin, V. A.; Voelskow, M.
Crystallization induced by thermal annealing with millisecond pulses in silicon-on-insulator films implanted with high doses of hydrogen ions
Semiconductors ***47****, 606 (2013)*

139. Tyschenko, I. E.; Volodin, V. A.; Voelskow, M.; Cherkov, A. G.; Popov, V. P.
Crystallization of the high-dose hydrogen ion implanted silicon-on-insulator layers under millisecond pulse annealing
Fizika i Tekhnika Poluprovodnikov ***47****, 591 (2013)*

140. Wallner, A.; Melber, K.; Merchel, S.; Ott, U.; Forstner, O.; Golser, R.; Kutschera, W.; Priller, A.; Steier, P.
Stable platinum isotope measurements in presolar nanodiamonds by TEAMS
*Nuclear Instruments and Methods in Physics Research B **294**, 496 (2013)*

141. Weatherup, R. S.; Baehtz, C.; Dlubak, B.; Bayer, B. C.; Kidambi, P. R.; Blume, R.; Schloegl, R.; Hofmann, S.
Introducing carbon diffusion barriers for uniform, high-quality graphene growth from solid sources
*Nano Letters **13**, 4624 (2013)*

142. Xie, Y. M.; Yang, Z. R.; Zhang, Z. T.; Yin, L. H.; Chen, X. L.; Song, W. H.; Sun, Y. P.; Zhou, S.; Tong, W.; Zhang, Y. H.
Magnetic-polaron–induced colossal magnetocapacitance in $CdCr_2S_4$
*Europhysics Letters **104**, 17005 (2013)*

143. Yildirim, C.; Schildgen, T.; Echtler, H.; Melnick, D.; Bookhagen, B.; Çiner, A.; Niedermann, S.; Merchel, S.; Martschini, M.; Steier, P.; Strecker, M.
Tectonic implications of fluvial incision and pediment deformation at the northern margin of the Central Anatolian Plateau based on multiple cosmogenic nuclides
*Tectonics **32**, 1107 (2013)*

144. Zech, R.; Röhringer, I.; Sosin, P.; Kabgov, H.; Akhmadaliev, S.; Merchel, S.; Zech, W.
Late Pleistocene glaciation in the Gissar Range, Tajikistan, based on ^{10}Be surface exposure dating
*Palaeogeography, Palaeoclimatology, Palaeoecology **369**, 253 (2013)*

145. Zhou, H. B.; Zhang, Y.; Ou, X.
Dissolution and diffusion behaviors of hydrogen in copper: A first-principles investigation
*Computational Materials Science **79**, 923 (2013)*

146. Zhou, H.; Ou, X.; Zhang, Y.; Shu, X.; Liu, Y.; Lu, G.
Effect of carbon on helium trapping in tungsten: A first-principles investigation
*Journal of Nuclear Materials **400**, 338 (2013)*

Patents

1. Abrasonis, G; Neidhardt, J.
Ratensteigerung mittels HiPMS
DE 10 2012 209293B3 - 20.06.2013 (granted)

2. Abrasonis, G.; Pollmann, K.; Raff, J.
Verfahren zur Herstellung für Kohlenstoffnanoröhrchen, durch das Verfahren hergestellte Kohlenstoffnanoröhrchen und deren Verwendung
DE 10 2008 023229 - 27.06.2013 (granted)
2123602GB - 16.01.2013 (granted)
2123602FR - 16.01.2013 (granted)
2123602DE - 16.01.2013 (granted)

3. Baumgart, C.; Helm, M.; Schmidt, H.; Skorupa, I.
Trägermaterial zur Sortierung und Manipulation für Biomaterialien, dessen Herstellung und Verwendung
WO 2013 029609A2 - 07.03.2013 (published)

4. Baumgart, C.; Müller, M.; Schmidt, H.; Skorupa, I.
Strukturierbares Trägermaterial zur kontrollierten Adsorption und Desorption von Polyelektrolytmaterialien, dessen Herstellung und Verwendung
DE 10 2011 055115A1 - 28.02.2013 (published)

5. Bürger, D.; Schmidt, H., Skorupa, I.
Funktionalisierte Festkörperoberflächen von Metallen, Halbleitern und Isolatoren mit Nanostrukturen
DE 10 2011 055604A1 - 23.05.2013 (published)
WO 2013 075712A1 - 30.05.2013 (published)

6. Kovács, G.; Schmidt, H.; Skorupa, I.; Bürger, D.; Varun, J; Slesazeck, S; Helm, M.
   Thermochromes Einzel- und Mehrkomponentensystem, dessen Herstellug und Verwendung
   DE 102 011056951A1 - 27.06.2013 (published)
   WO 2013 093110A1 - 27.06.2013 (published)
7. Neubert, M.; Vinnichenko, M.; Kolitsch, A.; Skorupa, W.
   Herstellung transparenter leitfähiger Titandioxidschichten, diese selbst und Verwendung
   DE 10 2012 104374A1 - 21.11.2013 (published)
   WO 2013 174824 - 28.11.2013 (published)
8. Schmidt, H.; Mok, K. M.; Scarlat, C.; Weber, I.
   Magnetisierbare Einzel- und Mehrschichtstrukturen, deren Herstellung und Verwendung
   DE10 2011 052217A1 – 31.01.2013 (published)
   WO 2013 013674A1 – 31.01.2013 (published)
9. Schmidt, H.; Shuai, Y.; Skorupa, I.; Zhou, S.
   Integriertes nichtflüchtiges Speicherbauelement, Herstellung und Verwendung
   DE 10 2011 051767A1 - 17.01.2013 (published)
   WO 2013 017131A1 - 07.02.2013 (published)
10. Shuai, Y.; Schmidt, H.; Ou, X.; Zhou, S.; Skorupa, I.; Luo, W.; Du, N.
    Integrierte Elektrode mit nichtflüchtig positionierbarer, statisch geladenen Grenzschicht, Aufbau und Verwendung
    DE 10 2012 104425 - 12.12.2013 (published)
11. Shuai, Y.; Schmidt, H.; Ou, X.; Zhou, S.; Skorupa, I. Mayr, C**.**
    Integrierter nichtflüchtiger Analogspeicher
    DE 10 2012 102326A1 - 26.09.2013 (published)

Concluded scientific degrees

Habilitation

1. Rebohle, L.
   Si-basierte Photonik
   TU BA Freiberg, 03.12.2013

PhD theses

1. Ball, D.
   From 2-D CoCrPt: SiO_2 films with perpendicular magnetic anisotropy to 3-D nanocones – A step towards bit patterned media
   TU Dresden, 19.04.2013
2. Fiedler, J.
   Elektrische und strukturelle Eigenschaften von supraleitenden Schichten in Ga-implantiertem Si und Ge
   TU Ilmenau, 21.08.2013
3. Fritzsche, M.
   Selbstorganisierte Nanostrukturen auf Germanium und Galliumantimonid und ihre Nutzung als Template
   TU Dresden, 15.11.2013
4. Heintze, C.
   Einfluss der Bestrahlung mit energiereichen Teilchen auf die Härte von Fe-Cr-Legierungen
   TU Dresden, 14.01.2013
5. Körner, M.
   Morphology induced magnetic phenomena studied by broadband ferromagnetic resonance
   TU Dresden, 02.09.2013
6. Kreller, M.
   Transport hochgeladener Ionen durch Nanokapillarfolien und makroskopische Glaskapillaren
   TU Dresden, 11.06.2013
7. Mok, K. M.
   Determination of the optical conductivity in ferromagnetic thin films by vector-magneto-optical generalized ellipsometry
   TU Dresden, 19.02.2013
8. Roshchupkina, O
   Ion beam induced structural modifications in nano-crystalline permalloy thin films
   TU Dresden, 02.05.2013
9. Shuai, Y.
   Nonvolatile resistive switching in $BiFeO_3$ thin films
   TU Dresden, 17.01.2013

Diploma theses

1. Schmidt, J.
   Zeitaufgelöste THz-Spektroskopie optisch angeregter Halbleiter-Quantenstrukturen
   TU Dresden, 31.01.2013

2. Yadav, R. K.
   Development of high power impulse magnetron sputtering process
   FH Furtwangen, 20.03.2013

BSc theses

1. Kretschmer, M.
   Modifikation von nanostrukturierten Silizium-Oberflächen durch nasschemisches Ätzen
   Westsächsische Hochschule Zwickau, 07.10.2013
2. Schneider, T.
   Untersuchung von Kopplungseffekten und magnetischer Anisotropie in Fe_3Si-Dreifachlagen mittels ferromagnetischer Resonanz
   TU Dresden, 24.03.2013
3. Spahn, N.
   Entwicklung eines Probenträgers für die Messung der Magnetoresistivität kombiniert mit in-situ Ionenbestrahlung in einer Hochvakuumanlage
   Westsächsische Hochschule Zwickau, 28.10.2013
4. Warnatz, T.
   Charaktierisierung von anisotropen Magnetowiderstandseffekten in Nanostrukturen aus Permalloy und Eisenaluminium
   Westsächsische Hochschule Zwickau, 27.05.2013

Appointments and honors

Appointments

1. **Gemming, Sibylle**
   Head oft he division „Scaling Phenomena“, accepted a W3 Professorship on „Scale-bridging Materials Modeling“ jointly appointed at the Technische Universität Chemnitz and the HZDR

Awards and honors

1. **Deac, Alina Maria**
   Scientist in the division “Magnetism” was awarded funding to establish a “Helmholtz Young Investigators Group” on the field of „Spin-torque devices for information and communication technologies“
2. **Fiedler, Jan**
   PhD candidate in the division “Semiconductor Materials” received the Young Scientist Award, Symp. J: Semiconductor nanostructures towards electronic and optoelectronic device applications IV, “Superconducting layers in Si – a new approach for quantum-bits?“ at the E-MRS 2013 Spring Meeting, 27.-31 May 2013, Strasbourg, France
3. **Hilger, Isabell**
   PhD candidate in the research group "Materials Characterization" of the division “Structural Materials” received the prize for best oral presentation for her presentation "The structure evolution of yttria in ferritic ODS alloys during mechanical alloying" at the HZDR PhD Seminar 2013, 07-09 October 2013, Bautzen,Germany
4. **Kowalska, Ewa**
   PhD candidate in the Helmholtz Young Investigator Group “Spintronics” of the division “Magnetism” was awarded a IEEE Magnetics Society School Grant, 4-9 June 2013, Assissi, Italy
5. **Ou, Xin**
   Scientist in the research group group „Ion Induced Nanostructures“ of the Ion Beam Center has received the Best Poster Award for the excellent poster presentation "Tuning the resistive switching characteristics of polycrystalline $BiFeO_3$ by Ar irradiation"at the European Materials Research Society Conference, 27-31 May 2013, Strasbourg, France
6. **Schneider, Harald**
   Head of the “Spectroscopy” division received a Poster Award in recognition of most impressive presentation of a poster first-authored by Dr. Jayeeta Bhattacharyya (on parental leave) at the International Workshop on Optical Science and Technology 2013 (OTST 2013), 01-05 April 2013, Kyoto, Japan
7. **Teshome, Bezuayehu**
   PhD candidate in the research group „Ion Induced Nanostructures“ of the Ion Beam Center was awared the Best Poster Prize 2013 for his poster "Topography-controlled alignment of DNA origami nanotubes on nanopatterned surfaces" presented at the IHRS NanoNet Annual Workshop 2013, 10 October 2013, Dresden, Germany.
8. **Wintz, Sebastian**
   PhD candidate in the research group “Transport in Nanostructures” of the division “Scaling Phenomena” received a DAAD Conference Grant, Joint MMM/Intermag Conference 2013, 14.-18 January 2013, Chicago, USA
9. **Wintz, Sebastian**
   PhD candidate in the research group “Transport in Nanostructures” of the division “Scaling Phenomena” received a GRC Conference Grant, Gordon Research Conferences: Spin Dynamics in Nanostructures, 18-23 August 2013, Hong Kong, China
10. **Zybell, Sabine**
    PhD candidate in the division “Spectroscopy” received a poster award in recognition for a most

impressive presentation of her poster at the International Workshop on Optical Science and Technology 2013 (OTST 2013), 01-05 April 2013, Kyoto, Japan.

Participation in conferences and lectures / talks

Invited conference talks

1. Abrasonis, G.
Energetic ion-assisted nanocomposite film growth: Sculpting matter in 3D at the nanoscale
2013 Energy Materials Nanotechnology (ENM Spring), 08.-11.04.2013, Orlando, USA

2. Bhattacharyya, J.; Zybell, S.; Eßer, F.; Winnerl, S.; Schneebeli, L.; Böttge, C. N.; Breddermann, B.; Kira, M.; Koch, S. W.; Helm, M.; Schneider, H.
THz free-electron laser spectroscopy of magnetoexcitons in semiconductor quantum wells
38th International Conference on Infrared, Millimeter and Terahertz Waves (IRMMW-THz'2013), 01.-06.09.2013, Mainz, Germany

3. Bischoff, L.; Böttger, R.; Heinig, K.-H.; Facsko, S.
Interaction of energetic ultraheavy ions with surfaces
DPG Spring Meeting of the Condensed Matter Section 2013, 10.-15.03.2013, Regensburg, Germany

4. Böttger, R.; Bischoff, L.; Liedke, B.; Heinig, K.-H.; Anders, C.; Urbassek, H. M.
Surface patterning by heavy-ion induced melt pools
International Symposium on Nanoscale Pattern Formation at Surfaces, 26.-30.05.2013, Copenhagen, Denmark

5. Facsko, S.
Interaction of highly charged ions with surfaces
11th European Conference on Atoms, Molecules and Photons, 24.-28.06.2013, Aarhus, Denmark

6. Gemming, S.
Microscopic processes in energy and data storage
21st Annual Conference of the German Crystallographic Society, 19.-22.03.2013, Freiberg (S), Germany

7. Gemming, S.; Seifert, G.
Size-effects in 2D transition metal chalcogenides
Flatlands Beyond Graphene, 17.-21.06.2013, Bremen, Germany

8. Gensch, M.
New THz and far-infrared lightsources
FEL13 - 35th International Free Electron Laser Conference, 25.-30.08.2013, New York, USA

9. Gensch, M.
Super-radiant THz sources: Perspectives
Workshop on "The Science and Technology of Accelerator-based THz Lightsources", 18.-19.11.2013, Upsala, Sweden

10. Grenzer, J.
X-ray diffraction and grazing-incidence diffraction
9th Autumn School on X-ray Scattering from Surfaces and Thin Layers, 25.-28.09.2013, Smolenice Castle, Slovakia

11. Grenzer, J. ; Gateshki, M.; Holz, Th.; Kharchenko , A. .
GISAXS Messungen am Labor-Diffraktometer
7. PRORA 2013 - Fachtagung Prozessnahe Röntgenanalytik, 21.-22.11.2013, Berlin, Germany

12. Heinig, K.-H.; Abrasonis, G.; Liedke, B.
Low-energy ion-beam-activated growth of ordered nanocomposites - modeling and computer simulations vs experiments
2013 MRS Spring Meeting, Symposium UU: Plasma and Low-Energy Ion-Beam-assisted Processing and Synthesis of Energy-related Materials, 01.-05.04.2013, San Francisco, USA

13. Heinig, K.-H.; Aydinli, A.; Turan, R.; Hauschild, D.
A Si-based nanocomposite absorber for thin film solar cells
2013 Energy Materials Nanotechnology (EMN Spring), 08.-11.04.2013, Orlando, USA

14. Heinig, K.-H.; Liedke, B.; Urbassek, H.; Anders, C.; Bischoff, L.; Böttger, R.
Mechanisms of surface pattern formation under irradiation with heavy ions
DPG Spring Meeting of the Condensed Matter Section 2013, 10.-15.03.2013, Regensburg, Germany

15. Heinig, K.-H.; Liedke, B.; Urbassek, H.; Anders, C.; Böttger, R.; Bischoff, L.
Surface nanopatterning by irradiation with heavy polyatomic ions
2013 EMN Spring Meeting "Energy Materials Nanotechnology", 08.-11.04.2013, Orlando, USA

16. Heinig, K.-H.; Liedke, B.; Urbassek, H.; Anders, C.; Böttger, R.; Bischoff, L.
Nanomelt-ionduced surface patterning by polyatomic ions
18th International Conference on Surface Modification of Materials by Ion Beams, 15.-20.09.2013, Kusadasi, Izmir, Turkey

17. Helm, M.
Strong-field THz spectroscopy of low-dimensional semiconductor systems
20th International Conference on Electronic Properties of Two-Dimensional Systems (EP2DS-20), 01.-05.07.2013, Wroclaw, Poland

18. Helm, M.
Semiconductor spectroscopy using THz free-electron lasers
38th International Conference on Infrared, Millimeter and Terahertz Waves (IRMMW-THz'2013), 01.-06.09.2013, Mainz, Germany

19. Helm, M.; Teich, M.; Wagner, M.; Stehr, D.; Winnerl, S.; Schneider, H.; Klettke, A. C.; Chatterjee, S.; Kira, M.; Koch, S. W.
Excitons in strong, narrowband terahertz fields: Rabi splitting and beyond
Fundamental optical processes in semiconductors (FOPS 2013), 12.-16.08.2013, Kodiak, Alaska, USA

20. Helm, M.; Teich, M.; Wagner, M.; Winnerl, S.; Schneider, H.; Klettke, A. C.; Chatterjee, S.; Kira, M.; Koch, S. W.
Terahertz nonlinear optics of excitons in quantum wells: The Autler-Townes effect and beyond
International Workshop on Optical Terahertz Science and Technology (OTST 2013), 01.-05.04.2013, Kyoto, Japan

21. Hinsche, N. F.; Yavorsky, B. Y.; Mertig, I.; Zahn, P.
Theory of thermoelectric transport in layered structures
529. WE-Heraeus-Seminar - Thermal transport at the nanoscale, 07.-10.04.2013, Bad Honnef, Germany

22. Lenz, K.
Two-magnon excitations: From periodical perturbations to magnonic crystals
DPG Spring Meeting of the Condensed Matter Section 2013, 10.-15.03.2013, Regensburg, Germany

23. Liedke, B.; Böttger, R.; Heinig, K.-H.; Bischoff, L.; Hübner, R.; Pilz, W.
Interaction of polyatomic Bi ions with Ge and Si
E-MRS 2013 Spring Meeting, 27.-31.05.2013, Strasbourg, France

24. Merchel, S.; Akhmadaliev, S.; Pavetich, S.; Rugel, G.; Ziegenrücker, R.
DREAMS: Die Zauberkugel für die Vergangenheit
WiN-Mitgliederversammlung (2. Runde WiN-Germany-Preis 2013), 22.11.2013, Kernkraftwerk Obrigheim, Germany

25. Ou, X.
Ion beam irradiation and doping effect on 1D and 2D materials
International School on Ion Beams in Material Science, 21.-22.10.2013, Jaipur, India

26. Ou, X.; Keller, A.; Helm, M.; Fassbender, J.; Facsko, S.
Nanopatterning of semidonductor surfaces by ion beam irradiation
International Conference on Nanostructuring by Ion Beams, 23.-25.10.2013, Jaipur, India

27. Paul, J.; Bleicher, F.; Bortolotto, L.; Geiger, G.; Kolitsch, A.; Langlade, C.; Masset, P.; Pelic, B.; Pyczak, F.; Rafaja, D.; Schimansky, F.-P.; Schumacher, P.; Schütze, M.; Wolf, G.; Yankov, R.
Embrittlement of TiAl after high temperature exposure
International Workshop on Gamma Alloy Technology (GAT 2013), 11.-14.06.2013, Toulouse, France

28. Posselt, M.
Atomistic modeling of solid phase recrystallization of amorphous Si and Ge
E-MRS 2013 Spring Meeting, Symposium K, 27.-31.05.2013, Strasbourg, France

29. Preu, S.; Regensburger, S.; Kim, S.; Mittendorff, M.; Winnerl, S.; Malzer, S.; Lu, H.; Burke, P. G.; Gossard, A. C.; Weber, H. B.; Sherwin, M. S.
Broadband THz detection and homodyne mixing using GaAs high-electron-mobility transistor rectifiers
6th International Conference on Millimetre Wave and Terahertz Sensors and Technology, 24.-25.09.2013, Dresden, Germany

30. Rebohle, L.
Rare earth implanted MOS structures: Advantages and drawbacks for optoelectronic applications
7th International Workshop “Functional Nanomaterials and Devices”, 08.-11.04.2013, Kyiv, Ukraine

31. Renno, A. D.; Merchel, S.; Akhmadaliev, S.; Rugel, G.; Ziegenrücker, R.; Döbeli, M.; Richnow, H.-H.; Wiedenbeck, M.
The Helmholtz SIMS network: Cooperation at multiple scales
7th Biennial Geo-SIMS Workshop, Lecture Series "SIMS: Current Strengths and Future Potential", 20.-22.08.2013, Potsdam, Germany

32. Reuther, H.
Thin layer analysis with electrons - AES, XPS, Mössbauer spectroscopy
XXXIV Brazilian Congress of Vacuum Applications in Industry and Science, 21.-25.10.2013, Ilheus, Brazil

33. Schneider, H.
Spectroscopy of low-dimensional semiconductors with a terahertz free-electron laser
9th National Conference on Nanoscience and Nanotechnology (NanoTR-9), 14.-28.07.2013, Ataturk University, Erzurum Province, Turkey

34. Schneider, H.
THz free-electron laser spectroscopy of zero- and two-dimensional semiconductors
6th Annual Meeting, Deutsches THz-Zentrum e.V., ISL Saint-Louis, 25.-26.02.2013, Saint-Louis, France

35. Schneider, H.; Bhattacharyya, J.; Zybell, S.; Winnerl, S.; Helm, M.
Terahertz interlevel spectroscopy of quantum well excitons
The 12th International Conference on Intersubband Transitions in Quantum Wells - ITQW 2013, 15.-20.09.2013, Bolton Landing, NY, USA

36. Skorupa, W.
Nanocrystalline approaches to electronic materials using subsecond thermal processing
223rd ECS Meeting, Symposium E3: Nanocrystal Embedded Dielectrics for Electronic and Photonic Devices, 12.-17.05.2013, Toronto, Canada

37. Skorupa, W.
Short time thermal processing and defects: History and ideology
International Symposium on Semiconductors: Defects, Doping and Diffusion (IS2D3), 24.-25.10.2013, Oslo, Norway

38. Wieser, M.; Sendler, T.; Kilibarda, F.; Teshome, B.; Keller, A.; Grebing, J.; Erbe, A.
Strategies for contacting single molecule devices
IHRS NanoNet Annual Workshop 2013, 10.10.2013, Dresden, Germany

39. Winnerl, S.
Relaxation dynamics in graphene close to the Dirac point
DPG Spring Meeting of the Condensed Matter Section 2013, 10.-15.03.2013, Regensburg, Germany

40. Winnerl, S.
Carrier dynamics in graphene near the Dirac point
The 18th International Conference on Electron Dynamics in Semiconductors, Optoelectronics and Nanostructures, 22.-26.07.2013, Matsue, Japan

41. Winnerl, S.; Mittendorff, M.; Schneider, H.; Helm, M.; Winzer, T.; Wendler, F.; Malic, E.; Knorr, A.
Graphene investigated in the THz range: Ultrafast dynamics and device perspectives
21st International Conference on Applied Electromagnetics and Communications, 14.-16.10.2013, Dubrovnik, Croatia

42. Zhou, S.
Ion beam synthesis of ferromagnetic semiconductors
7th Symposium on Vacuum based Science and Technology, 19.-21.11.2013, Kołobrzeg, Poland

43. Zhou, S.
Defect-induced ferromagnetism in semiconductors: A controllable approach by particle irradiation
The 17th International Conference on Radiation Effects in Insulators, 30.06.-05.07.2013, Helsinki, Finland

Conference talks

1. Abrasonis, G.; Krause, M.; Buljan, M.; Mücklich, A.; Fritzsche, M.; Facsko, S.; Zschornak, M.; Wintz, S.; Endrino, J. L.; Baehtz, C.; Shalimov, A.; Gemming, S.
Ion induced compositionally modulated ripples during composite film growth: 3D sculpting at the nanoscale
International Symposium on Nanoscale Pattern Formation at Surfaces, 26.-30.05.2013, Copenhagen, Denmark

2. Abrasonis, G.; Krause, M.; Muecklich, A.; Baehtz, C.; Shalimov, A.; Zschornak, M.; Wintz, S.; Endrino, J. L.; Gemming, S.
Ion assistance effects on the morphology of carbon-nickel composite films grown by physical vapor deposition at various metal contents
2013 MRS Spring Meeting & Exhibit, 01.-05.04.2013, San Francisco, CA, USA

3. Aleksandrov, Y.; Deac, Alina M.; Bernert, K.; Fowley, C.; Sluka, V.; Kowalska, E.; Lindner, J.; Fassbender, J.
Spin torque ferromagnetic resonance in MgO-based magnetic tunnel junctions
DPG Spring Meeting of the Condensed Matter Section 2013, 10.-15.03.2013, Regensburg, Germany

4. Aleksandrov, Y.; Lindner, J.; Farle, M.; Rod, I.; Zähres, H.
Electrical detection of inverse spin Hall effect induced by spin pumping
DPG Spring Meeting of the Condensed Matter Section 2013, 10.-15.03.2013, Regensburg, Germany

5. Alexandru, M.; Florentin, M.; Constant, A.; Schmidt, B.; Michel, P.; Godignon, P.
5MeV proton and 15MeV electron radiation effects study on 4H-SiC nMOSFET electrical parameters
Radiation Effects on Components and Systems 2013, 23.-27.09.2013, Oxford, United Kingdom

6. Baehtz, C.; Grenzer, J.; Roshchupkina, O.; Kidambi, P. R.; C. Bayer, B.; Wheaterup, R.; Hofmann, S.
X-ray diffraction investigations under non ambient conditions at the Rossendorf Beamline ROBL
Annual Conference of the German Crystallographic Society (DGK) 2013, 19.-22.3.2013, Freiberg, Germany

7. Banholzer, A.; Wintz, S.; Fowley, C.; Deac, A.; Raabe, J.; Lenz, K.; Lindner, J.; Fassbender, J.
Simultaneous STXM imaging and resistance measurements of trilayer vortices
Joint European Magnetic Symposia (JEMS) 2013, 25.-30.08.2013, Rhodos, Greece

8. Bemmerer, D.
Underground nuclear astrophysics

MASCHE annual meeting (Massive Stars as Agents of Chemical Evolution, part of EuroGENESIS), 03.12.2013, Darmstadt, Germany

9. Bischoff, L.; Böttger, R.; Facsko, S.; Schmidt, B.; Pilz, W.
Pattern formation by focused polyatomic ion beam irradiation on GaAs
18th International Conference on Surface Modification of Materials by Ion Beams, 15.-20.09.2013, Kusadasi, Izmir, Turkey

10. Bischoff, L.; Böttger, R.; Heinig, K.-H.
Surface morphologies of Ge and Si under heavy single-atom and poly-atom ion irradiation
Workshop „Ionenstrahlen in Forschung und Anwendung“ & Treffen der DFG-Forschergruppe FOR 845, 12.-14.06.2013, Leipzig, Germany

11. Bischoff, L.; Böttger, R.; Keller, A.; Facsko, S.
Mapping the local elastic properties of nanopatterned Ge
International Symposium on Nanoscale Pattern Formation at Surfaces, 26.-30.05.2013, Copenhagen, Denmark

12. Bischoff, L.; Schmidt, B.; Böttger, R.; Pilz, W.
Angle-dependent sputtering and pattern formation by polyatomic ion irradiation
The 17th International Conference on Radiation Effects in Insulators, 30.06.-05.07.2013, Helsinki, Finland

13. Blaschke, D.; Skorupa, I.; Scheumann, B.; Scholz, A.; Zahn, P.; Gemming, S.; Potzger, K.
Resistive switching in thermally oxidized Titanium
DPG Spring Meeting of the Condensed Matter Section 2013, 10.-15.03.2013, Regensburg, Germany

14. Blaschke, D.; Zahn, P.; Skorupa, I.; Scheumann, B.; Scholz, A.; Gemming, S.; Potzger, K.
Resistive switching in thermally oxidized Titanium films
International Semiconductor Conference Dresden-Grenoble, 26.-27.09.2013, Dresden, Germany

15. Bogusz, A.; Skorupa, I.; Blaschke, D.; Schmidt, O. G.; Schmidt, H.
Nonvolatile resistive switching in multiferroic YMnO3 thin films
DPG Spring Meeting of the Condensed Matter Section 2013, 10.-15.03.2013, Regensburg, Germany

16. Bogusz, A.; You, T.; Blaschke, D.; Scholz, A.; Shuai, Y.; Luo, W.; Du, N.; Bürger, D.; Skorupa, I.; Schmidt, Oliver G.; Schmidt, H.
Resistive switching in thin multiferroic films
International Semiconductor Conference Dresden-Grenoble, 26.-27.09.2013, Dresden, Germany

17. Böttger, R.; Bischoff, L.; Heinig, K.-H.; Liedke, B.; Anders, C.; Urbassek, H. M.
Surface patterning by heavy-ion induced melting
The 17th International Conference on Radiation Effects in Insulators 2013 (REI-17), 30.06.-05.07.2013, Helsinki, Finland

18. Chumak, A. V.; Obry, B.; Brächer, T.; Pirro, P.; Ciubotaru, F.; Serga, A. A.; Osten, J.; Fassbender, J.; Hillebrands, B.
Spin waves in a microstructured ion-implanted magnonic crystal
International Symposium on Spin Waves, 09.-15.06.2013, St. Petersburg, Russia

19. Deßmann, N.; Pavlov, S.; Mittendorff, M.; Winnerl, S.; Zhukavin, R.; Tsyplenkov, V.; Shengurov, V.; Shastin, V.; Abrosimov, N.; Riemann, H.; Hübers, H.-W.
Fast relaxation of free carriers in compensated n- and p-type germanium
38th International Conference on Infrared, Millimeter and Terahertz Waves, 01.-06.09.2013, Mainz, Germany

20. Devaraj, M.; Posselt, M.
Temperature-dependent free formation energies of Y, Ti and O in bcc Fe: A first principles study
EUROMAT 2013, 08.-13.09.2013, Sevilla, Spain

21. Devaraj, M.; Posselt, M.
Atomistic study on structure and energetics of yttria-based oxide nanoclusters in bcc-

iron
2013 MRS Fall Meeting & Exhibit, Symposium ZZ, 01.-06.12.2013, Boston, USA

22. Devaraj, M.; Posselt, M.
Structure and energetics of Y-Ti-O nanoclusters in bcc Fe: A combined DFT and Monte Carlo Study
International Workshop on ODS Materials, 08.07.2013, Dresden, Germany

23. Devaraj, M.; Posselt, M.
Properties of yttria-based oxide nanoclusters in iron: An atomistic study
5th Workshop on Nuclear Fe Alloys: Modeling and Experiment, 28.-29.11.2013, Rome, Italy

24. Donchev, A.; Galetz, M.; Schütze, M.; Yankov, R.; Kolitsch, A.
Surface treatment for improved high temperature environmental stability of Ti-alloys
Euro LightMAT 2013 - International Congress and Exhibition on Light Materials – Aluminium, Magnesium, Titanium and their Alloys, 03.-05.09.2013, Bremen, Germany

25. Drachenko, O.; Kozlov, D.; Ikonnikov, A.; Spirin, K.; Gavrilenko, V.; Schneider, H.; Helm, M.; Wosnitza, J.
Extra-long hole spin relaxation time in InGaAs/GaAs quantum wells probed by cyclotron resonance spectroscopy
2013 38th International Conference on Infrared, Millimeter, and Terahertz Waves (IRMMW-THz 2013), 01.-06.09.2013, Mainz, Germany

26. Eder, F. M.; Neelmeijer, C.; Pearce, N. J. G.; Sterba, J. H.; Bichler, M.; Merchel, S.
Vergleich komplementärer „Fingerprint“-Techniken an europäischen Obsidianvorkommen
24th Seminar Activation Analysis and Gamma-Spectroscopy (SAAGAS 24), 26.-28.02.2013, Garching, Germany

27. Engler, M.; Müller, S.; Will, M.; Frost, F.; Feder, R.; Spemann, D.; Hübner, R.; Facsko, S.; Michely, T.
Is silicide formation the decisive factor in impurity induced ion beam pattern formation?
Nanocale Pattern Formation at Surfaces, 26.-30.05.2013, Copenhagen, Denmark

28. Facsko, S.; Fritzsche, M.; Ou, X.; Keller, A.
Nanostructuring Ge surfaces by ion irradiation
18th International Conference on Surface Modification of Materials by Ion Beams (SMMIB 2013), 15.-20.09.2013, Kusadasi, Turkey

29. Facsko, S.; Ou, X.; Keller, A.
Reverse epitaxy: Patterns on crystalline Ge surfaces
Symposium on „Nanoscale Pattern Formation at Surfaces“, 26.-30.05.2013, Copenhagen, Danmark

30. Fehrenbacher, M.; Jacob, R.; Winnerl, S.; Bhattacharyya, J.; Schneider, H.; Wenzel, M. T.; von Ribbeck, H.-G.; Eng, L. M.; Akinson, P.; Schmidt, O. G.; Helm, M.
Spectroscopy on single buried InAs quantum dots by scattering scanning near-field infrared microscopy
DPG Spring Meeting of the Condensed Matter Section 2013, 10.-15.03.2013, Regensburg, Germany

31. Feige, J.; Wallner, A.; Fifield, L. Keith; Golser, R.; Korschinek, G.; Merchel, S.; Rugel, G.; Winkler, Stephan R.
AMS measurements of cosmogenic and supernova–ejected radionuclides in deep–sea sediment cores
Heavy Ion Accelerator Symposia on Fundamental and Applied Science (HIAS), 08.-12.04.2013, Canberra, Australia

32. Fiedler, J.
Supraleitende Schichten in Ga-implantiertem Si und Ge
34. Treffen der Nutzergruppe Heißprozesse und RTP, 06.11.2013, Frankfurt (Oder), Germany

33. Fiedler, J.
Supraleitende Schichten in Halbleitern
Ionenstrahlen in Forschung und Anwendung, 12.-14.06.2013, Leipzig, Germany

34. Fiedler, J.; Heera, V.; Skrotzki, R.; Herrmannsdörfer, T.; Voelskow, M.; Hübner, R.; Philipp, P.; Schmidt, B.; Skorupa, W.; Gobsch, G.; Helm, M.
Superconducting layers in Si – a new approach for quantum-bits?
E-MRS 2013 Spring Meeting (Ausgezeichnet mit dem "Young Scientist Award" - Symposium J), 27.-31.05.2013, Strasbourg, France

35. Florentin, M.; Alexandru, M.; Constant, A.; Schmidt, B.; Godignon, P.
Low energy proton radiation impact on 4H-SiC nMOSFET electrical parameters
International Conference on Silicon Carbide and Related Materials, 29.09.-04.10.2013, Phoenix Seagaia Resort, Miyazaki, Japan

36. Florentin, M.; Alexandru, M.; Constant, A.; Schmidt, B.; Godignon, P.
10 MeV proton irradiation effect on 4H-SiC nMOSFET electrical parameters HeteroSiC-*WASMPE, 17.-19.07.2013, Nice, France*

37. Gao, K.; Prucnal, S.; Baehtz, C.; Skorupa, W.; Helm, M.; Zhou, S.
GaPN dilute nitride fabricated by ion-implantation and pulsed laser melting
E-MRS 2013 Fall Meeting, 16.-20.09.2013, Warsaw, Poland

38. Germer, S.; Rebohle, L.; Skorupa, W.; Helm, M.
Basic structures of integrated photonic circuits for smart biosensor applications
Optics & Optoelectronics, 15.-18.04.2013, Pague, Czech Republic

39. Grenzer, J.; Facsko, S.; Holy, V. ; Bähtz, C.; Roshchupkina, O.
In-situ X-ray scattering & diffraction: Studying the formation of nanostructures using ion beam techniques
Workshop „Ionenstrahlen – Forschung und Anwendung“ 2013, 12.-14.06.2013, Leipzig, Germany

40. Heinig, K.-H.; Aydinli, A.; Schmidt, B.; Liedke, B.; Friedrich, D.; Keles, U.; Bulutay, C.
Network of percolated Si filaments in SiO_2: A nanocomposite-absorber for thin-film PV cells
2013 MRS Spring Meeting, Symposium A: Film Silicon Science and Technology, 01.-05.04.2013, San Francisco, USA

41. Heintze, C.; Hernández Mayoral, M.; Bergner, F.
Nanoindentation on ion-irradiated Fe−Cr alloys
5th Workshop on Nuclear Fe Alloys: Modeling and Experiment, 28.-29.11.2013, Roma, Italy

42. Hilger, I.; Bergner, F.; Palasse, L.; Shariq, A.; Kölling, S.; Garcia-Junced, A.
Characterization of spark plasma sintered ODS alloys
ODISSEUS workshop on ODS steels, 09.12.2013, Dresden, Germany

43. Hilger, I.; Bergner, F.; Palasse, L.; Shariq, A.; Kölling, S.; Garcia-Junced, A.
Dual-Beam irradiation of spark plasma sintered ODS Fe−14Cr alloys
EUROMAT 2013, 10.09.2013, Sevilla, Spain

44. Hilger, I.; Bergner, F.; Tegel, M.; Palasse, L.; Shariq, A.; Kölling, S.; García-Junceda, A.; Gorley, M.
Microstructure of spark plasma sintered ODS Fe−14Cr
International ODS meeting, 08.07.2013, Dresden, Germany

45. Husar, R.; Weiss, S.; Hennig, C.; Hübner, R.; Zänker, H.; Bernhard, G.
Investigation into the formation of Np(IV) silica colloids
Migration 2013, 08.-13.09.2013, Brighton, United Kingdom

46. Jacob, R.; Winnerl, S.; Fehrenbacher, M.; Bhattacharyya, J.; Schneider, H.; Wenzel, M. T.; von Ribbeck, H.-G.; Eng, L. M.; Atkinson, P.; Schmidt, O. G.; Helm, M.
Terahertz spectroscopy on single buried InAs quantum dots by scanning near-field nano-microscopy
International Workshop on Optical Terahertz Science and Technology (OTST), 01.-05.04.2013, Kyoto, Japan

47. Kaltenecker, K. J.; Wallauer, J.; Waselikowski, S.; Hodapp, J.; Fischer, C.; Winnerl, S.; Schneider, H.; Fischer, B. M.; Walther, M.
Plasmonic focusing on metal and semiconductor disks under radially polarized terahertz illumination

38th International Conference on Infrared, Millimeter, and Terahertz Waves (IRMMW-THz 2013), 01.-06.09.2013, Mainz, Germany

48. Kelling, J.; Heinig, K.-H.
Performing kinetic lattice Monte-Carlo simulations of far-from-equilibrium processes on GPUs
2nd International Symposium “Computer Simulations on GPU”, 27.-29.05.2013, Freudenstadt, Germany

49. Kolitsch, A.; Yankov, R.
Ion implantation based surface modification of TiAl materials
19th International Vacuum Congress (IVC’19), 09.-13.09.2013, Paris, France

50. Kowalska, E.; Bernert, K.; Aleksandrov, Y.; Fowley, C.; Sluka, V.; Mangin, S.; Lindner, J.; Fassbender, J.; Deac, A. M.
Thermally excited ferromagnetic resonance in MgO-based magnetic tunnel junctions
DPG Spring Meeting of the Condensed Matter Section 2013, 10.-15.03.2013, Regensburg, Germany

51. Krause, M.; Buljan, M.; Oates, T. W. H.; Mücklich, A.; Fritzsche, M.; Facsko, S.; Zschornak, M.; Wintz, S.; Endrino, J. L.; Baehtz, C.; Shalimov, A.; Gemming, S.; Abrasonis, G.
Ion-guided microstructure evolution of carbon-nickel nanocomposite films during ion beam assisted deposition: 3D sculpting at the nanoscale
E-MRS 2013 SPRING MEETING - Symposium W - Ion beam applications: new and innovative approaches, 26.-31.05.2013, Strasbourg, France

52. Kroll, F.; Cowan, T. E.; Herrmannsdörfer, T.; Masood, U.; Karsch, L.; Kraft, S. D.; Pawelke, J.; Schlenvoigt, H.-P.; Schramm, U.; Zherlitsyn, S.
HZDR pulsed power developments for laser plasma applications and the LIGHT collaboration
LaB 2013 - Exploring the coupling between intense magnetic fields and high-power lasers, 02.-04.12.2013, Palaiseau, France

53. Kroll, F.; Kluge, T.; Bussmann, M.; Cowan, T. E.; Herrmannsdörfer, T.; Kraft, S. D.; Metzkes, J.; Sauerbrey, R.; Schmidt, B.; Schramm, U.; Zeil, K.; Zier, M.; Zherlitsyn, S.
Dose enhancement and localisation by combining reduced mass targets and a pulsed solenoid for radiobiological effectiveness studies of laser accelerated protons
1st European Advanced Accelerator Concepts Workshop, 02.-07.06.2013, La Biodola, Elba, Italy

54. Lehmann, J.; Hübner, R.; Skorupa, W.; von Borany, J.; Mikolajick, T.; Schäfer, A.; Schubert, J.; Mantl, S.
Millisecond flash lamp annealing for $LaLuO_3$ and $LaScO_3$ high-k dielectrics
18th Conference of "Insulating Films on Semiconductors", 25.-28.06.2013, Kraków, Poland

55. Lenz, K.; Körner, M.; Gallardo, R.; Landeros, P.; Facsko, S.; Lindner, J.; Fassbender, J.
Frequency and field control of the magnetic relaxation in 2D magnonic crystals
12th Joint MMM-Intermag Conference, 14.-18.01.2013, Chicago, USA

56. Mazalski, P.; Kurant, Z.; Maziewski, A.; Liedke, M. O.; Fassbender, J.; Baczewski, L. T.; Wawro, A.
Forcing of out-of-plane magnetic anisotropy in ultrathin Co films by ion irradiation
12th Joint MMM/Intermag Conference, 14.-18.01.2013, Chicago, Illinois, USA

57. Mazalski, P.; Maziewski, A.; Rogalev, A.; Wilhelm, F.; Fassbender, J.; Baczewski, L. T.; Wawro, A.
XAS/XMCD studies of Ga^+ ions irardiated of Pt/Co/Pt trilayers
Joint European Symposia on Magnetism (JEMS 2013), 25.-30.08.2013, Rhodos, Greece

58. Merchel, S.; Akhmadaliev, S.; Pavetich, S.; Renno, A. D.; Rugel, G.; Several Dreams-Users
Ultrasensitive determination of long-lived radionuclides by accelerator mass spectrometry for applications from the earth sciences and cosmochemistry
24th Seminar Activation Analysis and Gamma-Spectroscopy (SAAGAS 24), 26.-28.02.2013, Garching, Germany

59. Merchel, S.; Akhmadaliev, S.; Pavetich, S.; Renno, A. D.; Rugel, G.; Ziegenrücker, R.
Ultimate detection limits by accelerator-based mass spectrometry
ANAKON 2013, 04.-07.03.2013, Essen, Germany

60. Mittendorff, M.; Winnerl, S.; Kamann, J.; Eroms, J.; Schneider, H.; Helm, M.
Graphene based broadband THz detector working at room temperature
International Workshop on Terahertz Science and Technology, 01.-05.04.2013, Kyoto, Japan

61. Mittendorff, M.; Winnerl, S.; Kamann, J.; Eroms, J.; Schneider, H.; Helm, M.
Broadband THz detection with graphene flakes
DPG Spring Meeting of the Condensed Matter Section 2013, 10.-15.03.2013, Regensburg, Germany

62. Mittendorff, M.; Winnerl, S.; Kamann, J.; Eroms, J.; Weiss, D.; Schneider, H.; Helm, M.
Ultrafast graphene-based THz detection at room temperature
38th International Conference on Infrared, Millimeter and Terahertz Waves, 01.-06.09.2013, Mainz, Germany

63. Mittendorff, M.; Winnerl, S.; Orlita, M.; Potemski, M.; Berger, C.; de Heer, Walter A.; Schneider, H.; Helm, M.
Time-resolved spectroscopy on intraband Landau-level transitions in graphene
Graphene Week 2013, 02.-07.06.2013, Chemnitz, Germany

64. Munnik, F.; Hanf, D.; Ziegenrücker, R.; Renno, A. D.
A new approach to chemical imaging with PIXE using an X-ray colour camera
Workshop „Ionenstrahlen – Forschung und Anwendung“, 12.-13.06.2013, Leipzig, Germany

65. Neelmeijer, C.; Hasselmeyer, L.; Eulitz, J.
Renaissance enamels - colouring and state of preservation non-destructive studies by external PIXE–PIGE–RBS
PIXE2013 - 13th International Conference on Particle induced X-Ray Emission, 03.-08.03.2013, Gramado, Brazil

66. Neubert, M.; Vinnichenko, M.; Cornelius, S.; Gebel, T.; Liepack, H.
Low-electrical resistivity polycrystalline TiO_2-based transparent conductors by millisecond flash lamp annealing of magnetron sputtered films
2013 MRS Spring Meeting & Exhibit, 01.-05.04.2013, San Francisco, USA

67. Neubert, M.; Vinnichenko, M.; Gemming, S.; Gebel, T.; Liepack, H.; Kolitsch, A.
Kurzzeittemperung zur Herstellung TiO_2-basierter TCOs
Workshop "Transparente leitfähige Materialien (TCO / TCM) – Festkörperphysikalische Grundlagen und Technologien", 04.-05.06.2013, Dresden, Germany

68. Ódor, G.; Schulz, H.; Kelling, J.; Heinig, K.-H.; Máté Ferenc, N.
Extremely large scale simulation of surface growth and lattice gases
GPU Technology Conference, 18.-21.03.2013, San Jose, USA

69. Osten, J.; Langer, M.; Lenz, K.; Linder, J.; Fassbender, J.
Simultaneous measurement of AMR and observation of magnetic domains
DPG Spring Meeting of the Condensed Matter Section 2013, 10.-15.03.2013, Regensburg, Germany

70. Ou, X.; Kögler, R.; Zhou, H. B.; Anwand, W.; Grenzer, J.; Hübner, R.; Voelskow, M.; Butterling, M.; Zhou, S.; Skorupa, W.; Fascko, S.
Formation of radiation damage and helium release in yttria-stabilized zirconia under dual ion beam irradiation
German workshop on Ion Beam Research and Application, 12.-14.06.2013, Leipzig, Germany

71. Ou, X.; Mücklich, A.; Fassbender, J.; Facsko, S.
Reverse epitaxy of Ge surface for nanopattern formation
European Materials Research Society Conference, 27.-31.05.2013, Strasbourg, France

72. Pavetich, S.; Akhmadaliev, Sh.; Arnold, M.; Aumaître, G.; Bourlès, D.; Buchriegler, J.; Golser, R.; Keddadouche, K.; Martschini, M.; Merchel, S.; Rugel, G.; Steier, P.
Interlaboratory study of the ion source memory effect in ^{36}Cl accelerator mass spectrometry
Heavy Ion Accelerator Symposia on Fundamental and Applied Science, 08.-12.04.2013, Canberra, Australia

73. Pavetich, S.; Akhmadaliev, Sh.; Arnold, M.; Aumaître, G.; Bourlès, D.; Buchriegler, J.; Golser, R.; Keddadouche, K.; Martschini, M.; Merchel, S.; Rugel, G.; Steier, P.

Ion source memory in ^{36}Cl accelerator mass spectrometry
DPG-Frühjahrstagung der Sektion AMOP (SAMOP), 18.-22.03.2013, Hannover, Germany

74. Pelic, B.; Bregolin, F.; Prucnal, S.; Skorupa, W.; Yankov, R.
Plasma-based nanotechnology against corrosion of organ pipes
The 12th International Workshop on Plasma-Based Ion Implantation and Deposition (PBII&D), 01.-05.07.2013, Poitiers, France

75. Pelic, B.; Bregolin, F.; Prucnal, S.; Wiesenhütter, K.; Yankov, R.; Skorupa, W.
Protection of organ pipes using plasma-based nanotechnology
E-MRS 2013 Spring Meeting, 27.-31.05.2013, Strasbourg, France

76. Pelic, B.; Skorupa, W.
Anticorrosion studies for pipe organ-related materials using plasma processing
Internationale Konferenz zur Korrosion in Pfeifen von historischen Orgeln, 21.02.2013, Bremen, Germany

77. Peplinski, B.; Adam, C.; Adamczyk, B.; Muller, R.; Schadrack, R.; Michaelis, M.; Emmerling, F.; Reuther, H.; Menzel, M.
Evidence of formation of the tridymite form of $AlPO_4$ in some municipal sewage sludge ashes
13. European Powder Diffraction Conference, 28.-31.10.2013, Grenoble, France

78. Pflumm, R.; Schütze, M.; Donchev, A.; Yankov, R.; Kolitsch, A.
Assessments of the oxidation resistance of technical TiAl-alloys under the influence of fluorine and depending on the high temperature exposure technique
International Conference Intermetallics 2013, 30.09.-04.10.2013, Bad Staffelstein, Germany

79. Radek, M.; Bracht, H.; Schmidt, B.; Bougeard, D.; Haller, E. E.
Ga implantation induced atomic mixing in crystalline and amorphous Ge isotope multilayers
E-MRS 2013 Spring Meeting, Symposium W, 27.-31.05.2013, Strasbourg, France

80. Rebohle, L.; Wutzler, R.; Germer, S.; Helm, M.; Skorupa, W.; Berencén, Y.; Garrido, B.; Hiller, D.
Correlation between efficiency and stability in Er- and Si-implanted MOS light emitting devices
EMRS 2013 Spring Meeting, 27.-31.05.2013, Strasbourg, France

81. Reinicke, S.; Akhmadaliev, C.; Bemmerer, D.; Zuber, K.
Entwicklung einer Terminal-Ionenquelle für den 5MV Pelletron-Beschleuniger im Dresdner Felsenkeller
DPG Frühjahrstagung, 04.-08.03.2013, Dresden, Germany

82. Ritter, R.; Wilhelm, R. A.; Stöger-Pollach, M.; Mücklich, A.; Werner, U.; Beyer, A.; Facsko, S.; Gölzhäuser, A.; Aumayr, F.
Nanopores milled in carbon nanomembranes due to impact of individual slow highly charged ions
1st Bielefeld Workshop on Nanolayers and Artificial Membranes, 04.-06.02.2013, Bielefeld, Germany

83. Roshchupkina, O. D.; Baehtz, C.; Facsko, S.; Bischoff, L.; Posselt, M.; Grenzer, J.
In-situ ion beam irradiation: X-ray scattering & diffraction experiments
9th Autumn School on X-ray Scattering from Surfaces and Thin Layers, 25.-28.09.2013, Smolenice, Slovakia

84. Rugel, G.; Akhmadaliev, Sh.; Merchel, S.; Pavetich, S.; Renno, A.; Ziegenrücker, R.
Höchstsensitiver Nachweis von Radionukliden mit der Dresdner AMS (DREAMS)
7. Workshop RCA, 10.-11.06.2013, Dresden, Rossendorf, Germany

85. Schmidt, K.; Akhmadaliev, C.; Anders, M.; Bemmerer, D.; Boretzky, K.; Caciolli, A.; Degering, D.; Dietz, M.; Dressler, R.; Elekes, Z.; Fülöp, Z.; Gyürky, G.; Hannaske, R.; Junghans, A. R.; Marta, M.; Menzel, M.-L.; Munnik, F.; Schumann, D.; Schwengner, R.; Szücs, T.; Wagner, A.; Yakorev, D.; Zuber, K.
Precise study of the supernova reaction ^{40}Ca(_α,γ) ^{44}Ti by activation and in-beam γ-spectroscopy

Workshop on "Open problems and future directions in heavy element nucleosynthesis", 10.-12.04.2013, Debrecen, Hungary

86. Schmidt, K.; Akhmadaliev, C.; Anders, M.; Bemmerer, D.; Boretzky, K.; Caciolli, A.; Degering, D.; Dietz, M.; Dressler, R.; Elekes, Z.; Fülöp, Z.; Gyürky, G.; Hannaske, R.; Junghans, A. R.; Marta, M.; Menzel, M.-L.; Munnik, F.; Schumann, D.; Schwengner, R.; Szücs, T.; Wagner, A.; Yakorev, D.; Zuber, K.
Precise study of the supernova reaction ^{40}Ca(α,γ) ^{44}Ti by activation and in-beam γ-spectroscopy
25th International Nuclear Physics Conference (INPC 2013), 02.-07.06.2013, Florence, Italy

87. Schmidt, K.; Akhmadaliev, C.; Anders, M.; Bemmerer, D.; Boretzky, K.; Caciolli, A.; Dietz, M.; Elekes, Z.; Fülöp, Z.; Gyürky, G.; Hannaske, R.; Junghans, A. R.; Marta, M.; Menzel, M.-L.; Schwengner, R.; Szücs, T.; Wagner, A.; Wagner, L.; Yakorev, D.; Zuber, K.
Untersuchung der ^{40}Ca(α,γ)^{44}Ti-Reaktion mittels Aktivierungsmessung im Felsenkeller Dresden
DPG Frühjahrstagung Dresden 2013, 04.-08.03.2013, Dresden, Germany

88. Schneider, H.; Winnerl, S.; Helm, M.
Mid-infrared and terahertz free-electron laser spectroscopy of zero- and two-dimensional semiconductors
41st Freiburg Infrared Colloquium, 26.-27.02.2013, Freiburg, Germany

89. Skrotzki, R.; Herrmannsdörfer, T.; Schönemann, R.; Heera, V.; Fiedler, J.; Kampert, E.; Wolf-Fabris, F.; Philipp, P.; Bischoff, L.; Voelskow, M.; Mücklich, A.; Schmidt, B.; Skorupa, M.; Helm, M.; Wosnitza, J.
Superconductivity and magneto-resistance oscillations in amorphous Ga films
11th European Conference on Applied Superconductivity - EUCAS 2013, 15.-19.09.2013, Genua, Italy

90. Sluka, V.; Kákay, A.; Deac, A. M.; Bürgler, D. E.; Schneider, C. M.; Hertel, R.
Resonance fine-splitting in a spin-torque nano-oscillator containing two stacked vortices
8th International Symposium on Metallic Multilayers (MML2013), 19.-24.05.2013, Kyoto, Japan

91. Smith, T.; Leya, I.; Merchel, S.; Rugel, G.; Pavetich, S.
Studying the constancy of galactic cosmic rays using noble gas and radionuclides data on iron meteorites
Joint meeting "Paneth Kolloquium" and workshop of the DFG special program "The first 10 million years of the solar system" (DFG SPP 1385), 21.-23.10.2013, Nördlingen, Germany

92. Viehrig, H.-W.; Altstadt, E.; Houska, M.; Valo, M.
Fracture mechanics and mechanical characterization of the beltline welding seam of the decommissioned WWER-440 reactor pressure vessels of nuclear power plant Greifswald Unit 4
26th Symposium on the Effects of Radiation on Nuclear Materials, 12.-13.06.2013, Indianapolis, USA

93. Viehrig, H.-W.; Houska, M.; Kalkhof, D.; Schindler, H.-J.
Bruchmechanische Bewertung von Reaktordruckbehälter Mehrlagenschweißnähten
45. Tagung DVM-Arbeitskreis Bruchvorgänge, Bruchmechanische Werkstoff- und Bauteilbewertung: Beanspruchungsanalyse, Prüfmethoden und Anwendungen, 19.-20.02.2013, Berlin, Germany

94. Viehrig, H.-W.; Houska, M.; Mottitschka, T.; Grundmann, N.; Trupitz, P.; Bär, W.; Gerwien, P.; Lucon, E.
Bestimmung der J-Risswiderstandskurve an einem zähen Reaktordruckbehälterstahl - Ergebnisse eines Round Robin Tests
45. Tagung DVM-Arbeitskreis Bruchvorgänge, Bruchmechanische Werkstoff- und Bauteilbewertung: Beanspruchungsanalyse, Prüfmethoden und Anwendungen, 19.-20.02.2013, Berlin, Germany

95. von Borany, J.; Munnik, F.; Neelmeijer, C.; Renno, A.; Merchel, S.
Ionenstrahlverfahren für die Element- und Spurenanalytik in Festkörpern
Workshop " Analyse von Spurenverunreinigungen auf Oberflächen und in Gasen", 03.12.2013, Dresden, Germany

96. Wagner, A.; Chaouadi, R.; Bergner, F.; Viehrig, H.-W.
On the acceleration of the microstructure evolution detected by SANS in low-Cu RPV steels
17th Meeting of the IGRDM, 19.-24.05.2013, Les Embiez, France

97. Wang, Y.; Chen, X.; Li, L.; Shalimov, A.; Tong, W.; Prucnal, S.; Munnik, F.; Yang, Z.; Skorupa, W.; Helm, M.; Zhou, S.
Structural and magnetic properties of irradiated SiC
The 58th Annual Magnetism and Magnetic Materials (MMM) Conference, 04.-08.11.2013, Denver, USA

98. Wenisch, R.; Gemming, S.; Abrasonis, G.
Nickel induced crystallization of carbon during deposition
DPG Spring Meeting of the Condensed Matter Section 2013, 10.-15.03.2013, Regensburg, Germany

99. Wilde, C.; Schmidt, B.; Vinnichenko, M.; Gemming, S.
Work function determination of degenerately Al-doped ZnO by thermionic emission
DPG Spring Meeting of the Condensed Matter Section 2013, 10.-15.03.2013, Regensburg, Germany

100. Winnerl, S.; Hubrich, R.; Mittendorff, M.; Schneider, H.; Helm, M.
Longitudinal fields in focused terahertz beams
DPG Spring Meeting of the Condensed Matter Section 2013, 10.-15.03.2013, Regensburg, Germany

101. Winnerl, S.; Hubrich, R.; Mittendorff, M.; Schneider, H.; Helm, M.
Longitudinal fields in focused terahertz beams
38th International Conference on Infrared, Millimeter and Terahertz Waves, 01.-06.09.2013, Mainz, Germany

102. Winnerl, S.; Hubrich, R.; Mittendorff, M.; Schneider, H.; Helm, M.
Longitudinal THz fields and their phase relation with respect to transverse fields
International Workshop on Terahertz Science and Technology, 01.-05.04.2013, Kyoto, Japan

103. Wintz, S.; Bunce, C.; Neudert, A.; Körner, M.; Strache, T.; Buhl, M.; Erbe, A.; Gemming, S.; Raabe, J.; Quitmann, C.; Fassbender, J.
Pairs of effective spin merons in ferromagnetic multilayer elements
58th Conference on Magnetism and Magnetic Materials (MMM), 04.-08.11.2013, Denver, USA

104. Wintz, S.; Bunce, C.; Neudert, A.; Körner, M.; Strache, T.; Buhl, M.; Erbe, A.; Gemming, S.; Raabe, J.; Quitmann, C.; Fassbender, J.
Effective spin meron pairs in ferromagnetic multilayers
Joint European Magnetic Symposia 2013, 25.-30.08.2013, Rhodos, Greece

105. Wintz, S.; Erbe, A.; Lindner, J.; Weigand, M.; Stoll, H.; Schütz, G.; Raabe, J.; Quitmann, C.; Tyberkevych, V.; Slavin, A.; Fassbender, J.
Coherent spin wave emission from magnetic vortex cores
The 8th International Symposium on Magnetic Multilayers (MML) 2013, 19.-24.05.2013, Kyoto, Japan

106. Wintz, S.; Weigand, M.; Stoll, H.; Schütz, G.; Raabe, J.; Quitmann, C.; Lindner, J. ; Erbe, A.; Fassbender, J.
Direct imaging of spin wave emission from magnetic vortex cores
12th Joint MMM/Intermag Conference, 14.-18.01.2013, Chicago, USA

107. Wintz, S.; Weigand, M.; Tyberkevych, V. S.; Slobodianiuk, D. V.; Stoll, H.; Raabe, J.; Erbe, A.; Lindner, J.; Slavin, A. N.; Fassbender, J.
Linear excitation of short propagating spin waves in a pair of layered vortices with opposite circulation
International Symposium on Spin Waves 2013, 09.-15.06.2013, St. Petersburg, Russia

108. Yankov, R.; Bleicher, F.; Bortolotto, L.; Geiger, G.; Kolitsch, A.; Langlade, C.; Masset, P.; Paul, J.; Pelic, B.; Pyczak, F.; Rafaja, D.; Schumacher, P.; Schütze, M.; Wolf, G.
Surface modification of protective coatings on titanium aluminides by plasma immersion ion implantation of fluorine to suppress environmental embrittlement at high temperatures

12th International Workshop on Plasma Based Ion Implantation and Deposition (PBII&D 2013), 01.-05.07.2013, Poitiers, France

109. Zahn, P.; Gemming, S.
Spin Nernst angle: Definition and qualitative estimate for Cu alloys
DPG Spring Meeting of the Condensed Matter Section 2013, 10.-15.03.2013, Regensburg, Germany

Posters

1. Akhmadaliev, Sh.; Heller, R.; Munnik, F.; Neelmeijer, C.; Abrasonis, G.; Rugel, G.; Pavetich, S.; Ziegenrücker, R.; Renno, A. D.; Merchel, S.; Kolitsch, A.; von Borany, J.
The 6 MV tandem accelerator and its applications at HZDR
ECAART11 - the 11th European Conference on Accelerators in Applied Research and Technology, 09.-13.09.2013, Namur, Belgium

2. Aleksandrov, Y.; Fowley, C.; Bernert, K.; Sluka, V.; Kowalska, E.; Farle, M.; Lindner, J.; Ocker, B.; Fassbender, J.; Deac, A. M.
Ferromagnetic resonance of perpendicular magnetic anisotropy MgO/CoFeB based tri-layers
IHRS NanoNet Annual Workshop 2013, 10.10.2013, Dresden, Germany

3. Aleksandrov, Y.; Fowley, C.; Bernert, K.; Sluka, V.; Kowalska, E.; Farle, M.; Lindner, J.; Ocker, B.; Fassbender, J.; Deac, A. M.
Ferromagnetic resonance of perpendicular magnetic anisotropy MgO/CoFeB based tri-layers
The 58th Annual Magnetism and Magnetic Materials (MMM) Conference, 04.-08.11.2013, Denver, Colorado, USA

4. Bali, R.; Wintz, S.; Meutzner, F.; Huebner, R.; Boucher, R.; Uenal, A. A.; Valencia, S.; Neudert, A.; Potzger, K.; Bauch, J.; Kronast, F.; Facsko, S.; Lindner, J.; Fassbender, J.
Printing nearly-discrete magnetic patterns using chemical disorder induced ferromagnetism
Joint European Magnetism Symposia, 25.-30.08.2013, Rhodos, Greece

5. Banholzer, A.; Wintz, S.; Fowley, C.; Deac, A.; Raabe, J.; Lenz, K.; Lindner, J.; Fassbender, J.
***In-situ* STXM imaging and resistance measurements of trilayer vortices**
17. Deutsche Physikerinnentagung, 31.10.-03.11.2013, Heidelberg, Germany

6. Bhattacharyya, J.; Zybell, S.; Winnerl, S.; Schneebeli, L.; Böttge, C. N.; Bredderman, B.; Kira, M.; Koch, S. W.; Helm, M.; Schneider, H.
Control of Coulomb-mediated excitonic 2s emission by an external magnetic field
International Workshop on Optical Terahertz Science and Technology 2013, 01.-05.04.2013, Kyoto, Japan

7. Blaschke, D.; Zahn, P.; Gemming, S.; Cornelius, S.; Scholz, A.; Skorupa, I.; Scheumann, B.; Potzger, K.
Memristive effects in titanium dioxide
Functional oxides for emerging technologies, 14.-18.10.2013, Bremen, Germany

8. Bogusz, A.; Blaschke, D.; Skorupa, I.; Scholz, A.; Schmidt, Oliver G.; Schmidt, H.
Resistive switching properties of multiferroic $YMnO_3$
6th European School on Multiferroics (ESMF6), 21.-26.07.2013, Wittenberg, Germany

9. Deb, D.; Grebing, J.; Erbe, A.; Helm, M.
Development of gated single molecules using reconfigurable SiNWs (by top-down process)
539. WE-Haraeus- Seminar Micro- and nanostructured interfaces for Biological and Medical Research, 30.06.-03.07.2013, Physikzentrum Bad Honnef, Germany.

10. Deb, D.; Helm, M.; Erbe, A.; Grebing, J.
Development of gated single molecule contacts using reconfigurable SiNWs (by top-down process)
IHRS NanoNet Annual Workshop 2013, 10.10.2013, Dresden, Germany

11. Eder, F. M.; Neelmeijer, C.; Pearce, N. J. G.; Sterba, Johannes H.; Bichler, M.; Merchel, S.
OLDAPS – Obsidian least destructive analysis provenancing system
13th International Conference on Particle Induced X-ray Emission and its Analytical Applications (PIXE), 03.-08.03.2013, Gramado, Brazil

12. Fowley, C.; Sluka, V.; Bernert, K.; Gan, H.; Fassbender, J.; Rippard, W. H.; Pufall, M. R.; Russek, S. E.; Deac, A.-M.
Effect of an in-plane field on microwave dynamics in point contact spin valve structures combining inplane and out-of-plane magnetic layers
12th Joint MMM/Intermag Conference, 14.-18.01.2013, Chicago, IL, USA

13. Germer, S.; Rebohle, L.; Skorupa, W.; Helm, M.
Si-based light emitter in an integrated photonic circuit for smart biosensor applications
Mircotechnologies, 24.-26.04.2013, Grenoble, France

14. Green, B.; Kovalev, S.; Hauser, J.; Kuntzsch, M.; Al-Shemmary, A.; Schneider, H.; Winnerl, S.; Seidel, W.; Zvyagin, S.; Wall, S.; Radu, I.; Eng, L. M.; Lehnert, U.; Helm, M.; Stojanovic, N.; Heberle, J.; Cavalleri, A.; Michel, P.; Gensch, M.
TELBE - the super-radiant THz test-facility at ELBE
77. Jahrestagung der DPG und DPG-Frühjahrstagung, 04.-08.03.2013, Dresden, Germany

15. Guillen, E.; Heras, I.; Abrasonis, G.; Pardo, A.; Krause, M.; Endrino, J. L.
Optical selectivity enhancement of carbon-based nanocomposites: Simulation and experiments
537th Wilhelm and Else Heraeus Seminar Physics of Ionized and Ion-Assisted PVD: Principles and Current Trends, 26.-28.06.2013, Dresden, Germany

16. Heidarian, A.; Potzger, K.; Lindner, J.; Heller, R.; Wilhelm, R.; Grenzer, J.; Reuther, H.; Bali, R.
Magnetic and structural properties of equiatomic FeRh thin films
The IEEE Magnetics Society Summer School, 09.-14.06.2013, Assisi, Italy

17. Heidarian, A.; Potzger, K.; Lindner, J.; Heller, R.; Wilhelm, R.; Grenzer, J.; Reuther, H.; Bali, R.
Magnetic and structural properties of equiatomic FeRh thin films
Joint European Magnetic Symposia (JEMS 2013), 25.-30.08.2013, Rhodes, Greece

18. Heidarian, A.; Potzger, K.; Lindner, J.; Heller, R.; Wilhelm, R.; Grenzer, J.; Reuther, H.; Bali, R.
Preparation of equiatomic FeRh thin films by MBE
DPG Spring Meeting of the Condensed Matter Section 2013, 10.-15.03.2013, Regensburg, Germany

19. Heintze, C.; Bergner, F.; Hernandez Mayoral, M.
Nanoindentation of ion-irradiated Fe-Cr alloys
Nano Measure 2013, 25.-26.06.2013, Warsawa, Poland

20. Heintze, C.; Bergner, F.; Hernandez Mayoral, M.
Ion-irradiation induced damage in Fe-Cr alloys characterized by nanoindentation
Getmat International Workshop, 17.-19.09.2013, Berlin, Germany

21. Heras, I.; Escobar Galindo, R.; Abrasonis, G.; Pardo, A.; Vinnichenko, M.; Endrino, J. L.
Advanced solar absorber coatings based on nanocomposites
2013 MRS Spring Meeting & Exhibit, 01.-05.04.2013, San Francisco, CA, USA

22. Hilger, I.; Bergner, F.; Weißgärber, T.; Garcia-Junceda, A.; Palasse, L.
Microstructural properties of spark plasma sintered ODS Fe-^{14}Cr alloys
GETMAT final workshop, 17.09.2013, Berlin, Germany

23. Hilger, I.; Heintze, C.; Bergner, F.; Ulbricht, A.; Weißgärber, T.; Garcia-Junced, A.; Palasse, L.
Ferritische ODS Stähle für die Kernfusion
4. Dresdner Werkstoffsymposium, 18.11.2013, Dresden, Germany

24. Hübner, R.; Friedrich, D.; Wolf, D.; Liedke, B.; Schmidt, B.; Heinig, K.-H.
Morphology studies of Si-SiO_2 nanocomposites using energy-filtered transmission electron microscopy
Microscopy Conference 2013, 25.-30.08.2013, Regensburg, Germany

25. Kelling, J.; Heinig, K.-H.
Large scale atomistic simulations on nanostructure evolution

DPG Spring Meeting of the Condensed Matter Section 2013, 10.-15.03.2013, Regensburg, Germany

26. Kelling, J.; Gemming, S.
Ab-initio investigation of carbides and of CNT junctions at finite temperature and under stress
IHRS NanoNet Annual Workshop 2013, 10.10.2013, Dresden, Germany

27. Klein, F.; Philipp, P.; Bischoff, L.; Mühl, T.
Scanning tunnelling spectroscopy of FIB-induced local phase changes in tetrahedral amorphous-carbon
DPG Spring Meeting of the Condensed Matter Section 2013, 10.-15.03.2013, Regensburg, Germany

28. König, G.; Thorn, M.; Zschornack, J.; Schmidt, A.
A compact, versatile low-energy electron beam ion source
International Conference on Ion Sources 2013, 09.09.2013, Chiba, Japan

29. Kowalska, E.; Bernert, K.; Aleksandrov, Y.; Fowley, C.; Sluka, V.; Mangin, S.; Lindner, J.; Fassbender, J.; Deac, A. M.
Thermally excited ferromagnetic resonance in MgO-based magnetic tunnel junctions
The IEEE Magnetics Society Summer School, 09.-14.06.2013, Assisi, Italy

30. Krause, M.; Buljan, M.; Oates, T. W. H.; Mücklich, A.; Fritzsche, M.; Facsko, S.; Zschornak, M.; Wintz, S.; Endrino, J. L.; Baehtz, C.; Shalimov, A.; Gemming, S.; Abrasonis, G.
Ion-guided microstructure evolution of carbon-nickel nanocomposite films during ion beam assisted deposition: 3D sculpting at the nanoscale
537th Wilhelm and Else Heraeus Seminar Physics of Ionized and Ion-Assisted PVD: Principles and Current Trends, 26.-28.06.2013, Dresden, Germany

31. Krause, M.; Haluska, M.; Kunze, T.; Mücklich, A.; Hübner, R.; Melkhanova, S.; Bayrak, T.; Abrasonis, G.; Gemming, S.
SWCNT growth from C:Ni nanocomposite templates
DPG Spring Meeting of the Condensed Matter Section 2013, 10.-15.03.2013, Regensburg, Germany

32. Krause, M.; Haluska, M.; Kunze, T.; Mücklich, A.; Hübner, R.; Melkhanova, S.; Bayrak, T.; Abrasonis, G.; Gemming, S.
SWCNT growth from C:Ni nanocomposite templates
27th International Winterschool on Electronic Properties of Novel Materials (IWEPNM), 02.-09.03.2013, Kirchberg, Austria

33. Langer, M.; Bali, R.; Kowalska, E.; Neudert, A.; Lenz, K.; Potzger, K.; Kostylev, M.; Lindner, J.; Adeyeye, A.; Fassbender, J.
Magnetization reversal mechanisms in Co-antidot arrays
DPG Spring Meeting of the Condensed Matter Section 2013, 10.-15.03.2013, Regensburg, Germany

34. Langer, M.; Gallardo, R.; Lenz, K.; Banholzer, A.; Grebing, J.; Körner, M.; Landeros, P.; Lindner, J.; Fassbender, J.
Two-magnon scattering and mode-splitting in 1-dimensional quasi-magnonic crystals
IEEE Magnetics Society Summer School 2013, 10.06.2013, Assisi, Italy

35. Lenz, K.; Gallardo, R. A.; Bali, R.; Neudert, A.; Banholzer, A.; Wagner, K.; Langer, M.; Körner, M.; Grebing, J.; Lindner, J.; Landeros, P.; Fassbender, J.
Spinwaves in nanostructures: The transition from periodical perturbations to magnonic crystals
Yamada Conference LXVII -The 8th International Symposium on Metallic Multilayers (MML2013), 19.-24.05.2013, Kyoto, Japan

36. Lenz, K.; Körner, M.; Gallardo, R. A.; Banholzer, A.; Facsko, S.; Lindner, J.; Landeros, P.; Fassbender, J.
Two-magnon scattering in the transition from periodical perturbations to magnonic crystals
3rd international conference on magnonics 2013, 04.-08.08.2013, Varberg, Sweden

37. Lomakina, F.; Drachenko, O.; Schneider, H.; Patanè, A.; Hopkinson, M.; Helm, M.
Investigation of the effective mass in GaAsN
20th International Conference on Electronic Properties of Two-Dimensional Systems (EP2DS-20) and 16th International Conference on Modulated Semiconductor Structures (MSS-16), 01.-05.07.2013, Wroclaw, Poland

38. Lomakina, F.; Drachenko, O.; Schneider, H.; Patanè, A.; Hopkinson, M.; Helm, M.
Investigation of the effective mass in dilute nitride semiconductors
DPG Spring Meeting of the Condensed Matter Section 2013, 10.-15.03.2013, Regensburg, Germany

39. Mährlein, S.; Radu, I.; Gensch, M.; Kimel, A.; Kalashnikova, A.; Kampfratth, T.; Wolf, M.
Driving magnetization dynamics via mid-infrared phonon excitation
DPG Spring Meeting of the Condensed Matter Section 2013, 10.-15.03.2013, Regensburg, Germany

40. Meriaux, A.-S.; Delunel, R.; Merchel, S.; Finkel, R.
Evidences for a more restricted Icelandic ice cap re-advance after the Bølling warming period
EGU General Assembly 2013, 07.-12.04.2013, Vienna, Austria

41. Michalak, P. P.; Renno, A. D.; Merchel, S.; Munnik, F.
Homogeneity testing of natural candidate reference materials for resource technology by three spatially-resolved X-ray methods
ANAKON 2013, 04.-07.03.2013, Essen, Germany

42. Michalak, P.-P.; Uecker, R.; Galazka, Z.; Munnik, F.; Renno, A. D.; Merchel, S.
Synthesis of multi trace element doped $Fe_{0.6}Mn_{0.4}Ta_2O_6$ tantalite reference crystals by Czochralski method
17th International Conference on Crystal Growth and Epitaxy (ICCGE-17), 11.-16.08.2013, Warszawa, Poland

43. Nazarov, A. N.; Tiagulskyi, S. I.; Tygulskyy, I. P.; Lysenko, V. S.; Rebohle, L.; Skorupa, W.
Hot electron effect on charge formation in SiO_2 layer enriched by rare-earth based nanoclusters
17th International conference on radiation effects in insulators, 30.06.-05.07.2013, Helsinki, Finland

44. Oertel, J.; Keller, A.; Weiss, S.; Stellato, F.; Barty, A.; Fahmy, K.
A biochemical approach to single particle X-FEL studies on membrane proteins
Kick-off meeting for the HIBEF User Consortium, 02.-05.06.2013, Hamburg, Germany

45. Ou, X.; Kögler, R.; Zhou, H.; Anwand, W.; Grenzer, J.; Hübner, R.; Voelskow, M.; Butterling, B.; Zhou, S.; Skorupa, W.
Formation of radiation damage and helium release in yttria-stabilized zirconia
E-MRS 2013 Spring Meeting, 27.-31.05.2013, Strasbourg, France

46. Ou, X.; Shuai, Y.; Luo, W.; Kögler, R.; Fiedler, J.; Reuther, H.; Zhou, S.; Hübner, R.; Facsko, S.; Helm, M.; Schmidt, H.
Tuning the resistive switching characteristics of $BiFeO_3$ by Ar^+ irradiation
European Materials Research Society Conference, 27.-31.05.2013, Strasbourg, France

47. Ozen, E.; Gundogdu, S.; Keles, U.; Bulutay, C.; Aydinli, A.; Heinig, K.-H.; Rigato, V.
Si nanocrystal networks for photovoltaic applications
2013 MRS Spring Meeting, Symposium R: Nanostructured Semiconductors and Nanotechnology, 01.-05.04.2013, San Francisco, USA

48. Pavetich, S.; Akhmadaliev, Sh.; Merchel, S.; Rugel, G.
Ultrasensitive Bestimmung von Radionukliden Mittels Beschleunigermassenspektrometrie bei DREAMS am Beispiel von ^{36}Cl
7. Workshop RCA, 10.-11.06.2013, Dresden, Germany

49. Posselt, M.
Confinement effects in solid phase recrystallization of silicon nanowires
2013 MRS Fall Meeting & Exhibit, Symposium SS, 01.-06.12.2013, Boston, USA

50. Posselt, M.; Devaraj, M.
Structure and energetics of oxidic nanoclusters in bcc-iron
EUROMAT 2013, 08.-13.09.2013, Sevilla, Spain

51. Posselt, M.; Devaraj, M.
Structure and energetics of oxidic nanoclusters in bcc-iron
GETMAT Int. Workshop, 17.-19.09.2013, Berlin, Germany

52. Prucnal, S.; Zhou, S. Q.; Bregolin, F. L.; Ou, X.; Liedke, M. O.; Huebner, R.; Helm, M.; Zuk, J.; Turek, M.; Pyszniak, K.; Drozdziel, A.; Skorupa, W.
Millisecond-range liquid phase recrystallization for III-V/Si heteronanojunction fabrication
16th International Conference on Modulated Semiconductor Structures, MSS-16, 01.-05.07.2013, Wroclaw, Poland

53. Ritter, E.; Zschornack, G.; Schmidt, M.; Schwan, A.
EBIS for the use in second generation synchrotron for medical particle therapy
International Conference on Ion Sources 2013, 09.09.2013, Chiba, Japan

54. Rugel, G.; Akhmadaliev, S.; Merchel, S.; Pavetich, S.; Renno, A.; Ziegenrücker, R.
Setting-up a Super-SIMS at DREAMS
DPG-Frühjahrstagung der Sektion AMOP (SAMOP), 18.-22.03.2013, Hannover, Germany

55. Schmidt, J.; Teich, M.; Wagner, M.; Winnerl, S.; Stehr, D.; Schneider, H.; Helm, M.
THz spectroscopy of optically excited InGaAs quantum wells in the high charge-carrier density regime
OTST 2013: International Workshop on Optical Terahertz Science and Technology 2013, 01.-05.04.2013, Kyoto, Japan

56. Schmidt, M.; Zschornack, G.; Kentsch, U.; Ritter, E.
Permanent magnet electron beam ion source/trap systems with bakeable magnets for improved operation conditions
International Conference on Ion Sources 2013, 09.09.2013, Chiba, Japan

57. Seidel, W.; Drachenko, O.; Gensch, M.; Helm, M.; Kuntzsch, M.; Justus, M.; Lehnert, U.; Michel, P.; Mittendorff, M.; Schneider, C.; Schneider, H.; Schurig, R.; Teich, M.; Teichert, J.; Winnerl, S.
The THz user facility FELBE at the radiation source ELBE of Helmholtz-Zentrum Dresden-Rossendorf
The 38th International Conference on Infrared, Millimeter and Terahertz Waves, 01.-06.09.2013, Mainz, Germany

58. Sendler, T.; Wieser, M.; Liu, S.-P.; Weisbrod, S.; Tang, Z.; Marx, A.; Wolf, J.; Kuhn, T.; Scheer, E.; Moresco, F.; Grebing, J.; Erbe, A.
Electrical characterization of single organic molecules via mechanically controllable break junctions
DPG Spring Meeting of the Condensed Matter Section 2013, 10-15.03.2013, Regensburg, Germany

59. Sendler, T.; Wieser, M.; Wolf, J.; Huhn, T.; Scheer, E.; Moresco, F.; Grebing, J.; Erbe, A.
Electrical characterization of single organic molecules via mechanically controllable break junctions
IHRS NanoNet Annual Workshop 2013, 10.10.2013, Dresden, Germany

60. Skrotzki, R.; Herrmannsdörfer, T.; Schönemann, R.; Heera, V.; Fiedler, J.; Kampert, E.; Wolff-Fabris, F.; Philipp, P.; Bischoff, L.; Voelskow, M.; Mücklich, A.; Schmidt, B.; Skorupa, W.; Helm, M.; Wosnitza, J.
Superconductivity in Ge and Si via Ga-ion implantation
DPG Spring Meeting of the Condensed Matter Section 2013, 10-15.03.2013, Regensburg, Germany

61. Sluka, V.; Fowley, C. J.; Bernert, K.; Gan, H.; Fassbender, J.; Deac, A. M.
Current-induced magnetization dynamics in a spin-valve comprising two spin-transfer torque-coupled ferromagnetic layers
12th Joint MMM/Intermag Conference, 14.-18.01.2013, Chicago, USA

62. Stößer, R.; Feist, M.; Willgeroth, C.; Emmerling, F.; Menzel, M.; Reuther, H.
The "quiet" Goldschmidt reaction $2Al + \alpha\text{-}Fe_2O_3 \rightarrow 2Fe + \alpha\text{-}Al_2O_3$

International Conference on the Applications of the Mossbauer Effect - 2013, 01.-06.09.2013, Opatija, Croatia

63. Teich, M.; Schneider, H.; Bhattacharyya, J.; Winnerl, S.; Wilson, L.; Helm, M.
Inter-sublevel dephasing in quantum dots
38th International Conference on Infrared, Millimeter, and Terahertz Waves (IRMMW-THz 2013), 01.-06.09.2013, Mainz, Germany

64. Teshome, B.; Facsko, S.; Keller, A.
Topography-controlled alignment of DNA origami nanotubes on nanopatterned surfaces
IHRS NanoNet Annual Workshop 2013, 10.10.2013, Dresden, Germany

65. Ulbricht, A.; Török, G.; Gillemot, F.; Bergner, F.; Wagner, A.
Analysis of SANS measurements on highly irradiated15H2MFA steel
International Conference on Neutron Scattering, 08.-12.07.2013, Edinburgh, United Kingdom

66. Wagner, A.; Ulbricht, A.; Bergner, F.
Robust Monte-Carlo fitting of small-angle neutron scattering curves for determining cluster-size distributions
German Neutron Scattering Conference, 24.-26.09.2013, Bonn, Germany

67. Warnatz, T.; Wintz, S.; Bali, R.; Wiesenhütter, U.; Grebing, J.; Lindner, J.; Fassbender, J.; Erbe, A.
Measurement of magnetoresistance effects in nanoscale metallic conductors
DPG Spring Meeting of the Condensed Matter Section 2013, 10.-15.03.2013, Regensburg, Germany

68. Wenisch, R.; Hübner, R.; Krause, M.; Gemming, S.; Abrasonis, G.
Nickel induced crystallization of carbon during deposition
2013 MRS Fall Meeting & Exhibit, 01.-06.12.2013, Boston, USA

69. Winnerl, S.; Mittendorff, M.; Kamann, J.; Eroms, J.; Weiss, D.; Schneider, H.; Helm, M.
Ultrafast graphene-based terahertz detector
Graphene Week, 02.-07.06.2013, Chemnitz, Germany

70. Winnerl, S.; Mittendorff, M.; Winzer, T.; Wendler, F.; Malic, E.; Knorr, A.; Orlita, M.; Potemski, M.; Berger, C.; de Heer, W. A.; Schneider, H.; Helm, M.
Relaxation dynamics of graphene investigated in the mid-infrared and THz spectral range
International Workshop on Terahertz Science and Technology, 01.-05.04.2013, Kyoto, Japan

71. Wintz, S.; Weigand, M.; Tyberkevych, V. S.; Slobodianiuk, D. V.; Stoll, H.; Raabe, J.; Neudert, A.; Erbe, A.; Lindner, J.; Slavin, A. N.; Fassbender, J.
Linear excitation of short propagating spin waves via a pair of layered vortex cores
Gordon Research Conferences: Spin Dynamics in Magnetic Nanostructures, 18.08.2013, Hong Kong, China

72. Xu, M.; Mittendorff, M.; Dietz, R.; Göbel, T.; Schneider, H.; Helm, M.; Winnerl, S.
InGaAs-based large area photoconductive emitters for 1.55 µm excitation
38th International Conference on Infrared, Millimeter and Terahertz Waves, 01.-06.09.2013, Mainz, Germany

73. Yadav, R. K.; Abrasonis, G.; Munnik, F.; Heller, R.; Hübner, R.; Möller, W.; Neidhardt, J.
Growth of carbon-tungsten nanocomposites by high power impulse magnetron sputtering from compound targets
537th Wilhelm and Else Heraeus Seminar Physics of Ionized and Ion-Assisted PVD: Principles and Current Trends, 26.-28.06.2013, Dresden, Germany

74. Yankov, R.; Kolitsch, A.; Johannes, V. B.; Donchev, A.; Bortolotto, L.; Masset, P.; Schütze, M.
Oxidation protection coatings for titanium, titanium-base alloys and titanium aluminides in high-temperature oxidizing environments
EUROMAT2013 - European Congress and Exhibition on Advanced Materials and Processes, 08.-13.09.2013, Sevilla, Spain

75. Yankov, R.; Kolitsch, A.; Johannes, V. B.; Masset, P.; Bortolotto, L.; Donchev, A.; Schütze, M.
Surface engineering of gamma-titanium aluminide alloys for combined improvements in environmental durability at elevated temperatures

International Workshop on Gamma TiAl Alloy Technology (GAT 2013), 11.-14.06.2013, Toluese, France

76. Yildirim, O.; Cornelius, S.; Vinnichenko, M.; Buterling, M.; Wagner, A.; Smekhova, A.; Potzger, K.
Magnetic and defect-properties of Co implanted TiO_2
DPG Spring Meeting of the Condensed Matter Section 2013, 10.-15.03.2013, Regensburg, Germany

77. Yildirim, O.; Cornelius, S.; Vinnichenko, M.; Buterling, M.; Wagner, A.; Smekhova, A.; Potzger, K.
Magnetic and defect-properties of Co implanted TiO_2
International Conference on Nanoscale Magnetism, 02.-06.09.2013, Istanbul, Turkey

78. Zahn, P.; Gemming, S.; Potzger, K.; Schmidt, H.; Mikolajick, T.; Slesazeck, S.; Stöcker, H.; Abendroth, B.; Meyer, D. C.; Dittmann, R.; Rana, V.; Waser, R.; Ronning, C.; Spaldin, N. A.; Basov, D.
Memory effects in resistive ion-beam modified oxides
E-*MRS Spring Meeting, 27.-31.05.2013, Strasbourg, France*

79. Ziegenrücker, R.; Hanf, D.; Gutzmer, J.; Ihle, S.; Merchel, S.; Renno, A. D.; Rugel, G.; Scharf, O.; Buchriegler, J.
High-speed PIXE – schnelle Multielementanalyse mit Ionenstrahlen
Wissenschaftsforum Chemie 2013, 01.-04.09.2013, Darmstadt, Germany

80. Ziegenrücker, R.; Merchel, S.; Renno, A. D.; Rugel, G.; Akhmadaliev, S.; Wustmann, B.
Technical concepts for the operation of a Cameca 7f-Auto as ion source for the HZDR Super-SIMS
Seventh Biennial Geo-SIMS Workshop, 20.-22.08.2013, Potsdam, Germany

81. Zybell, S.; Bhattacharyya, J.; Winnerl, S.; Helm, M.; Schneider, H.
Free-electron laser spectroscopy of exciton dynamics in GaAs quantum wells
OTST 2013 - International Workshop on Optical Terahertz Science and Technology 2013, 01.-05.04.2013, Kyoto, Japan

Lectures / talks

1. Bischoff, L.
Modern developments in FIB application
Instituts-Seminar, 28.02.2013, Vienna, Austria

2. Blaschke, D.; Zahn, P.; Gemming, S.; Cornelius, S.; Scholz, A.; Skorupa, I.; Scheumann, B.; Potzger, K.
Memristive effects in thermal oxidized Ti and magnetron sputtered TiOx films
DETI.2 Midterm meeting, 09.-14.10.2013, Moscow, Russia

3. Böttger, R.; Bischoff, L.; Liedke, B.; Heinig, K.-H.; Anders, C.; Urbassek, H. M.
Surface patterning by heavy-ion induced melt pools
Symposium TU Vienna, 28.02.2013, Vienna, Austria

4. Drachenko, O.
New insight into physics of the holes in semiconductors through terahertz studies in ultra-high magnetic fields
Seminar at Laboratory Charles Coulomb &TERALAB, Université Montpellier 2 &CNRS, 22.02.2013, Montpellier, France

5. Gensch, M.
Super-radiant THz sources: Challenges and opportunities
Seminar of the Pohang Accelerator Laboratory (PAL), 24.09.2013, Pohang, South Korea

6. Gensch, M.
Super-radiant THz sources: Challenges and opportunities
Seminar of the Center for Quantum-beam-based Radiation Research, KAERI, 25.09.2013, Daejeon, South Korea

7. Gensch, M.
Quasi-cw THz source TELBE: Challenges and opportunities
FLASH Seminar, 16.07.2013, Hamburg, Germany

8. Gensch, M.
Life sciences in High THz fields: Challenges and opportunities
Visegrad Retreat of the *HAS-ELTE Molecular Biophysics Research Group, University of Budapest, 04.-05.01.2013, Budapest, Hungary*

9. Gensch, M.
Super-radiant THz sources: Challenges and opportunities
Seminar of the Department of Physics and Photon Science at the Gwangju Institute of Science and Technology (GIST), 27.09.2013, Gwangju, South Korea

10. Gensch, M.
(T)ELBE: ARD Testanlage für Diagnose an quasi - cw Elektronenstrahlen.
MDI techn. Forum / DESY, 15.02.2013, Hamburg, Germany

11. Gensch, M.
Accelerator based super-radiant THz sources: Challenges and opportunities
Seminar, Lehrstuhl für Angewandte und Experimentelle Physik, Universität Regensburg, 28.05.2013, Universität Regensburg, Germany

12. Grenzer, J.
Material science at „home“ and at the synchrotron: Investigations of nanocrystalline films
Firma PANalytical B.V., 12.09.2013, Almelo, The Netherlands

13. Grenzer, J.
Material science „at home“ and at the synchrotron
Institutskolloquium, 21.01.2013, Freiberg, Germany

14. Helm, M.
How does a free-electron laser work and why is it useful in the THz range?
Terahertz Seminar (invited talk), 30.03.2013, Osaka, Japan

15. Helm, M.
THz spectroscopy of semiconductor nanostructures with the free electron laser
TeraNano Student Seminar, 02.-03.03.2013, Würzburg, Germany

16. Hilger, I.
Oxiddispersionsverfestigte (ODS) Stähle für nukleare Anwendungen
IFAM Seminar, 22.11.2013, Dresden, Germany

17. Hübner, R.
Transmission electron microscopy @ HZDR
Kolloquium des Helmholtz-Instituts Freiberg für Ressourcentechnologie, 04.03.2013, Freiberg, Germany

18. Keller, A.
Functional DNA origami nanostructures
B CUBE Seminar, 30.01.2013, Dresden, Germany

19. Keller, A.
Functional DNA origami nanostructures
Seminar Physikalische Chemie, 09.04.2013, Potsdam, Germany

20. Kelling, J.; Heinig, K.-H.
Performing kinetic lattice Monte-Carlo simulations of far-from-equilibrium processes on GPUs
Wigner RCP Institute Seminar, 30.08.2013, MTA-TTK, Budapest, Hungary

21. Langer, M.; Neudert, A.; Osten, J.; Mönch, J. Ingolf; Mattheis, R.; Lenz, K.; Fassbender, J.; Mccord, J.
Kerr microscopy analysis of stripe elements embedded in a synthetic antiferromagnet
TU Kaiserslautern, Institutsseminar, 21.01.2013, Kaiserslautern, Germany

22. Lenz, K.
    Magnetization dynamics in periodically modulated nanostructures
    Physikalisches Kolloquium, Technische Universität Chemnitz, 30.10.2013, Chemnitz, Germany

23. Merchel, S.; Akhmadaliev, S.; Pavetich, S.; Rugel, G.; Ziegenrücker, R.; Dreams-User, D.
    Using the "good" radionuclides for dating in geo-and cosmochemistry
    Seminar Instytut Geologii, Wydział Nauk Geograficznych i Geologicznych, Uniwersytet im. Adama Mickiewicza w Poznaniu, 08.10.2013, Poznan, Poland

24. Michalak, P.-P.; Renno, A. D.; Merchel, S.; Munnik, F.; Gutzmer, J.; Uecker, R.; Galazka, Z.; Heller, H.-P.; Radtke, M.; Reinholz, U.
    In search for the real value: Freiberg strategy for obtaining reference materials for resource technology microanalysis
    Seminar Instytut Geologii, Uniwersytet im. Adama Mickiewicza, 08.10.2013, Poznan, Poland

25. Munnik, F.; Heller, R.; Hanf, D.; Buchriegler, J.; Ziegenrücker, R.; Renno, A. D.
    Ion beam analysis for geosciences
    Seminar Instytut Geologii, Uniwersytet im. Adama Mickiewicza, 08.10.2013, Poznan, Poland

26. Pavetich, S.; Akhmadaliev, Sh.; Arnold, M.; Aumaître, G.; Bourlès, D.; Buchriegler, J.; Golser, R.; Keddadouche, K.; Martschini, M.; Merchel, S.; Rugel, G.; Steier, P.
    ^{36}Cl-AMS at the DREAMS facility
    Departmental seminar at the Nuclear Physics Department of the Australian National University, 04.04.2013, Canberra, Australia

27. Schmidt, K.; Akhmadaliev, S.; Anders, M.; Bemmerer, D.; Boretzky, K.; Caciolli, A.; Dietz, M.; Elekes, Z.; Fülöp, Z.; Gyürky, G.; Hannaske, R.; Junghans, Arnd R.; Marta, M.; Menzel, M.-L.; Schwengner, R.; Szücs, T.; Wagner, A.; Wagner, L.; Yakorev, D.; Zuber, K.
    Untersuchung der Supernovareaktion ^{40}Ca(α,γ)^{40}Ti durch Aktivierung an der PTB und γ-Zählung im Felsenkeller Dresden
    Vortrag an der Physikalisch-Technische Bundesanstalt Braunschweig, 27.11.2013, Braunschweig, Germany

28. Schneider, H.
    Terahertz spectroscopy of zero- and two-dimensional semiconductors
    Seminarvortrag, Okinawa Institute of Science and Technology Graduate University, 28.03.2013, Onna, Okinawa, Japan

29. Viehrig, H.-W.
    Bewertung der Werkstoffzähigkeit im duktil-spröden Übergangsbereich
    DVM Fortbildungsseminar für Anwender der Bruchmechanik: Bruchmechanische Bewertung rissbehafteter Strukturen, 18.02.2013, Berlin, Germany

30. Winnerl, S.
    Relaxation dynamics in graphene in the terahertz spectral range
    SFB Kolloquium, 14.11.2013, Konstanz, Germany

31. Zhou, S.
    Magnetic semiconductors: Created and modified by ion beams
    Seminar at Institut für Physik, Technische Universität Chemnitz, 06.03.2013, Chemnitz, Germany

32. Zhou, S.
    Hyperdoping semiconductors by ion implantation
    Invited seminar at Southeast University and Nanjing University, Nanjing, China, 07.-08.10.2013, Nanjing, China

Conferences, workshops, colloquia and seminars

Organization of conferences and workshops

1. Abrasonis, G.; Vinnichenko, M.; Gemming, S..
   537th Wilhelm and Else Heraeus Seminar
   Physics of ionized and ion assisted PVD: Principles and current trends
   26.-28.06.2013, Dresden, Germany
2. Helm, M.; Schmidt, O.; Schmult, S.; Nagler, K.
   Deutscher MBE Workshop 2013
   30.09-01.10.2013, Dresden, Germany
3. Erbe, A.; Cordeiro, A
   IHRS NanoNet annual workshop 2013
   10.10.2013, Dresden, Germany
4. Hilger, I.; Heintze, C.
   ODISSEUS Workshop (Oxide DIspersion Strengthened Steels group of young European Scientists)
   09.-10.12.2013, Dresden, Germany
5. Jaeger, C.; Gnauck, P.; Burek, T.; Fassbender, J.; von Borany, J.
   ZEISS Crossbeam user meeting
   09.-10.12.2013, Dresden, Germany
6. Jaeger, C.; Gnauck, P.; Burek, T.; Fassbender, J.; von Borany, J.
   ZEISS ORION user meeting
   10.-11.12.2013, Dresden, Germany

Colloquia

1. Basov, Dimitri
   University of California, San Diego
   Probing correlated electron matter by infrared nano-spectroscopy and nano-imaging
   18.07.2013
2. Grundler, Dirk
   Lehrstuhl für Physik funktionaler Schichtsysteme, Technische Universität München
   Spin waves in artificial band structures of periodically patterned ferromagnets
   06.06.2013
3. Heitmann, Johannes
   Institut für Angewandte Physik, Technische Universität Bergakademie Freiberg
   Synthesis and characterization of high-k materials and embedded nanocrystals for electronic and photonic applications
   20.06.2013
4. Huber, Rupert
   Universität Regensburg
   Faster than an oscillation cycle of light
   05.12.2013
5. Huels, Michael
   Dept. of Nuclear Medicine and Radiobiology, Faculty of Medicine and Health Sciences, University of Sherbrooke, Sherbrooke, Quebec, Canada
   Does nature care what, where, or how we ionize: from molecular radiation damage induced by ions and photons to something completely different (laser applications for a radiotherapeutic “dream beam”)
   05.09.2013

6. Kampfrath, Tobias
   FHI Berlin
   Beyond body scanners: How to use terahertz pulses to observe and control spin dynamics in solids"
   18.04.2013
7. Lugstein, Alois
   Institut für Festkörperelektronik, Technische Universität Wien
   Si and Ge nanowires as building blocks for novel devices
   25.04.2013
8. Mc Henry, Michael
   Materials Science and Engineering Department, Carnegie Mellon University
   Nanocomposite magnets for energy applications
   20.08.2013
9. Meijer, Jan
   Nuclear Solid State Physics, University Leipzig
   Single ion implantation in diamond with high lateral resolution: The key technology for the fabrication of quantum devices?
   21.03.2013
10. Seyller, Thomas
    Institut für Physik, TU Chemnitz
    Epitaxial graphene on SiC: Growth, properties, and manipulation
    11.07.2013
11. Shiraishi, Masashi
    Osaka University, Japan
    Silicon spintronics
    05.03.2013
12. Takanashi, Koki
    Institute for Materials Research, Tohoku University
    Advanced spintronic materials for generation and control of spin current
    03.07.2013
13. Temst, Kristiaan
    KU Leuven, Belgium
    Exchange bias revisited: Correlating structure with magnetism in Co-CoO systems made by oxygen implantation in Co thin films
    26.09.2013
14. Wende, Heiko
    Fakultät für Physik, Experimentalphysik - AG Wende, Universität Duisburg-Essen
    Revealing the crucial interactions in spin hybrid systems
    07.11.2013

Seminars

1. Bald, Ilko
   Optische Spektroskopie und Chemical Imaging, Institut für Chemie - Physikalische Chemie, Universität Potsdam, Germany
   Physical chemistry in the DNA nanolab - from optical spectroscopy to DNA radiation damage
   04.09.2013
2. Carbone, Dina
   ESRF, Grenoble, France
   Advanced x-ray methods for nanoscience: from average to single object properties
   17.05.2013
3. Ctistis, Georgios
   University of Twente, The Netherlands

All-optical switching of semiconductor microcavities
28.10.2013

4. Erko, Alexei
Institute for Nanometre Optics and Technology, Helmholtz Zentrum Berlin, Germany
Nano-optical elements exploiting of electrical, mechanical and optical properties of artificially-made nanostructures for the time-space-energy XUV beams control
09.07.2013

5. Gareev, Rashid
University of Regensburg, Germany
Antiferromagnetically coupled tunneling nanostructures
03.07.2013

6. Girt, Erol
Simon Fraser University, Vancouver, USA
Micromagnetism and spintronics in 2D and 3D nanostructures
11.12.2013

7. Gonzales, Raquel
Instituto de Fusión Nuclear, Universidad Politécnica de Madrid, Spain
Capabilities of nanostructured W as plasma facing material in future fusion reactors
12.12.2013

8. Hlawacek, Gregor
Universität Twente, The Netherlands
UHV Helium Ion Microscopy - A high resolution tool for the nano-world
12.09.2013

9. Ignatov, Anatoly A.
Max Planck Institute for the Physics of Complex Systems, Dresden, Germany
Interaction of semiconductor superlattices with intense terahertz radiation: The role of plasmon-polariton and plasma-Bloch excitations
12.11.2014

10. Ji, Yanda
University of Electronic Science and Technology of China (UESTC), China
Preparation and characterization of Vanadium dioxide thin films
19.06.2013

11. Jin, Chaoyuan
TU Eindhoven, The Netherlands
Coupled photonic crystal cavities: From nonlocal control of emitter-photon interaction to ultrafast lasing pulse generation
23.10.2013

12. Kabiraj, Debdulal
Inter University Accelerator Centre, New Delhi/India
Composite thin films to study modifications by thermal spike induced by Swift Heavy Ions
07.10.2013

13. Kákay, Attila
Forschungszentrum Jülich, Germany
The Spin Cherenkov effect and magnonic mach cones
10.06.2013

14. Kissinger, Gudrun
Innovations for High Performance Microelectronics, Leibniz-Institut für innovative Mikroelektronik, Frankfurt (Oder), Germany
Intrinsic point defect generation, oxygen precipitation, and dislocation propagation during flash lamp annealing
27.09.2013

15. Menard, Jean-Michel
Universität Regensburg, Germany
Ultrafast THz dynamics of polaritons in strong coupling regime
23.10.2013

16. Mironov, Oleg A.
    Nano Silicon Group, Department of Physics, University of Warwick (UK), and International Laboratory of High Magnetic Fields and Low Temperatures, Wroclaw, Poland
    Ultra high mobility 2DHG in pure 20 nm Ge quantum wells with remote B-doping
    24.07.2013
17. Novikau, Andrei
    Belarusian State University, Minsk, Belarus
    Properties of silicon dioxide layers with embedded metal nanocrystals produced by oxidation of Si:Ge(Me) thin films
    18.03.2013
18. Pashkin, Aleksej
    Universität Konstanz, Germany
    Ultrafast dynamics of low-energy excitations in solids
    21.10.2013
19. Reiche, Ina
    CNRS, France
    New imaging techniques at synchrotron sources and ion beam facilities and their application in art and archaeology
    30.09.2013
20. Schäfer, Hanjo
    Universität Konstanz, Germany
    Unravelling the order parameter of a charge density wave with stimulated Raman scattering
    15.07.2013
21. Sebastian, Thomas
    Fachbereich Physik und Landesforschungszentrum OPTIMAS, TU Kaiserslautern, Germany
    Linear and nonlinear spin dynamics in $Co_2Mn_{0.6}Fe_{0.4}Si$ Heusler microstructures
    14.11.2013
22. Swoboda, Marko
    B-Cube Dresden, Germany
    Using amplitude and phase to resolve dynamics across timescales
    21.10.2013
23. Tugushev, Victor V.; Rylkov, Vladimir
    National Reseach Center "Kurchatov Institute", Moscow, Russia
    Defect-induced high-temperature ferromagnetism in silicon-manganese alloys
    26.11.2013
24. Wagner, Kai
    Universität Duisburg-Essen, Germany
    Ferromagnetic resonance characterization of periodically structured magnetic thin films
    12.09.2013
25. Wang, Xinqiang
    Peking University, China
    Epitaxy and doping of InN by molecular beam epitaxy
    03.06.2013
26. Wu, Di
    Nanjing University, China
    Enhanced electroresistance and memristive behavior in metal/ferroelectric/semiconductor tunnel junctions
    03.06.2013
27. Xu, Qingyu
    Southeast University, Nanjing, China
    Low-temperature synthesis of $K_{0.5}FeF_3$ with tunable exchange bias
    02.09.2013
28. Zakeri, Khalil
    MPI für Mikrostrukturphysik Halle, Germany

Ultrafast magnons in ultrathin ferromagnets: Excitation, propagation and relaxation
09.12.2014

29. Zichner, Ralf
Fraunhofer-Institut für Elektronische Nanosysteme ENAS, Germany
Design and manufacturing of printed layers for wave-assisted functionalization
01.11.2013

Exchange of researchers

SPIRIT visitors

1. Artac, A.
   University of Vienna, Vienna, Austria; 27.-31.07.2013
2. Auchere, F.
   Université Paris, Paris, France; 09.-11.01.2013
3. Barlak, M.
   Institute of Nuclear Chemistry and Technology, Warsaw, Poland; 04.08.-10.08.2013
4. Burgo, B.
   Université Paris, Paris, France; 09.-11.01.2013
5. Chamorro, W.
   Jean Lamour Institute, Nancy, France; 29.-31.07.2013
6. Cordoba, R.
   Instituto Universitario de Investigación en Nanociencia de Aragón, Zaragoza, Spain; 24.-27.07.2013
7. Ferraro, F.
   Università degli Studi di Padova, Padova, Italy; 03.-13.06.2013
8. Gago, R.
   Instituto de Ciencia de Materiales de Madrid, Madrid, Spain; 09.-10.06.2013
9. Gruber, E.
   Vienna University of Technology, Vienna, Austria; 17.-21.06.2013; 15.-26.07.2013
10. Karlusic, M.
    Rudjer Boskovic Institute, Zagreb, Croatia; 17.-23.03.2013
11. Kozubek, R.
    Universität Duisburg-Essen, Duisburg, Germany; 17.-23.03.2013
12. Lenz, C.
    University of Vienna, Vienna, Austria; 27.-31.07.2013
13. Leya, I.
    University of Bern, Bern, Switzerland; 13.-18.01.2013
14. Lisowiec, K.
    Polish Academy of Sciences, Warsaw, Poland; 17.-23.02.2013
15. Malinsky, P.
    Nuclear Physics Institute of ASCR, Rez, Czech Republic; 21.-24.05.2013
16. Nardello, M.
    University of Padova, Padova, Italy; 06.-13.05.2013
17. Nowak, M.
    University Poznán, Poznán, Poland; 11.-15.03.2013
18. Pienaziek, A.
    Institute of Nuclear Chemistry and Technology, Warsaw, Poland; 21.07.-27.07.2013
19. Polito, V.
    University of Padova, Padova, Italy; 05.-17.05.2013
20. Pupikova, H.
    Nuclear Physics Institute of ASCR, Rez, Czech Republic; 21.-24.05.2013
21. Ratajczak, R.
    National Centre for Nuclear Study, Warsaw, Poland, 11.-18.05.2013; 15.-19.07.2013

22. Ritter, R.
    Technische Universität Wien, Vienna, Austria; 17.-21.06.2013
23. Sartowska, B.
    Institute of Nuclear Chemistry and Technology, Warsaw, Poland; 04.-10.08.2013
24. Sertsu, M.
    University of Padova, Padova, Italy; 13.-16.05.2013
25. Slemer, A.
    Università degli Studi di Padova, Padova, Italy; 03.-13.06.2013
26. *Starosta, W.*
    Institute of Nuclear Chemistry and Technology, Warsaw, Poland; 21.-27.07.2013
27. *Stonert, A.*
    National Centre for Nuclear Study, Warsaw, Poland; 11.-18.05.2013; 15.-19.07.2013

FEL visitors

1. Ahmad, Z.
   Johann Wolfgang Goethe-Universität Frankfurt, Frankfurt/ Main, Germany; 14.-16.09.2013
2. Akbar, D.
   Hacettepe University Technopolis, *Beytepe-Ankara, Turkey; 16.-23.02.2013*
3. Altan, H.
   METU, *Cankaya Ankara, Turkey; 12.-23.02.2013*
4. Aydinli, A.
   Bilkent University, *Ankara, Turkey; 13.-22.02.2013*
5. Boppel, S.
   Johann Wolfgang Goethe-Universität Frankfurt, Frankfurt/ Main, Germany; 14.-16.09.2013
6. Chatterjee, S.
   Philipps-Universität Marburg, Germany; 01.-12.02.2013; 02.-17.03.2013; 03.-18.06.2013
7. Danilov, S.
   Universität Regensburg,Germany; 27.07.-02.08.2013
8. Deßmann, N.
   Aerospace Center DLR, Berlin, Germany; 12.-15.02.2013; 20.-23.03.2013;
9. Elagoz, S.
   Cumhuriyet University, *Sivas, Turkey; 13.-22.02.2013*
10. Esentürk, O.
    METU, *Cankaya Ankara, Turkey; 12.- 23.02.2013*
11. Guler, I.
    Cankaya University, *Ankara, Turkey; 13.-22.02.2013*
12. Kaiser, S.
    Max Planck Research Department for Structural Dynamics der Universität Hamburg, Hamburg, Germany; 14.-26.03.2013; 02.-10.06.2013; 01.-10.11.2013
13. Kamann, J.
    Universität Regensburg,Germany; 27.07.-02.08.2013
14. Kaya, E.
    METU, *Cankaya Ankara, Turkey; 12.- 23.02.2013*
15. König, M.
    Universität Regensburg,Germany; 27.07.-02.08.2013
16. Laplace, Y.
    Max Planck Research Department for Structural Dynamics der Universität Hamburg, Hamburg, Germany; 16.-26.03.2013; 02.-10.06.2013; 28.10.2013 -10.11.2013

17. Lisauskas, A.
Johann Wolfgang Goethe-Universität Frankfurt, Frankfurt/ Main, Germany; 14.-16.09.2013

18. Liu, Q.
Zernike Institute for Advanced Materials, University of Groningen, The Netherlands; 30.11.-06.12.2013

19. Lörincz, I.
Eotvos University, Budapest, Hungary; 06.-08.03.2013; 16.-18.09.2013; 06.-08.11.2013

20. Malnasi-Csizmadia, A.
Eotvos University, Budapest, Hungary; 06.-08.03.2013; 16.-18.09.2013; 06.-08.11.2013

21. Müller, C.
Universität Erlangen-Nürnberg, Erlangen, Germany; 02.-05.07.2013

22. Mundt, M.
Johann Wolfgang Goethe-Universität Frankfurt, Frankfurt/ Main, Germany; 14.-16.09.2013

23. Nicoletti, D.
Max Planck Research Department for Structural Dynamics der Universität Hamburg, Hamburg, Germany; 14.-26.03.2013; 02.-11.06.2013; 28.10.2013 -10.11.2013

24. Orlita, M.
Grenoble High Magnetic Field Laboratory (GHMFL), Grenoble, France; 01.03.-04.03.2012; 30.10.-04.11.2013

25. Ozen, E. S.
Bilkent University, *Ankara, Turkey; 13.-22.02.2013*

26. Pavlov, S.
Aerospace Center DLR, Berlin, Germany; 12.-15.02.2013; 20.-23.03.2013;

27. Pohl, A.
Aerospace Center DLR, Berlin, Germany; 12.-15.02.2013; 20.-23.03.2013;

28. Preu, S.
Universität Erlangen-Nürnberg, Erlangen, Germany; 02.-05.07.2013

29. Rajasekaran, S.
Max Planck Research Department for Structural Dynamics der Universität Hamburg, Hamburg, Germany; 28.10.2013 -10.11.2013

30. Regensburger, S.
Universität Erlangen-Nürnberg, Erlangen, Germany; 02.-05.07.2013

31. Rosemann, N.
Philipps-Universität Marburg, Germany; 01.-12.02.2013; 02.-17.03.2013; 03.-18.06.2013

32. Sari, H.
Cumhuriyet University, Sivas, Turkey; 18.-22.02, 2013

33. Schay, G.
Eotvos University, Budapest, Hungary; 06.-08.03.2013; 16.-18.09.2013; 06.-08.11.2013

34. Tobey, R.
Zernike Institute for Advanced Materials, University of Groningen, The Netherlands; 30.11.-06.12.2013

35. de Vries, E.
Zernike Institute for Advanced Materials, University of Groningen, The Netherlands; 30.11.-06.12.2013

36. Wall, S.
ICFO - Institut de Ciències Fotòniques, Castelldefels, Spain; 13.-17.05.2013 ;10.-13.10.2013

37. Zhang, L.
Max Planck Research Department for Structural Dynamics der Universität Hamburg, Hamburg, Germany; 17.-26.03.2013; 02.-10.06.2013

ROBL-MRH visitors

1. Bayer B. C.
   University of Cambridge, Department of Engineering, Cambridge, United Kingdom; 17.-23.04.2013; 20.-26.11.13
2. Buljan M.
   Charles University, Dept. of Condensed Matter Physics, Czech Republic; 30.01.-05.02.2013
3. Buljan M.
   Ruder Boskovic Institute, Zagreb, Croatia; 23.-29.10.2013
4. Burlaka V.
   Georg-August-Universität Göttingen, Institut für Materialphysik, Göttingen, Germany; 12.-16.09.2013
5. Cabrero-Vilatela A.
   University of Cambridge, Centre for Advanced Photonics & Electronics, Cambridge, United Kingdom; 20.-26.11.2013
6. Caldeira V.
   CEA Grenoble, LITEN/DEHT/LBA, Grenoble, France; 24.-31.07.2013
7. Caneva S.
   University of Cambridge, Department of Engineering, Cambridge, United Kingdom; 17.-23.04.2013; 20.-26.11.2013
8. Chmelik D.
   Institute of Materials Science, Freiberg, Germany; 19.-25.06.2013
9. Colin J.-F.
   CEA Grenoble, LITEN/DEHT/LBA, Grenoble, France; 24.-31.07.2013
10. Coulet M.-V.
    CNRS UMR 6242, IM2NP, Universite Paul Cézanne, Marseille, France; 27.02.-04.03.2013
11. Da Costa Pereira L. M.
    Katholieke Universiteit Leuven, IKS, Leuven, Belgium; 30.10.-03.11.2013
12. Davtyan A.
    Universität Siegen, Siegen, Germany; 19.-23.07.2013
13. Endres J.
    Charles University, Dept. of Condensed Matter Physics, Praha, Czech Republic; 23.-29.10.2013
14. Gasse J.-C.
    Bergische Universität Wuppertal, Dept. of Physics, Wuppertal, Germany; 12.-17.12.2013
15. Gruber W.
    TU Clausthal, Institute of Metallurgy, Clausthal-Zellerfeld, Germany; 08.-13.03.2013
16. Hanzig F.
    Institute of Materials Science, Freiberg, Germany; 19.-25.06.2013
17. Hofmann S.
    University of Cambridge, Department of Engineering, Cambridge, United Kingdom; 17.-23.04.2013
18. Holy V.
    Charles University, Dept. of Condensed Matter Physics, Czech Republic; 30.01.-05.02.2013
19. Khanbabaee B.
    Universität Siegen, Siegen, Germany; 19.-23.07.2013
20. Kidambi P. R.
    University of Cambridge, Department of Engineering, Cambridge, United Kingdom; 17.-23.04.2013; 20.-26.11.2013
21. Kurz S.
    MPI for Intelligent Systems, Stuttgart, Germany; 10.-14.05.2013

22. Le Roux B.
CEA Grenoble, LITEN/LMB, Grenoble, France; 24.-31.07.2013

23. Lützenkirchen-Hecht D.
Bergische Universität Wuppertal, Institut für Materialwissenschaften, Wuppertal, Germany; 07.-10.05.2013; 12.-17.12.2013

24. Mariage N.
CEA Grenoble, LITEN/LMB, Grenoble, France; 24.-31.07.2013

25. Meka S. R.
Max Planck Institute for Intelligent Systems, Stuttgart, Germany; 10.-14.05.2013

26. Menendez Dalmau E.
Katholieke Universiteit Leuven, Instituut Voor Kern en Stralingsfysica, Leuven, Belgium; 30.10.-03.11.2013

27. Muller C.
CNRS UMR 6242-IM2NP, Universite Paul Cézanne, Marseille, France; 27.02.-04.03.2013

28. Multrus F.
Fraunhofer Institut IFAM, Dresden, Germany; 11.-16.04.2013

29. Ouled Khachroum T.
CNRS UMR 6242, IM2NP, Universite Paul Cézanne, Marseille, France; 27.02.-04.03.2013

30. Pajot S.
CEA Grenoble, LITEN/LMB, Grenoble, France; 24.-31.07.2013

31. Porcher W.
CEA-CENG, Grenoble, France; 24.-31.07.2013

32. Putero M.
CNRS UMR 6242, IM2NP, Universite Paul Cézanne, Marseille, France; 27.02.-04.03.2013

33. Rahn J.
TU Clausthal, Inst. Metallurgie Thermochemie & Mikrok., Clausthal-Zellerfeld, Germany; 08.-13.03.2013

34. Ratayski U.
Institute of Materials Science, Germany; 19.-25.06.2013

35. Rauscher T.
TU Dresden, Institut für Werkstoffwissenschaft, Dresden, Germany; 11.-16.04.2013

36. Röntzsch L.
Fraunhofer Institut IFAM, Dresden, Germany; 11.-16.04.2013

37. Schmidt H.
TU Clausthal, Institute of Metallurgy, Clausthal-Zellerfeld, Germany; 08.-13.03.2013

38. Simonin L.
CEA Grenoble, LITEN/DEHT/LBA, Grenoble, France; 24.-31.07.2013

39. Tegel M.
University of Munich-LMU, Department of Chemistry, München, Germany; 11.-16.04.2013

40. Uchida H. T.
Georg-August-Universität Göttingen, Institut für Materialphysik, Göttingen, Germany; 12.-16.09.2013

41. Vincens C.
CEA, Liten, 17 rü des Martyrs, Grenoble, France; 24.-31.07.2013

42. Wagner R.
Bergische Universität Wuppertal, Institut für Materialwissenschaften, Wuppertal, Germany; 07.-10.05.2013

43. Waninger M.
Georg-August-Universät Göttingen, Institut für Materialphysik, Göttingen, Germany; 12.-16.09.2013

44. Weatherup R.
University of Cambridge, Department of Engineering, Cambridge, United Kingdom; 17.-23.04.2013; 20.-26.11.2013

45. Wuestefeld C.
Institute of Materials Science, Freiberg, Germany; 19.-25.06.2013

Other guests

1. Bald, I.
Bundesanstalt für Materialforschung und –prüfung, Berlin, Germany; 02.-06.09.2013

2. Bayrak, T.
Ankara University, Ankara, Turkey; 04.02.-04.05.2013

3. Criollo, C.
Universidad de los Andes, Bogotá, Columbia; 01.09.-25.11.2013

4. Eder, F.
TU Wien, Wien, Austria; 01.01.-31.10.2013

5. El-Said, A. S.
Mansoura University, Mansoura, Egypt; 01.06.-15.08.2013

6. Ghosh, S.
Indian Institute of Technology, New Delhi, India; 10.-30.06.2013

7. Gilmore, J.
Swansea University, United Kingdom; 24.06.-13.09.2013

8. Hüls, M.
University of Sherbroke, Quebec, Canada; 02.-06.09.2013

9. Kilibarda, F.
Beograd, Serbia; 20.07.-20.09.2013

10. Liu, Y.
Chinese Academy of Science, Institute of Physics, Beijing, P.R. China; 15.08.-31.10.2013

11. Loussouarn, T.
CEA Saclay, Gif-sur-Yvette, France; 04.03.-02.08.2013

12. Novikau, A.
Belarusian State University, Minsk, Belarus; 17.-22.03.2013

13. Pointillon, A.
Paris, France; 04.02.-31.08.2013

14. Ranjan, M.
Institute for Plasma Research, Gandhinagar, India; 01.06.-31.07.2013

15. Smekhova, A.
Lomonosov Moscow State University, Moscow, Russia; 10.-29.04.2013; 04.11.-04.12.2013

16. Smith, R.
Loughborough University, Loughborough, United Kingdom; 30.06.-14.07.2013

17. Toprak, M.
Ankara University, Ankara, Turkey; 01.07.-02.09.2013

18. Voevodin, A.
University of Dayton, Dayton, USA; 23.-29.06.2013

19. You, T.
TU Chemnitz, Chemnitz, Germany; 04.-08.02.; 10.-15.03.; 03.-07.04.;29.04.-05.05.; 24.-30.06.; 12.-20.08.; 15.-20.09.; 14.-27.10.2013

20. Yuan, X.
TU Chemnitz, Chemnitz, Germany; 14.-27.10.2013

Laboratory visits

1. Aleksandrov, Y.
   Universität Duisburg, Germany; 29.04.-12.05.; 09.-16.09.2013
   Moscow State University, Moscow, Russia; 09.-14.10.2013
2. Bähtz, C.
   HZDR Dresden, Germany; 19.-28.03.2013
3. Blaschke, D.
   Moscow State University, Moscow, Russia; 09.-14.10.2013
4. Bregolin, F.
   Oslo University, Norway; 09.-15.09.2013
5. Buhl, M.
   PSI Villigen, Switzerland; 03.-07.04.2013
6. Drachenko, O.
   Kurchatov Institute, Moscow; RAS Nizhny Novgorod, Russia; 20.01.-02.02.2013
   Laboratoire Charles Coulomb, Montpellier, France; 16.-23.02.2013
   LNCMP Toulouse, France; 08.-11.12.2013
7. Erbe, A.
   Universität Konstanz, Germany, 15.-18.04.; 16.-19.06.2013
8. Gao, K.
   ESRF Grenoble, France; 24.-31.01.; 26.11.-05.12.2013
9. Grebing, J.
   Universität Konstanz, Germany; 16.-19.04.2013
10. Grenzer, J.
    ESRF Grenoble, France; 29.01.-06.02.; 25.06.-02.07.; 21.-29.10.2013
    Ruder Boskovic Institute, Zagreb, Croatia; 06.-12.05.; 01.-05.12.2013
11. Heidarian, A.
    Universität Duisburg, Germany; 12.-18.05.; 14.-19.07.2013
12. Khalid, M.
    HZB Berlin, Germany; 14.-20.05.; 10.-15.12.2013
13. Lindner, J.
    Universität Duisburg, Germany; 18.-22.07.; 14.-20.08.2013
14. Möller, W.
    ETH Zürich, Switzerland; 21.-24.04.2013
15. Pointillon, A.,
    Universität Duisburg, Germany; 01.-05.05.2013
16. Potzger, K.
    Moscow State University, Moscow, Russia; 09.-14.10.2013
17. Rebohle, L.
    Kiew University, Kiew, Ukraine; 08.-11.04.2013
18. Roshchupkina, O.
    ESRF Grenoble, France; 09.-23.04.; 01.06.-31.07.; 19.11.-04.12.2013
19. Schneider, H.
    Shanghai Jiao Tong University, Shanghai, P.R. China; 15.04.-12.05.; 09.-24.12.2013
    Universität Freiburg, Germany; 20.-25.05.2013
20. Schönherr, T.
    Universität Konstanz, Germany; 16.-19.04.2013
21. Skorupa, W.
    Oslo University, Norway; 09.-13.09.; 22.-27.10.2013

22. Sluka, V.
PSI Villigen, Switzerland; 30.03.-07.04.; 15.-21.12.2013
HZB Berlin, Germany; 27.05.-02.06.; 09.-15.12.2013

23. Steinbach, G.
PSI Villigen, Switzerland; 03.-07.04.2013

24. Ulbricht, A.
HZB Berlin, Germany; 21.-25.02.; 26.-30.08.2013
ESRF Grenoble, France; 09.-13.06.2013

25. Wagner, A.
HZB Berlin, Germany; 21.-25.02.; 26.-30.08.2013

26. Wang, Y.
ESRF Grenoble, France; 26.11.-05.12.2013

27. Warnatz, T.
PSI Villigen, Switzerland; 03.-07.04.2013

28. Weidauer, R.
Ruder Boskovic Institute, Zagreb, Croatia; 06.-12.05.; 01.-05.12.2013

29. Wiesenhütter, K.
Oslo University, Norway; 09.-15.09.2013

30. Wieser, M.
Universität Konstanz, Germany; 09.-19.04.2013

31. Wintz, S.
PSI Villigen, Switzerland; 30.03.-07.04.; 15.-21.12.2013
HZB Berlin, Germany; 27.05.-02.06.; 09.-15.12.2013

32. Yildirim, O.
Moscow State University, Moscow, Russia; 17.-28.06.; 09.-14.10.2013

33. Yuan, Y.
HZB Berlin, Germany; 10.-15.12.2013

34. Zhou, S.
ESRF Grenoble, France; 24.-27.01.2013
HZB Berlin, Germany; 13.-16.05.2013
ALS Berkeley, USA; 17.-25.06.2013

Projects

The projects are listed by funding institution and project starting date. In addition, the institute has several bilateral service collaborations with industrial partners and research institutions. These activities are not included in the following overview.

European Projects

1. 02/2008 – 10/2013 European Union EU
   GETMAT– Generation IV and transmutation materials
   Dr. F. Bergner *Phone: 0351 260 3186* *f.bergner@hzdr.de*
2. 03/2009 – 08/2013 European Union EU
   SPIRIT – Support of public and industrial research using ion beam technology
   Prof. W. Möller *Phone: 0351 260 2245* *w.moeller@hzdr.de*
3. 03/2009 – 12/2013 European Union EU
   PERFORM60 – Radiation effects in reactor materials (modelling)
   Dr. E. Altstadt *Phone: 0351 260 2276* *e.altstadt@hzdr.de*
4. 02/2010 – 01/2014 European Union EU
   LONGLIFE – Long term irradiation embrittlement effects
   Dr. E. Altstadt *Phone: 0351 260 2276* *e.altstadt@hzdr.de*
5. 01/2011 – 12/2014 European Union EU
   MATTER – Materials testing and rules
   Dr. F. Bergner *Phone: 0351 260 3186* *f.bergner@hzdr.de*
6. 06/2012 – 05/2015 European Union EU
   CALIPSO – Coordinated access to lightsources
   Prof. M. Helm *Phone: 0351 260 2260* *m.helm@hzdr.de*
7. 01/2013 – 12/2016 European Union EU
   SPRITE – Supporting postgraduate research
   Dr. J. v. Borany *Phone: 0351 260 3378* *j.v.borany@hzdr.de*
8. 11/2013 – 10/2017 European Union EU
   MatISSE – Materials' Innovations for a Safe and Sustainable nuclear in Europe
   Dr. E. Altstadt *Phone: 0351 260 2276* *e.altstadt@hzdr.de*

Helmholtz Association Projects

1. 03/2011 – 02/2016 Helmholtz–Gemeinschaft HGF
   Functional Materials – Helmholtz Young Investigators' Group
   Dr. Shengqiang Zhou *Phone: 0351 260 2484* *s.zhou@hzdr.de*
2. 07/2011 – 09/2018 Helmholtz–Gemeinschaft HGF
   NANONET – Helmholtz research school for nanoelectronic networks
   Dr. A. Erbe *Phone: 0351 260 2366* *a.erbe@hzdr.de*
3. 10/2011 – 09/2016 Helmholtz–Gemeinschaft HGF
   MEMRIOX – Virtual Institute – Memory effects in oxides
   Dr. P. Zahn *Phone: 0351 260 3121* *p.zahn@hzdr.de*
4. 02/2012 – 01/2015 Helmholtz–Gemeinschaft HGF
   HRJRG–DETI.2 – Helmholtz Russia joint research group – Magnetic TiO_2
   Dr. K. Potzger *Phone: 0351 260 3244* *k.potzger@hzdr.de*
5. 01/2013 – 12/2017 Helmholtz–Gemeinschaft HGF
   Professorship TU Chemnitz
   Prof. S. Gemming *Phone: 0351 260 2470* *s.gemming@hzdr.de*

6. 03/2013 – 02/2014 Helmholtz–Gemeinschaft HGF
   HEF–i3membrane – nanopore metal filter
   Prof. A. Kolitsch Phone: 0351 260 3348 a.kolitsch@hzdr.de

German Science Foundation Projects

1. 11/2009 – 08/2013 Deutsche Forschungsgemeinschaft DFG
   TCOMR – Electric field control of magnetoresistance
   Dr. H. Schmidt Phone: 0351 260 2724 heidemarie.schmidt@hzdr.de
2. 02/2010 – 06/2014 Deutsche Forschungsgemeinschaft DFG
   HybMagMat – Hybride magnetische Materialien
   Prof. J. Fassbender Phone: 0351 260 3096 j.fassbender@hzdr.de
3. 04/2010 – 08/2013 Deutsche Forschungsgemeinschaft DFG
   Strukturbildende Prozesse in amorphen Kohlenstoffschichten
   Dr. L. Bischoff Phone: 0351 260 2963 l.bischoff@hzdr.de
4. 08/2010 – 06/2014 Deutsche Forschungsgemeinschaft DFG
   SuSi – Supraleitung in hochdotierten Gruppe IV Halbleitern
   Dr. V. Heera Phone: 0351 260 3343 v.heera@hzdr.de
5. 09/2010 – 04/2015 Deutsche Forschungsgemeinschaft DFG
   TERATOP – Terahertz non–linear detection and quantum optical studies by resonant two–photon transitions in semiconductor quantum wells
   Dr. H. Schneider Phone: 0351 260 2880 h.schneider@hzdr.de
6. 11/2010 – 06/2014 Deutsche Forschungsgemeinschaft DFG
   Atomistische Simulation der Selbstorganisation bei der Ionenstrahlerosion
   Dr. K.–H. Heinig Phone: 0351 260 3288 k.h.heinig@hzdr.de
7. 11/2010 – 10/2013 Deutsche Forschungsgemeinschaft DFG
   Relaxation dynamics in graphene investigated in the mid– and far–infrared spectral range
   Dr. S. Winnerl Phone: 0351 260 3522 s.winnerl@hzdr.de
8. 01/2011 – 09/2014 Deutsche Forschungsgemeinschaft DFG
   Wechselwirkung langsamer hochgeladener Ionen mit der Oberfläche von Ionenkristallen und Isolatoren
   Dr. S. Facsko Phone: 0351 260 2987 s.facsko@hzdr.de
9. 01/2011 – 02/2014 Deutsche Forschungsgemeinschaft DFG
   Selbstorganisierte Oberflächenmuster auf Germanium durch schwere Clusterionen
   Dr. L. Bischoff Phone: 0351 260 2963 l.bischoff@hzdr.de
10. 03/2011 – 02/2014 Deutsche Forschungsgemeinschaft DFG
    HISENSE – High–field studies of the band dispersion in novel semiconductor materials
    Dr. O.Drachenko Phone: 0351 260 3593 o.drachenko@hzdr.de
11. 04/2011 – 08/2014 Deutsche Forschungsgemeinschaft DFG
    FRUSTPART – Nukleation von Spinordnung in niederdimensionalen kolloidalen Partikelsystemen
    Dr. A. Erbe Phone: 0351 260 2366 a.erbe@hzdr.de
12. 04/2011 – 08/2013 Deutsche Forschungsgemeinschaft DFG
    condDNA – Quantum transport at the molecular scale of DNA
    Dr. A. Erbe Phone: 0351 260 2366 a.erbe@hzdr.de
13. 08/2011 – 07/2014 Deutsche Forschungsgemeinschaft DFG
    Nanostrukturierung von Oberflächen mit direkter Extraktion der Ionen aus Plasmaquellen
    Dr. S. Facsko Phone: 0351 260 2987 s.facsko@hzdr.de

14. 09/2011 – 04/2013 Deutsche Forschungsgemeinschaft DFG
Terahertz dynamics in carbon based nanostructures
Prof. M. Helm *Phone: 0351 260 2260* *m.helm@hzdr.de*

15. 03/2012 – 04/2014 Deutsche Forschungsgemeinschaft DFG
Ortsaufgelöste ferromagnetische Resonanz
Dr. J. Lindner *Phone: 0351 260 3221* *j.lindner@hzdr.de*

16. 09/2012 – 09/2015 Deutsche Forschungsgemeinschaft DFG
ATOMIX – Atomares Mischen in Halbleitermultischichtstrukturen
Dr. M. Posselt *Phone: 0351 260 3279* *m.posselt@hzdr.de*

17. 01/2013 – 12/2015 Deutsche Forschungsgemeinschaft DFG
MWN – Magnetization dynamics in nanostructures
Dr. J. Lindner *Phone: 0351 260 3221* *j.lindner@hzdr.de*

18. 01/2013 – 10/2017 Deutsche Forschungsgemeinschaft DFG
Excellenzcluster – Center for Advancing Electronics Dresden
Prof. M. Helm *Phone: 0351 260 2260* *m.helm@hzdr.de*

19. 02/2013 – 01/2016 Deutsche Forschungsgemeinschaft DFG
Nanostrukturierte Thermoelektrika
Dr. P. Zahn *Phone: 0351 260 3121* *p.zahn@hzdr.de*

20. 08/2013 – 07/2014 Deutsche Forschungsgemeinschaft DFG
Magnetic Si:Mn
Dr. S. Zhou *Phone: 0351 260 2484* *s.zhou@hzdr.de*

Federally Funded Projects

1. 04/2010 – 12/2013 Bundesministerium für Bildung und Forschung BMBF
WTZ–Türkei: RainbowEnergy – Development of new solar cells
Dr. K–.H. Heinig *Phone: 0351 260 3288* *k.h.heinig@hzdr.de*

2. 05/2010 – 07/2013 AG Industrieller Forschungseinrichtungen (AiF) BMWi
TCO Grenzflächenoptimierung
Prof. A. Kolitsch *Phone: 0351 260 3348* *a.kolitsch@hzdr.de*

3. 06/2010 – 11/2013 Gesellschaft für Anlagen– und Reaktorsicherheit (GRS) BMBF
Alterungseffekte in RDB–Stahl
Dr. F. Bergner *Phone: 0351 260 3186* *f.bergner@hzdr.de*

4. 07/2010 – 06/2013 Gesellschaft für Chemische Technik und Biotechnologie DECHEMA
Ionenimplantation für Hochtemperatur–Oxidationsschutz
Prof. A. Kolitsch *Phone: 0351 260 3348* *a.kolitsch@hzdr.de*

5. 10/2010 – 09/2013 Bundesministerium für Bildung und Forschung BMBF
Photoinitiated dynamics studied in the fs to ns time and the THz to PHz frequency domain: Picosecond beamline at FELBE (PIDID)
Dr. H. Schneider *Phone: 0351 260 2880* *h.schneider@hzdr.de*

6. 05/2011 – 09/2013 Gesellschaft für Chemische Technik und Biotechnologie DECHEMA
Ionenimplantation für TiAl–Proben
Prof. A. Kolitsch *Phone: 0351 260 3348* *a.kolitsch@hzdr.de*

7. 10/2011 – 10/2013 Bundesministerium für Bildung und Forschung BMBF
WTZ Indien: Plasmonische Strukturen
Dr. S. Facsko *Phone: 0351 260 2987* *s.facsko@hzdr.de*

8. 01/2012 – 11/2014 AG Industrieller Forschungseinrichtungen (AiF) BMWi
Hochtemperaturoxidationsschutz für Titanlegierungen
Prof. A. Kolitsch *Phone: 0351 260 3348* *a.kolitsch@hzdr.de*

9. 02/2013 – 07/2015 AG Industrieller Forschungseinrichtungen (AiF) BMWi
CFD-Beschichtung und Halogeneffekt
Prof. A. Kolitsch *Phone: 0351 260 3348* *a.kolitsch@hzdr.de*

10. 05/2013 – 04/2015 PT Jülich BMWi
    Analytisches Ionenmikroskop
    Dr. J. v. Borany Phone: 0351 260 3378 j.v.borany@hzdr.de

11. 06/2013 – 05/2015 PT Jülich BMWi
    AIDA – Apparatus for in-situ defect analysis
    Dr. K. Potzger Phone: 0351 260 3244 k.potzger@hzdr.de

Saxony State Funded Projects

1. 12/2010 – 05/2013 Sächsische Aufbaubank SAB
   Kelvin–Kraft–Mikroskopie
   Dr. H. Schmidt Phone: 0351 260 2724 heidemarie.schmidt@hzdr.de

2. 04/2012 – 03/2014 Sächsische Aufbaubank SAB
   ADDE II: Untersuchung der H–Passivierung
   Dr. W. Skorupa Phone: 0351 260 3612 w.skorupa@hzdr.de

3. 06/2012 – 05/2014 Sächsische Aufbaubank SAB
   NanoKlang – Korrosionsunterdrückung an Metall–Orgelpfeifen
   Dr. W. Skorupa Phone: 0351 260 3612 w.skorupa@hzdr.de

4. 11/2013 – 10/2014 PT Jülich SMWK
   BFO auf Wafer-Niveau
   Dr. W. Skorupa Phone: 0351 260 3612 w.skorupa@hzdr.de

Personnel Exchange Projects

1. 01/2013 – 12/2014 Deutscher Akademischer Austauschdienst DAAD
   Projektbezogener Personenaustausch mit China: DFT and MC studies
   Dr. M. Posselt Phone: 0351 260 3279 m.posselt@hzdr.de

2. 01/2013 – 12/2014 Deutscher Akademischer Austauschdienst DAAD
   Projektbezogener Personenaustausch mit Norwegen: Flash-PV
   Dr. W. Skorupa Phone: 0351 260 3612 w.skorupa@hzdr.de

Bilateral Projects

1. 04/2010 – 03/2014 FHR Anlagenbau / Centrotherm Industry
   Entwicklung industrietauglicher Temperaturmessung
   Dr. W. Skorupa Phone: 0351 260 3612 w.skorupa@hzdr.de

2. 04/2010 – 05/2013 Swiss Federal Nuclear Safety Inspectorate ENSI
   Bruchmechanik bei Neutronenversprödung
   Dr. H.–W. Viehrig Phone: 0351 260 3246 h.w.viehrig@hzdr.de

3. 10/2010 – 09/2013 DTF Technology Dresden Industry
   DTF– Industriedoktoranden
   Prof. A. Kolitsch Phone: 0351 260 3348 a.kolitsch@hzdr.de

4. 05/2012 – 05/2013 IXYS Semiconductor Industry
   Machbarkeitsstudie
   Dr. J. v. Borany Phone: 0351 260 3378 j.v.borany@hzdr.de

5. 07/2012 – 06/2016 Abengoa Research, Seville, Spain Industry
   AR Framework Collaboration
   Dr. G. Abrasonis Phone: 0351 260 3578 g.abrasonis@hzdr.de

6. 10/2012 – 12/2015 Carl–Zeiss Microscopy Industry
   Kooperation Ionenmikroskopie
   Dr. J. v. Borany Phone: 0351 260 3378 j.v.borany@hzdr.de

7. 06/2013 – 12/2014 TUD-Energietechnik TUD
   Bruchmechanik bei Neutronenversprödung
   Dr. H.–W. Viehrig Phone: 0351 260 3246 h.w.viehrig@hzdr.de

8. 10/2013 – 06/2015 TÜV Süd
   Education and Training CAMBO Bratislava
   Prof. A. Kolitsch Phone: 0351 260 3348 a.kolitsch@hzdr.de

Doctoral training programme

International Helmholtz Research School NANONET

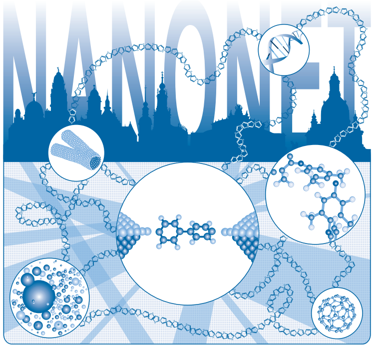

The Institute of Ion Beam Physics and Materials Research is coordinating the International Helmholtz Research School for Nanoelectronic Networks (IHRS NANONET) supported by the Initiative and Networking Fund of the Helmholtz Association. The project started in October 2012. The total funding is 1.200.000 € for a period of 6 years.

The IHRS NANONET is an international, interdisciplinary and thematically focused doctoral programme in the field of molecular electronics. The research school aims at attracting and promoting excellence by educating promising doctoral candidates with backgrounds in physics, chemistry, materials science and electrical engineering. During a period of 3 years PhD candidates benefit from well-structured, comprehensive training curricula and multiple mentorship, while performing cutting edge research projects within one of the 16 NANONET research groups. Under the supervision of outstanding scientists leading the field of nanoelectronics, the doctoral candidates have the unique opportunity to contribute to the advancement of molecular electronics by developing strategies for the real integration of single nanosized building blocks into large interconnected networks

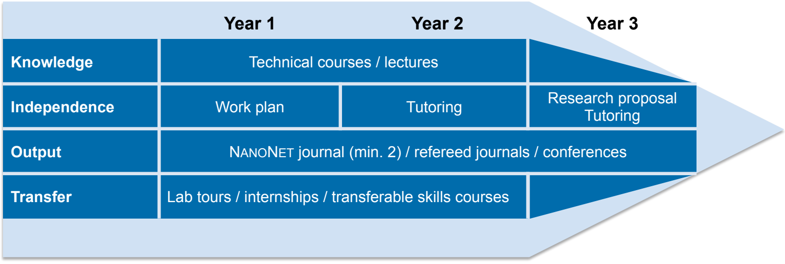

	Year 1	Year 2	Year 3
Knowledge	Technical courses / lectures		
Independence	Work plan	Tutoring	Research proposal Tutoring
Output	NANONET journal (min. 2) / refereed journals / conferences		
Transfer	Lab tours / internships / transferable skills courses		

Annual International NANONET Workshop
PhD seminar (with TAC)

The period of doctoral studies is crucial in the academic career of young scientists. Therefore, the IHRS NANONET fosters not only professional qualification but also personal development by equipping young graduates with competencies for successful careers in a wide variety of positions in academia and industry. The training programme invests on professional competencies, such as the capability to work across disciplines and cultures by promoting networking and the exchange of ideas and knowledge with fellows, mentors and collaboration partners. The cooperation with international scientific and industrial partners complements and broadens the expertise of the IHRS NANONET by establishing a unique research and training network for its doctoral candidates.

The consortium

Helmholtz-Zentrum Dresden-Rossendorf
Technische Universität Dresden
Leibniz Institute of Polymer Research Dresden
Fraunhofer Institute for Nondestructive Testing
NaMLab gGmbH

For further information please contact the NANONET coordinator, Dr. Ana Cordeiro (nanonet@hzdr.de) or visit the IHRS NANONET website: www.ihrs-nanonet.de

Experimental equipment

Accelerators, ion implanters and ion-assisted-deposition

Van de Graaff Accelerator (VdG)	1.8 MV	*TuR Dresden, DE*
Tandetron Accelerator (T1)	3 MV	*HVEE, NL*
Tandetron Accelerator (T2)	6 MV	*HVEE, NL*
Low-Energy Ion Implanter	0.5 - 50 kV	*Danfysik, DK*
High-Current Ion Implanter	20 - 200 kV	*Danfysik, DK*
High-Energy Ion Implanter	40 - 500 kV	*HVEE, NL*
Plasma Immersion Ion Implantation	5 - 60 keV	*GBR, DE / Home-built*
Focused Ion Beam (15 nm, variable ions)	30 keV, 10 A/cm^2	*Orsay Physics, FR*
Highly-Charged Ion Facility	25 eV – 25 keV × Q Q = 1…40 (Xe)	*Home-built*
Dual-Beam Magnetron Sputter Deposition		*Roth & Rau, DE*
Ion-Beam-Assisted Deposition		*Danfysik, DK*
Ion-Beam Sputtering	200 - 2000 V	*Home-built*
UHV Ion Irradiation (Ar, He, etc.)	0 - 5 keV Scan 10×10 mm^2	*VG, USA*

Ion Beam Analysis (IBA)

A wide variety of advanced IBA techniques are available at the MeV accelerators (see figure).

RBS	Rutherford Backscattering Spectrometry	(1), (9), (11), (12), (21)	*vdG, T1, T2*
RBS/C	RBS + Channelling	(1), (9), (11), (12)	*vdG, T1, T2*
HR-RBS	High-Resolution RBS/C	(9), (13)	*T1*
ERDA	Elastic Recoil Detection Analysis	(1), (4)	*vdG, T2*
HR-ERDA	High-resolution ERDA	(7)	*T2*
PIXE	Particle-Induced X-ray Emission	(1), (5), (6), (12)	*vdG, T1, T2*
PIGE	Particle-Induced γ Emission	(6), (12)	*T1, T2*
NRA	Nuclear Reaction Analysis	(3)	*T2*
NRRA	Nuclear Resonance Reaction Analysis	(11)	*T1*
NMP	Nuclear Microprobe	(12)	*T1*
AMS	Accelerator Mass Spectrometry (focused to cosmic radionuclides: ^{10}Be, ^{26}Al, ^{36}Cl, ^{41}Ca, ^{129}I)	(10)	*T2*

Some stations are equipped with additional process facilities enabling *in-situ* IBA investigations during ion irradiation, sputtering, deposition, annealing etc..

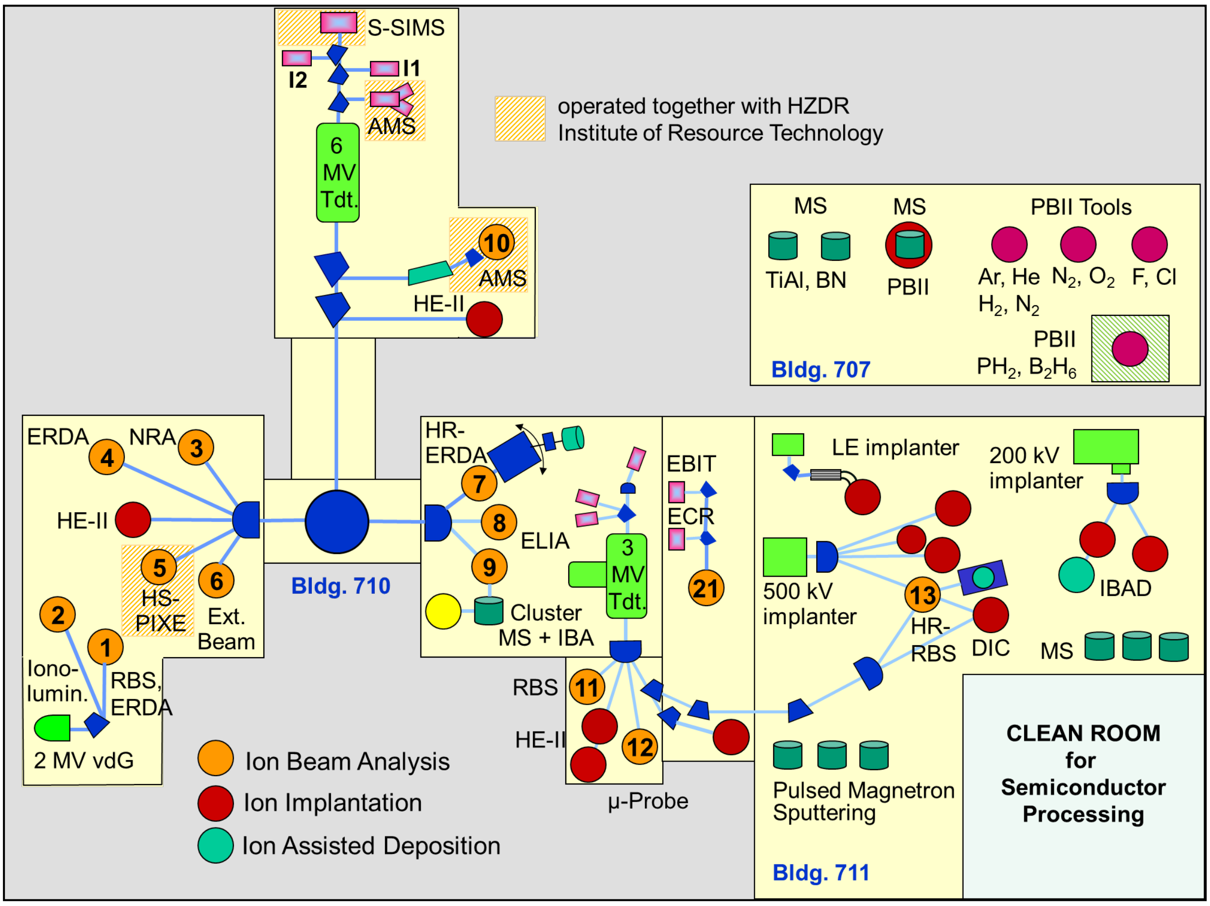

Schematic overview of the Ion Beam Center

Other particle-based analytical techniques

SEM	Scanning Electron Microscope	1 - 30 keV + EDX	*Hitachi, JP*
TEM	Transmission Electron Microscope (Titan 80-300 with Image Corrector)	80 - 300 keV + EDX, +GIF	*FEI, NL*
SIM	Scanning Ion Microscope (ORION NanoFab with He, Ne ions)	10 - 35 keV + GIS, Patterning	*Zeiss Microscopy, DE*
FIB/SEM	Focused Ion / Electron Cross Beam (NVision 40 with Elphy Plus Litho)	0.5 – 30 keV + EDX, EBSD	*Zeiss-NTS, DE* *Raith, Bruker, DE*
AES	Auger Electron Spectroscopy	+ XPS	*Fisions, UK*
CEMS	Mössbauer Spectroscopy	^{57}Fe source	*Home-built*
PAS	Positron Annihilation Spectroscopy	^{22}Na source 30 V - 36 kV	*Home-built*

Photon-based analytical techniques

XRD / XRR	X-Ray Diffraction and Reflection	Cu-Kα	*Bruker AXS, DE*
HR-XRD	High-Resolution XRD	Cu-Kα	*GE Inspection, DE*
TFA	Thin Film Analysis, including Grazing Incidence Small Angle Scattering (GiSAXS)	Cu-Kα	*PANalytical, NL*
XRD / XRR	with Synchrotron Radiation	5 – 35 keV	*ROBL at ESRF, FR*
SE	Spectroscopic Ellipsometry	250 - 1700 nm	*Woollam, US*
FTIR	Fourier-Transform Infrared Spectrometer	600 - 7000 cm^{-1}	*Nicolet, US*
FTIR	Fourier-Transform Infrared Spectrometer	50 - 15000 cm^{-1}	*Bruker, DE*
	Ti:Sapphire Femtosecond Laser	78 MHz	*Spectra Physics, US*
	Femtosecond Optical Parametric Osci.		*APE, DE*
	Ti:Sapphire Femtosecond Amplifier	1 kHz	*Femtolasers, AT*
	Ti:Sapphire Femtosecond Amplifier	250 kHz	*Coherent, US*
	Femtosecond Optical Parametric Amplifier		*Light Conversion, LI*
THz-TDS	Terahertz Time-Domain Spectroscopy	0.1 - 4 THz	*Home-built*
Raman	Raman Spectroscopy	> 45 cm^{-1} shift	*Jobin-Yvon-Horiba, FR*
PL	Photoluminescence	300 - 1500 nm	*Jobin-Yvon-Horiba, FR*
TRPL	Time-Resolved PL	τ = 3 ps - 2 ns τ > 5 ns	*Hamamatsu Phot., JP* *Stanford Research, US*
EL	Electroluminescence (10-300 K)	300 - 1500 nm	*Jobin-Yvon-Horiba, FR*
	Optical Split-Coil Supercond. Magnet	7 T	*Oxford Instrum., UK*
PR	Photomodulated Reflectivity	300 - 1500 nm	*Jobin-Yvon-Horiba, FR*
PLE	Photoluminescence Excitation	300 - 1500 nm	*Jobin-Yvon-Horiba, FR*
OES	Optical Emission Spectroscopy	250 – 800 nm	*Jobin-Yvon-Horiba, FR*

Magnetic thin film deposition and analysis

MBE	Molecular Beam Epitaxy with in-situ FIB		*CreaTec, DE*
MBE	Molecular Beam Epitaxy		*Home-built*
PLD	Pulsed Laser Deposition		*SURFACE, DE*
MFM	Magnetic Force Microscope	~ 50 nm resol	*VEECO / DI, US*
SQUID	Supercond. Quantum Interference Device	± 7 T	*Quantum Design, US*
MOKE	Magneto-Optic Kerr Effect (in-plane)	± 0.35 T	*Home-built*
MOKE	Magneto-Optic Kerr Effect (perpend.)	± 2 T	*Home-built*
SKM	Scanning Kerr Microscope		*Home-built*
	Kerr Microscope		*Evico Magnetics, DE*
TR-MOKE	Time-Resolved MOKE (Pump-Probe)		*Home-built*
VNA-FMR	Vector Network Analyzer Ferromagnetic Resonance		*Agilent / Home-built*
ME	Magnetoellipsometer		*LOT, DE; AMAC, US*

Other analytical and measuring techniques

STM	Scanning Tunneling Microscope (with AFM-Option)		*DME, DK*
STM	*In-situ* Scanning Tunneling Microscope (T variable)		*Omicron, DE*
AFM	Atomic Force Microscope (Tapping Mode)		*SIS, DE*
AFM	Atomic Force Microscope (with c-AFM, SCM-Module)		*Veeco Instruments, UK*
KFM	Kelvin Probe Force Microscopy		*Anfatec, DE*
	Dektak Surface Profilometer		*Veeco, US*
	Micro Indenter / Scratch Tester		*Shimatsu, JP*
MS	Mass Spectrometers (EQP-300, HPR-30)		*HIDEN, DE & US*
	Wear Tester (pin-on disc)		*Home-built*
LP	Automated Langmuir Probe		*Impedans, IE*
HE	Hall Effect Equipment	2 - 400 K, ≤ 9 T	*LakeShore, US*
RS	Sheet-Rho-Scanner		*AIT, South Korea*
DLTS	Deep Level Transient Spectroscopy	(+ I-U / C-V) (10 - 300 K, 1 MHz)	*PhysTech, DE*
IV / CV	Photocapacitance (+I-V/G-V)	(250 - 2500 nm)	*Home-built*
IV / CV	I-V and C-V Analyzer		*Keithley, US*
IV / CV	I-V and C-V Semi-Automatic Prober	(-60 – 300°C)	*Süss, DE; Keithley, US*
IV	I-V Prober	(4.2 – 600 K)	*LakeShore, Agilent, US*

Processing and preparation techniques

Physical Deposition	Sputtering DC / RF, Evaporation	*Nordiko, UK*
	Electron Beam Evaporation System	*Leybold Optics, DE*
	Thermal Evaporation	*Bal-Tec, LI*
Chemical Deposition	Plasma Enhanced CVD (for a-Si, SiO_2, SiON, Si_3N_4)	*Oxford Instruments, UK*
Dry Etching	Plasma and RIE Mode	*Sentech, DE*
Reactive Ion Beam Etching	∅ 6”, Ar, CF_4	*Roth & Rau, DE*
Etching / Cleaning	incl. Anisotropic Selective KOH Etching	
Photolithography	Mask-Aligner, 2 µm-level	*Süss, DE*
Electron Beam Lithography	Raith 150-TWO: ∅ 6”, 10 nm res.	*Raith, DE*
Thermal Treatment	Room Temperature - 2000°C	
• Furnace		*InnoTherm, DE*
• Rapid Thermal Annealing		*ADDAX, FR*
• Flash-Lamp Units (0.5 – 20 ms)		*Home-built; FHR, DE*
• RF Heating (Vacuum)		*JIP.ELEC, FR*
• Laser annealing (CW, 808 nm, 450 W)		*LIMO, DE*
• Laser annealing (30 ns pulse,10 Hz, 308 nm, 500 mJ)		*COHERENT, USA*
Bonding Techniques	Ultrasonic Wire Bonding	*Kulicke & Soffa, US*
Cutting, Grinding, Polishing		*Bühler, DE*
TEM Sample Preparation	Plan View and Cross Section incl. Ion Milling Equipment	*Gatan, US*

Hot cells laboratory

Mechanical testing of neutron irradiated structural materials	max. total activity 5 TBq (Co-60), T = -150 ... +315 °C	
Fracture mechanics testing	max load ±50 kN	MTS, US
Charpy impact testing	300 J	WPM Leipzig, DE
Small punch test	10 kN	Hegewald & Peschke, DE
Specimen preparation	Electrical discharge machining	AGIE, DE
Depth sensing nanoindentation/ AFM	UNAT, load range 1 … 500 mN	ASMEC, DE

User facilities and services

Ion Beam Center (IBC)

The IBC is a leading European user facility primarily dedicated to research and application of ion beam techniques in materials science. The IBC comprises various ion beam facilities providing a wide energy range between eV and about 60 MeV. The versatile instrumentation of IBC includes a variety of plasma tools, ion implanters, electrostatic accelerators, as well as specific equipment for the use of focused ion beams or highly-charged and low-energy ions. In addition to these ion beam facilities, structural analysis (electron microscopy and spectroscopy, X-ray scattering techniques) and sample or device processing under clean-room conditions can be utilized at IBC to deliver a "complete" user service. The use of the IBC facilities includes the scientific and technical support during planning, execution and subsequent evaluation of the experiments. Access to IBC is provided on the basis of scientific collaborations with research groups, by proposals of external users or taking advantage of the commercial service activities triggered by the HZDR Innovation GmbH (www.hzdr-innovation.de). Continuous proposal submission for all kind of beam time use (single experiments, projects, ion beam services) is possible via the IBC homepage www.hzdr.de/IBC.

In 2013 more than 350 users from 25 countries worldwide performed experiments at IBC or used the capabilities for ion beam services. The IBC has been recently qualified as a Helmholtz LK-II user facility and a large-scale facility within the "BMBF Verbundforschung" promoting long-term collaborations with universities. In addition, IBC coordinates the European Infrastructure Project "SPIRIT" dedicated to transnational user access to different European Ion Beam Centres.

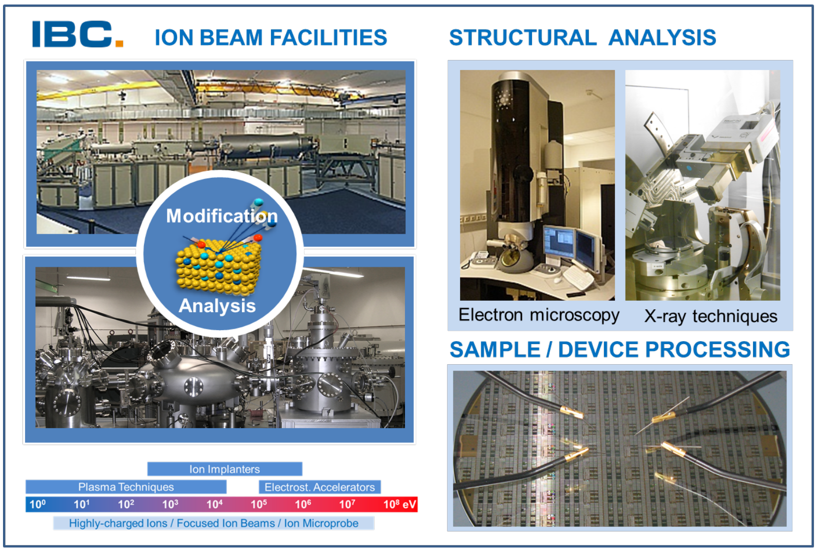

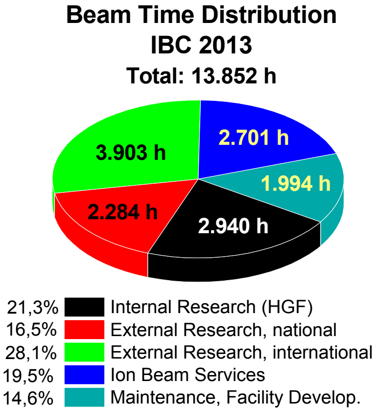

With respect to other ion beam centres worldwide, the IBC may be characterized by three specific features: (i) IBC research is focused to materials science, (ii) IBC activities cover both, material modification and analysis by ions, and (iii) IBC acts as a competence centre for ion beam applications in close collaboration with industry.

At IBC most common ion beam techniques are available, including dedicated end-stations for ion beam modification and analysis such as:

- High-energy ion implantation for semiconductor processing
- Plasma-based ion implantation for solar cell applications or surface patterning processes,

- Nanofabrication based on various focused ion beam facilities,
- Experiments using highly charged ions,
- End-stations allowing the simultaneous use of different IBA-techniques (e.g. RBS, He-ERDA, PIXE), partly as *in-situ* analysis during deposition or annealing experiments,
- Hydrogen (or other light elements) depth profiling using nuclear reaction analysis,
- Depth profiling (ERDA, RBS) with near-surface sub-nm resolution using magnetic spectrometers,
- Accelerator mass spectrometry @ DREAMS beam line (excluding ^{14}C detection)

In 2013, some new ion beam tools or end-stations have been commissioned (see figures below) which will attract new users by cutting-edge experimental instrumentation.

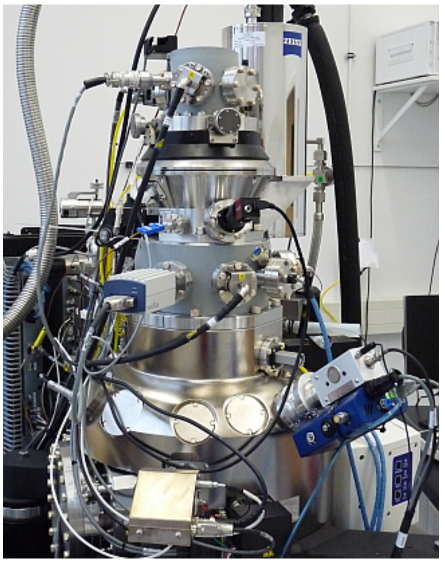

ORION NanoFab

Ion microscope and Nanofabrication tool (He / Ne ions, resolution < 0.5 nm).

PIXE Camera

Locally resolved PIXE analysis using a poly-capillary X-ray optics and a pn-CCD pixel detector. Broad beam proton excitation can be applied. Depending on the used X-ray optics the resolution will be in the range 10 – 50 µm.

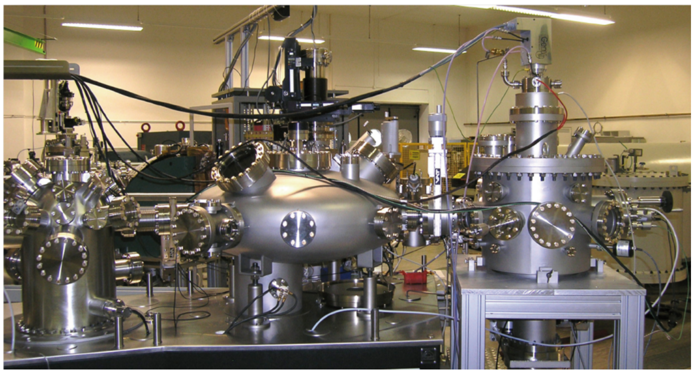

***In-situ* Tool**

Set-up for ion-assisted deposition and high-energy IBA for in-situ (partly real-time) experiments

In this context, a fruitful and close collaboration between the IBC and the Helmholtz Institute of Resource Technology (www.hzdr.FWG) has been developed during last years. With projects like “High-Speed-PIXE” and “Super-SIMS”, the interdisciplinary work of IBC will be substantially extended towards the application of ion beam analysis methods in geosciences and resource technology.

Main activities of the IBC are directed to industrial applications of ion beam technologies. This activity has been continuously extended and now uses more than 20% of total beam time at IBC which is unique among all Helmholtz LK-II facilities. Commercial ion beam service is delivered via the HZDR Innovation GmbH – founded in October 2011 as a spin-off from the HZDR – by using the technical infrastructure of the IBC. This commercial use of ion facilities in close collaboration with a commercial spin-off has been defined as a reference project within the Helmholtz Association. There are numerous collaborations with renewed global companies. Main applications of ion beam technologies are in the fields of electronics, optical devices or surface engineering. Thus, the IBC contributes also to product innovation in strategic business fields.

SPIRIT

SUPPORT OF **P**UBLIC AND **I**NDUSTRIAL
RESEARCH USING **I**ON BEAM
TECHNOLOGY

Integrated Activity, EU Project No. 227012
www.spirit-ion.eu

The Institute of Ion Beam Physics and Materials Research has been coordinating the Integrated Infrastructure SPIRIT under the FP7 Capacities Programme of the European Union. A total funding volume of 6.991.000 € was made available to 11 leading ion beam facilities from 6 European Member States and 2 Associated States. After a duration of 54 months, the project has been concluded on August-31, 2013.

SPIRIT has achieved almost all of its goals with 38 out of 39 milestones and 52 out of 55 deliverables having been fulfilled. In 205 user campaigns selected by an independent European User Selection Panel, 16179 hours have been delivered to users from 25 different countries. A pronounced multidisciplinarity is demonstrated, with 53% devoted to materials science and 47% to other fields including studies in nuclear physics and astrophysics, biomedicine, forensics and earth sciences, as well as cultural heritage, environmental and nuclear materials investigations.

In Joint Research Activities, new beam lines and end stations have been created in particular for in-situ diagnostics and for the single-ion irradiation of living cells. New detectors were developed to improve radiation hardness and detection efficiency, and to minimize sample damage. A high potential of ion-beam techniques also for chemical analysis has been demonstrated in pioneering studies of secondary ion mass spectrometry under MeV ion bombardment (MeV-SIMS). New and standardized software and data formats have been created. Networking Activities have produced several brochures and flyers, and Newsletters have been edited twice per year. With a dedicated exhibition stand, SPIRIT has exhibited at Conferences and Trade Fairs. Three thematic Workshops and four Tutorials combining lectures and hands-on training were arranged. An intra-SPIRIT Technician Exchange Program has been organized. For quality control, round robin experiments with standard samples for ion beam analysis and ion implantation fluence definition have been performed among the SPIRIT infrastructures. Future trends and aspects of ion beam technologies have been investigated and documented in a Foresight Review.

Several of the SPIRIT beneficiaries are strongly involved in industrial R&D and services, with up to more than 30% of the total beam time at the individual infrastructures. During the duration of SPIRIT, a significant increase of these activities (around 20% in average) has been observed, which might be partly attributed to SPIRIT TNA and advertising and promoting activities. Further, spin-off companies for the transfer of ion technologies were founded at three of the infrastructures. For extended discussion and information, a Documentation on the Industrial Impact of SPIRIT has been issued.

The SPIRIT Consortium

The top nine partners provided Transnational Access.

Helmholtz-Zentrum Dresden-Rossendorf	Germany
CNRS – CENBG Bordeaux	France
Katholieke Universiteit Leuven	Belgium
Jozef Stefan Institut Ljubljana	Slovenia
Universität der Bundeswehr München	Germany
CEA – JANNUS Saclay and CIMAP Caen	France
University of Surrey	U.K.
University de Pierre et Marie Curie Paris	France
Ruder Boskovic Institute Zagreb	Croatia
Institute Tecnologico e Nuclear Lisboa	Portugal
Swiss Federal Institute of Technology Zurich	Switzerland

Free Electron Laser FELBE

ELBE is an acronym for the free-electron laser (FEL) at the Electron Linear accelerator with high Brilliance and Low Emittance (ELBE) located at the Helmholtz-Zentrum Dresden-Rossendorf, Germany. The heart of ELBE is a superconducting linear accelerator operating in cw mode with a pulse repetition rate of 13 MHz. The electron beam (40 MeV, 1 mA max.) is guided to several laboratories where secondary beams (particle and electromagnetic) are generated. Two free-electron lasers (U27-FEL and U100-FEL) produce intense, coherent electromagnetic radiation in the mid and far infrared, which is tunable over a wide wavelength range (4 – 250 µm) by changing the electron energy or the undulator magnetic field. Main parameters of the infrared radiation produced by FELBE are as follows:

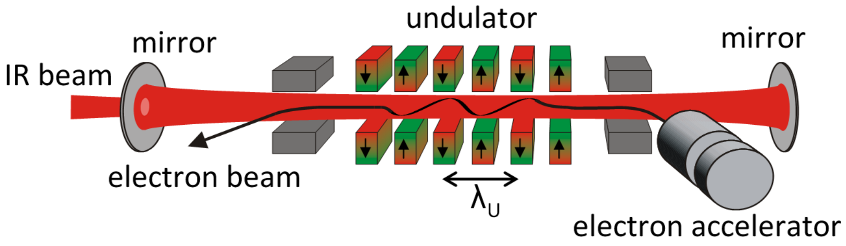

Wavelength λ	4 – 22 µm 18 – 250 µm	FEL with undulator U27 FEL with undulator U100
Pulse energy	0.01 – 2 µJ	depends on wavelength
Pulse length	1 – 25 ps	depends on wavelength
Repetition rate	13 MHz	3 modes: • cw • macropulsed (> 100 µs, < 25 Hz) • single pulsed (Hz…kHz)

The free electron laser is a user facility. Applications for beam time can be submitted twice a year, typically by April 15 and October 15. Users from EU countries can receive support through the FP7 Integrated Infrastructure Initiative (I3) CALIPSO (**C**oordinated **A**ccess to **LI**ghtsources to **P**romote **S**tandards and **O**ptimization).

Typical applications are picosecond pump-probe spectroscopy (also in combination with several other femtosecond lasers, which are synchronized to the FEL), near-field microscopy and nonlinear optics. The FELBE facility also serves as a far-infrared source for experiments at the High-Field Laboratory Dresden (HLD) involving pulsed magnetic fields up to 70 Tesla.

The statistics shows that the FEL used 1541 hours beamtime of the ELBE accelerator. This corresponds to 29 % of total beamtime, which is again distributed among internal and external users.

For further information please contact:
Prof. Manfred Helm (m.helm@hzdr.de)
or visit the FELBE webpage www.hzdr.de/FELBE.

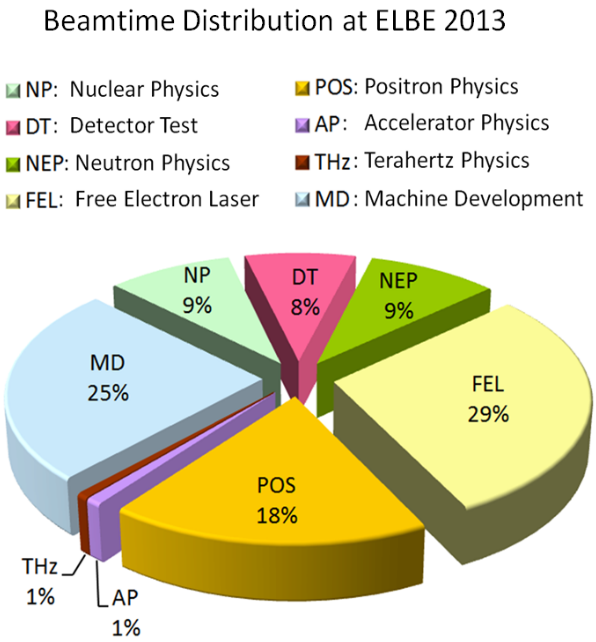

ROssendorf BeamLine (ROBL)

The HZDR operates a bending magnet beamline at the ESRF that is in user operation since 1998. Two experimental stations are available, one for X-ray spectroscopy of Actinides and other radionuclides (**R**adio **C**hemistry **H**utch RCH) and one for different kinds of diffraction and scattering experiments (**M**aterials **R**esearch **H**utch MRH). More than 660 8-hour shifts of beamtime per year are provided. Since 2012, the two alternately operated stations benefit from the complete exchange of the most important optical components. The new monochromator hosts three different sets of crystals and two different sets of multilayers. The higher photon flux of the multilayer is gained by a loss of energy resolution as displayed in the table below. In the energy range of 5 to 11.5 keV an unfocussed, parallel beam for high resolution diffraction experiments can be used, while from 9 to 35 keV the synchrotron radiation beam is focused by a toroidal mirror.

Energy resolution	$< 5\times10^{-4}$ ΔE/E (Si(111)) $< 1\times10^{-4}$ ΔE/E (Si(311)) $\sim 2\times10^{-2}$ ΔE/E (multilayer ML)
Beam size	(10×0.5) mm^2 unfocussed (0.3×0.3) mm^2 focussed
Photon flux	8×10^{9} phot./(s.mm^2) unfocussed $> 3\times10^{11}$ phot./(s.mm^2) focussed $> 2\times10^{13}$ phot./(s.mm^2) focussed ML

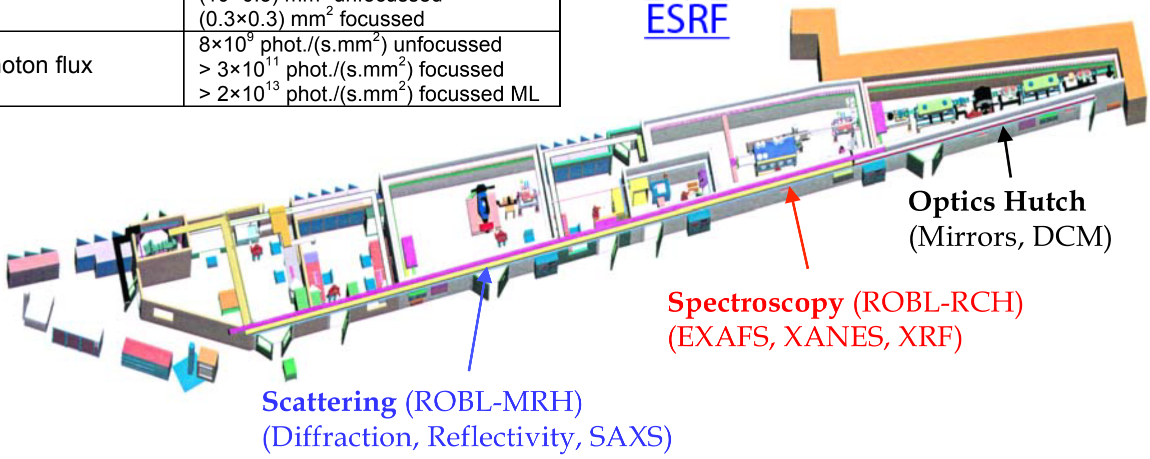

The main task of the MRH-station is the analysis of thin films, multilayers, (ion-beam synthesized) nano-sized as well as nano-structured materials by different X-ray diffraction and scattering methods like XRD, XRR, GID or GISAXS. These investigations can be combined with complementary absorption spectroscopy measurements.

In particular two specialized sample environments need to be mentioned here. A three-port magnetron sputtering chamber is available for in-situ growth and annealing studies. For surface irradiation or ion implantation experiments it is also possible to use an ion gun instead. The most requested device is a furnace equipped with a semispherical Be-dome operated under vacuum or operated close to atmospheric pressure using a dome with Kapton windows. The later setup is dedicated for in-situ measurements of different reactive gases like acetylene, hydrogen, ammonia, benzene etc. By this, hydrogen loading processes or chemical vapor depositions can be investigated. Furthermore electrical measurements of thin films during annealing can be measured in these furnaces. Additionally the six-circle goniometer hosts also sample environments provided by users like electrochemical hydrogen loading cells or lithium ion battery investigations. All these experiments aim at the correlation of structure with functionality and are the key for a better material understanding.

For further information please contact

Dr. Andreas Scheinost (ROBL-RCH): scheinost@esrf.fr
Dr. Carsten Bähtz (ROBL-MRH): baehtz@esrf.fr

or visit the ROBL webpage: www.hzdr.de/ROBL

Organization chart

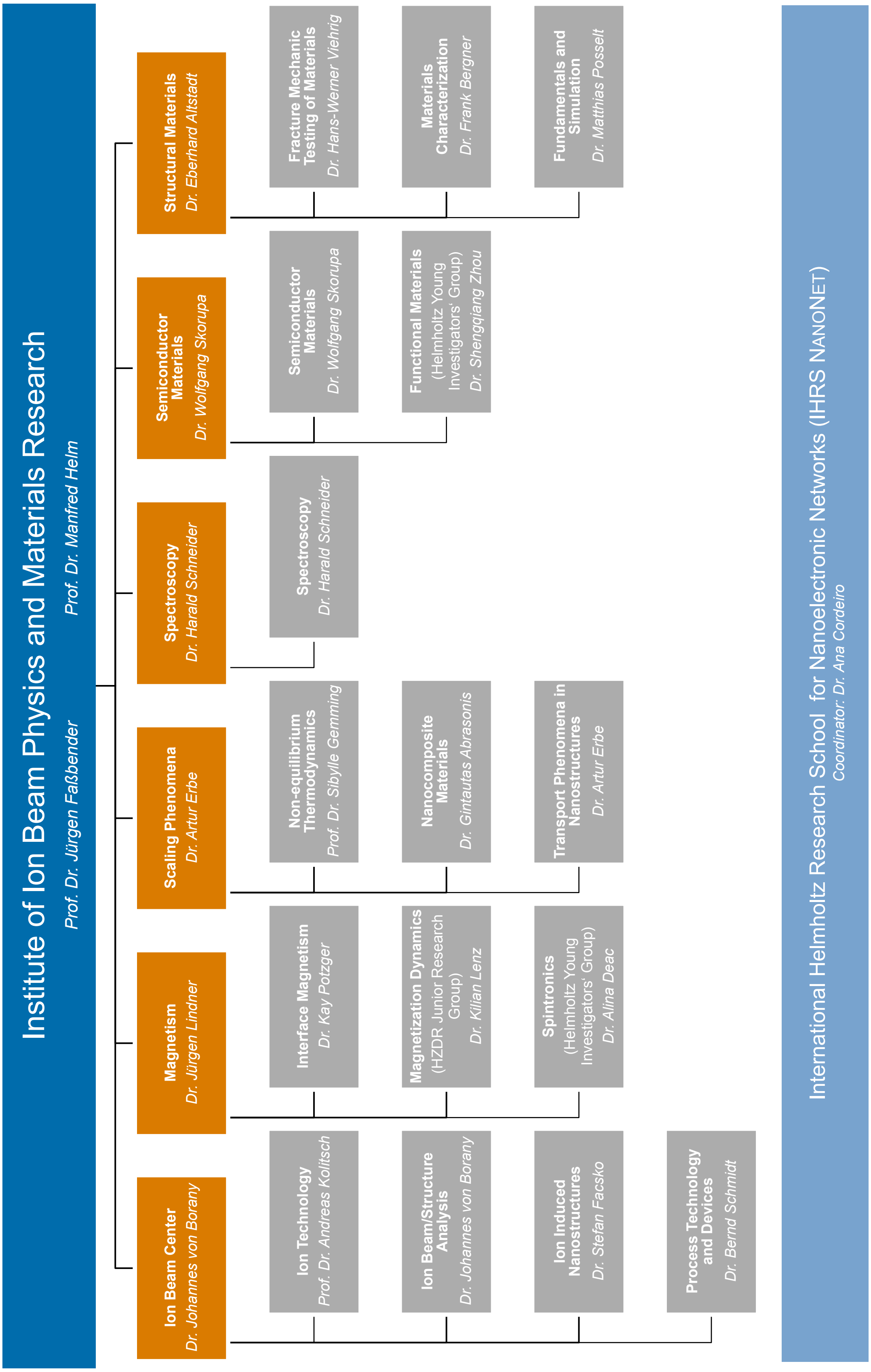

Institute of Ion Beam Physics and Materials Research
Prof. Dr. Jürgen Faßbender
Prof. Dr. Manfred Helm

- **Ion Beam Center** – *Dr. Johannes von Borany*
  - **Ion Technology** – *Prof. Dr. Andreas Kolitsch*
  - **Ion Beam/Structure Analysis** – *Dr. Johannes von Borany*
  - **Ion Induced Nanostructures** – *Dr. Stefan Facsko*
  - **Process Technology and Devices** – *Dr. Bernd Schmidt*
- **Magnetism** – *Dr. Jürgen Lindner*
  - **Interface Magnetism** – *Dr. Kay Potzger*
  - **Magnetization Dynamics** (HZDR Junior Research Group) – *Dr. Kilian Lenz*
  - **Spintronics** (Helmholtz Young Investigators' Group) – *Dr. Alina Deac*
- **Scaling Phenomena** – *Dr. Artur Erbe*
  - **Non-equilibrium Thermodynamics** – *Prof. Dr. Sibylle Gemming*
  - **Nanocomposite Materials** – *Dr. Gintautas Abrasonis*
  - **Transport Phenomena in Nanostructures** – *Dr. Artur Erbe*
- **Spectroscopy** – *Dr. Harald Schneider*
  - **Spectroscopy** – *Dr. Harald Schneider*
- **Semiconductor Materials** – *Dr. Wolfgang Skorupa*
  - **Semiconductor Materials** – *Dr. Wolfgang Skorupa*
  - **Functional Materials** (Helmholtz Young Investigators' Group) – *Dr. Shengqiang Zhou*
- **Structural Materials** – *Dr. Eberhard Altstadt*
  - **Fracture Mechanic Testing of Materials** – *Dr. Hans-Werner Viehrig*
  - **Materials Characterization** – *Dr. Frank Bergner*
  - **Fundamentals and Simulation** – *Dr. Matthias Posselt*

International Helmholtz Research School for Nanoelectronic Networks (IHRS NanoNet)
Coordinator: Dr. Ana Cordeiro

List of personnel 2013

DIRECTORS

Prof. Dr. M. Helm, Prof. Dr. J. Fassbender

OFFICE

S. Gebel, S. Kirch

SCIENTIFIC STAFF

Permanent staff

Dr. G. Abrasonis
Dr. C. Akhmadaliev
Dr. E. Altstadt
Dr. C. Bähtz
Dr. F. Bergner
Dr. L. Bischoff
Dr. J. von Borany
Dr. S. Facsko
Dr. S. Gemming
Dr. J. Grenzer
Dr. V. Heera
Dr. K.-H. Heinig
Dr. R. Hübner
Dr. R. Kögler
Prof. A. Kolitsch
Dr. A. Mücklich
Dr. G. Müller
Dr. F. Munnik
Dr. C. Neelmeijer
Dr. M. Posselt
Dr. K. Potzger
Dr. L. Rebohle
Dr. H. Reuther
Dr. B. Schmidt
Dr. H. Schneider
Dr. W. Skorupa
Dr. A. Ulbricht
Dr. H.-W. Viehrig
Dr. M. Voelskow
Dr. M. Werner
Dr. S. Winnerl

Non-permanent

Dr. R. Bali
Dr. J. Bhattacharyya
Dr. F. Bregolin (P)
Dr. A. Cordeiro (P)
Dr. A. Deac
Dr. M. Devaraj (P)
Dr. E. Dimakis
Dr. O. Drachenko (P)
Dr. A. Erbe
Dr. C. Fowley
Dr. M. Friedrich (P)
Dr. J. Grebing
Dr. C. Heintze
Dr. R. Heller
M. Houska (P)
Dr. A. Keller
Dr. M. Khalid (P)
Dr. M. Krause (P)
Dr. K. Lenz
Dr. B. Liedke (P)
Dr. J. Lindner
Prof. W. Möller (P)
Dr. A. Neudert
Dr. E. Oñorbe
Dr. X. Ou (P)
Dr. W. Pilz (P)
Dr. S. Prucnal (P)
Dr. H. Schmidt (P)
Dr. H. Schultheiß
Dr. V. Sluka
Dr. M. Vinnichenko (P)
Dr. K. Wiesenhütter (P)
Dr. R. Yankov (P)
Dr. P. Zahn (P)
Dr. S. Zhou (P)

TECHNICAL STAFF

Permanent staff

Rb. Aniol
Ry. Aniol
E. Christalle
S. Eisenwinder
B. Gebauer
D. Hanf
J. Haufe
A. Henschke
H. Hilliges
S. Klare
J. Kreher
A. Kunz
H. Lange
U. Lucchesi
F. Ludewig
R. Mester
M. Mißbach
C. Neisser
J. Pietzsch
A. Reichel
H. Richter
M. Roßner
S. Rott
B. Scheumann
G. Schnabel
A. Schneider
A. Scholz
T. Schumann
U. Skorupa
M. Steinert
U. Strauch
A. Thiel
K. Thiemig
A. Vetter
J. Wagner
W. Webersinke
R. Weidauer
A. Weise
R. Weiss
J. Winkelmann
I. Winkler
L. Zimmermann
J. Zscharschuch

Non-permanent

C. Frenzel (P)
F. Nierobisch
T. Putzke (P)
T. Schönherr (P)
I. Skorupa (P)
A. Weißig (P)

(P) Projects

PhD STUDENTS

Y. Aleksandrov
A. Banholzer
K. Bernert
D. Blaschke
A. Bogusz
R. Böttger
J. Buchriegler
M. Buhl
D. Bürger
S. Cornelius
D. Deb
R. Endler
F. Esser
M. Fehrenbacher
J. Fiedler
C. Franke
D. Friedrich
K. Gao
S. Germer
F. Günther
A. Heidarian
I. Hilger
Y. Ji
T. Kaspar
N. Klingner
M. Körner
E. Kowalska
A. Kranz
M. Langer
J. Lehmann
F. Liu
F. Lungwitz
M. Mittendorff
M. Neubert
J. Osten
B. Pelic
P. Philipp
D. Reichel
O. Roshchupkina
J. Schmidt
E. Schumann
T. Sendler
G. Steinbach
D. Stephan
M. Teich
B. Teshome
A. Wagner
Y. Wang
R. Wenisch
U. Wiesenhütter
M. Wieser
C. Wilde
R. Wilhelm
S. Wintz
R. Wutzler
O. Yildirim
Y. Yuan
S. Zybell

STUDENTS (diploma / MSc / BSc)

M. Braun
S. Bräunig
W. Feng
S. Hladki
R. Kießling
M. Kretschmer
M. Kusch
V. Liersch
S. Rupp
T. Schneider
N. Spahn
T. Warnatz
R. K. Yadav

HZDR

HELMHOLTZ
ZENTRUM DRESDEN
ROSSENDORF

Institute of Ion Beam Physics and Materials Research
P.O. Box 51 01 19 · 01314 Dresden/Germany
Phone +49 351 260-2345
Fax +49 351 260-3285
http://www.hzdr.de

Member of the Helmholtz Association